I. Observations and Photochemical Modeling of the Venus Middle Atmosphere
II. Thermal Infrared Spectroscopy of Europa and Callisto

Thesis by

Franklin Perry Mills

In Partial Fulfillment of the Requirements

for the Degree of

Doctor of Philosophy

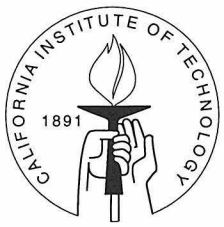

California Institute of Technology

Pasadena, California

1998

(Submitted November 21, 1997)

Acknowledgements

There are a large number of people who deserve recognition for the assistance they provided during my somewhat non-standard graduate career. The original plan for this dissertation grew out of discussions with Dave Crisp and Yuk Yung in 1992 - 1993. The goal was to conduct a series of observations that would provide a snapshot of the current conditions in the Venus middle atmosphere. Largely due to operational difficulties (instrument problems, telescope malfunctions, forest fires, and of course clouds), this dissertation evolved to its present emphasis on photochemical modeling of the Venus atmosphere. Nevertheless, observations were attempted or conducted at the Anglo-Australian Telescope (AAT), the NASA Infrared Telescope Facility (IRTF), Palomar Observatory, and the Caltech Submillimeter Observatory (CSO). The staff of all four observatories were very helpful in preparing for and conducting the observations. Special thanks are due to Dave Crisp for funding and assisting with the acquisition of data at the AAT and the IRTF. Mike Brown provided funding for the observations from Palomar which are described in Chapter 4 and assisted greatly with acquiring, processing, and analyzing the spectra. Gene Serabyn and Taco assisted in trying to collect useful data at the CSO. Tom Greene, Tom Hayward, Vikki Meadows, and Sean Ryan also assisted with data acquisition and generously lent their expertise in planning the observations. Dave Crisp, Vikki Meadows, and Alycia Weinberg provided needed advice on processing the spectra that were collected at a time when the planetary science department had no active optical spectroscopists. The high-resolution spectrometers used for the optical observations were developed by Francisco Diego and the astronomical optics group at Imperial College in London, Tom Greene and the Institute for Astronomy at the University of Hawaii, and Tom Hayward and colleagues at Cornell University. There is little present demand within the astronomical community for spectrometers with such high-resolution but the instruments they designed are excellent for planetary astronomy.

The photochemical modeling described in Chapter 2 would not have been possible without the efforts of a large supporting cast of laboratory chemists who are noted in the bibliography. Thanks are due to Mark Allen, Yuk Yung, and many previous graduate students for developing the standard photochemical model code. Thanks are also due to Mark Allen for suggestions on how to modify the code to suit the particular conditions that were examined in this work. Steve Bougher, Bill DeMore, Joop Hovenier, Jeffrey Joens, Stan Manatt, Julie Moses, Mitchio Okumura, Leon Phillips, Stan Sander, Tom Slanger, Mike Summers, Eric Weisstein, and Kouichi Yoshino provided either photochemical data and/or advice that is greatly appreciated.

The radiative transfer model used for interpretation of the observations in Chapter 1 was developed by Dave Crisp. The code works well once one finds the options that have been correctly implemented, and Dave freely advised how the code should be used. In addition, Dave provided many hours of instruction on the science and art of radiative transfer modeling.

Helpful reviews of material presented in this dissertation were provided by Mike Brown, Don Burnett, Barbara Burns, Dave Crisp, Peter Goldreich, Dave Hansen, Jack Salisbury, John Spencer, Albert Yen, and Yuk Yung. Barbara Burns, Albert Haldemann, and Ute Zimmerman assisted in translating some of the French and German articles that were consulted. The computing facilities that were used were provided by Arden Albee, Mark Allen, Mike Black, Dave Crisp, Ed Danielson, Eric De Jong, Cheryl Southard, Karl Stapelfeldt, and Yuk Yung. Mike Black assisted with setting up and using the planetary science computing facilities. Somehow he always managed to find a way to do what was needed.

Partial funding for this research was provided by Mark Allen and Yuk Yung via NASA grants NAGW-3507, NAGW-4334, NAG1-1806, and NAG5-6263 from NASA's Venus Data Analysis Program, Planetary Atmospheres Program, and Planetary Astronomy Program. Additional funding was provided by Dave Crisp and Henry Sinton via other NASA grants. Dave Crisp's assistance with developing and writing a coherent (and successful) grant proposal are gratefully acknowledged.

Thanks are also due to Steve Frautschi, Peter Goldreich, Andy Ingersoll, Dewey

Muhleman, and John Trauger for academic advice and assistance with the research projects I submitted for my Oral Candidacy Exam. Irma Betters, Kay Campbell, Donna Driscoll, Tammie Henderson, Donna Lathrop, Carolyn Porter, and Donna Sackett assisted with the various administrative tasks that necessarily accompany student life. Arden Albee, Bob Sharp, and Lee Silver organized geology field trips that were both educational and fun. Thanks. Yuk Yung gave me substantial freedom (perhaps too much?) to work independently and look for interesting problems. Thanks for providing the opportunities.

Since I first arrived at Caltech in 1984, there are three generations of graduate students and ~ 1.3 generations of faculty whom I have had the privilege to know. In addition, there are many more people whom I met or worked with during my seven year leave of absence between the second and third years of graduate school. I hope all of you have found our time together as rewarding as I. It would not be possible to provide a complete list of everyone who indirectly assisted with completion of my graduate studies, but there are some people who should be mentioned. Conversations and courses with Karl Stapelfeldt, Deborah Padgett, Steve Fels, Dave Crisp, and others at the Geophysical Fluid Dynamics Laboratory in Princeton changed my career interests from aeronautical engineering to atmospheric and planetary science. Thanks go to John Trauger for taking me to my first telescope, the 100-inch at Las Campanas in Chile. Cole Miller helped me survive graduate physics classes for which I had taken none of the typical undergraduate prerequisites. Kip Thorne taught great physics classes that successfully conveyed the philosophy that physics is not just equations. Brian Sandford provided a great experience in the Air Force, and the Infrared Signatures group is still a good example of a cooperative research program. Bridget Landry introduced me to ballroom and historical ethnic dance. The encouragement and support of the many groups with whom I have danced (Merrie Pryanksters, Commonwealth Vintage Dancers, Tokyo Scottish Blue Bell Club, Clan MacLeod Dancers, Celtic Spirit, and others) is greatly appreciated. Finally, thanks are due to my parents, Amy Lamborn Mills and Donald Mills, and Barbara Burns for their love, encouragement and not quite infinite patience in completing this endeavor.

Overview

The evolution of our solar system remains one of the most fascinating questions since ancient astronomers first realized that the "stars" which do not twinkle are planets. In the modern era, the future evolution of the Earth has become a topic that may arise even in lay conversations. For example, the effects of changes in the earth's climate and the ozone layer are debated in policy and economic discussions as well as in scientific forums. One method for assessing our understanding of the Earth's atmosphere is to examine the atmospheres of the other terrestrial planets. The atmospheres of Venus and Mars share some common features with that of the Earth, but there are important differences. These differences are important because they force us to examine the often implicit assumptions that lie within the tunable parameters that exist in all models. Consequently, studies of the atmospheric chemistry on Venus and Mars can provide a test of the degree to which our understanding of the fundamental physical and chemical principles that govern the Earth's atmosphere is correct.

The chemistry of the Martian atmosphere has been "solved" to the extent that modern photochemical models [e.g., *Nair et al.* 1994] can reproduce the primary observable characteristics to within a factor of $2 - 3$ using the results from laboratory studies of photochemical reaction rates. The chemistry of the Venus atmosphere, however, remains an "unsolved" problem in that the differences between the most recent generation of models [*Yung and DeMore* 1982] and some of the existing observations are greater than a factor of 10. The first part of this dissertation (Chapters 1, 2, and 3) combines several lines of research that focused on how the discrepancy between models and observations of the Venus atmosphere can be reduced. (The appendices for Chapter 2 are in Chapter 5.) The results provide a better understanding of the current photochemical processes in the Venus atmosphere and can serve as a baseline for future studies of its evolution.

The intervening chapter reports observations of Europa and Callisto in the $8 -$

13μm wavelength region. Those observations provide constraints on the composition and/or physical state of the surficial material on the two satellites.

Part I (Observations and Photochemical Modeling of the Venus Middle Atmosphere)

The primary photochemical cycle of the Venus middle atmosphere (within and above the upper cloud layer) is the photolysis of CO_2 to form CO and oxygen atoms on the dayside followed by the reformation of CO_2 from CO and oxygen, primarily via catalytic reactions. Previous photochemical models–using ClO_x, SO_x, NO_x, and HO_x radicals to catalyze the reformation of CO_2–could qualitatively explain the stability of Venus' CO_2 atmosphere. Despite the powerful catalytic reactions introduced, however, none of the previous models could quantitatively explain either the low column abundance of molecular oxygen or the intense nightside airglow in the $O_2(a^1\Delta)$ band. The most comprehensive of the previous models, that by *Yung and DeMore* [1982], predicted a column abundance of molecular oxygen that was a factor of $\sim$ 30 larger than the upper limit obtained the following year [*Trauger and Lunine* 1983], and it predicted a nightside airglow that was about three-quarters of the observed intensity. These discrepancies suggested that significant gaps remained in our understanding of the dominant chemical processes in the Venus middle atmosphere.

In the fifteen years since these studies, new observations have provided further insight into the current state of the Venus atmosphere, and our understanding of chlorine and sulfur chemistry has improved as a result of laboratory and field studies related to the terrestrial stratosphere. One idea that had been proposed is that the abundance of O_2 in the Venus atmosphere might vary by as much as a factor of 10 over time scales of years. This proposal was based on observations of SO_2 and SO at the top of the Venus clouds which showed a monotonic decrease in the abundances of both species from 1980 to 1995 with SO_2 declining by a factor of 10 and SO by a factor of 5. An alternate proposal was that rapid reactions on aerosol particles, such as

$$HOCl + HCl + \text{aerosol} \rightarrow H_2O + Cl_2 + \text{aerosol} \qquad \text{(G10)}$$

which converts Cl from a relatively nonreactive form, HCl, to a potentially highly reactive form, Cl_2, could greatly enhance the effectiveness of the chlorine catalytic reactions that oxidize CO to CO_2.

This project has attempted to reconcile the differences between observations and photochemical models with regard to the oxygen budget of the Venus middle atmosphere. To examine the potential temporal variability of the O_2 abundance, we attempted to detect molecular oxygen on the dayside of Venus using the Ultra-High Resolution Facility at the Anglo-Australian Telescope on 23 January 1995. We observed the 763.6325 and 763.2165 nm O_2 lines at a spectral resolving power, $\lambda/\Delta\lambda$, of 600000 with a square, 1.5 arc-second field of view. These observations reveal no evidence for O_2 above the Venus cloud tops within our detection limit which is equivalent to a uniform vertical mixing ratio of 3 ppm. Our upper limit on the abundance of O_2 in the Venus middle atmosphere is comparable to that obtained by *Traub and Carlton* [1974] and is a factor of ten larger (less stringent) than that obtained by *Trauger and Lunine* [1983] ($2\sigma = 0.3$ ppm). Within the obvious limitations imposed by the relative sensitivities of the non-detections, we find no evidence for an increase in the abundance of O_2 in association with the observed decreases in SO_2 and SO abundances.

The parallel branch to new observations was development of a new photochemical model for the Venus middle atmosphere that incorporates the most recent chemical kinetic rates and photoabsorption cross sections. Our one-dimensional, steady-state photochemical model can reproduce (within measurement uncertainty and temporal/spatial variability) the retrieved SO profile [*Na et al.* 1994], the retrieved SO_2 abundance and scale height at the cloud top [*Na et al.* 1994], the retrieved CO profile [*Clancy and Muhleman* 1991], and the observed "global average" $O_2(a^1\Delta)$ airglow [*Crisp et al.* 1996] using only gas-phase chemistry if we adjust key reaction rates within their assessed one standard deviation uncertainties. Our predicted column abundance for O_2 is a factor of 10 smaller than than from previous models. Our results suggest SCl_x and $ClSO_x$ compounds may be important in the chemistry of the upper cloud layer, and we find that Reaction G10 is not an important source of Cl_2

above the cloud top.

The current observational upper limit can be reconciled with the predictions from our photochemical model if one examines the absorption produced by our predicted O_2 distribution instead of the column abundance. Our model predicts that most of the O_2 in the Venus atmosphere will be located between 85 and 95 km altitude, several scale heights above the cloud top ($\sim$ 70−75 km altitude) and, thus, above the region in which multiple scattering is important. Radiative transfer model calculations indicate that the absorption due to our predicted O_2 distribution is equivalent to that produced for a uniform vertical distribution of O_2 with mixing ratio of 0.3 ppm, the two standard deviation upper limit from the observations. If the equilibrium constant for ClCO is adjusted by two standard deviations and the temperatures at $85 - 95$ km altitude are decreased by $\sim 15 - 20$ K (two standard deviations), the predicted O_2 absorption will lie below the observed one standard deviation upper limit.

Part II (Thermal Infrared Spectroscopy of Europa and Callisto)

The trailing hemispheres of Europa and Callisto were observed and a $9 - 13$ μm spectrum of Europa with better spectral resolution and better signal-to-noise than was previously possible has been derived. The ratio spectrum of the two satellites has a signal-to-noise ratio of approximately 30 and spectral resolving power of approximately 50. The ratio spectrum was combined with the average Voyager 1 spectrum of Callisto from *Spencer* [1987a] to obtain a $9 - 13$ μm spectrum of Europa with signal-to-noise that is a factor of 10 better than that in the average Voyager spectrum of Europa in *Spencer* [1987a]. No emissivity features due to water ice are apparent at the 3% level in our Europa spectrum. The disk-integrated, effective color temperature ratio for the two satellites is consistent with previous ground-based, broadband, thermal infrared photometry. One possible explanation for the absence of features in the thermal infrared spectra of Europa (at the 3% level) and Callisto (at the 1% level) is if the surfaces of both satellites have significant abundances of small particles ($\lesssim$ 50 micrometer in size). This explanation is consistent with most of the published observations by *Galileo*.

Contents

List of Figures

List of Tables

Chapter 1

A Spectroscopic Search for Molecular Oxygen in the Venus Atmosphere

Franklin P. Mills

Division of Geological and Planetary Sciences

California Institute of Technology

Pasadena, CA 91125

and

David Crisp

Jet Propulsion Laboratory

California Institute of Technology

Pasadena, CA 91109

1.1 Introduction

This chapter presents the results of new observations that attempted to determine the column abundance of molecular oxygen above the Venus clouds. The column abundance of molecular oxygen in the middle atmosphere has been below the detection limit of both previous earth-based spectroscopic observations [*Traub and Carleton* 1974; *Trauger and Lunine* 1983], but theoretical speculation has suggested that the column abundance of O_2 might have increased significantly in response to the observed decline in the abundances of SO_2 and SO at the cloud tops since 1982 [*Na et al.* 1994; *Na and Esposito* 1995].

A primary source of O_2 in the Venus atmosphere is believed to be the recombination of atomic oxygen (Chapter 1),

$$2O + M \rightarrow O_2 + M, \tag{G3}$$

where the atomic oxygen is produced by photolysis of CO_2. (M is a third molecule which collides with the intermediate complex formed by the two reacting species. The third molecule removes sufficient energy from the intermediate complex that the intermediate complex can form the stable product molecule.) CO_2, the primary constituent of the atmosphere of Venus (and Mars), is photolyzed by ultraviolet radiation (primarily at wavelengths $\lesssim$ 200 nm) to form CO and atomic oxygen. The direct three-body reaction to reform CO_2,

$$CO + O + M \rightarrow CO_2 + M, \tag{G2}$$

is spin-forbidden so it is five orders of magnitude slower than the competing reaction, Reaction G3, at the temperatures typical of planetary atmospheres. Consequently, atomic oxygen has a strong tendency to recombine as O_2. Both CO and O_2 are sufficiently stable that, in the absence of other species, mixing ratios of $\sim$ 7% for CO and $\sim$ 3.5% for O_2 would exist in steady-state in an atmosphere that was initially pure CO_2 [*Nair et al.* 1994].

The observed abundances (or upper limits) for CO and O_2 in the atmospheres of both Venus and Mars are significantly smaller than predicted by this simple model

due to the catalytic effect of trace constituents on the recombination rate for forming CO_2 from CO and oxygen. The observed column mixing ratios of CO and O_2 in the Martian atmosphere ($\sim 7\times10^{-4}$ and $\sim 1\times10^{-3}$, respectively) have been quantitatively explained by photochemical models that invoke gas-phase catalytic reactions involving hydrogen compounds (H, OH, and HO_2–collectively known as HO_x) and nitrogen compounds (N, NO, NO_2, NO_3, and N_2O_5–collectively known as NO_x) [*Nair et al.* 1994].

Photochemical models of the Venus middle atmosphere ($\sim 65-100$ km altitude), however, have not achieved comparable success. The most complete previous models [*Yung and DeMore* 1982] predicted a molecular oxygen abundance that is a factor of $>$ 10 larger than the current upper limit [*Trauger and Lunine* 1983]. This disagreement is the most egregious failing of current models of the Venus atmosphere. In addition, the lack of a definitive observation of the abundance of O_2 in the Venus atmosphere is the primary uncertainty in photochemical models.

The present attempt to detect molecular oxygen above the Venus clouds was prompted by the observed decrease in the abundances of SO_2 and SO at the cloud tops and speculation, based on predictions from the *Yung and DeMore* [1982] models, that a decrease in the abundance of SO_2 and SO could lead to a comparable increase in the O_2 abundance. The basis for this speculation is found in the primary reactions by which CO is oxidized to CO_2 while O_2 is simultaneously destroyed. In *Yung and DeMore*'s [1982] model C, the primary means by which these two processes occur is by the following series of sequential reactions.

$$Cl + CO + M \rightarrow ClCO + M$$

$$ClCO + O_2 + M \rightarrow ClCO_3 + M$$

$$ClCO_3 + Cl \rightarrow Cl + CO_2 + ClO$$

$$net : Cl + \ CO + O_2 \rightarrow ClO + CO_2$$

If the ClO reacts with SO

$$ClO + SO \rightarrow Cl + SO_2,$$

then there is a net destruction of O_2 accompanying the oxidation of CO to CO_2. If ClO combines with O

$$ClO + O \rightarrow Cl + O_2,$$

then there is no net destruction of O_2 in the process. In *Yung and DeMore*'s [1982] model C, the rates for these two losses of ClO are comparable (to within a factor of two) at 70 - 80 km altitude. Thus, if the abundance of SO decreases while the atomic oxygen abundance remains constant, then the abundance of O_2 will increase.

The cloud top abundances of SO_2 and SO in model C by *Yung and DeMore* [1982] were 30 ppb and 1 ppb respectively. These values are comparable to the most recent observed values [*Na and Esposito* 1995]. At the time of *Trauger and Lunine*'s [1983] attempt to detect O_2, however, the SO_2 abundance was a factor of ~ 3 larger and the SO abundance was a factor of ~ 10 larger [*Esposito et al.* 1988; *Na et al.* 1990; *Na et al.* 1994] than in *Yung and DeMore*'s [1982] model C. Scaling the *Yung and DeMore* [1982] results, the observed factor of ~ 3 decrease in the SO_2 abundance and the observed factor of ~ 10 decrease in the SO abundance since 1982 could produce a factor of $\sim 3 - 10$ increase in the O_2 abundance. The amount of change in the O_2 abundance would depend on what secondary reaction(s) become the limiting factors in the destruction of oxygen. These model predictions, however, suggest that if the O_2 abundance in 1982 was just below the upper limit set by *Trauger and Lunine* [1983], then a new attempt to detect O_2 might now succeed.

1.1.1 Previous Observations

The presence of molecular oxygen in the Venus atmosphere has been established by observations of airglow emission in the 1.27 μm band [e.g., *Connes et al.* 1979; *Crisp et al.* 1996]. This airglow is produced when O_2 in its lowest excited electronic state decays via a magnetic dipole transition to the ground electronic state, emitting a photon near 1.27 μm. The airglow observations cannot, however, be used to determine

the column abundance of molecular oxygen. First, the airglow observations give only a lower limit on the production rate of O_2. The actual production rate for O_2 could be inferred from laboratory and modeling studies, but none of the published modeling studies [e.g., *Yung and DeMore* 1982; *Bougher and Borucki* 1994] has been able to quantitatively reproduce the observed intensity of the airglow, $\sim 1.1 \times 10^{12}$ cm^{-2} s^{-1}, when temporally and spatially averaged over the nightside [*Crisp et al.* 1996]. Hence, the mechanism by which O_2 in the excited $^1\Delta$ state is produced is uncertain. The second reason the airglow cannot be used to infer the column abundance of O_2 is that the loss mechanisms for O_2 in the Venus middle atmosphere are highly uncertain. The loss rate for O_2 is linearly proportional to the O_2 abundance and in steady-state equals the O_2 production rate. However, the dominant reaction(s) that control loss of O_2 are not known so the rate constant for loss of O_2 is uncertain. A third reason the airglow cannot be used to estimate the column abundance of O_2 is that the altitude at which the airglow is produced has not been determined. The proposed mechanisms for production and loss of O_2 have rates that vary significantly with altitude so the O_2 abundance required for loss to balance production is highly dependent on altitude.

In-situ measurements of the O_2 abundance, reviewed in *von Zahn et al.* [1983], have yielded only two marginal detections: equivalent to volume mixing ratios of $(4.4\pm2.5)\times10^{-5}$ at 52 km altitude and $(1.6\pm0.7)\times10^{-5}$ at 42 km altitude [*Oyama et al.* 1980]. If accepted, these O_2 abundances would seem to require thermal disequilibrium below the Venus clouds since the reported O_2 abundances are not compatible with simultaneous measurements of CO, SO_2, and H_2O [*von Zahn et al.* 1983]. *von Zahn et al.* [1983], consequently, recommended discounting the validity of the marginal detections by *Oyama et al.* [1980]. Even if the detections by *Oyama et al.* [1980] were accepted, the uncertainties introduced by their extrapolation through the cloud layers to the middle atmosphere preclude their use for photochemical modeling of the middle atmosphere.

Spectroscopic searches for O_2 above the Venus clouds using the oxygen A band lines at 763.5 and 763.6 nm ($b^1\Sigma \leftrightarrow X^3\Sigma$)were made by *Traub and Carleton* [1974] and *Trauger and Lunine* [1983]. *Traub and Carleton* [1974] reported an upper limit

equivalent to a column mixing ratio of $\sim 1 \times 10^{-6}$ based on finding no evidence for absorption by Venusian molecular oxygen. *Trauger and Lunine* [1983] reinterpreted the *Traub and Carleton* [1974] result to be the equivalent of a column mixing ratio of $\sim 2 \times 10^{-6}$ based on evidence from *Pioneer Venus* that the cloud top was at $\sim$ 50 mbar instead of the $\sim$ 300 mbar level used in *Traub and Carleton*'s [1974] initial analysis. *Trauger and Lunine* [1983] also reported a 2σ upper limit based on their own non-detection of Venus O_2 that is equivalent to a column mixing ratio of $\sim 3 \times 10^{-7}$. Figures 1.1 and 1.2 present the spectra obtained by *Trauger and Lunine* [1983] for Venus and Mars, respectively.

1.1.2 Approach

Our observations are conceptually similar to those by *Traub and Carleton* [1974] and *Trauger and Lunine* [1983], although there are important differences in instrumentation. The source of the observed radiation is sunlight that has been reflected toward the Earth by the Venus clouds (cloud top $\sim$ 70 km altitude). As a result, the observed radiation has passed through the Venus middle atmosphere twice and may have been multiply scattered by aerosols within the upper cloud or the overlying haze. The O_2 lines selected for study were the P7P7, P9Q8, and P9P9 transitions of the Fraunhofer A band with rest line centers at 763.2165, 763.5191, and 763.6325 nm. All three lines have similar strengths (8.5, 7.3, and 8.4 $\times 10^{-24}$ $cm^{-1}/(molecule\ cm^{-2})$ in the 1996 edition of the HITRAN database [*Rothman et al.* 1992]) and all three lines were simultaneously within our free spectral range (0.66 nm). In addition, the number of molecules in the ground-states corresponding to these transition lines should differ by less than 15% at temperatures representative of the Venus middle atmosphere. A positive detection, therefore, should be seen at all three wavelengths and this would provide further confidence in the results. The 763.6325 nm line was used by *Trauger and Lunine* [1983] for their Venus observations, facilitating direct comparisons with their results.

The selected O_2 lines are strongly saturated in the telluric atmosphere so they

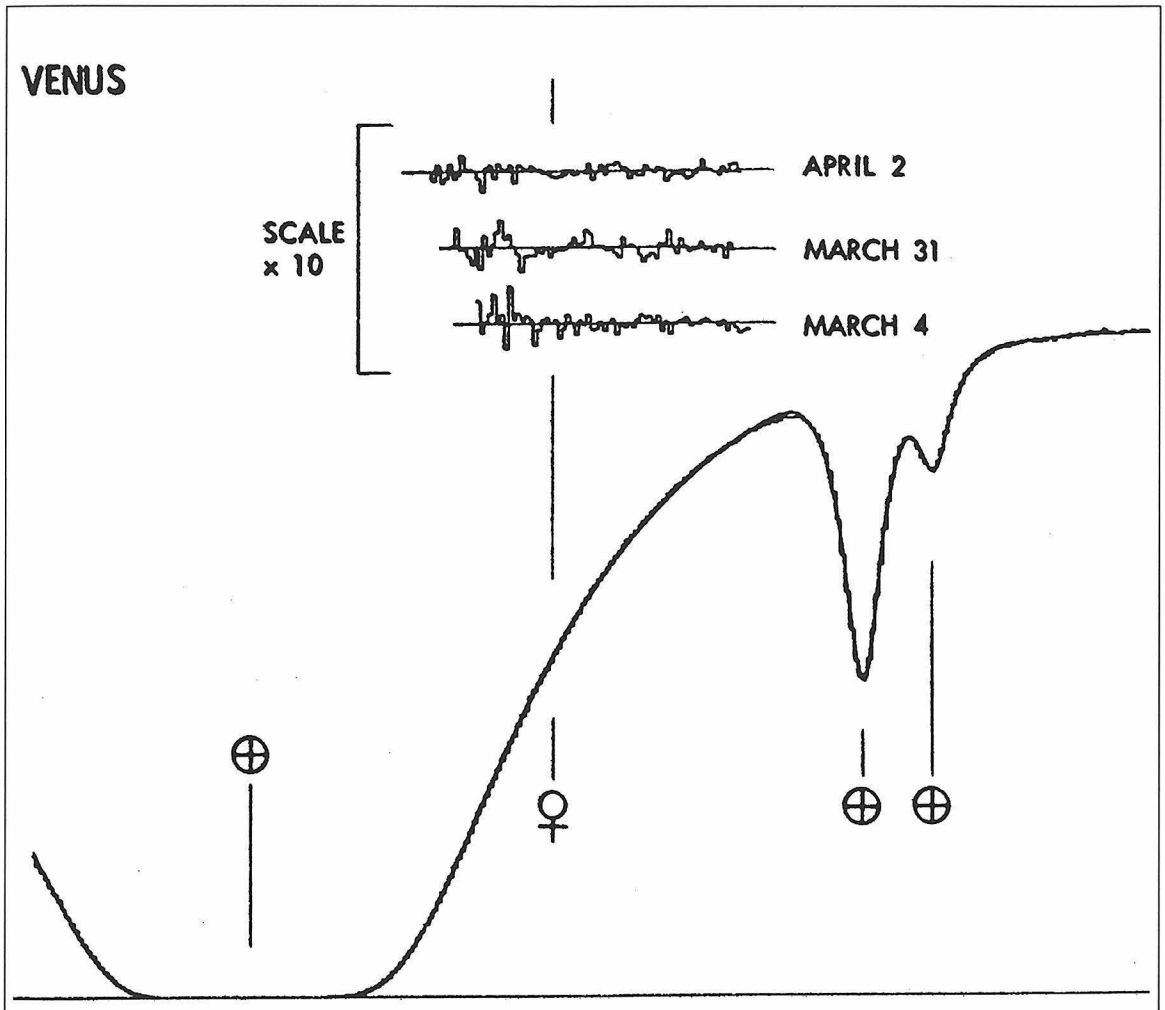

Figure 1.1: "Spectra at the predicted position of the O_2 P(9) line in the atmosphere of Venus. From left to right, the terrestrial features ($\oplus$) are $^{16}O_2$ P(9) (763.6328 nm), $^{18}O^{16}O$ Q(11) (763.7183 nm), and $^{17}O^{16}O$ P(10) (763.7276 nm). In the inset, three Venus spectra corrected to remove terrestrial lines, on a scale expanded in the vertical dimension by a factor of 10 are shown. No significant feature is seen at the predicted position for the Doppler-shifted Venus P(9) line." [*Trauger and Lunine* 1983]

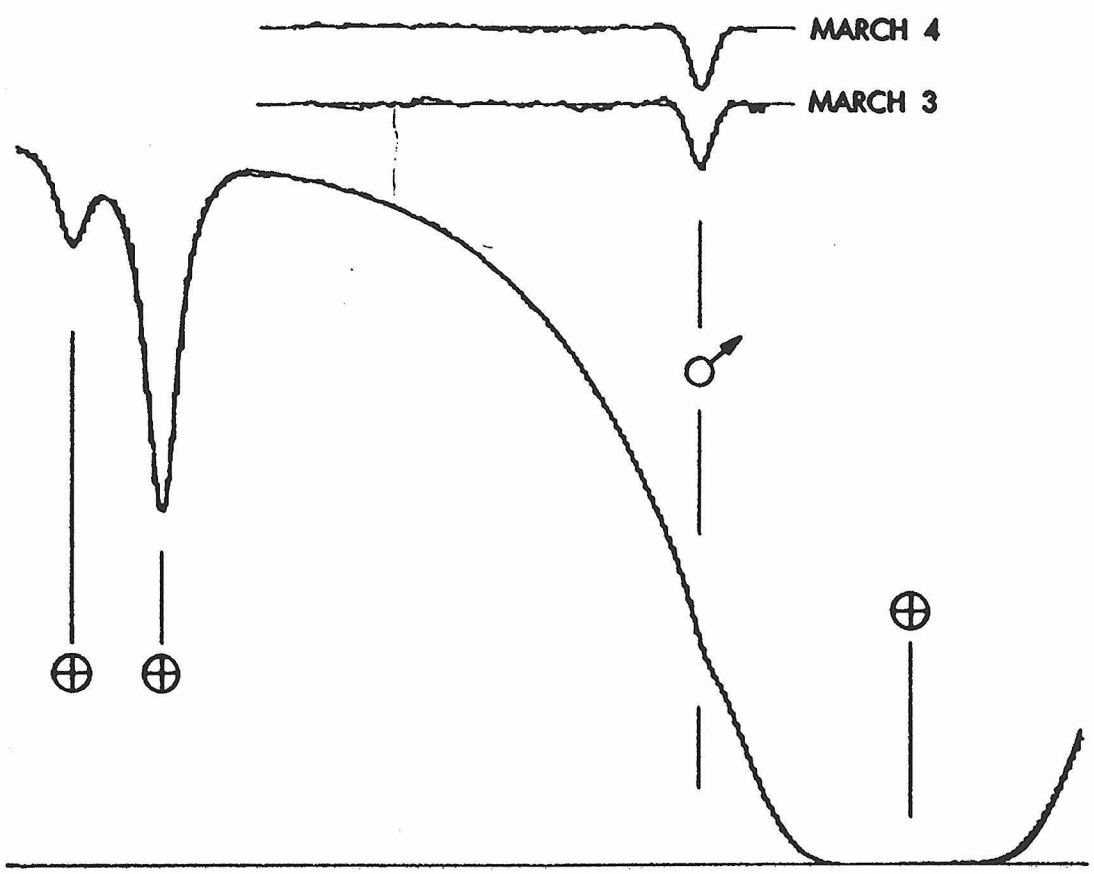

Figure 1.2: "Fabry-Perot spectra of Mars, in the P branch of the molecular oxygen A band. Listed from left to right, the terrestrial(⊕) lines are $^{17}O^{16}O$ Q(9) (763.4052 nm), $^{18}O^{16}O$ P(9) (763.4170 nm), and $^{16}O_2$ Q(9) (763.5192 nm). The Mars feature is the Doppler-shifted $^{16}O_2$ Q(9) line. In the inset, two Mars spectra after division to remove the terrestrial features are shown." [*Trauger and Lunine* 1983]

are only observable on Venus when the motion of Venus relative to the Earth along the line of sight to the Earth is sufficient to Doppler shift the Venus lines away from the saturated cores of their telluric counterparts. The Doppler shift is maximized twice in each 18 month period when Venus is near quadrature. For the time of our observations, Venusian O_2 lines would be expected to be shifted to larger wavelengths by $\sim 3.33 \times 10^{-2}$ nm due to the line-of-sight motion of Venus relative to the Earth. A smaller shift to smaller wavelengths, $\sim 5.9 - 10.2 \times 10^{-4}$ nm for the zenith angles at which we observed Venus, is expected due to the diurnal rotation of the Earth. The maximum wavelength difference resulting from the change in viewing zenith angle (4×10^{-4} nm) is < 0.67 pixel so it has been neglected. The maximum Doppler-shift due to the $\sim$ 100 m s^{-1} Venus cloud-top winds would be $\sim 2.6 \times 10^{-4}$ nm (< 0.5 pixel and smaller than the maximum uncertainty in the wavelength calibration) so it also has been neglected. The net Doppler-shift expected for the Venusian O_2 lines relative to the telluric lines is $\sim 3.24 \times 10^{-2}$ nm toward larger wavelengths. Spectra of the Moon and the air in the Coude room were used to confirm identification of the telluric O_2 lines.

Previous observations were done with an instrumental spectral resolution (full-width at half-maximum, FWHM) that was larger than the expected width of the Venus O_2 lines. Our observations were done at better spectral resolution than the previous observations to improve overall instrument throughput and to approximately match the instrumental resolution to the expected width of the Venus O_2 lines. If the O_2 lines are formed at high altitudes on Venus as predicted by analysis of the results from photochemical models (Chapter 3), then the better spectral resolution used for this study improves the ability to detect the Venus absorption lines. If the Venus O_2 lines form at the pressures assumed by *Trauger and Lunine* [1983], then the better spectral resolution used for this study will not improve the ability to detect the Venus absorption lines.

Unfortunately, there is significant uncertainty in the expected widths of the Venus O_2 lines because the distribution of molecular oxygen above the Venus clouds is unknown and because the CO_2-broadened widths of O_2 lines have not been deter-

mined. At minimum, the Venus O_2 lines would have a Doppler-broadened FWHM of $\sim 8 \times 10^{-4}$ nm if formed at an effective altitude of 84 km (2 mbar, near the temperature minimum in the middle atmosphere [*Seiff* 1983]). If the Venus O_2 lines were formed at an effective altitude of 68 km (50 mbar, optical depth $\sim$ 1 - 2 due to scattering by particles within the upper cloud layer), then the Lorentz-broadened FWHM for broadening of O_2 by air would be $\sim 3 \times 10^{-4}$ nm. If the Venus O_2 lines were formed at an effective altitude of 56 km (450 mbar, the base of the upper cloud, see Section 1.4), the Lorentz-FWHM for broadening by air would be $\sim 3 \times 10^{-3}$ nm. Consequently, for our measured instrumental FWHM of 1.1×10^{-3} nm (approximately 1.7 pixels), the expected FWHM for a Venusian O_2 line in our spectrum is $2-5$ pixels. Based on this range of possible widths for line Venus O_2 lines, the signal-to-noise ratio in the measured spectra might have been improved by using a factor of two worse spectral resolution. However, if we had tried to use a factor of two worse spectral resolution, we would have had to decrease the size of the UHRF entrance aperture by more than a factor of two to prevent overlapping orders at the detector. This would have resulted in a net *decrease* in instrument throughput and a net *decrease* in the measured signal-to-noise ratio.

1.2 Observations

Venus was observed during morning twilight and daylight on January 23, 1995, from 18:00 - 23:00 UT (9:00 - 12:00 local time) from the Anglo-Australian Observatory using the 4-meter Anglo-Australian Telescope and the Ultra-High-Resolution Facility (UHRF) instrument [*Diego et al.* 1995]. Venus' diameter was 22 arcsec and the solar phase angle was 84 degrees. The sub-Earth and sub-solar latitudes were both -2.4 degrees. Typical seeing was $3-4$ arcsec and the telluric airmass through which we observed was between 2.0 and 1.2 (airmass = $sec(\mu)$ where μ = the angle from the zenith). UHRF was used in its medium resolution mode (nominal resolving power $\sim 6 \times 10^5$) with the confocal image slicer dekker [*Diego* 1993] and the thinned Tektronix CCD. The entrance aperture was approximately 1.5×1.5 arcsec^2. The integration

time for a single Venus spectrum was typically 10 minutes to give a signal-to-noise ratio of $\sim$ 700 *in the continuum region between the telluric O_2 absorption lines.* Venus and the sky 120 arcsec south of Venus were observed alternately to determine the contribution due to scattered light from the Earth's atmosphere during the rapidly changing illumination of morning twilight. The UHRF field-of-view was positioned on the sunlit morning quadrant of Venus near its equator and about $30 - 45$ degrees of longitude from the sub-Earth longitude (which was approximately the morning terminator).

Trauger and Lunine [1983] and *Traub and Carleton* [1974] used multi-etalon Fabry-Perot interferometers for their observations. *Trauger and Lunine* [1983] were able to achieve a better signal-to-noise ratio ($\sim$ 1300 *in the continuum region between the telluric O_2 absorption lines*) than the observations reported here due, primarily, to the larger angular field of view of their instrument (effectively one-half of a hemisphere of Venus compared to our 1.5×1.5 arcsec^2 field of view). The longer integration time (due to observing all wavelengths simultaneously) and the larger telescope (the AAT 4-meter compared to Mount Wilson's 2.5-meter) for the current observations partially compensated for the field-of-view advantage in the *Trauger and Lunine* [1983] measurement.

1.2.1 Data Processing and Wavelength Calibration

The UHRF may be used with either a long slit or an image slicer at the entrance aperture. When used with the image slicer as we did, the UHRF does not preserve spatial information but the aperture is projected along a finite band across the detector. The output from the 1024×1024 UHRF detector was summed into four pixel bins parallel to the projected slit for recording. The full spectral resolution was maintained. A median bias frame was subtracted from each data frame then the result was divided by a median detector response frame. A data spectrum was derived by averaging parallel to the projected slit. A sky spectrum and an off-axis scattered light spectrum were subtracted from each data spectrum to produce an object spectrum. Bad pixels

were excluded from the data spectra and the off-axis scattered light spectra prior to the averaging.

The Venus spectra were obtained at sufficiently different airmasses that the spectra could not be directly added to try to improve the signal-to-noise ratio. Instead, we computed a (delta-intensity/intensity) $\{\delta I/I\}$ spectrum from each measured spectrum to remove the effects of the changing telluric airmass, then we averaged the $(\delta I/I)$ spectra to try to improve the signal-to-noise ratio in the $(\delta I/I)$ spectra. The $(\delta I/I)$ spectrum was computed by first smoothing each measured spectrum with a triangular kernel that had a FWHM of eight pixels. (This FWHM is larger than the $2-5$ pixel width expected for a Venus O_2 line as discussed in Section 1.1.2.) The smoothed spectrum was then subtracted from the measured spectrum and the difference was divided by the measured spectrum to create the $(\delta I/I)$ spectrum. In computing the average $(\delta I/I)$ spectrum, the Doppler-shift due to the Earth's diurnal rotation was assumed to be constant even though it is a function of the viewing zenith angle. The maximum wavelength difference resulting from the change in viewing zenith angle (4×10^{-4} nm) for the time period of the observations is < 0.67 pixel which is less than 40% of the instrumental FWHM, so our neglect of this change should not have a significant impact on the results.

As is common for long slit spectrometers, the spectral dispersion direction was not parallel to an axis of the detector array. However, the end-to-end difference in the position of a monochromatic line across the detector (determined from the spectrum of an He-Ne laser line) was approximately 0.5 pixel. This is smaller than the instrumental FWHM, so no attempt was made to correct for the skewness of the spectral dispersion direction.

The detector response frames were created by viewing a quartz calibration lamp directly (not through the image slicer) then using a median spatial filter with kernel of 10 (spatial) $\times$ 20 (spectral) pixels to remove the large-scale variations in illumination. No attempt was made to correct for any wavelength-dependent variations in the throughput of the image slicer because none were observed in spectra of the quartz lamp when viewed through the image slicer.

The off-axis scattered light spectra were derived from the outer edges of the recorded spectra since the image slicer did not fully illuminate the detector along the projected slit axis.

A Th-Ar arc lamp source and the telluric O_2 lines were used to determine the wavelength calibration and the spectral dispersion. Wavelengths in air for Ar were taken from *Reader and Corliss* [1986], wavelengths in air for Th were taken from *Palmer and Engelmann* [1983], and the $^{16}O^{16}O$ and $^{18}O^{16}O$ line positions in vacuum were taken from *Rothman et al.* [1992] then converted to wavelength in air using the index of refraction of standard air from *Edlen* [1966]. The wavelength scales derived from the arc lamp source and the O_2 lines differed by, at most, 4×10^{-4} nm (< 1 pixel) so this maximum difference was used as the uncertainty in the wavelength calibration. The spectral dispersion derived from the wavelength calibration was 6.42×10^{-4} nm/pixel. The measured FWHM spectral resolution derived from observations of a He-Ne laser at 632.8 nm was 1.7 pixels. This translates to a spectral FWHM of 1.1×10^{-3} nm at 763.5 nm.

1.2.2 Results

A typical Venus spectrum (10 minute integration time) is shown in Figure 1.3 with expanded views in Figure 1.4. All of the prominent absorption features seen in Figure 1.3 are from absorption by telluric O_2. No obvious feature was found at any of the expected locations for a Venus O_2 line. The average of all of our $(\delta I/I)$ spectra is shown in Figure 1.5 with expanded views in Figure 1.6. Again, no definitive absorption features are present at the expected positions for the Venusian O_2 lines. There is an apparent feature at 763.249 nm, but no significant absorption feature is present at either 763.552 or 763.665 nm.

The primary source of noise in our measurement is the photon counting noise in the radiation received from Venus. The sky spectra were $\lesssim 5\%$ of the data spectra and the off-axis scattered light spectra were $\lesssim 10\%$ of the data spectra so neither of these sources contributes significantly to our derived upper limit on the intensity of a

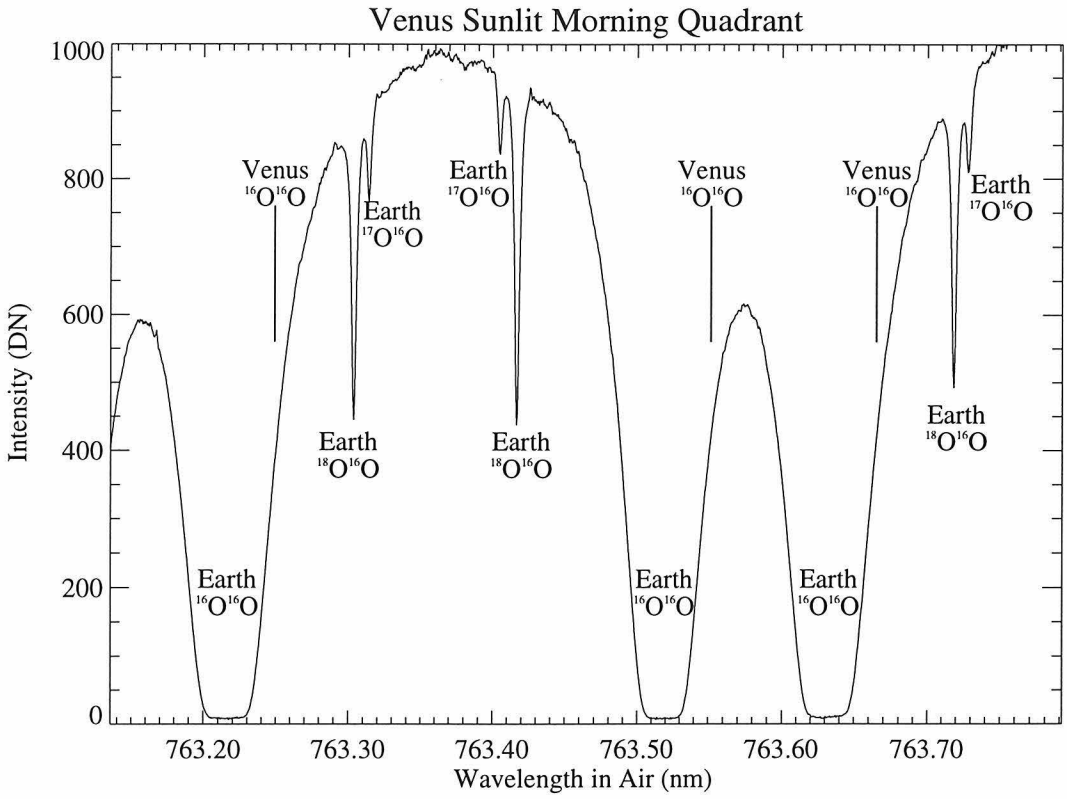

Figure 1.3: Measured spectrum of the sunlit quadrant of the Venus atmosphere as observed through the Earth's atmosphere. From left to right, the terrestrial absorption features are
$^{16}O_2$ (P7P7, 763.2165 nm, 13098.84 cm^{-1}, $b^1\Sigma_g(J'=6) \leftrightarrow X^3\Sigma_g(J''=7)$),
$^{18}O^{16}O$ (P9Q8, 763.3041 nm, 13097.33 cm^{-1}),
$^{17}O^{16}O$,
$^{17}O^{16}O$,
$^{18}O^{16}O$ (P9P9, 763.4174 nm, 13095.39 cm^{-1}),
$^{16}O_2$ (P9Q8, 763.5191 nm, 13093.64 cm^{-1}, $b^1\Sigma_g(J'=8) \leftrightarrow X^3\Sigma_g(J''=8)$),
$^{16}O_2$ (P9P9, 763.6325 nm, 13091.70 cm^{-1}, $b^1\Sigma_g(J'=8) \leftrightarrow X^3\Sigma_g(J''=9)$),
$^{18}O^{16}O$ (P11Q10, 763.7187 nm, 13090.22 cm^{-1}),
$^{17}O^{16}O$.
Line identifications and vacuum wavenumber positions for the $^{16}O_2$ and $^{17}O^{16}O$ lines are from the 1996 edition of the HITRAN database [*Rothman et al.* 1992]. Total angular quantum numbers for the $^{16}O_2$ lines are from *Burch and Gryvnak* [1969]. Wavelengths in Air for the lines were calculated using the index of refraction from *Edlen* [1966].

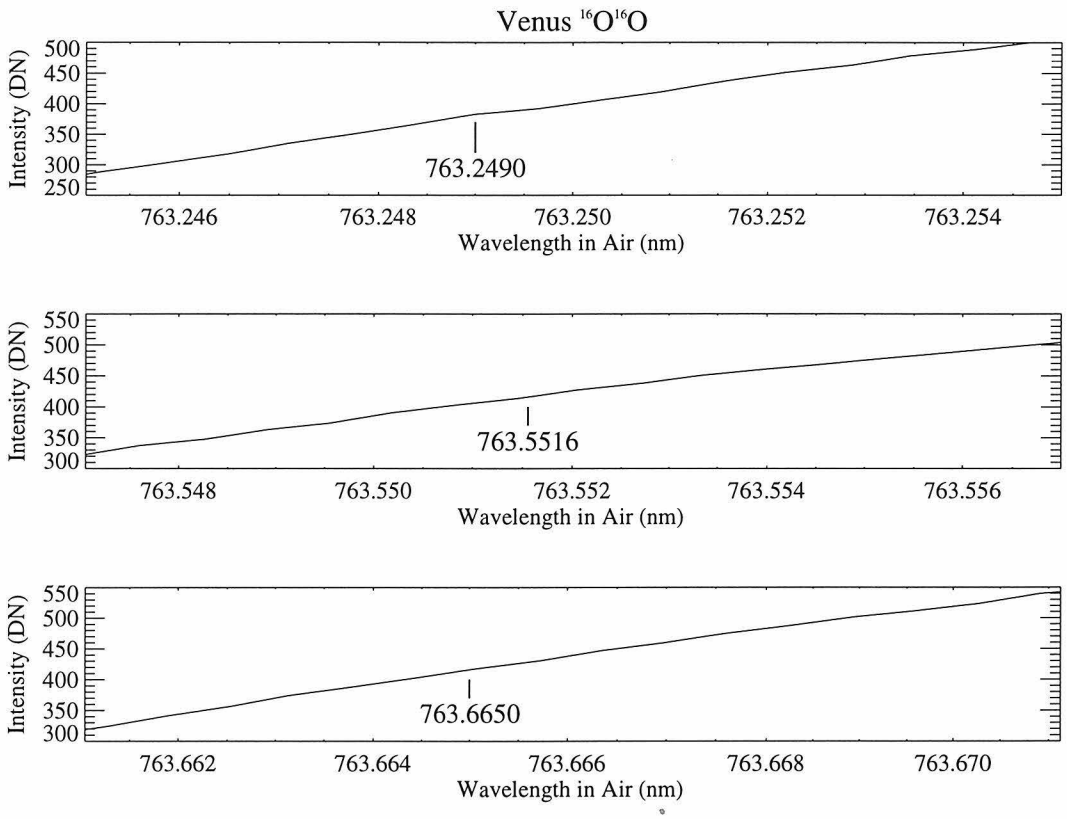

Figure 1.4: Measured spectrum of the sunlit quadrant of the Venus atmosphere as observed through the Earth's atmosphere. Expanded views showing the wavelength regions in which absorption by O_2 in the Venus atmosphere would be expected to be observed.

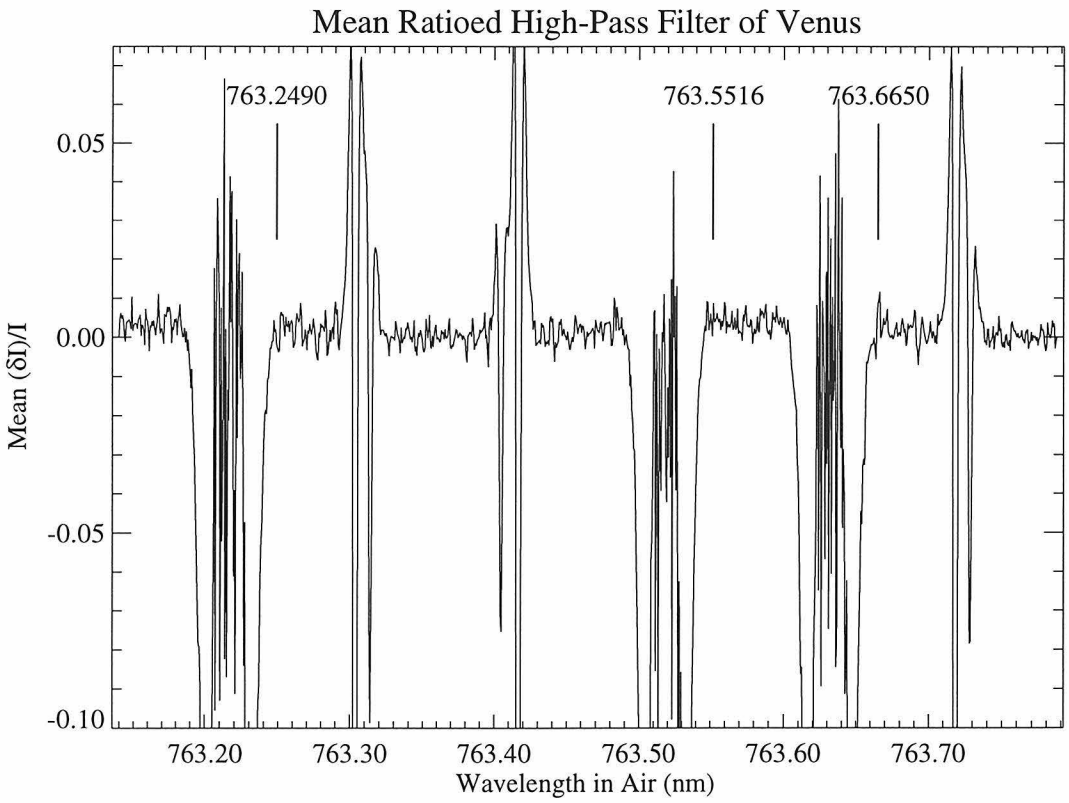

Figure 1.5: Measured spectrum of the Venus atmosphere after processing (described in the text) to remove the effects of telluric absorption.

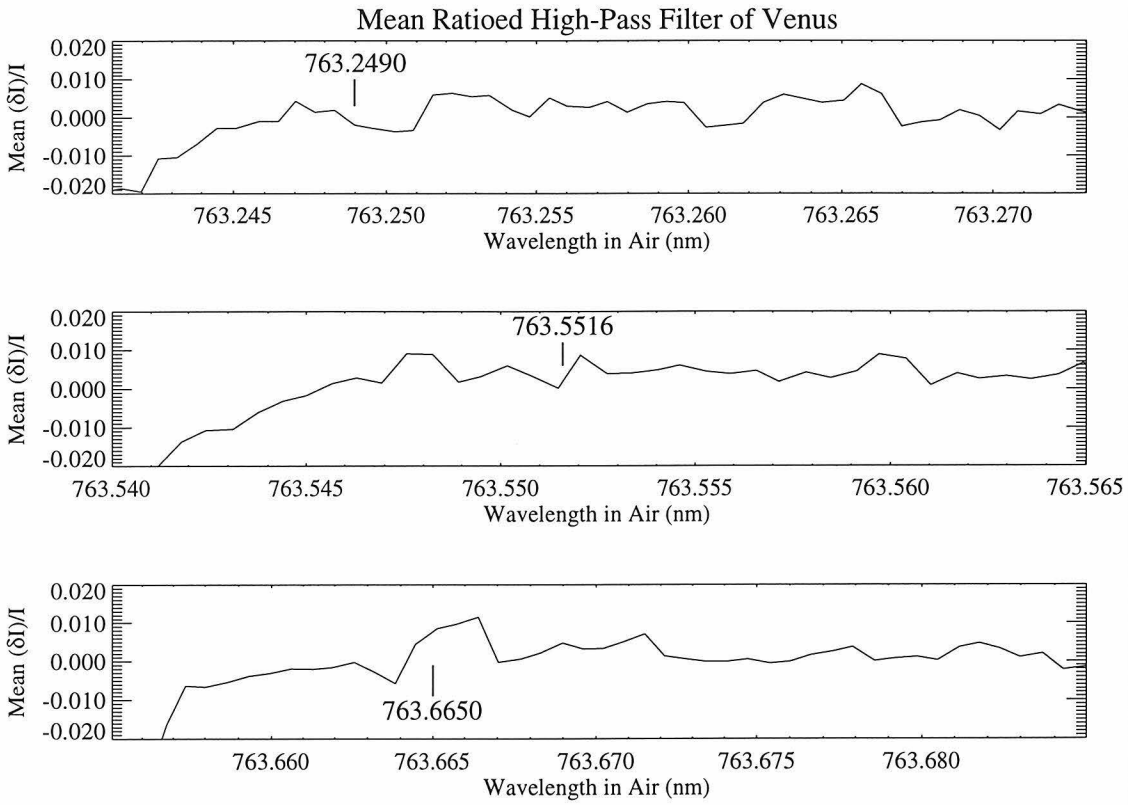

Figure 1.6: Measured spectrum of the Venus atmosphere after processing (described in the text) to remove the effects of telluric absorption. Expanded views showing the wavelength regions in which absorption by O_2 in the Venus atmosphere would be expected to be observed.

Venusian O_2 line. No wavelength-dependent variations over intervals of $2-5$ pixels were noted in either the sky or the scattered light spectra.

The signal-to-noise ratio *at the expected locations for the Venusian O_2 lines* in Figure 1.3 is ~ 400 so our individual Venus spectra give an upper limit on absorption by Venusian O_2 of $(1\sigma\ \delta I/I) \sim 0 \pm 3 \times 10^{-3}$. From the apparent feature at 763.249 nm in Figure 1.6, we obtain an upper limit $\sim 0.4\%$ on the depth of a possible feature and a $(\delta I/I)$ for a 4 pixel FWHM of $0 \pm 2 \times 10^{-3}$. The standard deviation for integrals at wavelengths where we do not expect to find any Venusian features is $(1\sigma\ \delta I/I)$ $\sim 2 \times 10^{-3}$ for a FWHM of $2-4$ pixels and $\sim 1 \times 10^{-3}$ for a FWHM of 5 pixels. The 5 pixel FWHM result, however, may be affected by the triangle filtering since the filtering used an 8 pixel FWHM kernel. The $(2\sigma\ \delta I/I)$ upper limit from our observation translates to a 2σ upper limit on the equivalent width for absorption by O_2 on Venus of $5-10 \times 10^{-6}$ nm, depending on the assumed width for the Venus O_2 lines. For comparison, the smallest 2σ upper limit on the equivalent width derived by *Trauger and Lunine* [1983] was 1×10^{-6} nm.

1.3 Radiative Transfer Model

Interpretation of our observation as an upper limit on the column abundance for molecular oxygen requires the use of a radiative transfer model. The model used for our calculations has been described in *Meadows and Crisp* [1996] so only the parameters relevant to this work are described here. This model uses the discrete ordinate method from *Stamnes et al.* [1988] to calculate angle-dependent spectra of a vertically inhomogeneous, nonisothermal, plane-parallel scattering and absorbing planetary atmosphere. Vertical inhomogeneity within the model atmosphere is accommodated using 50 two-kilometer thick vertical layers from $0-100$ km altitude. Optical properties are assumed constant within each layer but are allowed to vary between layers.

Eight discrete zenith angles (four up and four down) and seven discrete azimuth angles were used to describe the radiance field. Radiances at the top of the Venus

atmosphere were evaluated at the Gaussian quadrature points in the upper hemisphere (viewing zenith angles of 21.48, 47.93, 70.73, and 86.02 degrees) for viewing azimuth angles of $0 - 180$ degrees (relative to an incident solar azimuth angle of 0 degrees) and incident solar zenith angles of $0 - 85$ degrees. Radiances at intermediate angles were obtained by cubic or bicubic interpolation. Output was generated on an adaptive wavelength grid that fully resolves all absorption lines in each model layer while minimizing computation in continuum regions. The spectral mapping algorithm described in *Meadows and Crisp* [1996] was *not* used for these calculations. A line cut-off distance of 500 cm^{-1} was used for H_2O and O_2 and 1000 cm^{-1} was used for CO_2.

The input solar irradiance, attributed by *Crisp* [Personal Communication, 1997] to a calculation using a Kurucz model, was scaled to Venus' distance from the Sun. Line strengths for O_2 were taken from the 1996 edition of the HITRAN database [*Rothman et al.* 1992], and line strengths for CO_2 and H_2O were taken from the HITEMP database [*Pollack et al.* 1993]. Rayleigh scattering by CO_2 was included. Pressure and temperature profiles were taken from *Seiff* [1983], the volume mixing ratio for CO_2 was 0.965, and the volume mixing ratio for H_2O was 1 ppm above 75 km altitude and 30 ppm below 47 km altitude with a smooth transition through the cloud layers.

The most significant free parameters for interpretation of our observations are the scattering properties assumed for the cloud and haze particles and the assumed vertical distributions of molecular oxygen, cloud particles, and haze particles. For the nominal model calculations, the particle characteristics and optical depths (Tables 1.1 and 1.2) were taken from an updated version of the equatorial cloud model described in *Crisp* [1986]. The optical properties for the particles in the upper cloud and haze were obtained from the optical constants for 75-wt% sulfuric acid [*Palmer and Williams* 1975] using a Mie scattering algorithm [*Wiscombe* 1980; *Crisp* 1986]. This composition is consistent with (but not required by) polarization measurements by *Kawabata et al.* [1980] and *Hansen and Hovenier* [1974]. As described in *Crisp* [1986], the number densities for the Mode 1 particles (size $\sim 0.25\mu m$) were based on an

Table 1.1: Particle Characteristics for Nominal Cloud Model [a]

Particle Mode	Modal [b] Radius (μm)	Modal [b] Variance	Effective [cd] Radius (μm)	Effective [cd] Std Dev
1	0.49	0.22	0.55	0.05
1'[e]	0.49	0.22	0.55	0.05
2	1.05	0.19	1.15	0.04
2'	1.40	0.207	1.56	0.04
3	3.85	0.262	4.57	0.07

[a] Composition of all particles was 75-wt% H_2SO_4

[b] Size parameters are for a log-normal distribution:

$$n(r) = (2\pi\sigma_g)^{-0.5} r^{-1} \exp[-(\ln(r/r_g))^2/(2\sigma_g^2)]$$

where r_g is the modal radius and σ_g is the variance given above [*Hansen and Travis* 1974]. n(r) is normalized such that the integral over all sizes equals one.

[c] Integration limits for the size distribution were 0.001 and 25 μm.

[d] The effective radius and standard deviation are weighted over the distribution and are related to the modal radius and variance as described in *Hansen and Travis* [1974].

[e] UV absorber in *Crisp* [1986].

empirical fit to the *Pioneer Venus* Solar Flux Radiometer measurements [*Tomasko et al.* 1980], and the number densities for the Mode 2 particles (size $\sim 1\mu$m) were taken from Model A of *Tomasko et al.* [1980] since they gave the best fit to the *Pioneer Venus* Cloud Particle Spectrometer measurements. The extra UV absorption required by previous radiative transfer modeling studies [e.g., *Crisp* 1986] was attributed to the Mode 1 particles in the upper cloud as described in *Crisp* [1986]. The UV absorber's absorption efficiency is 0.1% of its extinction efficiency at these wavelengths.

There has been no detection of ground-state molecular oxygen in the Venus middle atmosphere even though intense airglow has been observed in the $O_2(a^1\Delta)$ band. Consequently, its vertical distribution is unknown. The assumption for our nominal model calculations was that molecular oxygen has a volume mixing ratio that is independent of altitude. This also will permit direct comparison with the radia-

Table 1.2: Optical Depths for Nominal Cloud Model

Pressure	Mode 1		Mode 1/		Mode 2		Mode 2/		Mode 3	
(bar)	$\Delta\tau$	H (km)	$\Delta\tau$	H (km)	$\Delta\tau$	H (km)	$\Delta\tau$	H (km)	$\Delta\tau$	H (km)
0.0003	0.00		0.00		0.00		0.00		0.00	
0.005	0.20	3.85								
0.028	0.14	4.75			0.66	4.75				
0.100			1.81	2.05	1.67	9.00				
0.160			3.50	3.20	1.20	5.25			0.30	0.00
0.250			2.60	9.00	1.50	10.60			0.34	0.00
0.375			1.70	-1.00	1.10	-2.50			0.30	0.00
0.600	0.23	0.00				1.19	2.00	1.66	2.00	
1.000	0.50	0.00			2.71	0.00	2.27	0.00		
1.400	1.00	0.00			1.44	0.00	3.40	0.00		
9.300	0.20	0.00			0.05	0.00				

$\Delta\tau$ is the differential optical depth at 0.63 μm within the layer whose base lies at the specified pressure. H is the scale height for the particles within the layer.

tive transfer modeling by *Trauger and Lunine* [1983] because they used the same assumption.

1.4 Discussion

Calculated spectra for uniform molecular oxygen volume mixing ratios of 1.4×10^{-6}, 1.4×10^{-7}, and 1.4×10^{-8} at all altitudes $\geq$ 58 km are shown in Figure 1.7. These synthetic spectra have been normalized so that the maximum intensity in each spectrum has a value of 1.0, and the vertical scale has been enhanced to show the molecular oxygen absorption features. The synthetic spectra have been converted to wavelength in air, Doppler-shifted by the appropriate amount, and convolved with a triangle kernel filter (simulating the UHRF spectrometer response function) so that Figure 1.7 may be compared to the measured spectra in Figure 1.4. The relatively broad feature near 763.41 nm is a solar feature that has been Doppler-shifted along with the synthetic Venus O_2 absorption lines. It can be seen in our measured spectrum, Figure 1.3, near 763.38 nm which is the position for this solar feature with no Doppler-shift. The Doppler-shifted position of this solar feature lies within a telluric $^{18}O^{16}O$ absorption

Table 1.3: $(\delta I/I)$ for Calculated Spectra for Uniform Mixing Ratios

O_2 Mixing Ratio (ppm v/v) [a]	Viewing [b] Zen Angle	$10^3 \times (\delta I/I)$ Averaged Over FWHM (pixels) 2	3	4	5
1.4	29	2.4	2.0	1.8	1.5
	34	2.4	2.0	1.8	1.5
	44	2.4	2.0	1.8	1.4
	54	2.4	2.0	1.8	1.5
0.14	29	0.23	0.20	0.18	0.15
	34	0.24	0.20	0.19	0.15
	44	0.24	0.20	0.18	0.15
	54	0.24	0.20	0.18	0.15
0.014	34	0.024	0.020	0.018	0.015
	44	0.024	0.020	0.018	0.015
	54	0.024	0.020	0.018	0.015

[a] ppm v/v = volume (number) mixing ratio in parts per million (1×10^{-6})
[b] Viewing zenith angle is given in table. The incident solar zenith angle was 84−(viewing zenith angle). The relative viewing azimuth angle was 180 degrees.

so it is not readily observable in our measured spectrum.

High-pass filtered spectra were computed from those in Figure 1.7 in the manner described earlier for the measured spectra. Table 1.3 presents the $(\delta I/I)$ for these three oxygen mixing ratios (invariant with altitude) at four viewing geometries selected to span our range of observational geometries. These calculations indicate there is no significant dependence on viewing geometry over this range. Based on these calculations, our 2σ observational upper limit on absorption by molecular oxygen corresponds to an O_2 mixing ratio of 3×10^{-6}, if the molecular oxygen is uniformly mixed throughout the Venus atmosphere. The column abundance of O_2 above 68 km altitude (50 mbar) for our 2σ upper limit is $\sim 2 \times 10^{18}$ molecules cm^{-2}, for the same assumption.

Our upper limit on $(\delta I/I)$ for a Venus O_2 absorption feature is a factor of 10 larger than *Trauger and Lunine*'s [1983] and comparable to the upper limit obtained by *Traub and Carleton* [1974]. *Trauger and Lunine*'s [1983] instrumental resolution was comparable to a FWHM of 5 UHRF pixels so our upper limit on $(\delta I/I)$ is $0 \pm 3 \times 10^{-3}$ compared to *Trauger and Lunine*'s [1983] value of $0 \pm 3 \times 10^{-4}$. *Traub and Carleton*

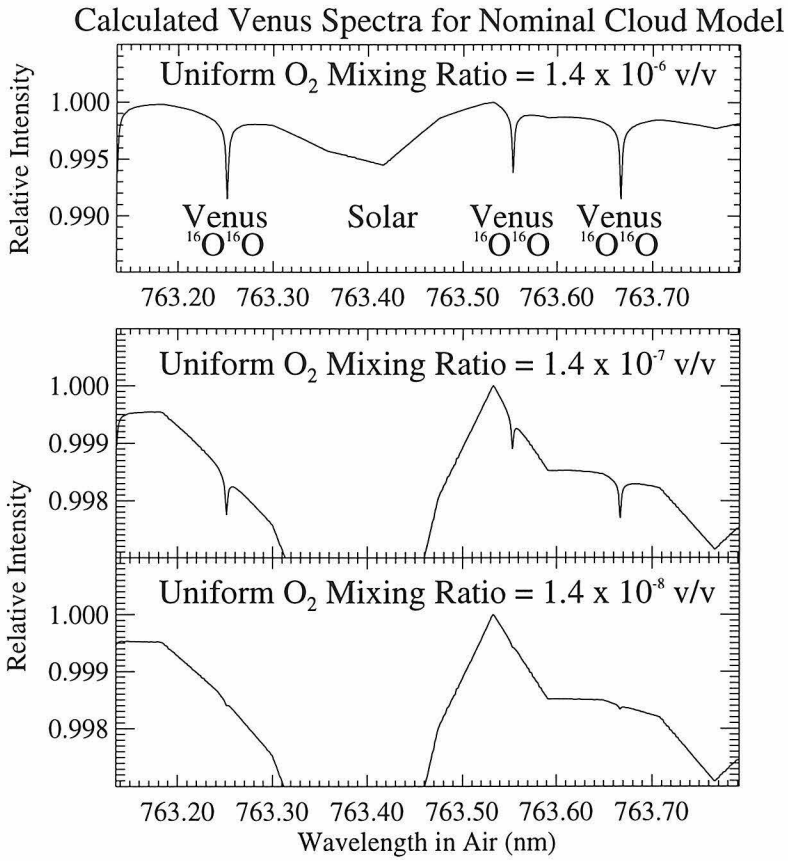

Figure 1.7: Synthetic spectra of the Venus atmosphere for three uniform O_2 profiles. The spectra in these figures were calculated for an incident solar zenith angle of 40 degrees, a viewing zenith angle of 44 degrees, and a relative viewing azimuth angle of 180 degrees. The synthetic spectra have been converted to wavelength in air, Doppler-shifted by the appropriate amount, and convolved with a triangle kernel filter (simulating the UHRF spectrometer response function) to the wavelength resolution and sampling of the UHRF data.
Note the factor of five change in vertical scale between the upper plot and the two lower plots.

[1974] reported a maximum absorption depth of 0.5% which is comparable to the 0.4% maximum absorption depth in Figure 1.6 at 763.249 nm.

There are two potentially significant differences between our observations and modeling and those for the previous studies. First, we measured the radiance from a relatively small aperture centered on the sunlit quadrant of Venus whereas both previous measurements integrated the radiance from the entire sunlit quadrant. Second, *Trauger and Lunine* [1983] used a different radiative transfer model and a different cloud model to interpret their results and to reinterpret *Traub and Carleton*'s [1974] results. Our calculations suggest, however, that neither effect is important *for a uniform vertical distribution of* O_2. For the first, our calculations find no significant variations with viewing geometry over the range of viewing zenith angles that were examined. For the second, the results from our calculations agree well with those from *Trauger and Lunine* [1983]. *Trauger and Lunine*'s [1983] modeling found that $(\delta I/I) \sim 0 \pm 3 \times 10^{-4}$ corresponded to an upper limit on the mixing ratio of O_2 of 3×10^{-7}. The calculations in Table 1.3 give the same correspondence between observed $(\delta I/I)$ and mixing ratio. In addition, we have done further calculations using a cloud model similar to that used by *Trauger and Lunine* [1983]. The results from those calculations agree to within 10% with those presented in Table 1.3.

One critical variable that has not been examined in the previous studies is the vertical distribution of O_2. There are no observations that directly constrain the distribution because ground-state O_2 has not been detected in the Venus middle atmosphere. Consequently, *Trauger and Lunine* [1983] (and so far ourselves) made the reasonable simplifying assumption that the mixing ratio of O_2 does not vary with altitude. Photochemical models (Chapter 2), however, predict most of the O_2 will reside above 80 km altitude. We have calculated the absorption that would be produced by this type of O_2 profile (Chapter 3) and find that this may be the key point for reconciling the predictions from the photochemical models with the observed low abundance of O_2. The source of radiation for spectroscopic searches, such as the present one, is sunlight that has been (multiply) scattered toward the Earth by the aerosol particles in the Venus cloud layers. Due to the multiple scattering that occurs

within the cloud layers, the spectroscopic results are most sensitive to O_2 that is within the cloud layers. If the O_2 abundance is large above the cloud layers and very small within the cloud layers, as predicted by the photochemical models, then the absorption due to a given column abundance will be smaller than the absorption produced by a vertical profile in which the mixing ratio is constant at all altitudes.

1.5 Conclusions

The spectroscopic observations reported here did not detect absorption that could be produced by O_2 in the Venus atmosphere. The 2σ upper limit on the column abundance of O_2 is equivalent to a volume mixing ratio of 3×10^{-6} if the volume mixing ratio is constant at all altitudes above 58 km and if the effective width of the Venus O_2 absorption line is 3×10^{-3} nm. This upper limit is consistent with those obtained by *Trauger and Lunine* [1983] (3×10^{-7}). Our radiative transfer modeling suggests the upper limit from *Traub and Carleton* [1974] also is equivalent to a volume mixing ratio of $\sim 3 \times 10^{-6}$, slightly larger than the 2×10^{-6} determined by *Trauger and Lunine* [1983] in their reanalysis of the *Traub and Carleton* [1974] data. The new observations confirm the depletion of O_2 relative to CO in the Venus atmosphere, and indicate the observed secular decrease in the abundance of SO_2 and SO did not result in an O_2 abundance that could be detected in the new observations.

The following chapter describes the predictions from a new photochemical model of the Venus middle atmosphere. As will be discussed in Chapter 3, the O_2 abundance predicted in the new photochemical model can be brought below the upper limit obtained by *Trauger and Lunine* [1983] if certain parameters are adjusted within the range permitted by experimental uncertainties.

1.6 References

Bougher, S.W., and W.J. Borucki, Venus O_2 and IR Nightglow: Implications for Lower Thermospheric Dynamics and Chemistry, *J. Geophys. Res.* **99**, 3759-3776, 1994.

Burch, D.E., and D.A. Gryvnak, Strengths, Widths, and Shapes of the Oxygen Lines Near 13,100 cm^{-1} (7620 Angstrom), *Appl. Opt.* **8**, 1493-1499, 1969.

Connes, P., J. Connes, F. Noxon, W. Traub, and N. Carlton, O_2 ($^1\Delta$) Emission in the Day & Night Airglow of Venus, *Ap. J.* **233**, L29-L32, 1979.

Crisp, D., Radiative Forcing of the Venus Mesosphere I: Solar fluxes and heating rates, *Icarus* **67**, 484-514, 1986.

Crisp, D., V.S. Meadows, B. Bezard, C. de Bergh, J-P Maillard, and F.P. Mills, Ground-based Near-Infrared Observations of the Venus Night Side: Near-Infrared O_2 ($^1\Delta$) Airglow from the Upper Atmosphere, *J. Geophys. Res.* **101**, 4577-4593, 1996.

Diego, F., Confocal Image Slicer, *Appl. Opt.* **32**, 6284-6287, 1993.

Diego, F., A.C. Fish, M.J. Barlow, I.A. Crawford, J. Spyromilio, M. Dryburgh, D. Brooks, I.D. Howarth, and D.D. Walker, The Ultra-High-Resolution Facility at the Anglo-Australian Telescope, *Mon. Not. Roy. Astronom. Soc.* **272**, 323-332, 1995.

Edlen, B., The Refractive Index of Air, *Metrologia* **2**, 71-80, 1966.

Esposito, L., M. Copley, R. Eckert, L. Gates, A. Stewart, and H. Worden, Sulfur Dioxide at the Venus Cloud Tops, 1978 - 1986, *J. Geophys. Res.* **93**, 5267-5276, 1988.

Hansen, J.E., and J.W. Hovenier, Interpretation of the Polarization of Venus, *J. Atmos. Sci.* **31**, 1137-1160, 1974.

Hansen, J.E., and L.D. Travis, Light Scattering in Planetary Atmospheres, *Space Sci. Rev.* **16**, 527-610, 1974.

Kawabata, K., D.L. Coffeen, J.E. Hansen, W.A. Lane, M. Sato, and L.D. Travis, Cloud and Haze Properties from *Pioneer Venus* Polarimetry, *J. Geophys. Res.* **85**, 8129-8140, 1980.

Meadows, V.S., and D. Crisp, Ground-based Near-Infrared Observations of the Venus Nightside: The Thermal Structure and Water Abundance Near the Surface, *J. Geophys. Res.* **101**, 4595-4622, 1996.

Na, C.Y., and L.W. Esposito, UV Observations of Venus with HST, American Astronomical Society Division of Planetary Sciences conference, (Mauna Lani, HI, October), 1995.

Na, C.Y., L.W. Esposito, and T.E. Skinner, "International Ultraviolet Explorer Observation of Venus SO2 and SO," *J. Geophys. Res.* **95**, 7485-7491, 1990.

Na, C.Y., L.W. Esposito, W.E. McClintock, and C.A. Barth, Sulfur Dioxide in the Atmosphere of Venus, *Icarus* **112**, 389-395, 1994.

Nair, H., M. Allen, A.D. Anbar, and Y.L. Yung, A Photochemical Model of the Martian Atmosphere, *Icarus* **111**, 124-150, 1994.

Oyama, V.I., G.C. Carle, F. Woeller, J.B. Pollack, R.T. Reynolds, and R.A. Craig, Pioneer Venus Gas Chromatography of the Lower Atmosphere of Venus, *J. Geophys. Res.* **85**, 7891-7902, 1980.

Palmer, B.A., and R. Engleman, Jr., *Atlas of the Thorium Spectrum*, Los Alamos National Laboratory Technical Report LA-9615 (UC-4), issued February 1983.

Palmer, K.F., and D. Williams, Optical Constants of Sulfuric Acid: Applications to the Clouds of Venus?, *Appl. Opt.* **14**, 208-219, 1975.

Pollack, J.B., J.B. Dalton, D. Grinspoon, R.B. Wattson, R. Freedman, D. Crisp, D.A. Allen, B. Bezard, C. de Bergh, L.P. Giver, Q. Ma, and R. Tipping, Near-Infrared Light from Venus' Nightside: A Spectroscopic Analysis, *Icarus* **103**, 1-42, 1993.

Reader, J., and C.H. Corliss, Line Spectra of the Elements, in *CRC Handbook of Chemistry and Physics* 67th Edition, (CRC Press, Boca Raton, FL), E204, 1986.

Rothman, L.S., R.R. Gamache, R.H. Tipping, C.P. Rinsland, M.A.H. Smith, D. Chris Benner, V. Malathy Devi, J-M. Flaud, C. Camy-Peyret, A. Perrin, A. Goldman, S.T. Massie, L.R. Brown, and R.A. Toth, The HITRAN Molecular Database: Editions of 1991 and 1992, *J. Quant. Spectrosc. Radiat. Transfer* **48**, 469-507, 1992.

Seiff, A., Models of Venus's Atmospheric Structure, in *Venus*, ed. Hunten, D.M., L. Colin, T.M. Donohue, and V.I. Moroz, (Univ. of Arizona Press, Tucson, AZ), 1045-1048, 1983.

Stamnes, K., S-C. Tsay, W. Wiscombe, and K. Jayaweera, Numerically Stable Algorithm for Discrete-Ordinate-Method Radiative Transfer in Multiple Scattering and Emitting Layered Media, *Appl. Opt.* **27**, 2502-2509, 1988.

Traub, W.A., and N.P. Carleton, Observation Of O_2, H_2O, and HD in Planetary Atmospheres, in *Exploration of the Planetary System*, ed. A. Woszczyk and C. Iwaniszewska, (Reidel, Dordrecht, The Netherlands), 223-228, 1974.

Trauger, J., and J. Lunine, Spectroscopy of Molecular Oxygen in the Atmospheres of Venus and Mars, *Icarus* **55**, 272-281, 1983.

von Zahn, U., S. Kumar, H. Niemann, and R. Prinn, Composition of the Venus Atmosphere, in *Venus*, ed. Hunten, D.M., L. Colin, T.M. Donohue, and V.I. Moroz, (Univ. of Arizona Press, Tucson, AZ), 299-430, 1983.

Wiscombe, W.J., Improved Mie Scattering Algorithm, *Appl. Opt.* **19**, 1505-1509, 1980.

Yung, Y., and W. DeMore, Photochemistry of the Stratosphere of Venus: Implications for Atmospheric Evolution, *Icarus* **51**, 199-247, 1982.

Chapter 2

A One-Dimensional Photochemical Model of the Venus Middle Atmosphere

Franklin P. Mills, Mark A. Allen, and Yuk L. Yung

Division of Geological and Planetary Sciences

California Institute of Technology

Pasadena, CA 91125

2.1 Introduction

The primary constituent of the Venus atmosphere is CO_2, $\sim 96.5 \pm 0.8\%$ by volume or number density [*von Zahn et al.* 1983] (Table 2.1). CO_2 photodissociates primarily at wavelengths $\lesssim 200$ nm (possibly with weaker photodissociation at $200 \leq \lambda \lesssim 230$ nm, see Appendix D) to form CO and atomic oxygen:

$$CO_2 + h\nu \rightarrow CO + O. \tag{G1}$$

(All kinetic reactions used in the photochemical model are listed in Table 5C.2. All photolysis reactions used in the photochemical model are listed in Table 5A.1. All other reactions that are referenced in the text are listed in Table 5C.1.) Direct three-body recombination,

$$CO + O + M \rightarrow CO_2 + M, \tag{G2}$$

is spin-forbidden, so reaction G2 is five orders of magnitude slower than the competing reaction,

$$2O + M \rightarrow O_2 + M, \tag{G3}$$

at the temperatures typically found in planetary atmospheres ($\sim$ 200 K). (M is a third molecule which collides with the intermediate complex formed by the two reacting species. The third molecule removes sufficient energy from the intermediate complex that the intermediate complex can form the stable product molecule.) Consequently, the atomic oxygen produced in photolysis of CO_2 preferentially combines to form O_2 rather than reacting with CO to produce CO_2. O_2 is relatively stable in an initially pure CO_2 atmosphere because (1) O_2 is unreactive toward CO and (2) O_2 photodissociates readily at < 200 nm (and less readily at $200 \leq \lambda \leq 240$ nm) which is the same wavelength region in which CO_2 absorbs strongly. As a result, an initially pure CO_2 atmosphere on Venus would evolve to an equilibrium state in which CO comprises $\sim 7\%$ and O_2 $\sim 3.5\%$ of the atmosphere (by volume). However, measurements indicate the CO and O_2 abundances on Venus are orders of magnitude smaller

than these equilibrium state values for an initially pure CO_2 atmosphere. Thus, the primary problem that all photochemical models have faced for the Venus atmosphere is explaining the stability of Venus' predominantly CO_2 atmosphere in a manner that quantitatively agrees with the observed CO abundance and the observed upper limits on the O_2 abundance. This question is among the most significant outstanding issues in planetary science.

Modelers have recognized that reaction G2 was too slow to account for the observed abundances of CO and O_2 in the Venusian atmosphere so they have sought both catalytic cycles (involving trace constituents such as OH and Cl) that could increase the rate at which CO_2 is produced and reservoir species (such as H_2SO_4) in which oxygen could be stored as mechanisms for decreasing the predicted steady-state abundances of CO and O_2. All of the previously proposed photochemical models have qualitatively explained the stability of a predominantly CO_2 atmosphere, but none has succeeded in quantitatively explaining the CO and O_2 observations for Venus. In particular, no model has been able to come within an order of magnitude of the observed upper limit on the O_2 abundance.

The region of the Venus atmosphere in which most photochemistry occurs is the "middle atmosphere" which extends from $\sim$ 60 km altitude to $\sim$ 110 km altitude. This region, which has been described as the mesosphere and/or the stratosphere in prior publications, is where a majority of the photochemically important solar irradiance is absorbed. The last significant attempts to model the photochemistry of the Venus middle atmosphere were in the early 1980s (*Yung and DeMore* [1982]; *Krasnopol'sky and Parshev* [1983]). Since that time, laboratory studies have improved our understanding of the photochemical processes that may occur in the Venus atmosphere, and observations since 1982 (from spacecraft and Earth- based telescopes) have provided much better constraints on the composition of the Venus atmosphere. The objectives for this work were (1) to develop a self-consistent photochemical model of the Venus atmosphere with minimal imposed constraints, (2) to assess the impact of the recent laboratory studies and observations on our understanding of the photochemistry of the Venus atmosphere, and (3) to determine the range of values for key

Table 2.1: Observations of the Venus Middle Atmosphere (part 1)

species	mixing ratio (v/v)	uncertainty	altitude	reference and remarks
CO_2	0.965	0.008	$\lesssim 100$	*von Zahn et al.* [1983]
CO	30 ppm[a]		42	*von Zahn et al.* [1983]
	45 ppm		~ 42	*de Bergh et al.* [1991]
	51 ppm	1 ppm		*Young* [1972] analysis of *Connes et al.* [1968]
	45 ppm	10	~ 64	*Connes et al.* [1968]
	75 ppm		~ 64	*Bezard et al.* [1990]
	3 ppm		~ 75	*Bezard et al.* [1990]
	0.0015		$\gtrsim 100$	*Bezard et al.* [1990]
O_2	< 2 ppm		~ 70	*Traub & Carlton* [1974] revised by *Trauger and Lunine* [1983]
	< 0.3 ppm		~ 70	*Trauger and Lunine* [1983]
	< 3 ppm		~ 70	Chapter 1
$O_2(a^1\Delta)$	dayglow ~ 1.5 MR[†]	0.25 MR		*Connes et al.* [1979]
	nightglow ~ 1.2 MR	0.25 MR		*Connes et al.* [1979]
	nightglow ~ 1 MR	0.2 MR		*Crisp et al.* [1996]
O_3	< 6 ppm		70 - 95	*Wilson et al.* [1981]
	< 2 ppm		> 95	*Wilson et al.* [1981]
N_2	0.035	0.008	$\lesssim 100$	*von Zahn et al.* [1983]
HF	1-5 ppb[b]		~ 34	*Pollack et al.* [1993]
	4.5 ppb		troposphere	*Bezard et al.* [1990]
	5 ppb		~ 64	*von Zahn et al.* [1983]
	$\lesssim 10$ ppb		$\lesssim 68$	*Young* [1972] analysis of *Connes et al.* [1967]
	5 ppb	+5,−3	~ 68	*Connes et al.* [1967]
HCl	0.48 ppm	0.12	~ 24	*Pollack et al.* [1993]
	0.5 ppm			*Bezard et al.* [1990]
	0.4 - 0.6 ppm		$\sim 67 - 70$	*Young* [1972] analysis of *Connes et al.* [1967]
	0.6 ppm	0.12	~ 68	*Connes et al.* [1967]

[†] 1 MR $= 1 \times 10^{12}$ photons cm^{-2} s^{-1} / (4π sr)
[a] ppm = parts per million (10^{-6})
[b] ppb = parts per billion (10^{-9})

Table 2.1: Observations of the Venus Middle Atmosphere (part 2)

species	mixing ratio (v/v)	uncertainty	altitude	reference and remarks
H_2O	100 ppm[a]		$\lesssim 55$	*von Zahn et al.* [1983]
	40 ppm	> 10	$\lesssim 55$	*Bezard et al.* [1990] inferred from HDO
	0.8 ppm	> 0.2	$\gtrsim 65$	*Bezard et al.* [1990] inferred from HDO
	1-40 ppm		~ 70	*von Zahn et al.* [1983]
	1.0 ppm	+1.0,−0.5	~ 70	*Encrenaz et al.* [1995] for 1991
	7.0 ppm	+5.0,−4.0	~ 70	*Encrenaz et al.* [1995] for 1993 inferred from HDO
	3.5 ppm	2	$65 - 95$	*Encrenaz et al.* [1991] for 1990 inferred from HDO
	0.03 ppm	factor of 10	~ 95	*Encrenaz et al.* [1995] for 1991
	$\gtrsim 0.2$ ppm		~ 95	*Encrenaz et al.* [1995] for 1993
CH_4	$\lesssim 0.1$ ppm		~ 30	*Pollack et al.* [1993]
SO_2	< 10 ppm		~ 55	*von Zahn et al.* [1983]
	50 ppb[b]		~ 70	*von Zahn et al.* [1983]
	380 ppb	70	~ 70	*Na et al.* [1990] for 1979
	50 ppb	20	~ 70	*Na et al.* [1990] for 1988
	80 ppb	40	~ 70	*Na et al.* [1994] equator 1988
	120 ppb	60	~ 70	*Na et al.* [1994] equator 1991
	300 ppb	150	~ 70	*Na et al.* [1994] 50 deg S 1988
	20 ppb	10	~ 70	*Na and Esposito* [1995] for 1995
	3 km scale height	1	~ 70	*Na et al.* [1994]
SO	20 ppb	10	~ 70	*Na et al.* [1990] for 1979
	10 ppb	5	~ 70	*Na and Esposito* [1995] for 1988
	12 ppb	5	~ 70	*Na et al.* [1994] for 1991
	3 ppb	2	~ 70	*Na and Esposito* [1995] for 1995
	< 50 ppb		70 - 95	*Wilson et al.* [1981]
	< 20 ppb		> 95	*Wilson et al.* [1981]
H_2S	1 ppm		~ 55	*von Zahn et al.* [1983]
OCS	0.2 - 1.0 ppm		troposphere	*Carlson et al.* [1991]
	0.25 ppm		$\lesssim 50$	*Bezard et al.* [1990]
	0.010 ppm		$\gtrsim 65$	*Bezard et al.* [1990]
	< 0.5 ppm		70 - 95	*Wilson et al.* [1981]
	< 0.08 ppm		> 95	*Wilson et al.* [1981]
H_2SO_4(g)	0 - 25 ppm		35 - 55	*Jenkins et al.* [1994]
aerosol	9 cm^{-3}	4	84	particle density *Lane and Opstbaum* [1983]
	2.2 km scale height	1.5	84	*Lane and Opstbaum* [1983]

[a] ppm = parts per million (10^{-6})
[b] ppb = parts per billion (10^{-9})

parameters such that the predicted CO and O_2 abundances lie within the observational constraints.

Section 2.2 describes our photochemical model and the primary input parameters. Section 2.3.1 presents the results from our "Nominal" model in which all photochemical rates have been set at their nominal measured or estimated values. The remainder of Section 2.3 will discuss the sensitivity of our nominal model results to changes in selected important model parameters and present the results from models in which the key parameters were adjusted within the uncertainties allowed by existing measurements to achieve a suitable match to the observations. The concluding sections discuss the implications of our results for the chemistry of the lower atmosphere and the recent evolution of the Venus atmosphere.

2.1.1 Observations

Observations of relevance to the Venus middle atmosphere are listed in Table 2.1. The most important observations for this work are the abundance of HCl (which is believed to be uniformly distributed in the upper cloud), the SO_2 abundance at the cloud top, the retrieved vertical distribution of SO, the retrieved vertical distribution of CO, the non-detection of O_2 in spectroscopic observations, and the abundance of H_2^+ (or possibly D^+) in the ionosphere.

The only published measurement of HCl in the Venus middle atmosphere is that by *Connes et al.* [1967] with a revised analysis by *Young* [1972]. *Connes et al.* [1967] identified three pairs of HCl lines near 5750 cm^{-1} (1.74 μm) in their high-resolution (resolving power $\sim$ 70000) spectra of the sunlit quadrant of Venus that were not blended with other lines and for which both the $H^{35}Cl$ and $H^{37}Cl$ isotopic lines had been observed. *Connes et al.* [1967] compared these lines to nearby CO_2 lines to derive a mixing ratio for HCl of $6(\pm 1.2) \times 10^{-7}$ with an effective line formation pressure of $\sim$ 80 mbar. *Young* [1972] revised the analysis of the *Connes et al.* [1967] spectra using newer (and more appropriate) laboratory data. (The most recent values (in the 1996 edition of the HITRAN database [*Rothman et al.* 1992]) for line strength and self-

broadened half-widths of the HCl lines are within 15% of the values used by *Connes et al.* [1967] and *Young* [1972].) If HCl is uniformly mixed in the Venus atmosphere, *Young* [1972] found the mixing ratio for HCl would be $4.2(\pm 0.7) \times 10^{-7}$ with an effective line formation pressure of $\sim$ 36 mbar or $6.1(\pm 0.6) \times 10^{-7}$ with an effective line formation pressure of $\sim 50 - 60$ mbar. If the effective pressure for line formation were $\gtrsim$ 100 mbar, then *Young* [1972] found "the conclusion that HCl is not uniformly mixed cannot be avoided." The two major uncertainties in *Young*'s [1972] analysis were the width of the HCl lines when broadened by CO_2 and the effects of multiple scattering within the cloud layers. *Young* [1972] did not attempt to determine the effects of multiple scattering but quotes results from *Belton* [1968]. *Belton* [1968] found that the HCl lines that had been observed by *Connes et al.* [1967] might have formed at an effective pressure of 270 mbar and that the CO_2 lines used as reference by *Connes et al.* [1967] might have formed at an effective pressure of 200 mbar (with a stated uncertainty of a factor of 2 on these values). Recently, two measurements have been published of the HCl mixing ratio in the lower Venus atmosphere. *Pollack et al.* [1993] analyzed spectra of the nightside of Venus (resolving power $\sim$ 1800) from *Crisp et al.* [1991] that had been collected in the same 1.74 μm region. *Pollack et al.* [1993] found the best fit model had an HCl mixing ratio of $4.8(\pm 1.2) \times 10^{-7}$ at an altitude of 23.5 km. This is consistent with the HCl mixing ratio, 5×10^{-7} below the clouds, that *Bezard et al.* [1990] had derived from higher-resolution (resolving power $\sim$ 25000) spectra of the nightside of Venus in the same 1.7-μm region. *Pollack et al.* [1993] suggested the similarity of their HCl mixing ratio in the lower atmosphere to that obtained by *Connes et al.* [1967] indicated the HCl mixing ratio was constant throughout the lower atmosphere and cloud layers. However, although the *Connes et al.* [1967] spectra were for the sunlit quadrant whereas the lower resolution spectra were for the nightside of Venus, radiative transfer modeling for the 760 nm O_2 line in the Venus atmosphere (Chapter 3) suggests the effective pressure for the *Connes et al.* [1967] spectra could be larger than the 35 - 50 mbar inferred by *Young* [1972]. A new assessment of the *Connes et al.* [1967] spectra using a modern radiative transfer model with multiple scattering cloud layers should reduce this uncertainty. For our

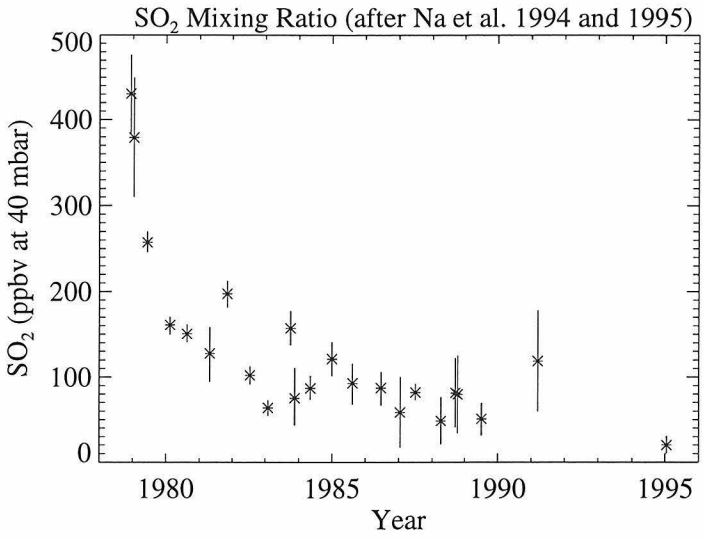

Figure 2.1: Retrieved SO_2 abundances at the cloud top from *Na et al.* [1994] and *Na and Esposito* [1995] based on ultraviolet observations.

photochemical model, we used an HCl mixing ratio of 4×10^{-7} as our nominal lower (58-km) boundary condition but considered values as large as 8×10^{-7}.

The SO_2 abundance at the cloud tops has varied by a factor of ~ 10 with time, as shown in Figure 2.1 from *Na et al.* [1994] and *Na and Esposito* [1995]. The mixing ratio of SO_2 at the lower boundary of our model was selected so that the SO_2 mixing ratio at 68 - 70 km altitude (40 mbar) would lie within the observed range.

Figure 2.2 shows the retrieved profiles of SO from *Na et al.* [1990] and *Na et al.* [1994]. The values for key model parameters were adjusted so that our predicted SO profile would lie within the range determined by the retrieved profiles in Figure 2.2.

Selected retrieved CO profiles from *Clancy and Muhleman* [1991] are shown in Figure 2.3. The profiles shown were selected to represent the maximum observed range of values for CO in the Venus middle atmosphere. The values for key model parameters were adjusted so that our predicted CO profile would lie near or within the range determined by the retrieved profiles in Figure 2.3. Diurnal variations in CO

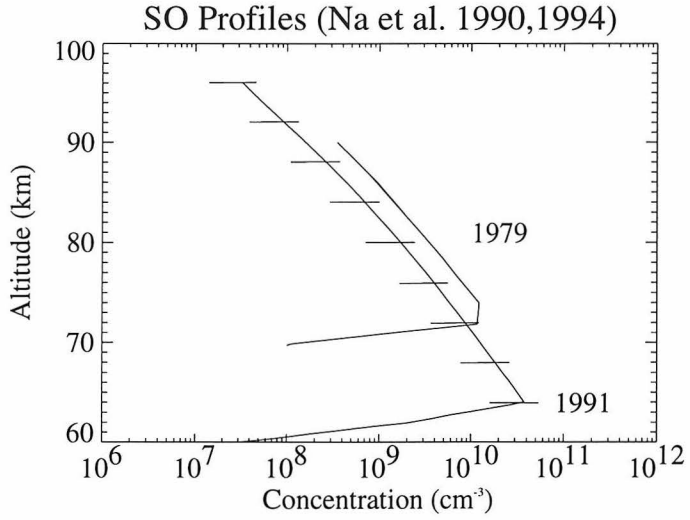

Figure 2.2: Retrieved SO profiles from *Na et al.* [1990] and *Na et al.* [1994] based on ultraviolet observations.

abundances at 80 - 90 km altitude [*Schloerb et al.* 1980; *Wilson et al.* 1981; *Clancy et al.* 1981; *Gurwell et al.* 1995] have found a nightside depletion of CO, relative to the dayside, at 80 - 90 km altitude. These variations may provide a potential discriminant by which to assess proposed photochemical models [*Yung and DeMore* 1982], but the diurnal variations at these altitudes could be controlled by the global circulation pattern [*Clancy and Muhleman* 1985].

The upper limit on the O_2 abundance in Table 2.1 was calculated by *Trauger and Lunine* [1983] assuming a constant mixing ratio for O_2 at all altitudes. As will be discussed in Chapter 3 the vertical distribution of O_2 can have a significant impact on the measured absorption so a radiative transfer model has been used to assess the expected absorption due to our predicted O_2 profiles. The results from these calculations were used to determine which O_2 profiles are compatible with the upper limit obtained by *Trauger and Lunine* [1983].

There are no direct measurements of the H_2 abundance in the Venus atmosphere,

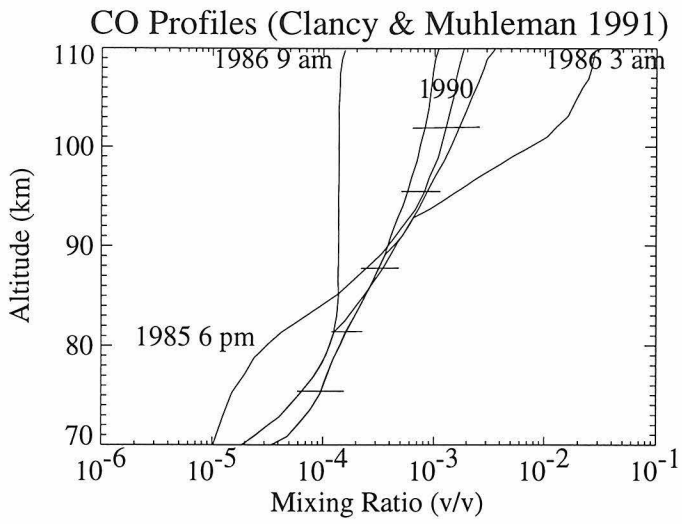

Figure 2.3: Retrieved CO profiles from microwave observations [*Clancy and Muhleman* 1991]. Profiles were selected to illustrate the diurnal and inter-annual variations that have been observed.

but *Pioneer Venus* detected a mass 2 ion above 130 km altitude [*Taylor et al.* 1980]. Interpretation of that measurement has been a significant source of controversy and there is still disagreement between the *Pioneer Venus* result and that obtained from studies of Lyman-α resonant scattering. *Taylor et al.* [1980] interpreted the mass 2 ion as H_2^+. Based on that interpretation, *Kumar et al.* [1981] developed a thermospheric model which required an H_2 mixing ratio in the middle atmosphere of 10 ppm. *McElroy et al.* [1982] suggested, however, that the mass 2 ion was D^+ and derived a D/H ratio ($\sim 1 \times 10^{-2}$) that is close to the D/H ratio ($1.9 \pm 0.6 \times 10^{-2}$) determined from spectroscopic observations of H_2O and HDO in the lower atmosphere [*de Bergh et al.* 1991]. Analysis by *Hartle and Taylor* [1983] confirmed the D^+ interpretation, and *Kumar and Taylor* [1985] determined the H_2 mixing ratio must be < 0.1 ppm at $\sim$ 130 km altitude since no significant change in the abundance of O^+ was observed in regions in which the mass 2 ion abundance increased significantly. *Kumar and Taylor*'s [1985] upper limit is consistent with what would be expected from thermochemical equilibrium among H_2, H_2O, CO, and CO_2 near Venus' surface [*McElroy et*

al. 1973]. *Bertaux and Clarke* [1989], however, found no evidence in IUE spectra of the deuterium Lyman-α line which *Donahue* [1989] interpreted as an upper limit of 5×10^{-3} on the D/H ratio. This is a factor of four smaller than the D/H ratio determined for the *lower* atmosphere by *de Bergh et al.* [1991] and a factor of two smaller than the *in-situ* interpretation by *McElroy et al.* [1982]. The remaining disagreement between these observations has not been resolved. The other extant constraint on the hydrogen abundance in the Venus thermosphere is the rate at which hydrogen atoms are lost due to escape processes. The escape rate for H postulated by *Kumar et al.* [1981] was an order of magnitude larger than suggested in more recent calculations [*Hunten et al.* 1989]. These more recent estimates of the H escape flux are comparable to the photodissociation rate of HCl above 110 km altitude, so a large thermospheric abundance of H_2 may not be necessary. Based on these considerations, the only H_2 in our nominal model is produced photochemically from photodissociation of HCl.

An additional constraint on the hydrogen abundance is provided by models of the ionosphere and upper atmosphere ($\geq$ 100 km altitude). The VIRA (Venus International Reference Atmosphere) model for the neutral components of the thermosphere by *Keating et al.* [1986] was constructed based on *Pioneer Venus* measurements. Extrapolating from the H densities predicted in the noon (Local Venus Time) VIRA model at 150 km altitude to the homopause ($\sim$ 130 km altitude), *Krasnopol'sky and Parshev* [1983] and *Fox and Bougher* [1991] found the H mixing ratio at the homopause needed to be $\sim 2-5$ ppm ($\pm$ a factor of three due to the extrapolation [*Fox and Bougher* 1991]). At 100 km altitude, *Krasnopol'sky and Parshev* [1983] predicted the H abundance was $\sim 1 \times 10^8$ cm^{-3}, the H_2 abundance was $\sim 5 \times 10^7$ cm^{-3}, the HCl abundance was $\sim 2 \times 10^8$ cm^{-3}, and the H_2O abundance was $\sim 1 \times 10^8$ cm^{-3}. This gives a total hydrogen atom concentration of $\sim 4.5 \times 10^8$ cm^{-3} at $\sim$ 100 km altitude.

2.1.2 Photochemistry from Previous Models

As noted in Section 2.1, the direct oxidation of CO via Reaction G2 is too slow to account for the observed abundances of CO and O_2 in the Venus atmosphere, so CO in the Venus atmosphere is predominantly oxidized to CO_2 via catalytic cycles. (A catalytic cycle is a series of reactions in which the intermediate compounds that are formed in one reaction are consumed in another reaction. A cycle provides a path by which a reaction that is energetically feasible but kinetically inhibited can proceed in a more rapid manner. The reactions in a catalytic cycle are typically rapid because many of the intermediate compounds formed in the cycle are highly reactive chemical radicals.) Previous photochemical models (e.g., *Prinn* [1971], *McElroy et al.* [1973], *Sze and McElroy* [1975], *Yung and DeMore* [1982], *Krasnopol'sky and Parshev* [1983]) have examined four classes of catalytic chemistry: hydrogen species (such as H and OH, collectively known as HO_x), sulfur oxides (SO_x), chlorine oxides (ClO_x), and nitrogen oxides (NO_x). These models were based on detections of H_2O, SO_2, and HCl in the Venus atmosphere (Section 2.1.1, and on indirect evidence suggesting the occurrence of lightning which could lead to production of NO_x in the Venus atmosphere [e.g., *Ksanfomaliti* 1979]. Of these four classes of compounds, the reaction of OH with CO has been demonstrated definitively in laboratory studies to lead to rapid production of CO_2 [*Kaufman* 1969], and there is strong evidence from laboratory studies that oxidation of ClCO also leads to rapid production of CO_2 (although the mechanism has not been definitively identified) [*Spence et al.* 1978; *Hewitt et al.* 1996]. All four classes of compounds, however, may reduce the abundance of O_2 by shifting the equilibrium between O_2 and odd oxygen (O plus O_3, collectively known as O_x) toward O_x. This shift may indirectly enhance the rates of the HO_x and $CClO_x$ catalytic cycles that use atomic oxygen to oxidize CO. In addition, oxygen can be sequestered in ClO_x (e.g., Cl_2O_3) or SO_x (e.g., H_2SO_4) for transport from higher altitudes (where CO oxidation is relatively inefficient) to lower altitudes (where oxidation of CO is more rapid).

Early quantitative photochemical models for Venus [e.g., *McElroy et al.* 1973] ex-

amined the role of HO_x chemistry since laboratory studies [*Kaufman* 1969] had shown that catalytic cycles involving OH, such as Cycles C1 and C2, could significantly enhance the production rate of CO_2, compared to production via reaction G2. (All catalytic cycles are listed in Appendix E.) These HO_x models had been very successful at explaining the photochemistry of the Martian atmosphere [e.g., *McElroy and Donahue* 1972; *Parkinson and Hunten* 1972], and they confirmed that HO_x chemistry could maintain the stability of Venus' atmosphere. (*McElroy et al.* [1973] predicted the O_2 mixing ratio would be $\sim 1 \times 10^{-7}$ near the cloud top, but they did not present quantitative estimates for higher altitudes.) However, the abundances for the key HO_x species involved in catalyzing the oxidation of CO in *McElroy et al.* [1973] were as much as an order of magnitude larger than those calculated in *Yung and DeMore*'s [1982] model A (which also studied HO_x chemistry). This difference occurred, in part, because *McElroy et al.* [1973] did not include several reactions between Cl and HO_x that were included in the *Yung and DeMore* [1982]. These reactions significantly increase the loss rate for HO_x.

McElroy et al. [1973] implicitly derived the HO_x needed for catalyzing the oxidation of CO from H_2, and they derived 20 - 25% of the H_2 in their model from conversion of H_2O to H_2 in the lower atmosphere. *Yung and DeMore* [1982] examined a case, their model A, in which the H_2 mixing ratio was sufficiently large (2×10^{-5}) that H_2 explicitly became the primary source for HO_x and HO_x cycles dominated the chemistry of the middle atmosphere. The predictions from that model gave reasonable agreement with the then extant CO and O_2 observations, but the upper limit for O_2 determined by *Trauger and Lunine* [1983] was a factor of 20 smaller than the prediction for model A by *Yung and DeMore* [1982]. There were two other problems with the large H_2 abundance postulated for *Yung and DeMore*'s [1982] model A. First, *Yung and DeMore* [1982] noted that an H_2 mixing ratio of $\sim 1 \times 10^{-5}$ is much larger than would be expected from thermochemical equilibrium among CO_2, CO, H_2O, and OCS in the lower atmosphere. Second, the basis for proposing a model with such a large abundance of H_2 was *Taylor et al.*'s [1980] interpretation that the mass 2 ion in *Pioneer Venus* entry probe mass spectrometer data was H_2^+ (Section 2.1.1). That

interpretation has been discarded in favor of *McElroy et al.*'s [1982] interpretation that the mass 2 ion is D^+, although there is continuing disagreement over *McElroy et al.*'s [1982] interpretation (Section 2.1.1).

The chemistry of sulfur in the Venus atmosphere was studied by *Prinn* [1975], *Prinn* [1978], and *Winick and Stewart* [1980]. *Prinn* [1975] considered the primary source of sulfur in the middle atmosphere to be OCS that was formed in the lower atmosphere and transported upward through the clouds. *Prinn* [1975] suggested Cycles C3 and C4 dominate the chemistry in the cloud layers. Using a reasonable choice for the eddy diffusion coefficient and a mixing ratio for OCS in the lower atmosphere that is larger than currently accepted, *Prinn* [1975] obtained reasonable rates for CO oxidation and H_2SO_4 production given the information available at the time. *Prinn*'s [1975] model did not include the influence of chlorine oxides on the sulfur oxide chemistry and did not extend to sufficiently high altitude to permit quantitative comparisons with subsequent observations of CO and the current upper limit on O_2. *Prinn* [1975] noted that cycle C3 could lead to production of significant quantities of elemental sulfur, but there have been no subsequent attempts to quantify the production rate for elemental sulfur. OCS has been essentially neglected in more recent models despite the marginal detections by Venera 13 and 14 [*Mukhin et al.* 1983] because those detections were an order of magnitude larger than the upper limit established by *Pioneer Venus* [*Oyama et al.* 1980]. The recent detections of OCS in the lower Venus atmosphere via near-infrared spectroscopy [*Bezard et al.* 1990; *Pollack et al.* 1993], however, suggests OCS may be important in the photochemistry of the cloud layers, though not the dominant role proposed by *Prinn* [1975].

In later work, *Prinn* [1978] examined possible reactions involving H_2S. Most of *Prinn*'s [1978] work was concerned with chemistry in the lower Venus atmosphere, but *Prinn* [1978] proposed three possible fates for the photolysis products of H_2S: Cycles C5, C6, and C7. The local, relative abundances of O_2 and OCS determine which cycle dominates at each altitude. Subsequent measurements by *Pioneer Venus* [*Hoffman et al.* 1980; *Oyama et al.* 1980] yielded a marginal detection (3 ± 2 ppm) below 20 km altitude, an upper limit of 2 ppm at 22 km altitude, and a marginal

detection ($\sim$ 1 ppm) at $\sim$ 55 km altitude. Based on the apparently low abundance of H_2S, it has not been included explicitly in more recent photochemical models. *Yung and DeMore* [1982] mentioned, however, that the rapid reaction between H_2S and H could be a significant source of H_2 in the upper cloud layer.

Data collected in the late 1970s (*Barker* [1979]; *Conway et al.* [1979]; *Gel'man et al.* [1979]; *Oyama et al.* [1980]) suggested that SO_2 was probably the dominant form of sulfur in and above the upper cloud layer rather than either OCS or H_2S. *Winick and Stewart* [1980] examined the photochemistry of SO_2 in the context of a reasonably comprehensive photochemical model that included chlorine, hydrogen, and sulfur oxides. *Winick and Stewart* [1980] introduced three catalytic sulfur cycles (Cycles C8, C9, and C10) that are efficient mechanisms for splitting the O-O bond in O_2 and sequestering oxygen in H_2SO_4. Cycles C8 and C9 use Reaction K151 to split the O-O bond. The oxygen atoms are then consumed in Cycle C10 in the process of forming H_2SO_4. H_2SO_4 has a low vapor pressure at the conditions present in the upper cloud layer so it readily condenses and is transported downward through the cloud layers in liquid form. Below the lower cloud layer, H_2SO_4 evaporates and thermally decomposes [*Krasnopol'sky and Pollack* 1994]. The *Winick and Stewart* [1980] model successfully reproduced the observed SO_2 distribution with an appropriate (and reasonable) choice for the eddy diffusion coefficient. However, the concentrations of CO and O_2 predicted near the cloud tops were factors of $\sim$ 6 and $\sim$ 100, respectively, higher than the then extant observations. (Their predicted O_2 abundance is a factor of $\sim$ 300 larger than the current upper limit.)

The HO_x and SO_x cycles discussed so far have not included direct coupling between these species, only the minimum coupling necessary for oxidizing SO_2 to H_2SO_4. *Yung and DeMore* [1982] proposed two extensions of Cycle C1, Cycles C11 and C12 couple HO_x and SO_x chemistry to split the O-O bond in O_2 *and* produce CO_2 (as well as H_2SO_4 in Cycle C12). These cycles can enhance the production of CO_2 above the top of the upper cloud where the SO_2 abundance is still relatively large and the production of HO_x from H_2O (but especially from H_2) can be significant.

Chlorine oxide chemistry is believed to play a dual role in the Venus atmosphere.

In the classic cycle (Cycle C13) whose importance for the stratosphere was recognized by *Molina and Rowland* [1974], ClO_x rapidly converts odd oxygen (O and O_3) into O_2. *Sze and McElroy* [1975] and *Winick and Stewart* [1980] introduced the Molina-Rowland cycle to studies of Venusian atmospheric chemistry. Cycle C13 was sufficiently efficient at producing O_2 in the Winick and Stewart model that it negated the sequestration of oxygen in H_2SO_4 via Cycles C8, C9, and C10.

The second role for chlorine oxide chemistry is catalyzing the oxidation of CO to CO_2. *Prinn* [1975] suggested

$$ClOO + CO \rightarrow ClO + CO_2 \qquad \text{(G4)}$$

was an important mechanism for oxidizing CO. This reaction, however, is no longer believed to be important because (1) Prinn required that the rate for the competing reaction

$$ClOO + M \rightarrow Cl + O_2 + M \qquad \text{(G5)}$$

be five orders of magnitude smaller than the currently accepted value [*DeMore et al.* 1997] and (2) there is no experimental evidence suggesting Reaction G4 actually occurs [*Yung and DeMore* 1982].

Krasnopol'sky and Parshev [1981 and 1983] and *Yung and DeMore* [1982] considered reactions analogous to Reaction G4 that involve oxidation of the ClCO radical to form CO_2. *Krasnopol'sky and Parshev* [1981 and 1983], based on laboratory studies reviewed in *Heicklen* [1969], suggested

$$ClCO + O_2 \rightarrow ClO + CO_2 \qquad \text{(G6)}$$

could be a significant pathway for oxidizing CO to CO_2. However, (1) the equilibrium constant that *Krasnopol'sky and Parshev* [1983] assumed for ClCO (equal to the rate for formation of ClCO divided by the rate for decomposition of ClCO) was two orders of magnitude larger than the currently accepted value [*DeMore et al.* 1997], and (2) experimental work reported in *Yung and DeMore* [1982] and *Spence et al.* [1978] indicated the oxidation of ClCO by O_2 was a three-body reaction,

$$ClCO + O_2 + M \rightarrow ClCO_3 + M, \qquad \text{(K178)}$$

forming the peroxychloroformyl radical, $ClCO_3$. *Yung and DeMore* [1982] and *Krasnopol'sky and Parshev* [1983] also proposed

$$ClCO + O \rightarrow Cl + CO_2, \qquad \text{(K179)}$$

but their modeling indicated this pathway was not an important pathway for oxidizing CO. *Yung and DeMore* [1982] found that two catalytic cycles (Cycles C14 and C15) using $ClCO_3$ as an intermediary were important mechanisms for oxidizing CO Cycles C14 and C15 accounted for $\sim$ 40% of the CO_2 production in *Yung and DeMore*'s [1982] Model C. However, neither cycle results in a net loss of O_2, and their predicted column abundance of O_2 was almost a factor of 100 larger than the upper limit later established by *Trauger and Lunine* [1983].

An alternate cycle (Cycle C16) for oxidizing CO that is analogous to the Molina-Rowland cycle was proposed by *Sze and McElroy* [1975] and *Krasnopol'sky and Parshev* [1983]. The rate used by *Sze and McElroy* [1975] and *Krasnopol'sky and Parshev* [1983], 1.7×10^{-15} cm^3 s^{-1}, for Reaction K150 is, however, several orders of magnitude faster than the estimated upper limit rate recommended by *DeMore et al.* [1997], 1×10^{-12} exp(−3700/T) cm^3 s^{-1}, so Cycle C16 is no longer considered significant.

The first models in which chlorine oxide and sulfur oxide chemistry were linked were those by *Yung and DeMore* [1982] and *Krasnopol'sky and Parshev* [1983]. Both suggested Cycle C17 as a method for both oxidizing CO and destroying O_2. In *Yung and DeMore*'s [1982] Model C, Cycle C17 accounted for $\sim$ 60% of the CO_2 production. This is one reason *Yung and DeMore*'s [1982] predicted O_2 column abundance was a factor of $\sim$ 3 smaller than that predicted by *Winick and Stewart* [1980].

The importance of nitrogen chemistry in the Venus middle atmosphere is one of the major unresolved questions that can only be satisfactorily addressed by new observations. The only nitrogen species detected have been N_2 in the bulk atmosphere and NO at $\gtrsim$ 110 km altitude. N_2 is not photochemically active at the altitudes considered in this model so photochemically active NO_x would have to be produced either

by photodissociation of N_2 (at altitudes > 110 km followed by downward transport of NO_x) or locally as a result of lightning. Based on model B of *Yung and DeMore* [1982], the former alternative is not likely to be important. *Yung and DeMore* [1982] calculated that the downward flux of NO_x produced by photodissociation above 110 km altitude was four orders of magnitude smaller than that needed to have a significant impact on the photochemistry. That leaves lightning as the remaining mechanism for creating photochemically active NO_x in the middle atmosphere. The intensity of lightning on Venus is unknown and it has not even been definitively observed. Waves have been detected in the ionosphere that are consistent with those produced by lightning on Earth (*Ksanfomality et al.* [1983]; *Gurnett et al.* [1991]; *Hunten* [1995]), but (1) the implied intensities for lightning on Venus are significantly larger than the upper limits derived from optical observations [*Borucki et al.* 1991; *Hunten* 1995] and (2) local plasma sources for some of the observed waves have been identified [*Hunten* 1995]. Optical detections of lightning have been reported [*Hansell et al.* 1995], but the quality of the detections is sufficiently poor that there is substantial disagreement over whether the detections are significant. Furthermore, the optical systems can only detect lightning of high energy and the energy spectrum of lightning on Venus is unknown so it is not clear what the extant optical detections would imply for the production rate of photochemically active NO_x.

2.1.3 Current Approach

We have focused the current modeling on chlorine chemistry, similar to that proposed by *Yung and DeMore* [1982] and *Krasnopol'sky and Parshev* [1983], due to (1) the lack of satisfactory alternatives for oxidizing CO to CO_2 and (2) a favorable change of up to an order of magnitude in the measured ClCO equilibrium constant since *Yung and DeMore*'s [1982] work. As summarized in Section 2.1.2, previous photochemistry models have examined the potential roles of HO_x, ClO_x, SO_x, and NO_x catalytic chemistry in the Venus atmosphere. From their modeling, *Yung and DeMore* [1982] concluded that HO_x and NO_x likely play relatively minor roles compared to ClO_x

and SO_x since neither HO_x nor NO_x chemistry would produce the observed diurnal variation in CO abundances at 80 - 90 km altitude (Section 2.1.1). Furthermore, the observational premise for the large abundances of HO_x and NO_x that were considered in the *Yung and DeMore* [1982] models has subsequently been questioned (Sections 2.1.1 and 2.1.2). Consequently, from our present understanding of the Venus atmosphere, it is not likely that either HO_x or NO_x catalytic chemistry is important for the oxidation of CO to CO_2.

Other chemistry that might be important in the Venus atmosphere is that involving bromine compounds, fluorine compounds, or heterogeneous chemistry (chemistry occurring within or on the surfaces of aerosols). However, bromine compounds that could play a role in oxidizing CO to CO_2, such as BrCO, are generally more unstable than their chlorine counterparts, so bromine's role in the Venus atmosphere is likely limited to catalyzing the conversion of O_3 to O_2. In contrast, comparable fluorine compounds, such as FCO, are generally more stable than their chlorine counterparts, but the primary reservoir for fluorine, HF, photodissociates primarily above 110 km altitude (since the threshold for photodissociation is near 170 nm). Consequently, neither bromine nor fluorine compounds are likely to play important roles in the oxidation of CO to CO_2.

Two possible roles have been proposed for heterogeneous chemistry in the oxidation of CO to CO_2. *Mills and Phillips* [1993] proposed the direct photo-induced oxidation of CO to CO_2 on sulfuric acid aerosols but *Mills and Phillips* [1996] found the yields were too small to be significant. *Leu, M-T., and Y.L. Yung* [Personal Communication, 1995] proposed that aerosols in the Venus atmosphere could rapidly convert chlorine from the relatively unreactive form, HCl, to a more labile form, Cl_2, via reaction with HOCl

$$HCl + HOCl + \text{aerosol} \rightarrow H_2O + Cl_2 + \text{aerosol}. \qquad \text{(G10)}$$

By analogy to the chlorine chemistry found in the Antarctic ozone hole, a larger abundance of Cl_2 could enhance the effectiveness of the $CClO_x$ chemistry that was examined by *Yung and DeMore* [1982] and *Krasnopol'sky and Parshev* [1983]. Our

calculations, however, found that reaction G10 is not likely to be an important source of Cl_2 because (1) the solubility of HCl in concentrated sulfuric acid is low, (2) the abundance of HOCl is small due to condensation of H_2O on the sulfuric acid aerosols, and (3) the aerosol number density above 85 km altitude is small so the Cl_2 produced via reaction G10 would have to be transported upward by at least a scale height from $\lesssim$ 80 km altitude if reaction G10 is to be important for the oxidation of CO. Consequently, heterogeneous chemistry does not appear to be important in the oxidation of CO to CO_2.

Based on the foregoing analysis of possible mechanisms for oxidizing CO to CO_2, the oxygen budget in the Venus middle atmosphere appears to be controlled by chlorine and sulfur chemistry. Sulfur chemistry is most important within and slightly above the upper cloud, but it is not believed to play a direct role in the oxidation of CO. This suggests that chlorine catalytic chemistry is the primary mechanism for oxidizing CO. In our model and in those by *Yung and DeMore* [1982] and *Krasnopol'sky and Parshev* [1983] the primary intermediary for oxidizing CO is ClCO. Recent laboratory measurements of the stability of ClCO [*Nicovich et al.* 1990] suggest the molecule is more stable at low temperatures ($\lesssim$ 250 K) than previously believed (see Section 2.2.8). Consequently, cycles C14, C15, and C17 will be more efficient at oxidizing CO than they were in the *Yung and DeMore* [1982] models. For these reasons, we have focused our modeling effort on understanding the chlorine and sulfur chemistry that might occur in the Venus atmosphere.

2.1.4 New Photochemistry in Current Model

Several new elements have been considered in addition to those studied by *Yung and DeMore* [1982] in their model C: (1) formation of higher oxides of chlorine (Cl_xO_y where x and/or y is greater than 2), (2) additional reactions via $CClO_x$ that oxidize CO to CO_2, (3) OCS and polysulfur (S_x) chemistry and (4) $ClSO_x$ and SCl_x chemistry.

The higher oxides of chlorine are potential reservoirs in which oxygen could be stored as it is transported downward through the middle atmosphere. As will be

evident in the discussion, however, these compounds are sufficiently unstable that they appear to have negligible impact on the oxygen budget in the Venus atmosphere.

We have increased the number of paths by which CO may be oxidized to CO_2 via $CClO_x$ while simultaneously destroying O_2. First, due to the increased stability of ClCO at < 250 K (compared to that used by *Yung and DeMore* [1982]), we find that reactions K179 and K288, that were largely neglected in the *Yung and DeMore* [1982] model, are minor but important paths for oxidizing CO. These reactions are most important at 80 - 90 km altitude where the largest abundances of $ClCO_3$, ClCO, and O are predicted. In addition, three modifications of Cycle C14 (Cycles C18, C19, and C20) provide new paths for oxidizing CO that may lead to net loss of O_2, depending on the subsequent fate of the atomic oxygen produced. These cycles (C18, C19, and C20) are likely to be important only near the cloud top where the abundance of SO_x is comparable to that of Cl and O.

The sulfur chemistry in the current model is more comprehensive than that proposed in *Yung and DeMore* [1982]. This was done to provide a better assessment of the chemistry that may occur within the upper cloud layer, such as that involving OCS and S_x. OCS that diffuses upward from the lower atmosphere provides two potential sinks for oxygen in the upper cloud layer–oxidation of CO to CO_2 and oxidation of S to H_2SO_4 via SO_3 as in Cycle C21. The CO_2 (or CO) and H_2SO_4 that could be produced from extensions of cycle C21 would, subsequently, be transported to the lower atmosphere to balance the upward diffusion of OCS. An alternate fate for the sulfur atoms produced by photodissociation of OCS is the accretion of sulfur to form S_8. S_8 would then be transported with CO to the lower atmosphere to balance the upward diffusion of OCS. The balance between formation of H_2SO_4 and S_8 is governed by the local oxidation state of the atmosphere so there is a transition from formation of S_8 at lower altitudes to formation of H_2SO_4 at higher altitudes. We find that this transition occurs within the upper cloud.

The final new element of our photochemistry is consideration of $ClSO_x$ and SCl_x compounds. No quantitative modeling has been published for these compounds, although there has been speculation that they might be present [*Toon et al.* 1982],

and *DeMore et al.* [1985] qualitatively examined the impact that $ClSO_2$ chemistry might have on the results from *Yung and DeMore*'s [1982] model C. Within the upper cloud layer, $ClSO_x$ and SCl_x compounds serve as intermediaries in the formation of S_2 (as in Cycle C22) with the S_2 eventually accreting additional sulfur to form S_8. This occurs principally in the lower part of the upper cloud and has little effect on the oxygen budget. However, $ClSO_2$ also serves as a reservoir for SO_2 that can shelter SO_2 from rapid oxidation to SO_3 and, thus, reduce the gradient in the SO_2 mixing ratio within the upper cloud (Cycle C23). One of the proposed $ClSO_x$ or SCl_x compounds (most likely $ClSO_2$) may be able to explain the ultraviolet absorption that is required in radiative transfer models to match the albedo of the upper cloud layer at 300 - 400 nm [*Pollack et al.* 1980]. Further study of the UV absorber problem requires laboratory measurements of the absorption cross section for $ClSO_2$.

2.2 Description of Model

Atmospheric chemistry is commonly studied using numerical models. Since a variety of numerical methods are used, a brief description of our technique is provided in this section. This section also describes the data used as input parameters to the model, such as the chemical kinetic reaction rates and the photoabsorption cross sections. Additional information on the input data and calculation parameters used for the modeling are given in Appendices F, G, H, I, J, and K. All relevant chemistry studied in previous Venus models (*Krasnopol'sky and Parshev* [1983]; *Yung and DeMore* [1982]; *Winick and Stewart* [1980]; *Sze and McElroy* [1975]; *Prinn* [1975]) has been included, but the rates have been critically assessed and updated. We also have added several procedures that enhance the fidelity of our model compared to previous Venusian photochemistry models.

2.2.1 General Characteristics

Our photochemical model is similar to that used by *Nair et al.* [1994] to study the photochemistry of Mars. The Caltech/JPL photochemical model solves the one-

dimensional continuity equation for the species of interest,

$$\frac{\partial n_i}{\partial t} + \frac{\partial \Phi_i}{\partial z} = P_i - L_i, \qquad (2.2.2.1)$$

where n_i, Φ_i, P_i, and L_i are the concentration, vertical diffusive flux, chemical production, and chemical loss terms, respectively, for species i [*Allen et al.* 1981]. The vertical diffusive flux, Φ_i, is given by

$$\Phi_i = -D_i\left(\frac{dn_i}{dz} + \frac{n_i}{H_i} + \frac{n_i(1+\alpha)}{T}\frac{dT}{dz}\right) - K\left(\frac{dn_i}{dz} + \frac{n_i}{H} + \frac{n_i}{T}\frac{dT}{dz}\right), \qquad (2.2.2.2)$$

where D_i is the molecular diffusion coefficient of species i through the background atmosphere, H_i is the scale height of species i, T is the temperature, α is the thermal diffusion factor, K is the eddy diffusion coefficient, and H is the scale height of the background atmosphere [*Allen et al.* 1981]. For the Venus photochemical model, we simultaneously solve the continuity equation for 48 species: CO_2, CO, O_3, O_2, $O_2(^1\Delta)$, O, $O(^1D)$, H_2, H, OH, HO_2, H_2O_2, HCl, HOCl, CHClO, Cl_2, Cl, ClO, ClOO, OClO, Cl_2O, Cl_2O_2, ClO_3, Cl_2O_3, $ClOClO_3$, ClCO, $COCl_2$, $ClCO_3$, SO_2, SO, S, S_2O, $(SO)_2$, OCS, SO_3, S_2, S_3, S_4, S_5, S_6, S_7, S_8, SCl, SCl_2, S_2Cl, S_2Cl_2, OSCl, and $ClSO_2$. The abundances for four species (S_8, SO_3, N_2, and H_2O) have been held fixed at specified values. S_8 is assumed to condense out of the gas-phase and become non-reactive. SO_3 is assumed to react rapidly with H_2O to form H_2SO_4 which condenses out of the gas-phase and becomes non-reactive. Consequently, the abundances for both S_8 and SO_3 are specified to be zero at all altitudes and only their production rates have been calculated. N_2 has been assumed to have a uniform, fixed mixing ratio (3.4%) at all altitudes. The H_2O profile has been specified as described in Section 2.2.3.

This photochemical model is intended to represent the "global average" photochemistry of the Venus atmosphere. Consequently, diurnal variations (which are important for some species) have not been explicitly modeled, although they have have been considered in the analysis of our results. To approximate "global average" conditions, photodissociation calculations were done for 45 degrees latitude at local noon

(effective solar zenith angle of 44.1 degrees) then the calculated photodissociation rates were divided by a factor of two.

We use a finite difference iterative algorithm [*Logan et al.* 1978; *Allen et al.* 1981] over a series of time steps of variable length to converge to a steady-state solution ($\partial n_i/\partial t = 0$). The steady-state solution was defined as the converged solution for a time step of 1×10^{15} seconds when successive iterations yield solutions differing by less than one part in 10^4 for all species whose volume mixing ratios were at least 1 ppbv (10^{-9}). The radiation field was calculated at the beginning of each model run then recalculated at the beginning of each time step. Up to 10 iterations per time step were used to achieve convergence.

2.2.2 Boundary Conditions

Ideally, a model should have as few imposed conditions as possible to minimize the degree to which the calculated results simply reflect the imposed assumptions. However, since our model includes only the middle portion of the Venus atmosphere, it is necessary to specify conditions at both boundaries of the model that represent the chemistry occurring outside the modeled altitudes. For this project, we placed the lower and upper boundaries of our model at 58 and 112 km altitude since this range includes the region in which most of the photochemistry relevant to the oxygen budget on Venus occurs.

The lower boundary for our model is more than two scale heights below the level at which cloud opacity reaches optical depth unity [*Crisp* 1986]. In addition, landers have generally found the 58 km altitude region to be stable against convection so the diffusive flux across the lower boundary should be minimized. The stability near 58 km means the chemistry occurring at lower altitudes can be represented well by specifying the mixing ratio of a species at the boundary if the species (1) is produced in the lower atmosphere, (2) is destroyed in the upper atmosphere, and (3) has a photochemical lifetime near 58 km that is much larger than the vertical mixing time. These conditions are true for HCl, CO, and CO_2, but (3) is not true for OCS, and the

photochemical lifetime for SO_2 near 58 km is comparable to the transport timescale. Consequently, the modeled vertical profiles for OCS and SO_2 in the upper cloud will be sensitive to both the specified mixing ratios at the lower boundary and the chosen eddy diffusion coefficient. The nominal boundary conditions we have used are listed in Table 2.2.

The primary sources for sulfur, OCS and SO_2, are produced in the lower atmosphere then transported upward and, predominantly, lost within the modeled altitude region. Likewise, the primary source for hydrogen and chlorine, HCl, is produced in the lower atmosphere and primarily lost above 60 km altitude. Consequently, the mixing ratios for OCS, SO_2, and HCl at the lower boundary of the model were specified based on observations (Section 2.1.1). The nominal OCS mixing ratio, 0.1 ppm, was linearly interpolated (for natural logarithm of pressure versus mixing ratio) between the values retrieved by *Bezard et al.* [1990]. The SO_2 mixing ratio at 58 km was empirically adjusted to give an abundance of SO_2 at 70 km altitude that is within the range of measured values [*Na et al.* 1994; *Na and Esposito* 1995]. The nominal HCl mixing ratio, 0.4 ppm, was taken from the analysis by *Young* [1972] of the spectra collected by *Connes et al.* [1967]. The role of the lower atmosphere in the carbon cycle is not clearly understood, yet, and may depend on the oxidation state of the upper cloud, so the mixing ratios for CO and CO_2 at the lower boundary of the model were specified based on observations. For example, the *Yung and DeMore* [1982] models implicitly assumed there was a downward flux of CO and an upward flux of CO_2 through their lower boundary. As discussed in Section 2.3.3, however, these fluxes could have opposite signs if the upper cloud is very depleted in oxygen. The lower boundary condition for all other species (except H_2O) was the maximum downward diffusive flux. This minimizes the variation in the species mixing ratio across the boundary and implicitly assumes that these species are produced within the modeled altitude region and that the vertical mixing time is smaller than the photochemical lifetime.

The upper boundary for the model, 112 km, is sufficiently high that less than 10% of the CO_2 photolysis occurs above the upper boundary, and the modeled altitudes

Table 2.2: Boundary Conditions for the Nominal Photochemical Model

Species	Lower Boundary (58 km)	Upper Boundary (112 km)
CO_2	$f = 0.965$	$\phi = 5 \times 10^{11}$
CO	$f = 4.5 \times 10^{-5}$	$\phi = -5 \times 10^{11}$
O_2		$\phi = 9 \times 10^{8}$
†HCl	$f = 4.0 \times 10^{-7}$	$\phi = 1 \times 10^{7}$
SO_2	$f = 1.2 \times 10^{-6}$	
O		$\phi = -5.024 \times 10^{11}$
Cl		$\phi = -1 \times 10^{7}$
OCS	$f = 1.0 \times 10^{-7}$	
$O_2(^1\Delta)$		$\phi \sim 3 \times 10^{8}$

† The upward flux of chlorine in the form of HCl is balanced at the upper boundary by a downward flux of chlorine as Cl. The upward flux of hydrogen in the form of HCl is comparable to the calculated escape rate for hydrogen (Section 2.1.1) so there is no downward flux of hydrogen through the upper boundary.

Notes: The symbols f and ϕ denote volume mixing ratio and flux (cm^{-2} sec^{-1}), respectively. The sign convention for ϕ is positive for upward flow. For all species not explicitly listed here, the lower boundary condition was maximum downward diffusive flux (minimum gradient in the mixing ratio), and photochemical equilibrium ($\phi = 0$) was assumed at the upper boundary condition. The maximum deposition velocity at the lower boundary is determined by $v = -K/H$, where K = eddy diffusion coefficient, H = scale height, and v is a velocity (cm sec^{-1}). The upward flux for $O_2(^1\Delta)$ at the upper boundary was the maximum upward diffusive flux (minimum gradient in the mixing ratio). The mixing ratio for H_2O was fixed as described in Section 2.2.3. The mixing ratio for N_2 was held fixed at 0.034.

include the primary range over which our model calculations indicate the $O_2(^1\Delta)$ airglow is produced. The modeled altitudes, thus, should include all of the observed phenomena related to the oxygen budget of the Venus atmosphere. The upper boundary was placed several scale heights below the homopause ($\sim 130-135$ km [*von Zahn et al.* 1983]) and the ionosphere ($\gtrsim 130$ km [*Cloutier et al.* 1993]) to simplify the modeling.

The upper boundary conditions were determined, primarily, by the photodissociation of CO_2 and HCl. The upward fluxes of CO_2, O_2, and HCl were set equal to the estimated photodissociation rates for these species integrated over the column above our upper boundary, as discussed in the next paragraph. The specified rates are smaller than the maximum upward diffusive flux so there is no hydrodynamic limitation on these fluxes. The upward flux of $O_2(^1\Delta)$, on the other hand, was set to the maximum diffusive flux because the estimated column-integrated photodissociation rate would have been larger than the hydrodynamic limit. The downward fluxes of CO, O, and Cl at the upper boundary balance the upward fluxes of carbon, oxygen, and chlorine. There is no flux of H_2 nor of H through the upper boundary since the photodissociation rate of HCl above the upper boundary is comparable to the estimated escape flux for hydrogen from the Venus atmosphere (Section 2.1.1). The fluxes of all other species were set to zero since their concentrations are sufficiently small that the maximum upward diffusive flux through the upper boundary would have a negligible impact on the photochemistry in our model.

For CO_2, photodissociation in the wavelength bins in which the optical depth above the top of the model was $\gtrsim 3$ was approximated as the total incident solar flux divided by a factor of four to account for the conversion from the planets cross section to the planet's surface area. For O_2 and HCl, photodissociation in these wavelength bins was estimated from

$$j_i(\lambda, z > 112) \approx \frac{J(\lambda, \tau = 1)}{2} \times n_i(\tau = 1) \times H(z = 112), \qquad (2.2.2.3)$$

where $J(\lambda, \tau = 1)$ is the estimated photodissociation rate ($\sec^{-1}$) at the altitude at

which the optical depth is unity, $n_i(\tau = 1)$ is the estimated number density of species i at the same altitude, $H(z = 112)$ is the scale height at 112 km altitude, and the factor of two accounts for diurnal averaging. For wavelength bins in which the optical depth above the top of the model was $\sim 1 - 3$, photodissociation for all three species (CO_2, O_2, and HCl) was estimated using equation 2.2.2.3. For wavelength bins in which the optical depth above the top of the model was < 1, the column-integrated photodissociation rates above the upper boundary were estimated from

$$j_i(\lambda, z > 112) \approx J_i(\lambda, z = 112) \times n_i(z = 112) \times H(z = 112), \qquad (2.2.2.4)$$

where $J_i(\lambda, z = 112)$ is the diurnally averaged photolysis rate for species i in wavelength bin λ at 112 km altitude.

The most significant differences between our boundary conditions and those used for previous models (Table 2.3) are (1) the mixing ratios for HCl and SO_2 at the lower boundary, (2) the inclusion of OCS, and (3) the escape of hydrogen through the upper boundary. Our mixing ratio for HCl at 58 km altitude is more consistent with the current inferences from observations [*Young* 1972; *Pollack et al.* 1993] than the HCl mixing ratio used in earlier models, but the *Yung and DeMore* [1982] value is less than 3σ larger than than the currently accepted value. The mixing ratio for SO_2 at 58 km altitude is a free parameter in our model whose value is controlled by the relative time scales for vertical transport versus oxidation to SO_3. We have decreased the efficiency of the oxidation and have increased the efficiency of the vertical transport by sequestering some of the SO_2 in $ClSO_2$ and strengthening the eddy diffusion (compared to *Yung and DeMore* [1982]). These changes lead to a smaller value for the SO_2 mixing ratio at 58 km altitude. The effects of OCS on the photochemistry within the upper cloud will be discussed in Section 2.3. As noted earlier in this section, the photodissociation rate for HCl above 112 km altitude is comparable to the estimated escape rate for hydrogen. As a result, we have accounted for the loss of hydrogen from the Venus atmosphere via an upward flux of HCl (and downward flux of Cl) through the upper boundary.

Table 2.3: Boundary Conditions for Previous Photochemical Models

	Yung and DeMore [1982]†		*Krasnopol'sky and Parshev* [1983]	
Species	(58 km)	(110 km)	(50 km)	(200 km)
CO_2			0.965	
CO	$f = 4.5 \times 10^{-5}$	$\phi = -1.0 \times 10^{12}$	$f = 4.0 \times 10^{-5}$	
O_2	$v = -2.0 \times 10^{-2}$			
HCl			$f = 6.0 \times 10^{-7}$	
SO_2	$f = 4.0 \times 10^{-6}$		$f = 1.3 \times 10^{-4}$	
O	$v = -2.0 \times 10^{-2}$	$\phi = -1.0 \times 10^{12}$		
Cl_2	$v = -2.0 \times 10^{-2}$			
H_2	$v = -2.0 \times 10^{-2}$			
H				$\phi = 1.0 \times 10^{7}$
H_2O			$f \sim 2 \times 10^{-4}$	

†Values are for Model C.

Notes : The symbols f, v, and ϕ denote volume mixing ratio, velocity (cm sec^{-1}), and flux (cm^{-2} sec^{-1}), respectively. The sign convention for ϕ is positive for upward flow. For all species not explicitly listed here, *Yung and DeMore* [1982] assumed photochemical equilibrium ($\phi = 0$) at both boundaries. Their mixing ratio for H_2O was fixed at 1 ppm and that for HCl was fixed at 8×10^{-7}. *Krasnopol'sky and Parshev* [1983] assumed the fluxes of all components except H were zero at the upper boundary and determined mixing ratios for all other species at the lower boundary based on estimates of their photochemical and vertical transport lifetimes in the lower atmosphere.

2.2.3 H_2O

The water vapor abundances in our photochemical model differ significantly from those used in previous models. We have assumed the water vapor abundance will be determined by the temperature and composition of the H_2SO_4 aerosols in the upper cloud and haze layer, whereas previous models have neglected the possible condensation of water on the aerosols. As a result, our water vapor abundances are as much as several orders of magnitude smaller than those in previous photochemical models.

Previous photochemical models (for example, *Winick and Stewart* [1980] and *Yung and DeMore* [1982]) assumed the mixing ratio for water vapor was 1 ppm at all altitudes. This assumption was based on the presumption that there was no photochemical loss for water below $\sim$ 90 km altitude. Their presumption that water is not lost photochemically at lower altitudes is probably correct because water vapor photodissociates only at wavelengths $\lesssim$ 195 nm and CO_2 is optically thick for altitudes $\lesssim$ 80 km at these wavelengths. Consequently, direct photolysis of H_2O is slow below $\sim$ 100 km altitude and minimal below $\sim$ 80 km altitude. The primary alternate path for destroying H_2O is via reaction with $O(^1D)$. This is the primary means by which H_2O is converted to OH in the terrestrial troposphere, but the production rate for $O(^1D)$ in the Venus atmosphere is small compared to that in the terrestrial atmosphere. (In our model, the dominant loss of H_2O at *all* altitudes is via direct photolysis.) Thus, as was assumed in previous models, we expect the water vapor mixing ratio to be approximately constant below $\sim$ 80 km altitude. *Encrenaz et al.* [1995] implicitly adopted the same assumption (that there was no significant loss process for water vapor below $\sim$ 90 km) when they found they needed to decrease the temperature at $\sim$ 95 km altitude to 140 K (the freezing point for water ice at that altitude) to obtain the best match to their microwave spectrum.

Above $\sim$ 80 km altitude, however, there are two potential loss mechanisms for water vapor. One is the direct photolysis of H_2O, but due to the shielding by CO_2 this is not rapid below $\sim$ 100 km altitude. The second potential loss is condensation

of water vapor onto the sulfuric acid aerosols that have been observed below $\sim$ 90 km. Condensation will be important if the timescale for condensation is smaller than the vertical mixing time. As we show in Appendix F, the water vapor abundance below $\sim$ 90 km altitude should be controlled by condensation.

For our nominal profile, we fixed the H_2O abundance at $\leq$ 90 km altitude to be the smaller of 0.5 ppm or the equilibrium vapor pressure of H_2O over 75 wt% H_2SO_4. The water vapor mixing ratios above 90 km altitude were set equal to the mixing ratio for H_2O at 90 km altitude by analogy to the situation in the earth's lower stratosphere. Within the uncertainties associated with determining the equilibrium vapor pressure for water over concentrated sulfuric acid (Appendix G), the water vapor profile we derive is consistent with the measurements by *Encrenaz et al.* [1995]. Calculations have also been done for other H_2O distributions to assess the sensitivity of our results to our assumed water vapor profile. The results for these alternate profiles will be discussed in Section 2.3.

Our choice of 0.5 ppm for the water vapor mixing ratio in the upper cloud layer is somewhat arbitrary since the observations described in Section 2.1.1 found water vapor mixing ratios within the upper cloud layer of $\sim 0.5 - 2$ ppm.

The 75 wt% H_2SO_4 composition we have used for the aerosol particles is based on polarization measurements of the upper cloud and haze. *Hansen and Hovenier* [1974] found the optical properties of the mode 2 ($\sim$ 1 μm size) aerosol particles in the upper cloud were compatible with (but not required to be) 75 wt% H_2SO_4 ($+10, -5$ wt% H_2SO_4 [*Hovenier, J.*, Personal Communication, 1997]). Later measurements of the polar haze [*Sato et al.* 1996] suggest the composition of the mode 1 ($\sim$ 0.25 μm size) particles is similar to that of the mode 2 particles. Consequently, we have assumed the composition of all aerosol particles in the upper cloud and haze are 75 wt% H_2SO_4. The relations we used to estimate the equilibrium vapor pressure for water vapor over concentrated sulfuric acid are discussed in Appendix G.

2.2.4 Radiative Transfer

Photochemistry in the Venus middle atmosphere is driven by energy received from the Sun. The primary means by which the solar energy incident on the atmosphere is converted into chemical potential energy is via the photodissociation of relatively unreactive species (such as H_2O) to form highly reactive radical species (such as OH). This conversion process is governed by the transport of solar radiation through the Venus atmosphere and may be described using a radiative transfer model. The total solar flux (the actinic flux) at a point is the sum of the direct solar irradiance (irradiance that has been neither absorbed nor scattered) and the diffuse flux (the radiance integrated over 4π steradian that has been scattered by molecules or aerosols). Accurate calculation of photodissociation rates requires consideration of both components of the actinic flux because both components have comparable intensities within the upper cloud layer at wavelengths $\gtrsim$ 200 nm. This section describes how the actinic flux is calculated for each level in the photochemical model. The primary data required for the radiative transfer calculations, the incident solar irradiance and the photoabsorption cross sections, are described in Sections 2.2.5 and 2.2.6, respectively.

The direct irradiance in our model is calculated in the same manner as in previous Venus photochemical models. Assuming a plane-parallel atmosphere the direct irradiance at each level is described by the Beer-Lambert law,

$$F_s(\lambda, z) = F_t e^{-\frac{1}{\cos(\mu)}\Sigma_i N_i(z)\sigma_i(\lambda)}, \qquad (2.2.2.5)$$

where F_t is the solar irradiance incident at the top of the atmosphere, μ = solar zenith angle, $N_i(z)$ is the column density of each absorber or scatterer above the model altitude, and $\sigma_i(\lambda)$ is the extinction cross section for each species. (The extinction cross section is the sum of the absorption and scattering cross sections.) In the Venus atmosphere, extinction of the direct solar irradiance at wavelengths $\lesssim$ 192.5 nm is primarily due to absorption by CO_2. Between 192.5 and 310 nm, extinction is primarily due to absorption by SO_2 and scattering by aerosol particles in the upper cloud layer. For wavelengths $\gtrsim$ 310 nm, scattering by aerosol particles dominates the

extinction of the direct solar irradiance.

Although the direct solar irradiance has been properly considered in previous Venus photochemical models, the diffuse flux has been ignored or treated in an approximate manner due to the limited computational capability available in the early 1980s. For example, *Yung and DeMore* [1982] did not include the diffuse flux in their calculations. Instead, they assumed the aerosols in the upper cloud were purely absorbing and modeled the attenuation of the incident solar irradiance at all wavelengths below 70 km altitude based on the measurements by *Ragent and Blamont* [1980]. *Krasnopol'sky and Parshev* [1983] approximated the effects of multiple scattering by increasing the absorption cross sections of all species at > 320 nm by a factor of 10 since they assumed the number of scatters is ~ 1 for < 320 nm and ~ 10 for > 320 nm. We have used the Feautrier method [*Feautrier* 1964; *Prather* 1976], generalized to arbitrary anisotropic scattering [*Michelangeli et al.* 1992], to determine the diffuse flux. Our inclusion of diffuse flux in a rigorous manner increases the actinic flux (compared to *Yung and DeMore* [1982]) and, thus, increases photodissociation rates. Appendix H provides an assessment of the accuracy of our radiative transfer calculations; Appendix I describes the parameters used for computing Rayleigh scattering; and Appendix J describes the scattering characteristics we have assumed for the aerosols in the upper cloud and haze.

2.2.5 Solar Flux

One of the key inputs required for the radiative transfer calculation is the solar irradiance at the top of the atmosphere. The wavelength range of interest for the Venus middle atmosphere is from HI Lyman-α (121.57 nm) to $\sim 750 - 800$ nm, particularly at Lyman-α and in the 165 - 320 nm region. Solar irradiance at < 120 nm is absorbed in the thermosphere or ionosphere, several scale heights above the upper boundary of our model, and the integrated irradiance at < 120.0 nm is an order of magnitude smaller than that at 122.5 - 182.5 nm so irradiance at < 120 nm has a negligible effect on the altitudes we are modeling. Solar irradiance at > 800 nm is absorbed

in the upper cloud layer (by the aerosol particles, H_2O, and CO_2) but the energy of a photon at $\gtrsim$ 800 nm is generally too small to photodissociate a molecule. An important exception is O_3 which can be photodissociated by radiation at $<$ 1180.0 nm [*Okabe* 1978]. However, even though the integrated solar irradiance at 805 - 1180 nm is comparable to that at 400 - 805 nm, the photoabsorption cross section of O_3 at $>$ 800 nm is an order of magnitude smaller than in the Chappuis band (400 - 750 nm). Consequently, solar irradiance at $>$ 800 nm has a negligible effect on the photochemistry we are modeling.

The relevant wavelength range, 120 - 805 nm, has been divided into 5 or 10 nm intervals as shown in Table 2.4. These intervals are generally larger than those used by *Yung and DeMore* [1982] but they are commonly used in photochemical calculations for the terrestrial atmosphere. These intervals were selected primarily for computational convenience since most of the photoabsorption cross sections were available on this grid, but our tests using the *Yung and DeMore* [1982] grid found no significant effect on the oxygen chemistry. The irradiances in Table 2.4 have been integrated over the specified interval and are for 1 AU. They were increased in the model by the factor $(1/0.72)^2$ to account for Venus' smaller distance from the Sun. Data for high and low solar activities have been included in Table 2.4. Model calculations and measurements have found that the solar irradiance varies primarily at $<$ 300 nm. Consequently, for 300 - 805 nm, the irradiances for both high and low solar activity are approximately the same.

The solar irradiances in Table 2.4 are primarily from two sources, *Woods et al.* [1996] and *Neckel and Labs* [1984]. The *Woods et al.* [1996] data were selected because they are available at $\sim$ 1 nm resolution and resulted from an intercomparison of multiple instruments which should enhance the reliability of the data. The *Neckel and Labs* [1984] data were selected because they are also available at $\sim$ 1 nm resolution and have been used for previous environmental assessments (e.g., *WMO* [1985]). The solar irradiance data used by *Yung and DeMore* [1982] was taken from *Mount et al.* [1980] and *Ackerman* [1971]. However, *Nicolet* [1981] concluded that the irradiances derived by *Ackerman* [1971]. overestimated the solar irradiance by about 30% and

Table 2.4: Solar Irradiance at 1 A.U. for Low and High Solar Activity. See text.

Solar Irradiance (πF, cm^{-2} sec^{-1} (*lambda* interval)$^{-1}$)								
λ	low	high	λ	low	high	λ	low	high
121.25	1.23(11)	1.34(11)	277.5†	1.30(14)	1.31(14)	480	4.91(15)	4.91(15)
121.57	2.51(11)	3.70(11)	282.5†	1.69(14)	1.70(14)	490	4.68(15)	4.68(15)
125	4.80(10)	6.48(10)	287.5†	2.43(14)	2.42(14)	500†	4.84(15)	4.84(15)
130	1.69(10)	2.04(10)	292.5†	4.19(14)	4.19(14)	510	4.95(15)	4.95(15)
135	2.22(10)	2.63(10)	297.5†	3.91(14)	3.90(14)	520	4.77(15)	4.77(15)
140	1.87(10)	2.22(10)	302.5†	4.08(14)	4.10(14)	530	5.01(15)	5.01(15)
145	2.22(10)	2.46(10)	307.5†	4.61(14)	4.63(14)	540	5.10(15)	5.10(15)
150	3.45(10)	3.77(10)	312.5†	5.49(14)	5.52(14)	550	5.20(15)	5.20(15)
155	7.11(10)	7.82(10)	317.5†	5.64(14)	5.68(14)	560	5.20(15)	5.20(15)
160	8.12(10)	8.66(10)	322.5†	6.07(14)	6.10(14)	570	5.30(15)	5.30(15)
165	1.49(11)	1.61(11)	327.5†	8.18(14)	8.21(14)	580	5.40(15)	5.40(15)
170	2.62(11)	2.76(11)	332.5†	8.34(14)	8.36(14)	590	5.30(15)	5.30(15)
175	4.60(11)	4.86(11)	337.5†	7.88(14)	7.89(14)	600†	5.35(15)	5.35(15)
180	8.45(11)	9.04(11)	342.5†	8.33(14)	8.37(14)	610	5.33(15)	5.33(15)
185	1.15(12)	1.22(12)	347.5†	8.24(14)	8.29(14)	620	5.29(15)	5.29(15)
190	1.82(12)	1.91(12)	352.5†	9.34(14)	9.36(14)	630	5.29(15)	5.29(15)
195†	2.61(12)	2.74(12)	357.5†	8.28(14)	8.30(14)	640	5.29(15)	5.29(15)
200†	3.70(12)	3.86(12)	362.5†	9.16(14)	9.20(14)	650†	5.21(15)	5.21(15)
205†	5.51(12)	5.75(12)	367.5†	1.13(15)	1.14(15)	660	5.07(15)	5.07(15)
210†	1.31(13)	1.34(13)	372.5†	1.01(15)	1.02(15)	670	5.18(15)	5.18(15)
215†	1.96(13)	1.99(13)	377.5†	1.15(15)	1.15(15)	680	5.12(15)	5.12(15)
220†	2.53(13)	2.56(13)	382.5	9.40(14)	9.42(14)	690	5.07(15)	5.07(15)
225†	3.03(13)	3.05(13)	387.5	1.05(15)	1.05(15)	700†	4.98(15)	4.98(15)
230†	2.99(13)	3.01(13)	392.5	1.07(15)	1.07(15)	710	4.97(15)	4.97(15)
235†	2.87(13)	2.90(13)	397.5	1.30(15)	1.30(15)	720	4.88(15)	4.88(15)
240†	2.96(13)	2.98(13)	402.5†	1.79(15)	1.80(15)	730	4.89(15)	4.89(15)
245†	3.70(13)	3.74(13)	410	3.56(15)	3.57(15)	740	4.80(15)	4.80(15)
250†	3.34(13)	3.38(13)	420	3.66(15)	3.66(15)	750†	4.80(15)	4.80(15)
255†	3.15(13)	3.16(13)	430	3.45(15)	3.45(15)	760	4.76(15)	4.76(15)
257.5†	5.80(13)	5.83(13)	440	4.08(15)	4.08(15)	770	4.67(15)	4.67(15)
262.5†	9.52(13)	9.53(13)	450†	4.53(15)	4.53(15)	780	4.67(15)	4.67(15)
267.5†	1.72(14)	1.73(14)	460	4.74(15)	4.74(15)	790	4.63(15)	4.63(15)
272.5†	1.45(14)	1.46(14)	470	4.73(15)	4.73(15)	800†	4.59(15)	4.59(15)

†Wavelengths at which the full diffuse flux calculation was done. See text.
1.00(13) = 1×10^{13}. Wavelengths are in nanometers. Fluxes have been integrated over wavelength intervals that are (generally) centered on the specified wavelength.

that the irradiances derived by *Mount et al.* [1980] should be regarded as systematically low. Consequently, we selected newer solar irradiance measurements for use in our calculations. Appendix K describes in more detail the solar irradiances that were used in our calculations.

For the calculations presented in Section 2.3, there were three errors in the solar irradiances: (1) the low solar activity irradiance at Ly-α was 2.6×10^{11}, (2) the high solar activity irradiance at Ly-α was 4.0×10^{11}, and (3) the solar irradiance at 121.25 nm was not included in the calculations. No significant effect is expected from these errors.

2.2.6 Photoabsorption Cross Sections

The absorption of sunlight is the ultimate energy source for photochemistry in the atmosphere of Venus. The primary means by which solar energy is converted into chemical potential energy is via photodissociation reactions. These are reactions in which a molecule absorbs a photon of sufficient energy that the molecule is split into two or more components.

The most important photodissociation reactions for understanding the oxygen budget of the Venus middle atmosphere are the photodissociation of CO_2, SO_2, SO, OCS, and HCl. The data we have used to compute the photodissociation rates for these species were based on our own review of the chemistry literature (Appendix B), guided by the recommendations in *DeMore et al.* [1994] and *DeMore et al.* [1997]. The data for most other species were drawn from similar assessments that were completed for previous Caltech modeling efforts or from *DeMore et al.* [1994] and *DeMore et al.* [1997] (see Table 5A.1 and Appendix B). Photodissociation rates at 70 and 112 km are given in Table 5A.1.

Photodissociation rates ("J values") are calculated by integrating over all wavelengths,

$$J_i(z) = \int_\lambda \sigma_i(\lambda, T, P)\varphi_i(\lambda, T, P)F(\lambda, z)d\lambda, \qquad (2.2.2.6)$$

where σ_i is the absorption cross section for species i, φ_i is the photodissociation quantum yield for species i, and F is the actinic flux (the sum of the direct solar irradiance and the diffuse flux). In general, σ_i and φ_i can be functions of temperature (T) and pressure (P). Equation 2.2.2.6 is commonly solved by subdividing the wavelength interval and converting the integral into a summation,

$$J_i(z) \approx \Sigma_j \sigma_{ij}(T,P)\varphi_{ij}(T,P)F_j(z), \qquad (2.2.2.7)$$

where σ_{ij} is the *mean* absorption cross section for species i on wavelength interval j, φ_{ij} is the *mean* photodissociation quantum yield for species i on wavelength interval j, and F_j is the actinic flux *integrated* over wavelength interval j. In addition, the direct irradiance component of $F(\lambda, z)$ depends exponentially on the total opacity in the column above z (Equation 2.2.2.5). The opacity due to all important species was included in determining the $F(\lambda, z)$.

The temperature-dependence indicated in Equations 2.2.2.6 and 2.2.2.7 has been shown to be very important for the photodissociation of CO_2 and H_2O in the Martian atmosphere [*Nair et al.* 1994; *Anbar et al.* 1993], but has not been included in previous Venus photochemical models due to computational limitations [*Yung and DeMore* 1982]. For example, *Yung and DeMore* [1982] calculated the CO_2 cross section at 250 K and then used that cross section at all altitudes in their model. Our inclusion of the temperature-dependent cross section for CO_2 should decrease the photolysis of CO_2 at higher altitudes and increase the photolysis at lower altitudes (compared to *Yung and DeMore* [1982]) because the photoabsorption cross section of CO_2 decreases as temperature decreases. Temperature-dependent cross sections have also been included in the current model for O_3, SO_2, and OCS. The temperatures at which these cross sections were measured are given in Appendix B. The cross sections at other temperatures were determined by piecewise linear interpolation. For our nominal model calculations, we did not extrapolate the temperature-dependence to lower temperatures than had been measured in the laboratory.

A second factor that may be important in calculating photodissociation rates is the

size of the wavelength intervals used in Equation 2.2.2.7. We have used the $5.0 - 10.0$ nm intervals in Table 2.4 to compute photodissociation rates. These wavelength intervals are a standard set used for terrestrial photochemical modeling, but absorption in the highly structured SO_2 bands may not follow the Beer-Lambert law at this resolution due to saturation in the strongest absorption bands. *Yung and DeMore* [1982] averaged the most important molecular cross sections (CO_2, SO_2, SO, and HCl) over 1 nm intervals at $180.0 - 235.0$ nm because the cross sections for SO_2 and SO vary by up to an order of magnitude over 1 nm intervals. Early in our modeling effort, we compared the results from our standard wavelength intervals to those we obtained using the Yung and DeMore [1982] wavelength intervals. Those tests suggested the detailed cloud-level chemistry, where photolysis of SO_2 and SO is most important, *may* be dependent on the spectral resolution used for the calculations, but the higher spectral resolution did not significantly alter the results at higher altitudes.

For the calculations presented in Sections 2.3, there was one error in the photodissociation cross sections. The estimated 5% effective yield of $O_2(a^1\Delta)+ O(^3P)$ at wavelengths ≤ 199.7 nm was not included (see Appendix B). The effect of this on the results is negligible.

2.2.7 Chemical Kinetics

Most of the chemical potential energy that was created in photodissociation reactions (Section 2.2.6) is converted into thermal energy via chemical (kinetic) reactions. This conversion occurs as the products of the photodissociation and kinetic reactions collide with other molecules and transfer some of their excess energy to the other molecules. An additional process occurs at relatively high altitudes where the time interval between molecular collisions is comparable to the lifetime against spontaneous emission for the excited state molecules that are produced in photodissociation or kinetic reactions. In this situation, airglow emission can radiate some of the absorbed solar energy directly to space. Ultimately for a steady-state system, all of the absorbed solar energy is converted to thermal energy or radiated to space and the

original molecules are reformed.

The kinetic reactions that convert the products of photodissociation reactions back to the original species may be divided into eight types: (1) collisional quenching, (2) airglow emission, (3) spin-permitted association reactions, (4) spin-forbidden association reactions, (5) thermal dissociation, (6) heterogeneous, (7) two-body radical-radical and (8) other two-body reactions. To understand the process by which we adjusted measured (or estimated) reaction rates to obtain better agreement between model predictions and observations, it is useful to review some of the salient characteristics of each type of reaction.

(1) Collisional quenching reactions transfer energy from the (higher energy) electronic or vibrational modes of a molecule to the translational and rotational modes. These reactions eventually leave the molecule in its ground (equilibrium) state. These reactions can be very fast if there is a good match between the energy levels of the two species. Otherwise, they may be orders of magnitude slower (e.g., Reactions K205 and K202). (The example reactions are listed in Table 5C.2.)

(2) Airglow emission reactions are an alternate means by which molecules can go from an excited electronic state toward (or to) the ground state. The rates for these reactions are the inverse of the lifetime against spontaneous radiative emission for the excited electronic state. Due to the competition with collisional quenching reactions, airglow emission is only important at higher altitudes where the total number density is smaller. Reaction K203 is an example.

(3) Association reactions generally combine two reactant species to form a single product molecule with the assistance of third molecule/atom. (The third species is often referred to as the "third-body" for the reaction.) CO_2, $\gtrsim 96\%$ of the Venus atmosphere, is the primary third-body that needs to be considered for association reactions in our modeling. Because CO_2 has a larger number of low-lying energy levels than N_2 or O_2, CO_2 is generally more efficient as a third-body, and the rates for association reactions in a predominantly CO_2 atmosphere

generally will be faster than they would be in the terrestrial atmosphere. The rates for association reactions are typically expressed in terms of two rates (e.g., Reaction K105)–one gives the two-body (high-pressure) limit and the other is the three-body (low-pressure) limit for the rate. This is done because the reaction rate at high pressure is limited by the gas kinetic collision rate between the reacting species, not the availability of a third-body to stabilize the intermediate complex. Reaction rates at intermediate pressures (the typical region for a planetary atmosphere) are calculated from the two limiting rates as described in *DeMore et al.* [1997] and *Atkinson et al.* [1992].

(4) A spin-forbidden association reaction, such as Reaction K97, is one in which the spin state of the product molecule equals neither the sum of nor the difference between the spin states of the reactant species. Consequently, these reactions, to first order, are forbidden by the quantum mechanical selection rules. However, they do occur and can be important. Their rates are typically several orders of magnitude slower than those for spin-permitted association reactions (Reaction K97 versus Reaction K101).

(5) Thermal dissociation reactions can occur when the bond energy holding a molecule together is comparable to the translational (kinetic) energy of a molecule. In this situation, a statistically significant fraction of the collisions that each weakly-bound molecule undergoes will have enough energy to split the weakly-bound molecule. Reaction K177 provides an example. The importance of these reactions is determined by the binding energy for the molecule, the temperature of the gas, and the rates for competing loss reactions.

(6) Heterogeneous reactions are ones in which a liquid or solid aerosol particle serves as a catalyst for a reaction between two molecules that are predominantly found in the gas-phase. Their rates are proportional to the solubilities of the gases (for a liquid aerosol particle) and the surface area available (i.e., the number density and diameter of the aerosol particles, assuming the particles are spherical).

(7) Reactions in which both reactants are radicals, such as Reaction K118, are typically very fast ($\gtrsim 10^{-11}$ cm^2 s^{-1}) and can occur at rates near the gas kinetic collision rate. The rates for these reactions can be difficult to measure in a laboratory due partly to the difficulties of determining the concentrations of the reactants. Consequently, we have had to estimate rates for many of the radical-radical reactions proposed in the model.

(8) Other two-body reactions typically involve a radical and a stable molecule, such as Reactions K136 and K137. Their rates depend on the bond(s) in the stable reactant, the interaction with the radical, and the bond(s) in the products, so the rates for these reactions have a broader range of values than those for radical-radical reactions.

The number of kinetic reactions that could be included in the photochemical model is very large. However, laboratory studies have shown that many potential kinetic reactions either do not occur or occur very slowly. In addition, reaction rates can be strong functions of temperature and/or pressure. We, therefore, have attempted to select (primarily) the reactions that would have the greatest impact on the oxygen budget of the Venus middle atmosphere (Table 5C.2). For the reasons discussed in Section 2.1.3, we have focused on sulfur and chlorine chemistry similar to that in Model C of *Yung and DeMore* [1982]. In addition, we have studied the potential roles of higher oxides of chlorine, OCS, polysulfur (S_x), $ClSO_x$, and SCl_x (Section 2.1.4). None of these has been examined in previous photochemical models for the Venus middle atmosphere.

The first set of reactions we included in the model were the relevant ones from *DeMore et al.* [1994] (most of which were not changed in *DeMore et al.* [1997]). Next, we extracted relevant reactions from other critically-reviewed assessments (such as *Atkinson et al.* [1992]) and from a review of recent chemistry literature. Third, we took reactions from previous Venus photochemical models whose rates had been estimated and updated the rates based on our literature survey. Finally, we have included plausible reactions that may occur in the Venus middle atmosphere but which have

not been studied previously, either in the laboratory or in previous models. Through this process, the model includes the relevant chemistry from previous Venus models with rates that reflect the most recent assessments for these reactions. The sources from which we obtained reaction rates are listed in Table 5C.2 and Appendix D.

Table 5C.2 lists the kinetic reactions included in the photochemical model and the nominal rates. The number of reactions is much larger than in previous Venus models because we are examining several new classes of chemical compounds and we have included separate entries for CO_2 and N_2 as the third-body for many association reactions. The latter was done mainly to clarify the assumptions (or estimates) we made in specifying the rates for each third-body. Three groups of reactions require further elaboration in the following paragraphs because they are directly tied to the observations we have tried to model and because we have adjusted the rates for key reactions within each group to achieve better agreement between the model predictions and the observations.

The primary observational constraint on the model is the upper limit on the abundance of O_2 (Section 2.1.1). In the model, the O_2 abundance is controlled by the reactions that oxidize CO to CO_2 via ClCO (Cycles C14, C15, and C17). The efficiency of these cycles is determined by the stability of ClCO and the speed of the reactions that produce CO_2 (Reactions K179, K198, and K197). The stability of ClCO will be discussed in Section 2.2.8. The rates for the reactions that produce CO_2 in these cycles, unfortunately, are unknown. Because these reactions are between two radical species, we have presumed the reactions will be near the gas kinetic collision rate. Similar assumptions have been made in previous models of the Venus middle atmosphere and in models of hydrocarbon combustion.

A second key observational constraint is the intensity of the airglow emission in the $O_2(a^1\Delta)$ band produced as $O_2(a^1\Delta)$ spontaneously decays to the ground state, $O_2(X^3\Sigma)$ (Section 2.1.1). Based on laboratory studies such as *Leu and Yung* [1987] and our modeling, the primary reaction for producing $O_2(a^1\Delta)$ is Reaction G3. The overall rate for Reaction G3 is reasonably well known but the *effective* yield of $O_2(a^1\Delta)$ from it has significant uncertainties. The measured direct yield of $O_2(a^1\Delta)$ [reviewed

in *Wayne* 1994] is too small to account for the observed Venus airglow emission [*Yung and DeMore* 1982; this work]. One proposed mechanism for increasing the *effective* yield of $O_2(a^1\Delta)$ in Reaction G3 is via relatively rapid collisional quenching from the higher excited states of O_2 that are produced in Reaction G3 to $O_2(a^1\Delta)$ [*Crisp et al.* 1996; *Slanger, T.*, Personal Communication, 1995]. An initial estimate of the *effective* yields for $O_2(a^1\Delta)$ that might be produced via this collisional cascade was reported in *Crisp et al.* [1996] based on the then extant laboratory measurements. The nominal *effective* yields given in Table 5C.2 are smaller than those in *Crisp et al.* [1996] based on recent unpublished work [*Slanger, T.*, Personal Communication, 1997]. Collisional quenching and spontaneous radiative decay are the primary competing reactions that consume $O_2(a^1\Delta)$. Unfortunately, the rate coefficients for collisional quenching of $O_2(a^1\Delta)$ by CO_2, N_2, CO, and O are unknown. *DeMore et al.* [1997] give only upper limits for these quenching reaction rates so those upper limits have been included in Table 5C.2 as our nominal quenching rates. In contrast, the rate at which $O_2(a^1\Delta)$ spontaneously decays has been measured [*Hsu et al.* 1992; *Lin et al.* 1988; *Badger et al.* 1965], but the reported measurements differ by more than a factor of 2 [*Gamache et al.* 1998; *Mlynczak and Nesbitt* 1995]. The rate given in Table 5C.2 is that obtained by *Badger et al.* [1965] and agrees well with the rate used in compiling the 1996 edition of the HITRAN database [*Rothman et al.* 1992]. In order to achieve reasonable agreement between the predicted and observed airglow emission (Section 2.3), it was necessary to adjust most of the relevant reaction rates within the uncertainties of the laboratory measurements. The rate for Reaction G3 was increased; the *effective* yield of $O_2(a^1\Delta)$ from Reaction G3 was increased; the collisional quenching rates were decreased; and the rate at which $O_2(a^1\Delta)$ spontaneously decays was increased.

A third observational constraint is the vertical profile for SO (Section 2.1.1). The photochemical lifetime for SO is much smaller than the vertical mixing time so its abundance should be close to that for photochemical equilibrium at the observable altitudes ($\sim 65 - 85$ km). Two of the parameters controlling the SO distribution are the rates for Reactions K244 and K248. The rate for Reaction K244 has been measured by *Herron and Huie* [1980] and *Cobos et al.* [1985]. The nominal rate in

Table 5C.2 for Reaction K244 was taken from *Herron and Huie* [1980] because we believe the upper limit derived by *Cobos et al.* [1985] may be incorrect. *Cobos et al.* [1985] deduced from their measurements that the rate for Reaction K244 must be a factor of 100 smaller than the rate obtained by *Herron and Huie* [1980] because *Cobos et al.* [1985] believed photoabsorption by $(SO)_2$ would have been apparent in their measurements if the rate for reaction K244 were faster than the upper limit they proposed. However, the spectrum that *Cobos et al.* [1985] attributed to $(SO)_2$ has been attributed to S_2O by several other investigators [*Lakshminarayana* 1975; *Hopkins et al.* 1973; *Meschi and Myers* 1959]. The rate for Reaction K248 was a free parameter in our model that we adjusted to obtain a reasonable match to the retrieved vertical profiles of SO (Section 2.1.1). The rate for Reaction K248 that was used in *Na and Esposito* [1997] and *Yung and DeMore* [1982] was an estimate by *Yung and DeMore* [1982]. As best we can determine, there are no experimental constraints on the rate for Reaction K248.

Although the current photochemical model is similar to Model C of *Yung and DeMore* [1982], there are important differences (Table 2.5). The most significant differences are for Reactions G7 and G8 which will be discussed in Section 2.2.8.

For the calculations presented in Sections 2.3, there was one error in the kinetic rates. The rate $4.8 \times 10^{-33}\ (T/300)^{-3.8}$ was used for Reaction K175 instead of the correct nominal rate of $4.2 \times 10^{-33}\ (T/300)^{-3.8}$. The effect of this on the results is negligible.

2.2.8 ClCO Stability

Our sensitivity studies found that the most critical parameter for increasing the rate at which CO is oxidized to CO_2 (and decreasing the predicted abundance of O_2) is the stability of ClCO. ClCO is predominantly formed via Reaction G7, and is readily destroyed by thermal decomposition (Reaction G8). The stability of ClCO, thus, may be expressed as the ratio of the rates for Reactions G7 and G8 which is the equilibrium constant, K_{ClCO}.

Table 2.5: Comparison of Important Kinetic Reaction Rates

		Rate at 250 K in Model				
	Reaction	SM74	WS80	KP83	YD82	[a]This Work
K100	†$2O+CO_2 \rightarrow O_2(a^1\Delta)+CO_2$				9.2(-33)	1.2(-32)
K203	$O_2(a^1\Delta)+CO_2 \rightarrow O_2+CO_2$			3(-20)	3.0(-20)	2.0(-20)
K207	$O_2(a^1\Delta) \rightarrow O_2 + h\nu$				2.6(-4)	2.6(-4)
K146 + K145	$ClO + O$			4.6(-11)	4.6(-11)	4.0(-11)
K144 + K143	$Cl + O_3$			1.1(-11)	9.7(-12)	1.0(-11)
K179	$ClCO + O$			1(-13)	3(-11)	3(-11)
K178	†$ClCO + O_2$			[b]2(-14)	[c]4.2(-31)	[c]4.2(-31)
K197	$ClCO_3 + O$				1(-11)	1(-11)
K198	$ClCO_3 + Cl$				1(-11)	1(-11)
K151	$S + O_2$			2.2(-12)	2.2(-12)	2.3(-12)
K154	†$SO + O + CO_2$		1.9(-31)	5(-31)	6.0(-31)	4.2(-30)
K166	$SO + HO_2$				2.3(-11)	2.8(-11)
K167	$2SO \rightarrow SO_2 + S$		8.3(-16)	3.0(-15)	8.3(-15)	1.1(-15)
K160	†$SO_2 + O + CO_2$		3.7(-34)	1(-32)	1.5(-33)	1.8(-33)
K162	†$SO_2 + OH + CO_2$		1.6(-31)	1.6(-31)	2.3(-30)	2.6(-30)
K163	$SO_2 + HO_2$		9.0(-16)	3(-16)	1.0(-18)	1.0(-19)
K244	†$2SO + M \rightarrow (SO)_2 + CO_2$				4.4(-31)	4.4(-31)
K248	$(SO)_2 + M$				9.0(-23)	1.7(-13)
K165	$SO + ClO$				2.3(-11)	2.8(-11)
K168	†$Cl + SO_2 + M$				4.6(-33)	5.6(-33)
K194	$ClSO_2 + Cl$					1(-11)
K137	$O + HCl$	2.1(-16)	1.4(-17)	2.1(-16)	1.5(-17)	1.9(-17)
K135	$H + HCl$	1.6(-14)	1.3(-14)	1.7(-14)	2.3(-14)	1.4(-14)
K136	$OH + HCl$	5.8(-14)	5.5(-13)	5.8(-14)	5.5(-14)	6.4(-13)
K138	$Cl + H_2$	3.9(-15)	1.1(-15)	3.9(-15)	4.0(-15)	3.7(-15)
K141 + K140	$Cl + HO_2$	1.0(-13)	3.0(-11)	1.0(-13)	4.1(-11)	3.6(-11)
G9	$NO + HO_2$				[d]9.5(-12)	

† Rates for association reactions are evaluated in the three-body limit
[a] Nominal reaction rates for this work from Table 5C.2
[b] Rate for two-body reaction
[c] Rate for three-body association reaction
[d] Recommended rate from *DeMore et al.* [1997] is 1.3×10^{-12}

$$K_{ClCO} = \frac{k_{G7}}{k_{G8}} = \frac{[\mathrm{ClCO}]}{[\mathrm{Cl}][\mathrm{CO}]}, \tag{2.2.2.8}$$

where k_{G7} is the rate for Reaction G7, k_{G8} is the rate for Reaction G8, and [ClCO], [CO], and [Cl] are the number densities of these three species at equilibrium. The equilibrium constant may also be expressed as

$$K_{ClCO} = (\frac{\Delta S_r(G7)}{R})\exp(-\frac{\Delta H_r(G7)}{RT}), \tag{2.2.2.9}$$

where $\Delta S_r(G7)$ is the reaction entropy, $\Delta H_r(G7)$ is the reaction enthalpy for Reaction G7, R is the universal gas constant, and T is the temperature. A larger value for the equilibrium constant implies greater stability for ClCO and a larger abundance of it. Equations 2.2.2.8 and 2.2.2.9 imply the equilibrium constant may be determined either by measuring the rates for Reactions G7 and G8 or by measuring $\Delta S_r(G7)$ and $\Delta H_r(G7)$ as functions of temperature. Both methods have been tried and the experimental results agree to within their mutual uncertainties. However, the assessed uncertainty in the equilibrium constant is still large [*DeMore et al.* 1997].

The rate of Reaction G7 has been measured by several investigators. *Clark et al.* [1966] measured the rate for M = Ar at 195 and 300 K as shown in Table 2.6. *Nicovich et al.* [1990] measured the rate for M = CO and N_2 at 185 - 260 K and 14 - 200 Torr and for M = CO_2 and Ar at 215 K. The results from their study are also summarized in Table 2.6. Most recently, *Hewitt et al.* [1996] measured the rate for M = Air at 298 K and 760 Torr. The results from all three studies are consistent within the stated uncertainties.

The only attempt to directly measure the rate of Reaction G8 has been by *Nicovich et al.* [1990] (Table 2.6). A potential problem in their measurements is the reaction of Cl and ClCO with impurities in their sample gases. *Nicovich et al.* [1990] passed the CO samples (minimum purity 99.99%) through a Pyrex trap at 77 K before mixing it with the other gases, but they found the background Cl atom loss rate in the absence of CO was an order of magnitude larger in CO_2 than in N_2 or Ar even though the stated purity of the CO_2 gas was also > 99.99%. The equilibrium constant obtained by

Table 2.6: Measurements of the Stability of ClCO

[a]Study	[b]k_{G11}	[c]k_{G12}	[d]K_{ClCO}	[e]M	[f]T
D1997	$(1.3 \pm 0.5) \times 10^{-33}(\frac{T}{300})^{-(3.8\pm0.5)}$		[g]$1.6 \times 10^{-25}\exp(\frac{4000\pm500}{T})$	CO, N_2	$200 - 260$
H1996	$(1.4 \pm 0.3) \times 10^{-33}$			Air	298
N1990	$(1.31 \pm 0.15) \times 10^{-33}(\frac{T}{300})^{-(3.8\pm0.5)}$		[h]$1.3 \times 10^{-25}\exp(\frac{3940\pm210}{T})$	CO, N_2	[i]$185 - 260$
N1990	$(1.05 \pm 0.36) \times 10^{-34}\exp(\frac{810\pm70}{T})$	$(4.1 \pm 3.1) \times 10^{-10}\exp(-\frac{2960\pm160}{T})$	[j]$6.03 \times 10^{-28}T\exp(\frac{3940\pm210}{T})$	CO, N_2	$185 - 260$
C1966	$(9.1 \pm 3.0) \times 10^{-34}$			Ar	300
C1966	$(5.2 \pm 1.1) \times 10^{-33}$			Ar	195
B1952			$1.1 \times 10^{-24}\exp(-\frac{3180}{T})$	CO	$298 - 328$

Study	$\Delta S_f(ClCO)$	$\Delta H_f(ClCO)$	T
D1997	63.5	-5 ± 1	298
N1990	63.0 ± 2.0	-5.2 ± 0.6	298
W1966		-4.0 ± 3	298
C1966		[k]$\sim -3.5 - -4.5$	298

[a] D1997 = *DeMore et al.* [1997], H1996 = *Hewitt et al.* [1996], N1990 = *Nicovich et al.* [1990], W1966 = *Walker and Prophet* [1966], C1966 = *Clark et al.* [1966], B1952 = *Burns and Dainton* [1952]. [b] k_{G11} = rate (cm^6 mol^{-2} sec^{-1}) for Reaction G11 ($Cl + CO + M \rightarrow COCl + M$). [c] k_{G12} = rate (cm^3 mol^{-1} sec^{-1}) for Reaction G12 ($COCl + M \rightarrow Cl + CO + M$). [d] K_{ClCO} = equilibrium constant (cm^3 mol^{-1}) for ClCO. [e] M = buffer gas used for experiment. [f] T = temperature (K) at which experiment was conducted. [g] stated uncertainty for the pre-exponential factor is a factor of 5 at 298 K. [h] stated uncertainty for the pre-exponential factor is a factor of 3. [i] K_{ClCO} has been evaluated at 220 K. [j] Pre-exponential temperature dependence arises because K_{ClCO} was measured in (atm^{-1}) and the specified units are (mol cm^{-3}). [k] $\Delta H_f(ClCO) = \Delta H_f(Cl) + \Delta H_f(CO) - D^0(Cl - CO)$ where $D^0(Cl - CO)$ is the bond strength for the Cl-CO bond in ClCO.

The uncertainties from *DeMore et al.* [1997] are assessed 1σ values. The uncertainties from *Nicovich et al.* [1990] are 2σ but precision only. *Clark et al.*'s [1966] measurements of Reaction G11 are consistent with an apparent activation energy of -2 kcal $mole^{-1}$. Relative collision efficiencies for stabilization of the energized ClCO adduct at 214 ± 2 K are 3.2 : 1.0 : 0.8 for $M = CO_2 : N_2 : Ar$ [*Nicovich et al.* 1990].

Nicovich et al. [1990], however, is reasonably consistent with that obtained by *Burns and Dainton* [1952] at higher temperatures (Figure 2.4), and the reaction enthalpy and entropy derived by *Nicovich et al.* [1990] are consistent with the values derived in earlier studies [*Bodenstein et al.* 1929; *Jacox and Milligan* 1965; *Clark et al.* 1966; *Walker and Prophet* 1966; *Francisco and Goldstein* 1988].

A more common experimental technique has been to measure the equilibrium constant, K_{ClCO}, directly or the reaction entropy and enthalpy as functions of temperature. The equilibrium constant obtained by *Nicovich et al.* [1990] implies a reaction enthalpy for ClCO of -7.7 ± 0.3 kcal mol^{-1} and a reaction entropy of -23.8 ± 1.0 cal mol^{-1} K^{-1} (both at 298 K). Comparing the reaction enthalpy from *Nicovich et al.* [1990] to the other results presented in Table 2.6, the measured reaction enthalpy has increased in magnitude (i.e., the stability of ClCO has increased) as the stated precision of the measurements has improved, although all measurements agree to within their mutual uncertainties.

The currently recommended value for the equilibrium constant, K_{ClCO}, in *DeMore et al.* [1997] (Table 2.6) is that obtained by *Nicovich et al.* [1990]. *DeMore et al.* [1997], however, ascribe a factor of 5 uncertainty to the recommended equilibrium constant at 298 K and a 12% uncertainty to the recommended reaction enthalpy. The 1σ *DeMore et al.* [1997] uncertainties are a factor of 4 and a factor of 5 larger, respectively, than the 1σ precision uncertainties estimated by *Nicovich et al.* [1990] for the equilibrium constant and reaction enthalpy. No information is provided in *DeMore et al.* [1997] regarding the rationale for selecting such large uncertainties.

The nominal rates given in Table 5C.2 for Reactions G7 and G8 with $M = N_2$ are the recommended rates from *DeMore et al.* [1997]. For $M = CO_2$, our nominal rate for Reaction G7 is a factor of 3.2 larger than that for $M = N_2$, based on the measured relative efficiencies of these two buffer gases at 215 K from *Nicovich et al.* [1990]. (The nominal rate for Reaction G8 is derived from the equilibrium constant. Because the equilibrium constant is independent of the identity of the third-body, the nominal rate for Reaction G8 with $M = CO_2$ will also be a factor of 3.2 larger than that for $M = N_2$.) Figure 2.4 compares the values for the equilibrium constant,

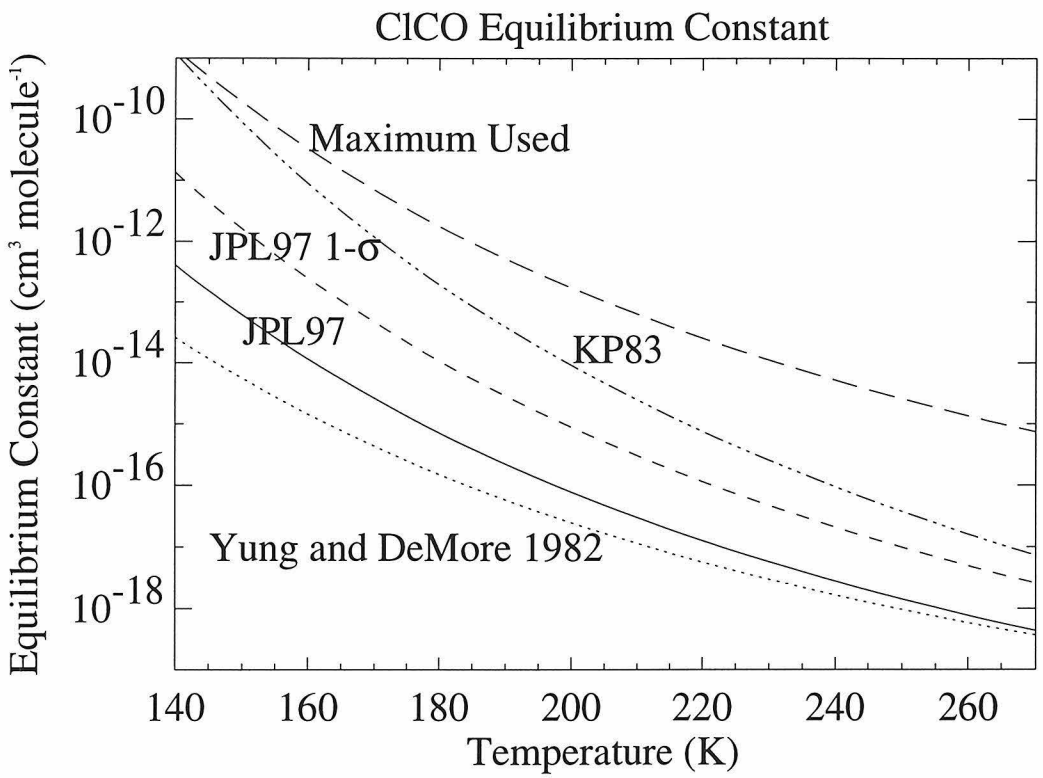

Figure 2.4: Equilibrium constant for ClCO. The curve marked "Yung and DeMore 1982" was used in *Yung and DeMore* [1982]. It was an extrapolation to lower temperatures of the laboratory result from *Burns and Dainton* [1952]. "KP83" is the value used by *Krasnopol'sky and Parshev* [1983] which was based on rates given in *Kondrat'yev* [1971]. "JPL97" is the recommended value from *DeMore et al.* [1997] which is based on the laboratory measurements by *Nicovich et al.* [1990]. This recommended value was used for the results presented in Section 2.3.1. "JPL 1-σ" is the assessed uncertainty in the equilibrium constant from *DeMore et al.* [1997]. The equilibrium constant used in Section 2.3.2 was a factor of two smaller than the one standard deviation value. "Maximum Used" is the equilibrium constant that was used for the results discussed in Section 2.3.4.

K_{ClCO}, from *Yung and DeMore* [1982], *Krasnopol'sky and Parshev* [1983], *DeMore et al.* [1997], and the present work. The *Yung and DeMore* [1982] equilibrium constant was taken from *Burns and Dainton* [1952]. The *Krasnopol'sky and Parshev* [1983] equilibrium constant was from *Kondrat'yev* [1971].

Using the nominal equilibrium constant for ClCO, we cannot obtain a steady-state solution that satisfies the observed extreme depletion of O_2. Consequently, we have examined a case in which the ClCO equilibrium constant was increased almost two standard deviations [from *DeMore et al.* 1997] (Figure 2.4) and the temperatures in the middle atmosphere were decreased by $\sim$ 20 K (Figure 2.5). An equilibrium constant this large had been considered "unrealistic" [*Yung and DeMore* 1982], but the currently recommended equilibrium constant at 200 K is an order of magnitude larger than the 1982 value due to revisions in the temperature dependence.

The most critical region of the Venus atmosphere for assessing the ClCO equilibrium constant lies at nominal temperatures of 160 - 180 K (possibly as low as $\sim$ 140 K if one includes measurement uncertainties). These temperatures are colder than those considered by *Nicovich et al.* [1990]. Further laboratory studies of the equilibrium constant for ClCO, particularly at 150 - 180 K are needed to reduce the present uncertainty in this parameter.

2.2.9 Model Atmosphere

Our model atmosphere, from *Seiff* [1983] for Noon Local Solar Time, extends from 58 to 112 km altitude and has 28 layers, each 2 km thick. Figures 2.5, 2.6, and 2.7 show our nominal temperature, pressure, and total number density profiles. Pressures were computed assuming hydrostatic equilibrium (for the specified temperature and total number density at each altitude) and agree with those in *Seiff* [1983]. Figures 2.5 and 2.6 also show alternate temperature and pressure profiles used for some model calculations. For the calculations using the alternate temperature profiles, the total number density profile was not changed so the alternate pressure profiles reflect the changes to the atmospheric temperatures.

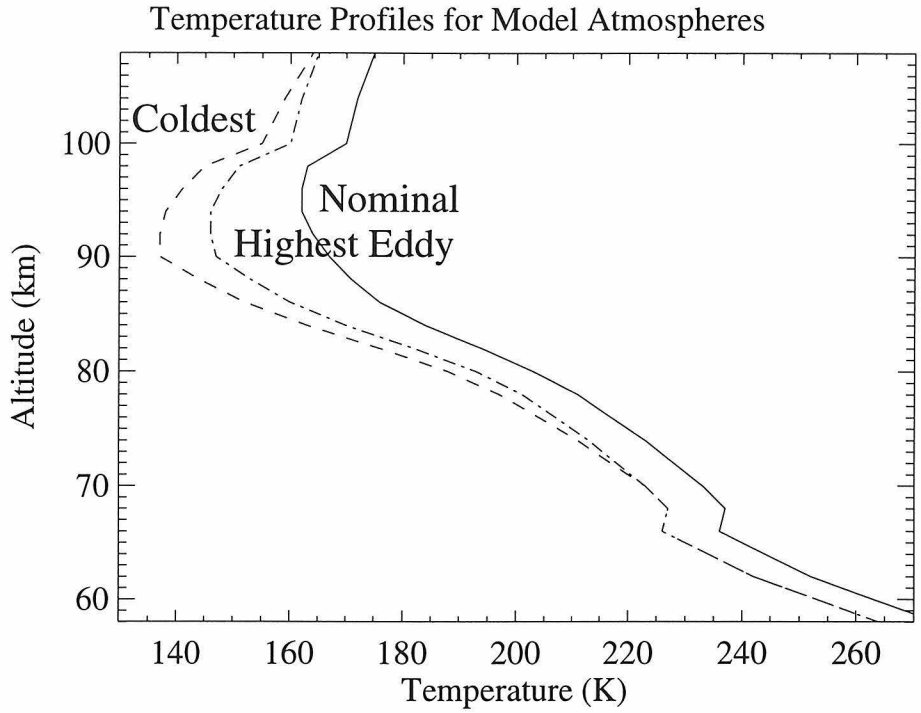

Figure 2.5: Nominal and alternate temperature profiles used for model calculations. The "Coldest" profile was used for the results presented in Section 2.3.3 and the "Highest Eddy" profile was used for calculations that are not presented in the dissertation because the results did not lie within a reasonable range of the observational constraints.

For most calculations, the total number density was *not* recomputed as the sum of the partial number densities for all species. However, the mixing ratio for CO_2 deviates by less than 1% from the value specified at the lower boundary so the error from this approximation is usually negligible. For calculations in which we began with an initially pure CO_2 atmosphere, the change in total number density as a result of the photochemical evolution of the model atmosphere is *not* negligible so additional appropriate three-body reactions (with CO, O, and O_2 as the third-body) were included in the model (Table 5C.2).

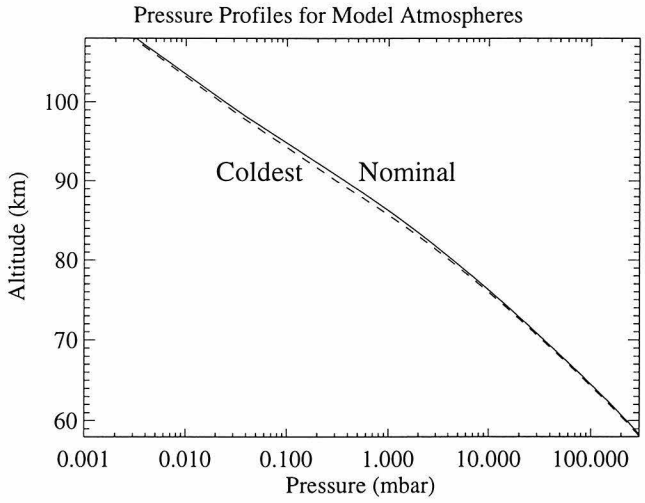

Figure 2.6: Pressure profiles corresponding to the nominal and coldest model atmosphere temperature profiles (Figure 2.5) that were used for model calculations.

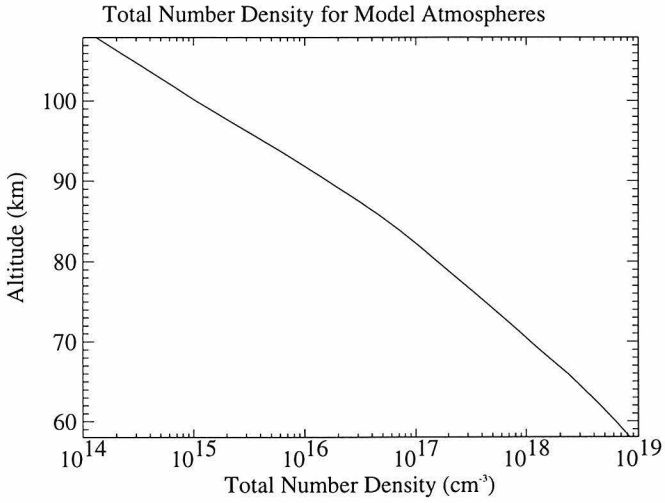

Figure 2.7: Total number density profile used for all model calculations.

2.2.10 Diffusion

Vertical transport is an important element of Venusian photochemistry models. O_2, for example, is produced principally at 85 - 100 km altitude but destroyed predominantly below 90 km altitude (based on the current and previous model results). In a one-dimensional model atmosphere, vertical transport is parameterized as the sum of eddy and molecular diffusion. Eddy diffusion is a modeling concept that was introduced to describe the vertical mixing that occurs via, for example, large-scale convection within the atmosphere. Since its effects are model-dependent, it is best assessed by the indirect method of examining the vertical profiles of species, such as CO, that have relatively long photochemical lifetimes. For the altitudes we are modeling (58 - 112 km), eddy diffusion is much larger than molecular diffusion so eddy diffusion is the only mode of vertical transport that is significant in our photochemical model. Clear observational evidence for this conclusion is that the homopause (above which species have vertical scale heights that depend on their molecular weight and, consequently, are no longer uniformly mixed) is several scale heights above the upper boundary of our model: *von Zahn et al.* [1980] reported the homopause for He was $\sim$ 130 km and that for N_2 was $\sim$ 135 km altitude.

Two measurements have been published that directly constrain the magnitude of the eddy diffusion coefficient: (1) *Woo and Ishimaru* [1981] determined that radio scintillations detected by *Pioneer Venus* were compatible with an eddy diffusion coefficient of $\lesssim 4 \times 10^4$ cm^2 s^{-1} at the tropopause ($\sim$ 60 km altitude) and (2) *von Zahn et al.* [1980] found the eddy diffusion near the homopause ($\sim 130 - 135$ km) obeyed Relation 2.2.2.10 to within a factor of two:

$$K_{eddy} = 1.4 \times 10^{13} n^{-1/2} \qquad (2.2.2.10)$$

where n = number density of the ambient atmosphere (molecules cm^{-3}) and K_{eddy} is in units of cm^2 s^{-1}.

At intermediate altitudes (65 - 125 km), there are no measurements that directly constrain the eddy diffusion but the vertical profiles that have been derived for CO,

SO, and SO_2 can be used to infer the magnitude of the eddy diffusion. CO vertical profiles [e.g., *Clancy and Muhleman* 1991; *Gurwell et al.* 1995] provide general constraints on the eddy diffusion. However, there is variability in the retrieved profiles (Figure 2.3), and above $\sim$ 80 km the CO distribution may be strongly affected by horizontal advection [*Clancy and Muhleman* 1985]. At $65 - 80$ km altitude, the vertical profiles of SO (Figure 2.2) retrieved from ultraviolet observations of Venus by *Na et al.* [1990] and *Na et al.* [1994] provide an additional constraint. Unfortunately, the photochemical lifetime for SO is comparable to the transport time at these altitudes so a broad range of eddy diffusion values can satisfy the observational constraints (depending on the values selected for key reaction rates). The SO_2 scale heights near the cloud top inferred from ultraviolet observations by *Na et al.* [1994] and earlier studies (Table 2.1) also constrain the eddy diffusion near 70 km altitude, but (1) the photochemical lifetime for SO_2 is comparable to the transport time near 70 km and (2) previous model results indicate the SO_2 scale height changes from $\sim$ 1 to $\sim$ 5 km near 70 km [*Yung and DeMore* 1982, Figures 25 and 30], spanning the range of observed values. An additional constraint on the eddy diffusion coefficient in the middle atmosphere is the vertical scale height for the aerosol particles at 85 km altitude derived by *Lane and Opstbaum* [1983] from *Pioneer Venus* Orbiter Ultraviolet Spectrometer (OUVS) limb sounding observations. (Our modeling suggests the vertical profile of OCS could be an excellent constraint on the eddy diffusion coefficient below the cloud top, but the existing measurements [*Bezard et al.* 1990] do not have sufficient vertical resolution.)

Based on these observational constraints, *Yung and DeMore* [1982] derived two empirical eddy diffusivity profiles (YD82A and YD82B in Figure 2.8) and *Krasnopol'sky and Parshev* [1983] derived a third empirical profile for the eddy diffusion (KD83 in Figure 2.8).

The eddy diffusivity profiles used in our modeling are given in Figure 2.8. Our eddy diffusivities are stronger than those used by *Yung and DeMore* [1982] and *Krasnopol'sky and Parshev* [1983] but they are smaller than the eddy diffusivities used by *Sze and McElroy* [1975] (not shown). At 60 - 80 km altitude, comparison to

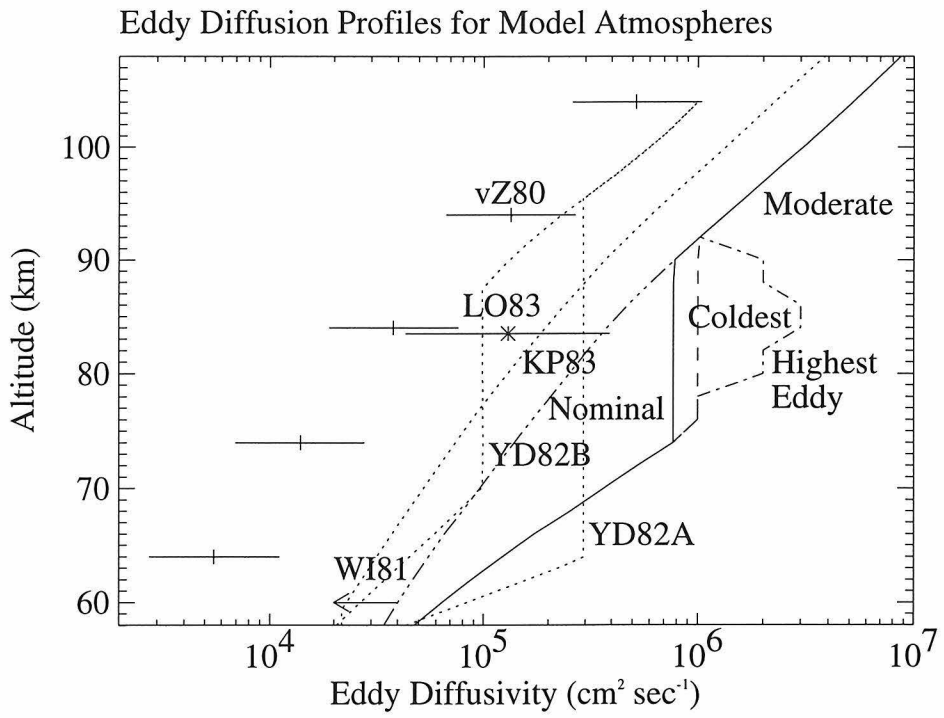

Figure 2.8: vZ80 (+) is an extrapolation to lower altitudes of the eddy diffusivity measured near 130 km altitude [*von Zahn et al.* 1980]. WI81 (←) is the upper limit on eddy diffusivity near 60 km altitude that was inferred by *Woo and Ishimaru* [1981] from scintillations in radio occultation measurements. LO83 (∗) is the eddy diffusivity inferred from measurements of the aerosol particle scale height by *Lane and Opstbaum* [1983]. YD82A and YD82B (dotted lines) are the empirical eddy diffusivity profiles used by *Yung and DeMore* [1982]. KP83 (dotted line) is the empirical eddy diffusivity profile used by *Krasnopol'sky and Parshev* [1983]. "Nominal" (dash-multidot line) is the eddy diffusivity used for the results presented in Section 2.3.1. The "Moderate" profile (solid line) was used for the results in Section 2.3.2. The "Coldest" profile (dashed line) was used for the results in Section 2.3.3 in which the temperature profile was changed to the coldest curve in Figure 2.5. The "Highest Eddy" profile (dash-dot line) was used for calculations that are not presented in the dissertation because the results did not lie within a reasonable range of the observational constraints.

the CO profiles and the measurement by *Woo and Ishimaru* [1981] suggests that our eddy diffusivities may be too large, but there is sufficient uncertainty (or variability) in the observations to encompass the results we have obtained. Above 90 km, our nominal model eddy diffusivity,

$$K_{eddy} = 1 \times 10^{14} n^{-1/2}, \qquad (2.2.2.11)$$

is a factor of 3 larger than the one standard deviation value obtained by *von Zahn et al.* [1980] at 130 - 135 km altitude. This may be reasonable if internal gravity waves generated near the cloud top break at $\sim 90 - 110$ km altitude, as was proposed by *Alexander* [1992], since breaking internal gravity waves can produce significant eddy mixing.

2.3 Model Results

A series of calculations have been performed using the model described in Section 2.2. The first results that will be discussed are those from the nominal model (Section 2.3.1). Section 2.3.2 then describes the results from varying key parameters of the nominal model within their assessed, measured, or estimated one standard deviation range. Finally, Section 2.3.3 presents the results from, effectively, increasing the stability of ClCO by several standard deviations. Comparisons among the model predictions and observations are included in each section then summarized in Section 2.3.4 and Chapter 3. The implications of the model predictions for the chemistry occurring in the lower atmosphere will be discussed in Section 2.4.

2.3.1 Nominal Model Results

The nominal model was based, primarily, on the chemistry in Model C from *Yung and DeMore* [1982] so the major processes for oxidizing CO to CO_2 are Cycles C14, C15, and C17. These are the same processes that dominated the oxidation of CO in the *Yung and DeMore* [1982] model so the differences between the nominal model

and that developed by *Yung and DeMore* [1982] for oxidation of CO are principally due to revisions in laboratory and observational data. The nominal model, however, also provides the first quantitative examination of the chemistry of higher-oxides of chlorine, SCl_x, $SOCl_x$, and S_x in the Venus atmosphere. In general, the results from the nominal model are closer to the observations than the results from previous photochemical models, but there are still important differences between the predictions of the nominal model and the current observations.

Predicted profiles for CO, O_2, and SO_2 are shown in Figure 2.9 along with those from *Yung and DeMore* [1982] model C. The O_2 profile predicted in the nominal model is similar to that calculated by *Yung and DeMore* [1982], but the predicted O_2 column abundance for the nominal model is a factor of 2 smaller than that predicted by *Yung and DeMore*'s [1982] model C. However, the nominal model's predicted O_2 abundance is still a factor of $\sim$ 20 larger than the upper limit from *Trauger and Lunine* [1983]. The differences in Figure 2.9 between the nominal model and the *Yung and DeMore* [1982] model for CO, O_2, and SO_2 are primarily due to the increased stability of ClCO and the stronger eddy diffusion coefficient in the nominal model.

CO_2 and CO

The primary reactions producing and destroying CO_2 are shown in Figures 2.10, 2.11, and 2.12. These figures indicate that the primary processes for reforming CO_2 are the same as in the *Yung and DeMore* [1982] model, Cycles C14, C15, and C17. The fluxes of CO and CO_2 are shown in Figure 2.13. The difference between the downward flux of CO and the upward flux of CO_2 at low altitudes is balanced by an upward flux of OCS. The calculated CO profile does not increase as rapidly with increasing altitude as that from *Yung and DeMore* [1982] model C, but the nominal model's CO profile is within the range that has been retrieved via microwave measurements (Section 2.1.1).

O_2 and $O_2(^1\Delta)$ Airglow

Predicted profiles for oxygen species are shown in Figure 2.14; the primary reactions producing and destroying O_2 and $O_2(^1\Delta)$ are shown in Figures 2.15, 2.16, 2.17, and 2.18; and the fluxes of the primary oxygen containing species are shown in Figure

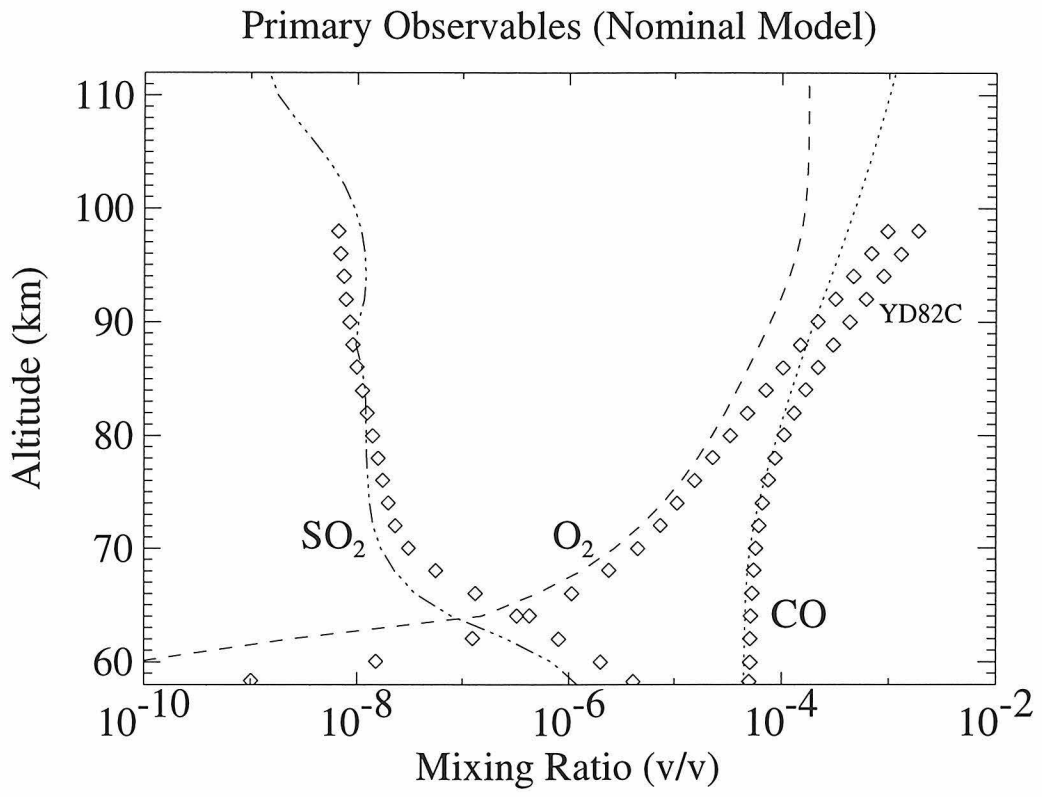

Figure 2.9: Predicted mixing ratios for CO, O_2, and SO_2 from the Nominal Model are shown in the dotted, dashed, and dot-dashed lines, respectively. The adjacent plots (in diamonds) are for the same species from *Yung and DeMore* [1982] Model C.

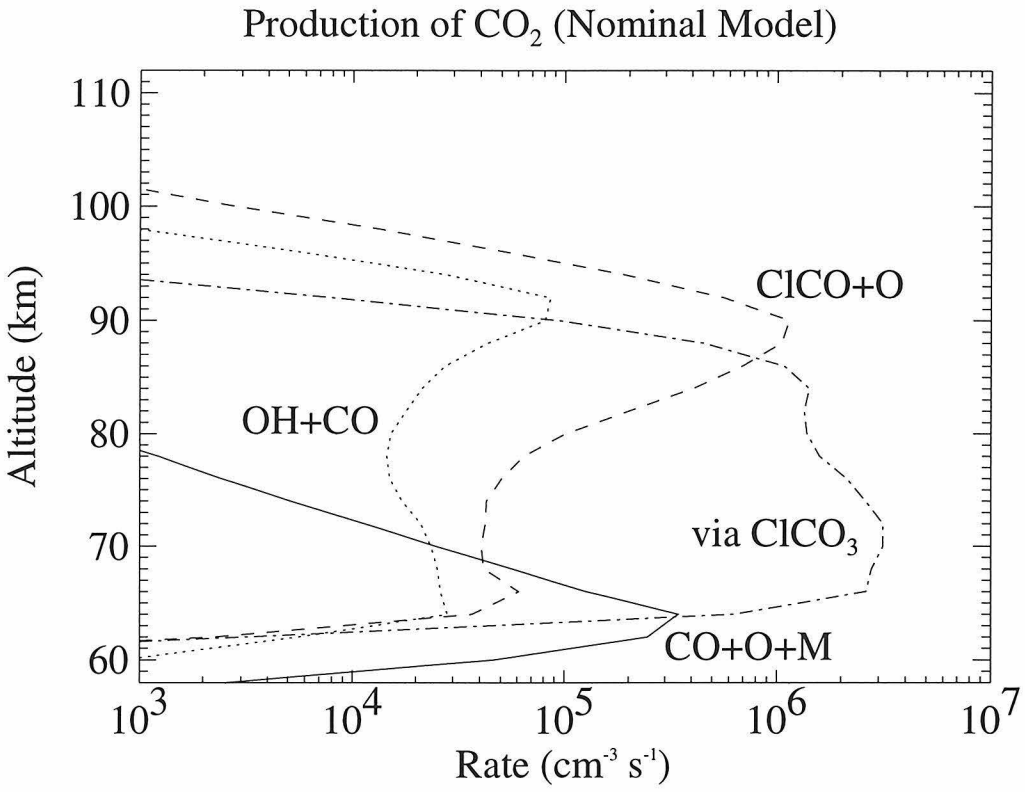

Figure 2.10: Primary reaction producing CO_2 in the Nominal Model.

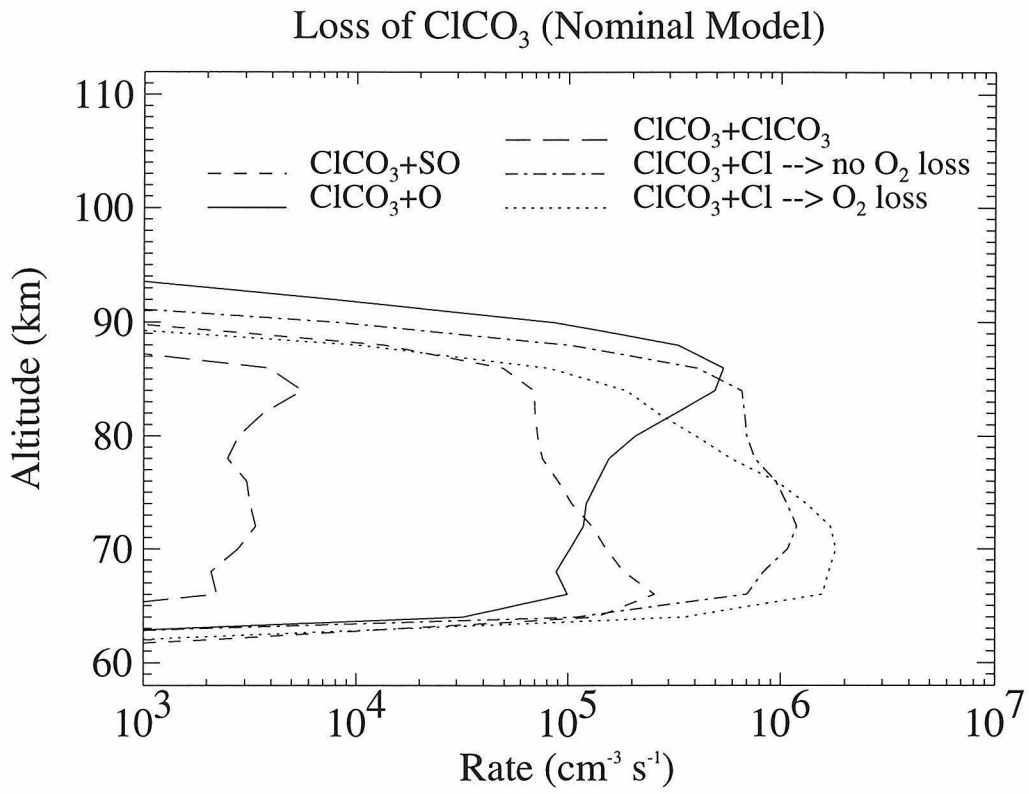

Figure 2.11: Primary reactions destroying $ClCO_3$ in the Nominal Model.

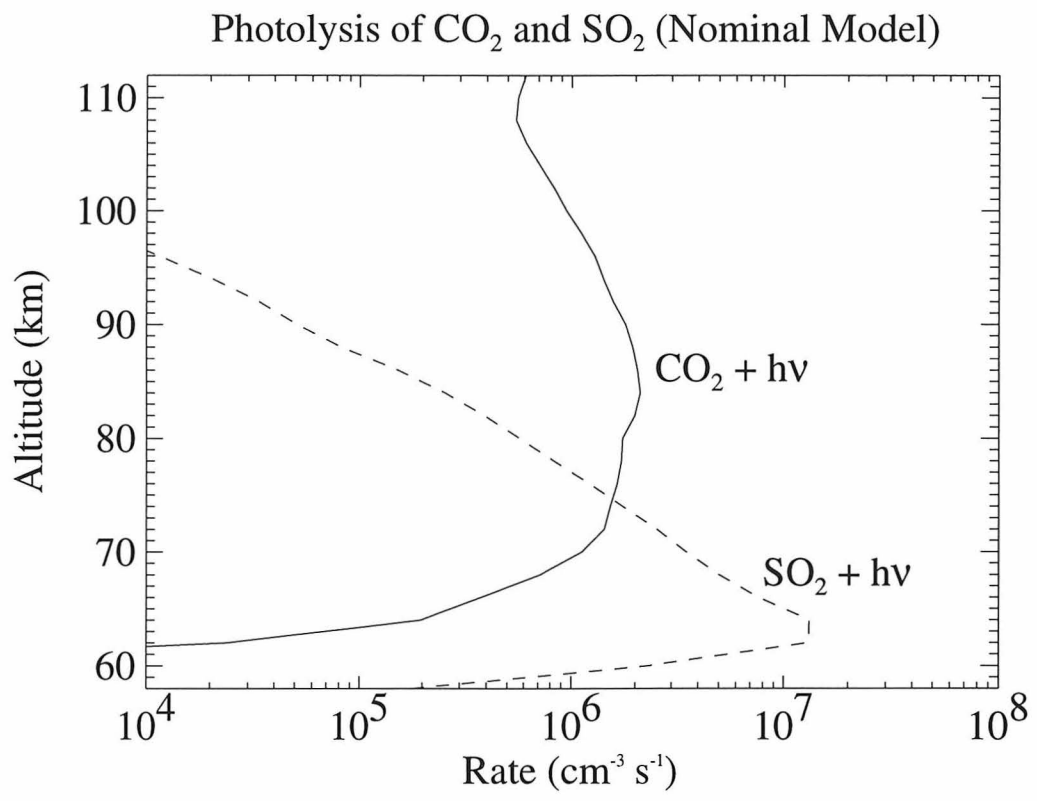

Figure 2.12: Photolysis of CO_2 and SO_2 in the Nominal Model.

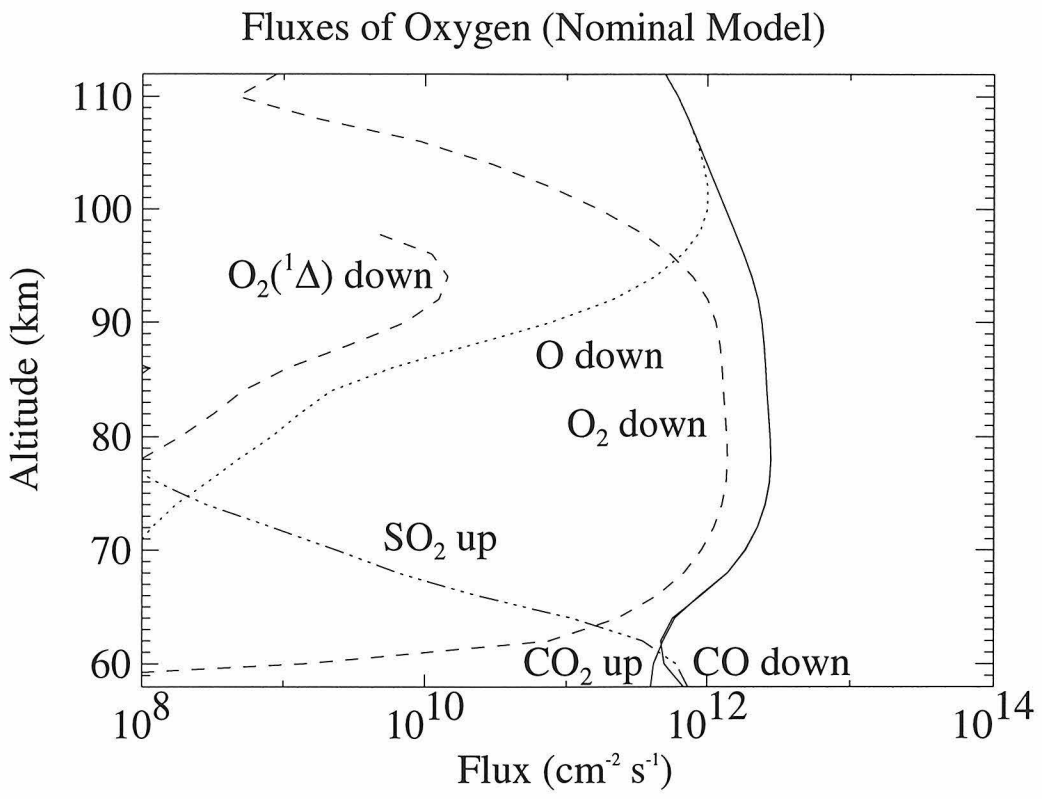

Figure 2.13: Fluxes of oxygen in the Nominal Model.

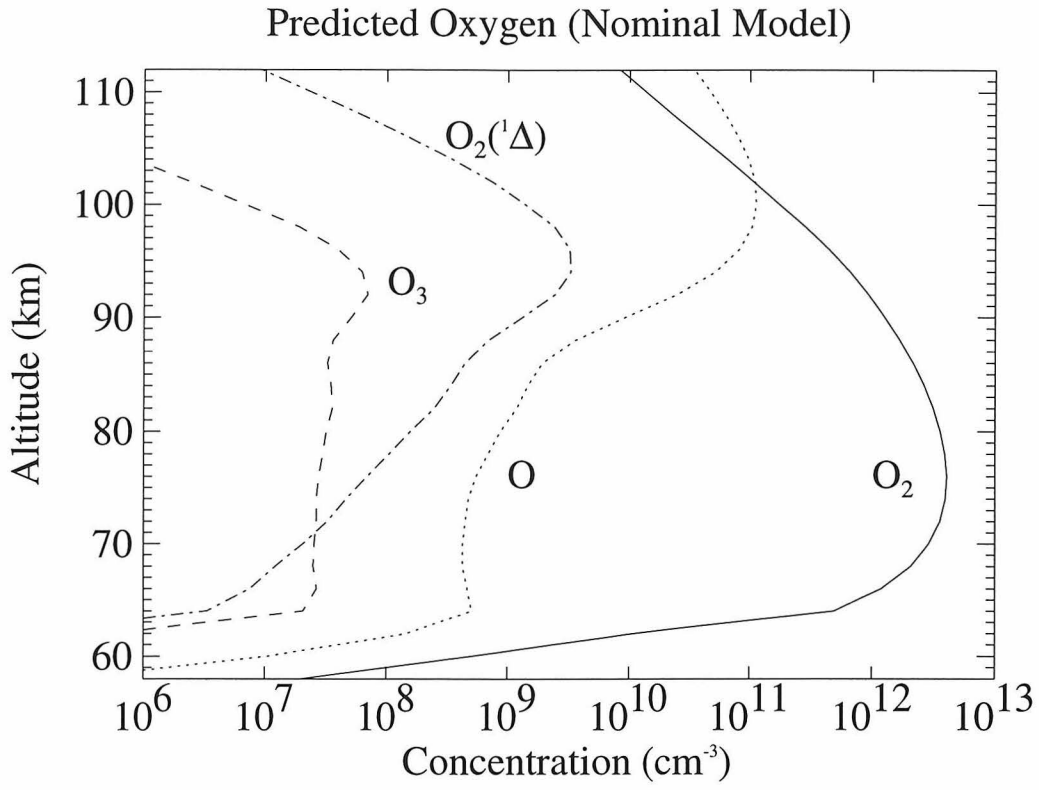

Figure 2.14: Predicted abundances of oxygen species in the Nominal Model.

2.13.

O_2 production is dominated by the Molina-Rowland Cycle (Cycle C13), particularly at $\lesssim$ 90 km altitude. O_2 is primarily lost via the the same cycles that reform CO_2 so the competition between Cycles C17 and C15 controls the rate at which O_2 is lost. As shown in Figure 2.11, the primary fate for ClO below $\sim$ 75 km altitude is either reaction with SO to form Cl + SO_2 or photolysis to form Cl + O, both of which result in a net loss of O_2. Above 75 km altitude, the primary fate for ClO is reaction with O to form Cl + O_2 which does not result in a net loss of O_2. In the nominal model, 60% of the ClO loss leads to a net loss of O_2. This is approximately the same fraction as in *Yung and DeMore* [1982] model C. Oxidation of SO_2 (Figure 2.19) is a minor but significant sink for oxygen below 70 km altitude.

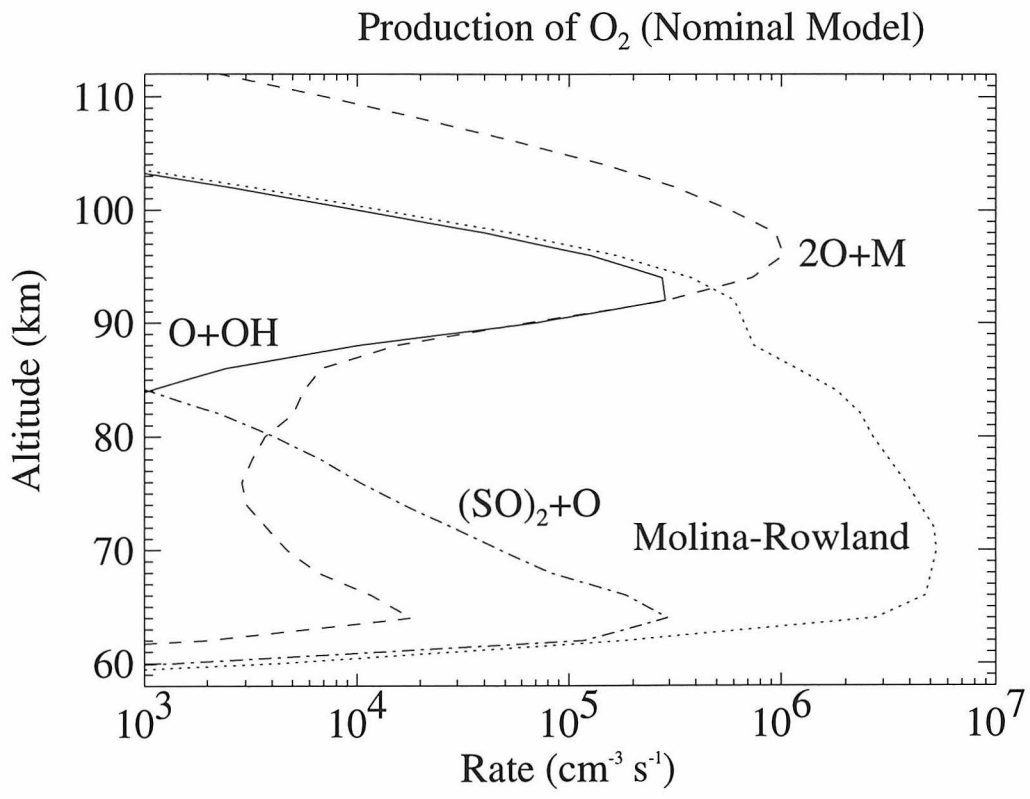

Figure 2.15: Primary reaction producing O_2 in the Nominal Model.

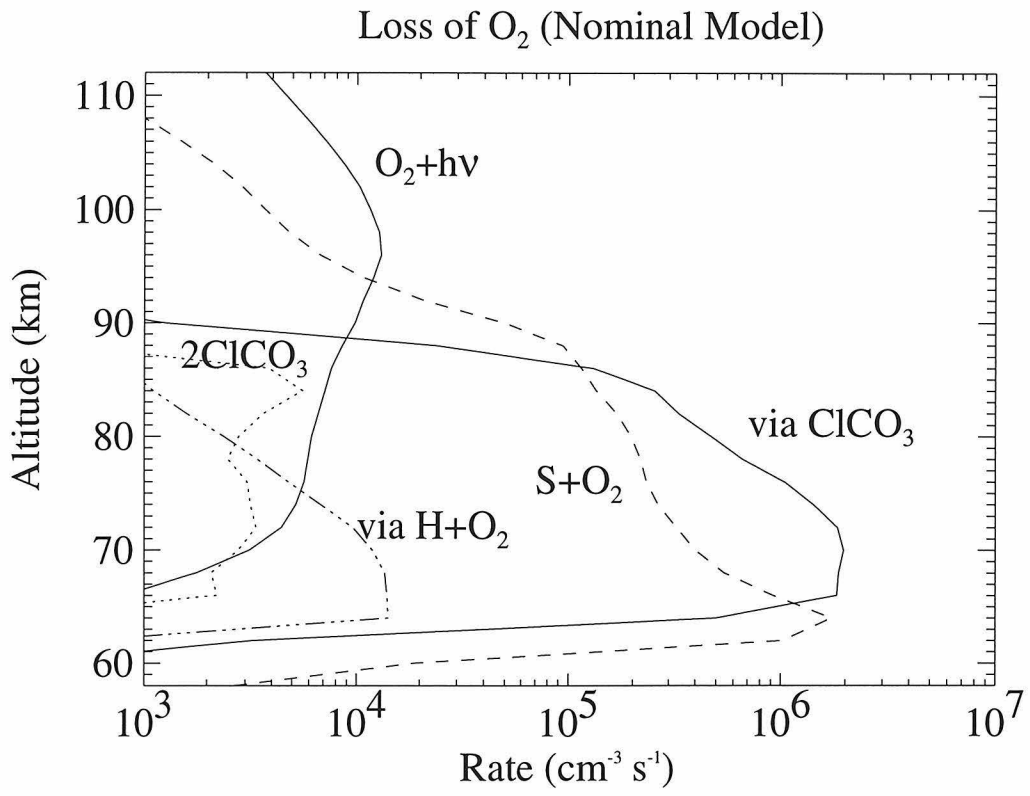

Figure 2.16: Primary reactions destroying O_2 in the Nominal Model.

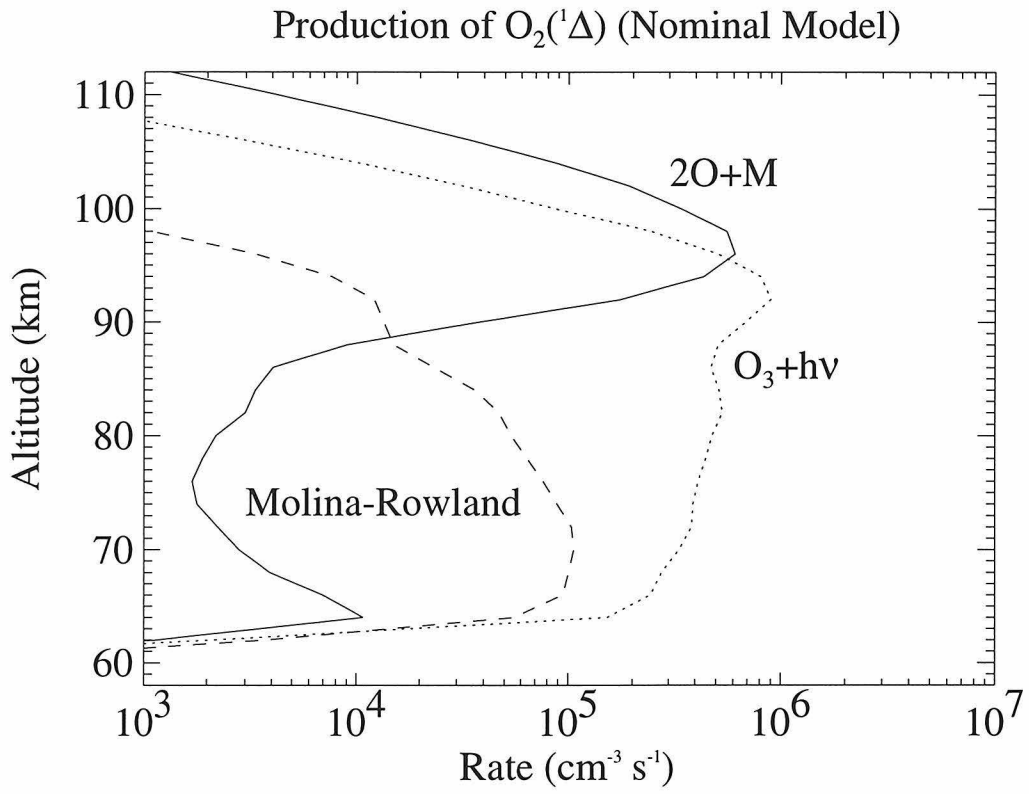

Figure 2.17: Primary reaction producing $O_2(^1\Delta)$ in the Nominal Model.

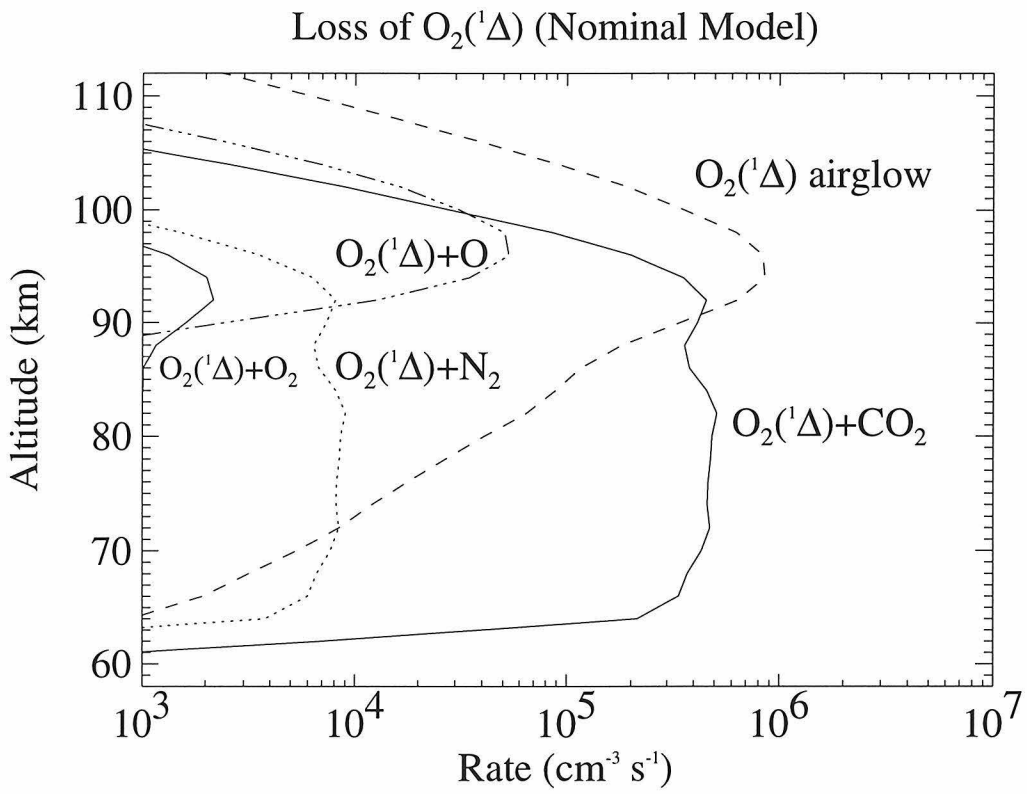

Figure 2.18: Primary reactions destroying $O_2(^1\Delta)$ in the Nominal Model.

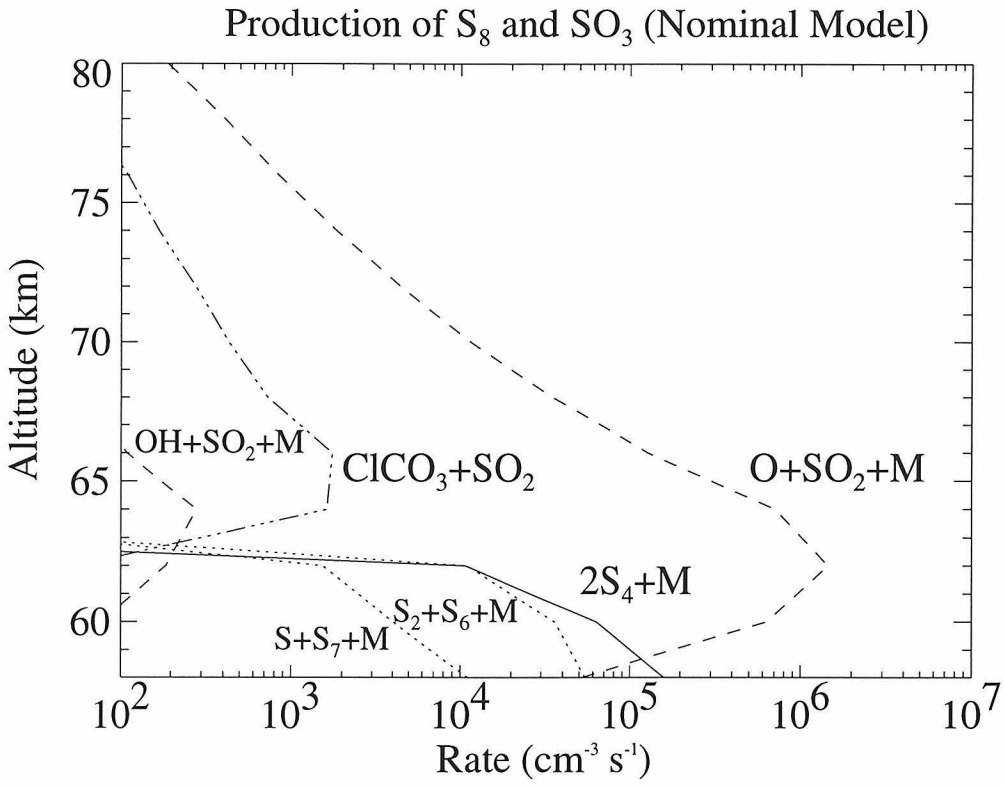

Figure 2.19: Primary reactions producing S_8 and SO_3 in the Nominal Model.

The calculated column-integrated airglow emission in the nominal model is ~ 0.9 MR where 1 MR = 1 MegaRayleigh = 1×10^{12} photons cm^{-2} sec^{-1}. This is $\sim 10\%$ larger than that calculated by *Yung and DeMore* [1982] and is within 30% of the observed global average (~ 1.3 MR, Section 2.1.1). However, the fraction of this airglow emission (0.45 MR) that results from photolysis of O_3 (which can produce O_2 in the $(^1\Delta)$ state) is larger than the observed difference between the dayside and nightside airglow emission (~ 0.3 MR). The radiative lifetime of $O_2(^1\Delta)$ is ~ 1 hour so some of the $O_2(^1\Delta)$ that is produced on the dayside will be transported to the nightside prior to emitting a photon to decay to the ground state. This transport does not, however, resolve the disagreement between the nominal model prediction and the observations. First, the maximum airglow emission from the Venus nightside is observed near the anti-solar point. The transport time from the terminator to the anti-solar point is ~ 24 hours, much larger than the radiative lifetime for $O_2(^1\Delta)$. Second, the observed average nightside emission was determined by excluding airglow emission from near the terminator [*Crisp et al.* 1996]. The nominal rates for collisional quenching of $O_2(^1\Delta)$ by N_2 and CO_2 are only upper limits, however, and there are significant uncertainties in the net yield of $O_2(^1\Delta)$ from Reaction G3 so this disagreement between the nominal model's predictions and the observations is not unexpected. Alternate quenching rates and yields for $O_2(^1\Delta)$ from Reaction G3 will be examined in Sections 2.3.2 and 2.3.3 to obtain a more reasonable fit to both the dayside and the nightside airglow emission.

HO_x and ClO_x

The predicted abundances for HO_x are given in Figure 2.20 and those for ClO_x are given in Figure 2.21. The primary reactions that produce and destroy these species are shown in Figure 2.22. As expected from the work by *Yung and DeMore* [1982] the concentrations of HO_x are significantly smaller than those of ClO_x below ~ 100 km altitude and comparable to those of ClO_x at higher altitudes. This occurs because the primary source of both HO_x and ClO_x in our nominal model is photolysis of HCl but HO_x is preferentially lost via formation of H_2SO_4 below 90 km altitude. As a result, HO_x plays only a minor role in the formation of CO_2 and the destruction of

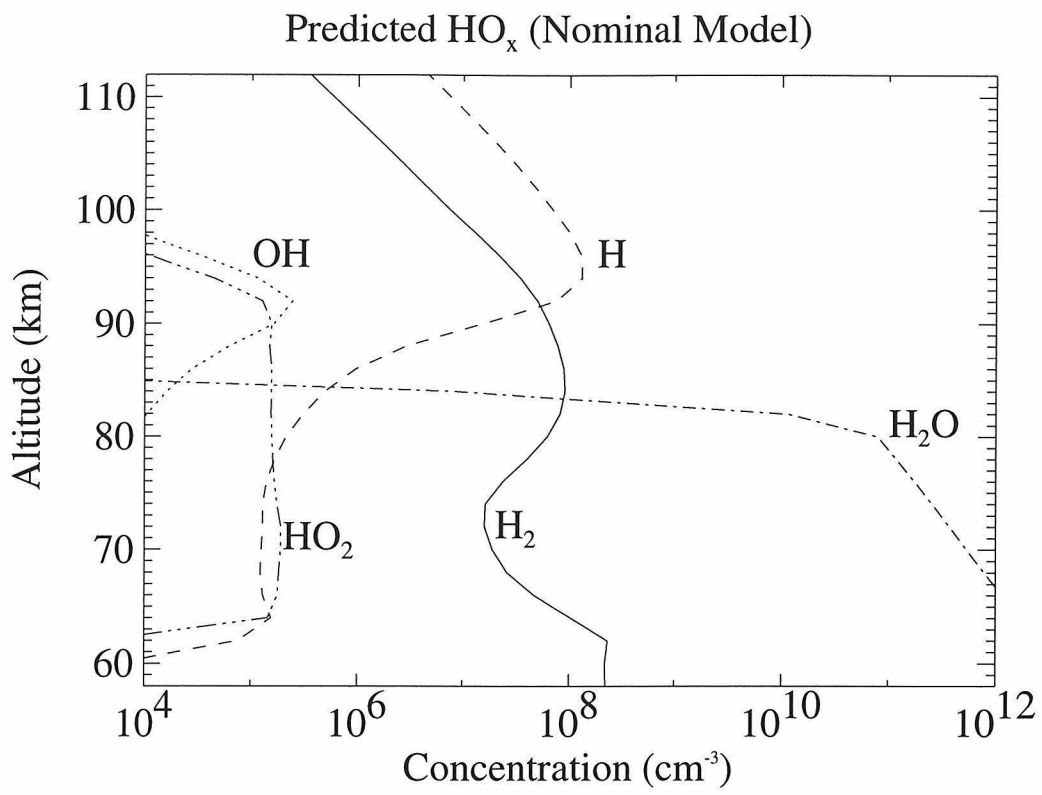

Figure 2.20: Predicted HO_x abundances in the Nominal Model.

O_2, and HO_x is only important in the *formation* of O_2 above $\sim$ 95 km altitude.

The total hydrogen abundance at 100 km altitude in the nominal model is 3.7×10^8 cm^{-3}. This is smaller than the 4.5×10^8 cm^{-3} calculated in the *Krasnopol'sky and Parshev* [1983] model but within the uncertainties associated with their modeling. The H_2 mixing ratio predicted in the nominal model is 8×10^{-9} at 110 km altitude which is more than an order of magnitude smaller than the upper limit (1×10^{-7}) derived by *Kumar and Taylor* [1985] for $\sim$ 130 km altitude. About two-thirds of the hydrogen at 110 km altitude in the nominal model is in HCl with the remainder primarily in the form of atomic hydrogen.

Higher Oxides of Chlorine

The predicted abundances for these species are shown in Figure 2.23. These species

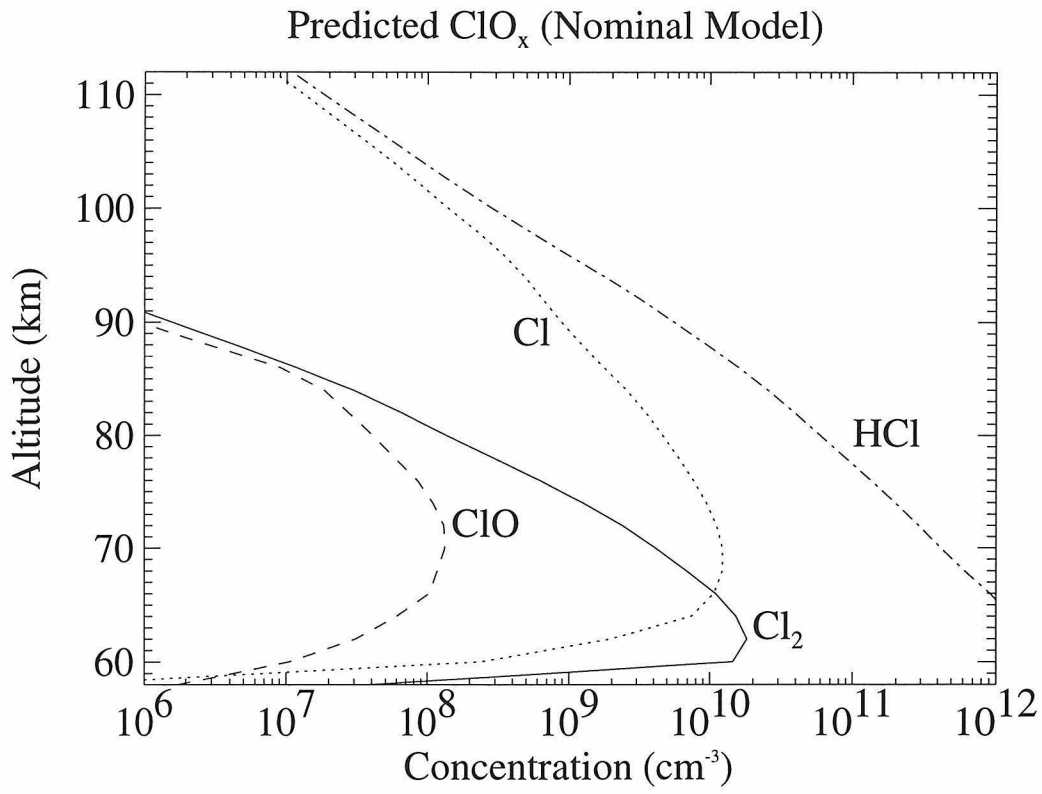

Figure 2.21: Predicted ClO_x abundances in the Nominal Model.

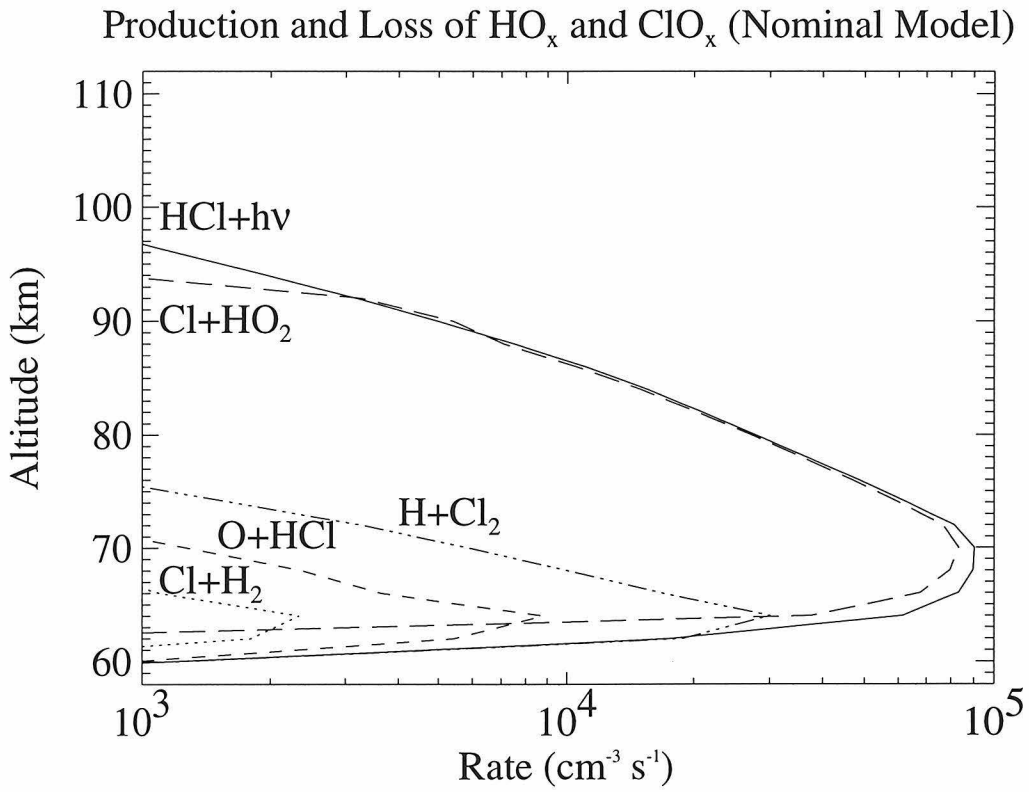

Figure 2.22: Primary reactions producing and destroying HO_x and ClO_x in the Nominal Model.

were included in the nominal model to assess whether they could provide a reservoir in which oxygen could be transported from higher altitudes where the CO oxidation cycles are relatively inefficient to lower altitudes where they are more efficient. The chemical loss timescales for almost all of the Cl_xO_y species, however, are < 100 seconds which is much smaller than the vertical transport timescale ($\gtrsim 1 \times 10^5$) seconds. Consequently, the Cl_xO_y species are not a viable mechanism for vertical transport of oxygen in the Venus middle atmosphere. The small calculated abundances for these species further indicate they do not even provide a local reservoir in which significant amounts of oxygen could be sequestered and thus explain the small upper limit on the oxygen column abundance. The short lifetimes and small abundances for these species are due to the thermal dissociation of these species and/or their rapid reaction with atomic chlorine.

Comparing Figures 2.23 and 2.24 one can see that the rate for Reaction G4 (proposed by *Prinn* [1975]) would have to be at least two orders of magnitude faster than the two-body equivalent rate for Reaction K178 if Reaction G4 were to be an important path for oxidizing CO to CO_2. This would require that either (1) the rate for Reaction G4 is $\gtrsim 1 \times 10^{-11}$ or (2) the enthalpy of reaction in the equilibrium constant for ClOO is at least 1.5 assessed standard deviations more stable than the currently assessed value [*DeMore et al.* 1997] *and* the rate for Reaction G4 is $\gtrsim 1 \times 10^{-13}$. Because there is no laboratory evidence that Reaction G4 occurs [*Yung and DeMore* 1982], our neglect of this mechanism in the current model is reasonable.

We have not examined other potential reactions between Cl_xO_y species and CO as paths for oxidizing CO, but the predicted Cl_xO_y abundances are sufficiently small at $\gtrsim 80$ km altitude that any such reaction would have to be even faster than the $\sim 1 \times 10^{-11}$ required for Reaction G4. This is not likely to occur since CO is a relatively stable molecule.

The Sulfur Budget

The altitude profiles for SO_x, OCS, and S_x are given in Figures 2.25 and 2.26. Comparing Figures 2.25 and 2.21, the abundance of SO_2 is smaller than that of ClO above ~ 75 km altitude. Because of this and because the reactions for oxidizing SO_2

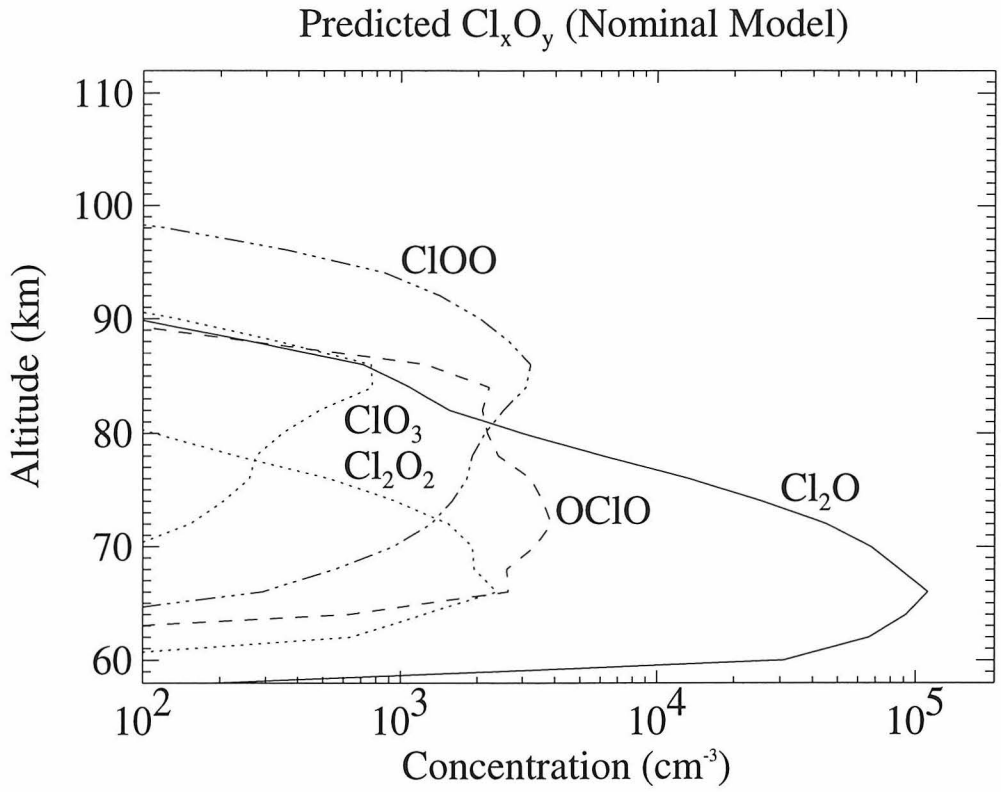

Figure 2.23: Predicted abundances for the higher oxides of chlorine (Cl_xO_y) in the Nominal Model.

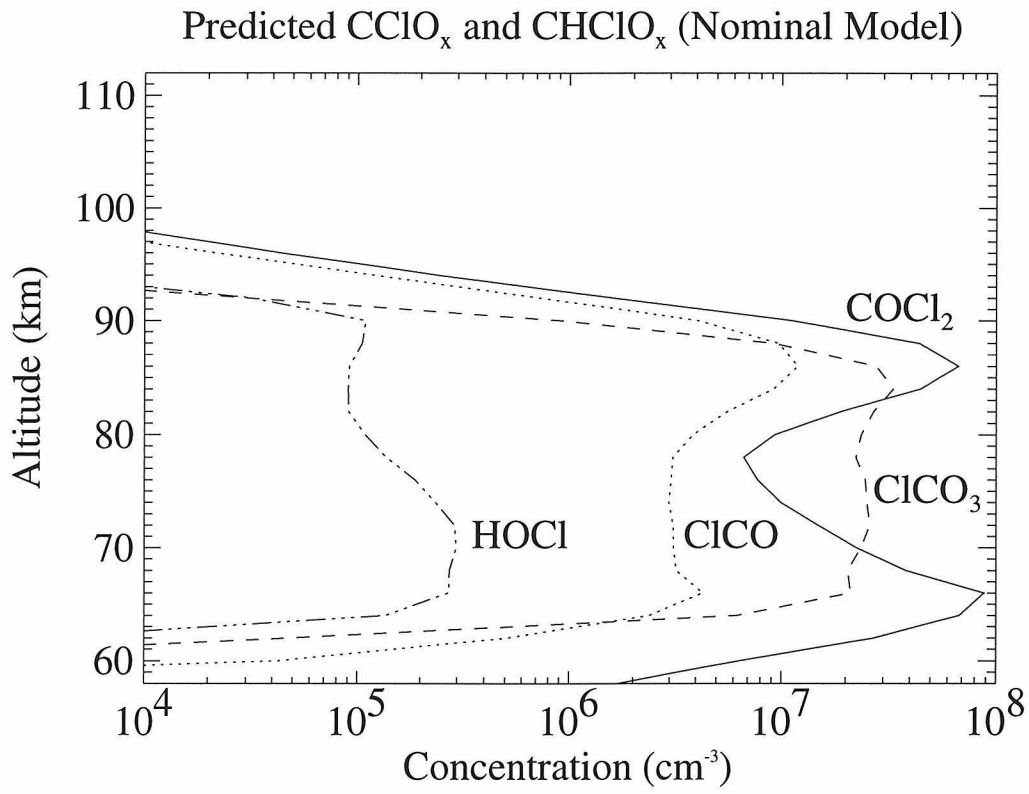

Figure 2.24: Predicted abundances for $CClO_x$) in the Nominal Model.

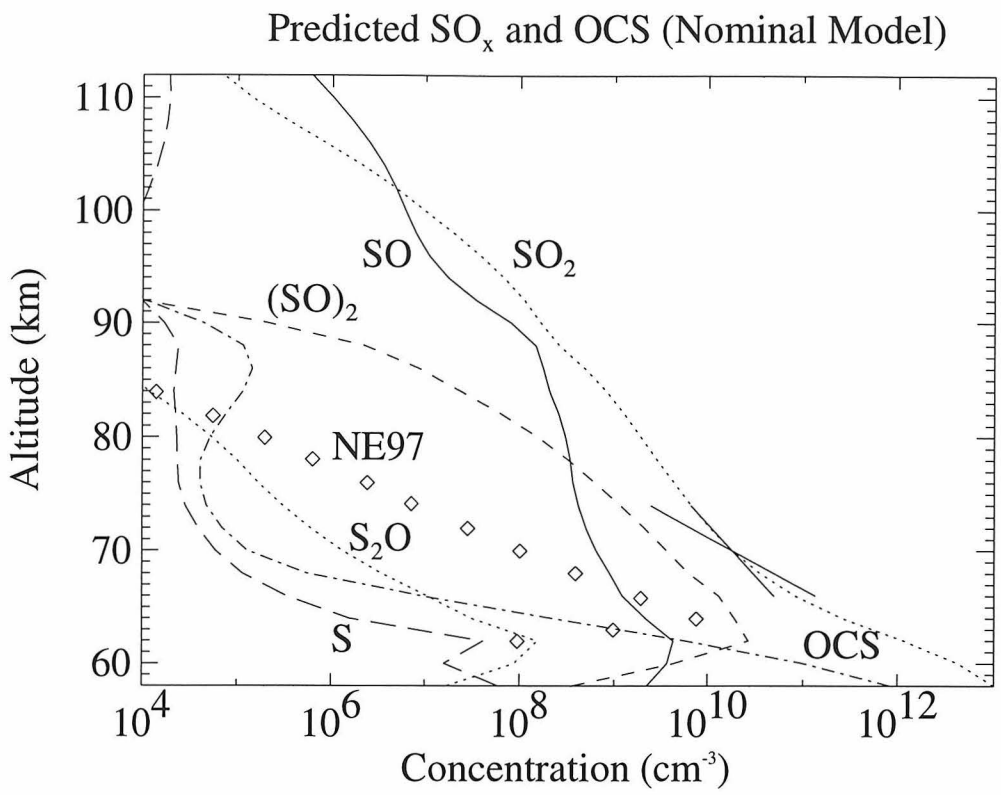

Figure 2.25: Predicted SO_x abundances in the Nominal Model. The "NE97" plot (diamonds) is the profile predicted for S_2O in *Na and Esposito* [1997]. The short bars intersecting the predicted SO_2 profile near 70 km altitude represent the range of SO_2 scale heights inferred by *Na et al.* [1994] from ultraviolet observations.

are slower than Reaction K146, atomic oxygen above the upper cloud layer is rapidly converted to O_2 via Cycle C13. This was one of the primary conclusions from the photochemical models developed in the early 1980s [*Winick and Stewart* 1980; *Yung and DeMore* 1982; *Krasnopol'sky and Parshev* 1983].

Below $\sim$ 75 km altitude, the production of oxygen is dominated by photolysis of SO_2 (Figure 2.12). As one goes deeper into the upper cloud layer, sulfur chemistry plays an increasingly dominant role. The primary reactions producing and destroying SO_2 and SO are shown in Figures 2.27, 2.28, 2.29, and 2.30. Below 70 km altitude, the abundance of SO_2 is controlled by Reactions K168 and K194. In a similar manner,

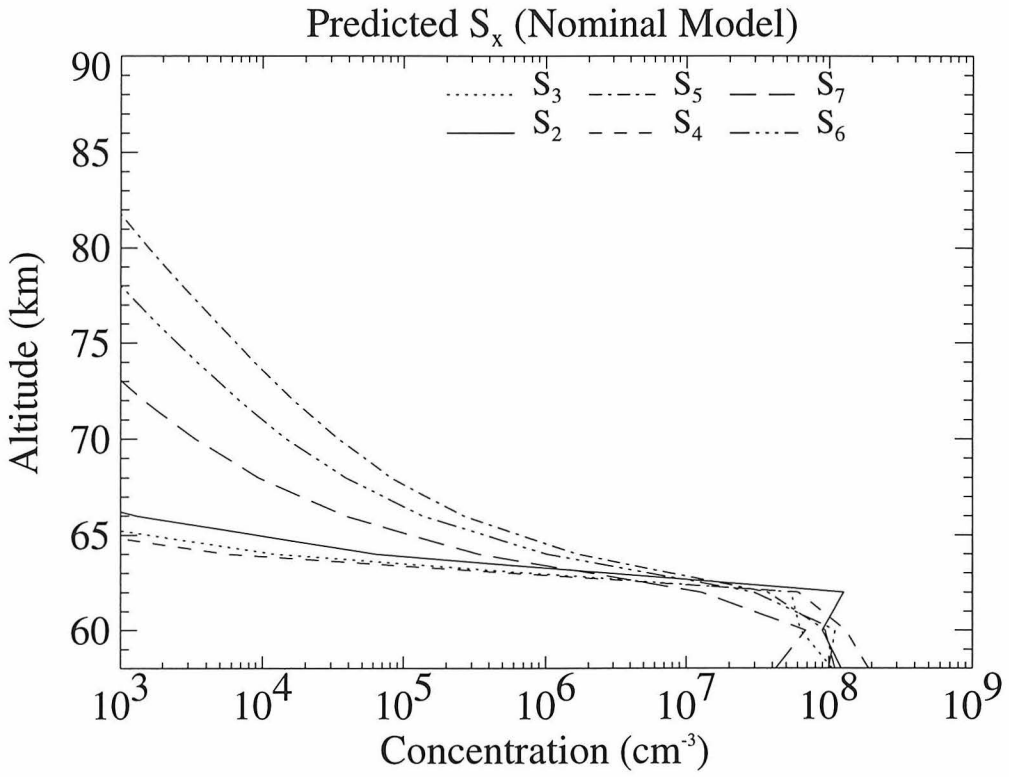

Figure 2.26: Predicted S_x abundances in the Nominal Model.

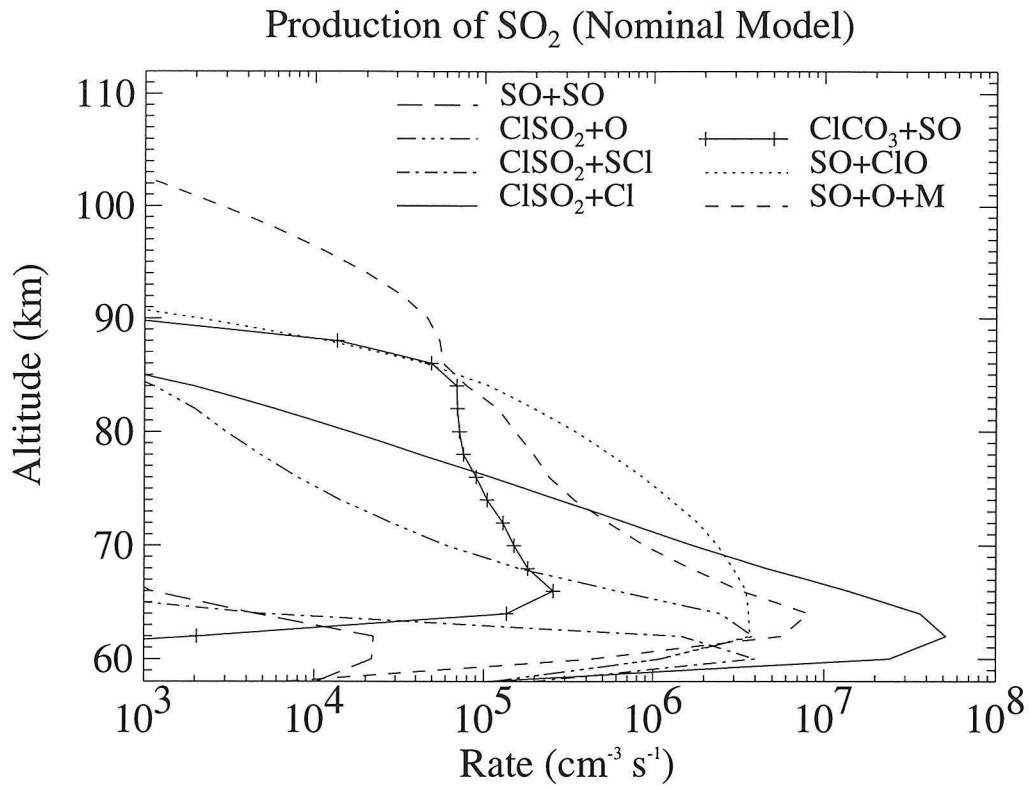

Figure 2.27: Primary reactions producing SO_2 in the Nominal Model.

the abundance of SO below 65 km altitude is controlled by Reactions K244 and K248 (i.e., the equilibrium constant for $(SO)_2$). At $70 - 85$ km altitude, the abundances of SO_2 and SO are controlled by Reactions G11 and K165 which are part of Cycle C17. This confirms the importance of Cycle C17 in the loss of O_2 as had been proposed by *Yung and DeMore* [1982]. This also suggests that a large change in the abundance of SO_2 and SO might have a significant impact on the O_2 abundance in the Venus middle atmosphere.

As discussed in Section 2.2.2, the mixing ratio of SO_2 at the lower boundary has been adjusted to give a mixing ratio for SO_2 near 70 km that is is within the observed range (Figure 2.1). The predicted SO abundances, however, are smaller than those retrieved from ultraviolet observations (Figure 2.2), particularly below 75 km altitude.

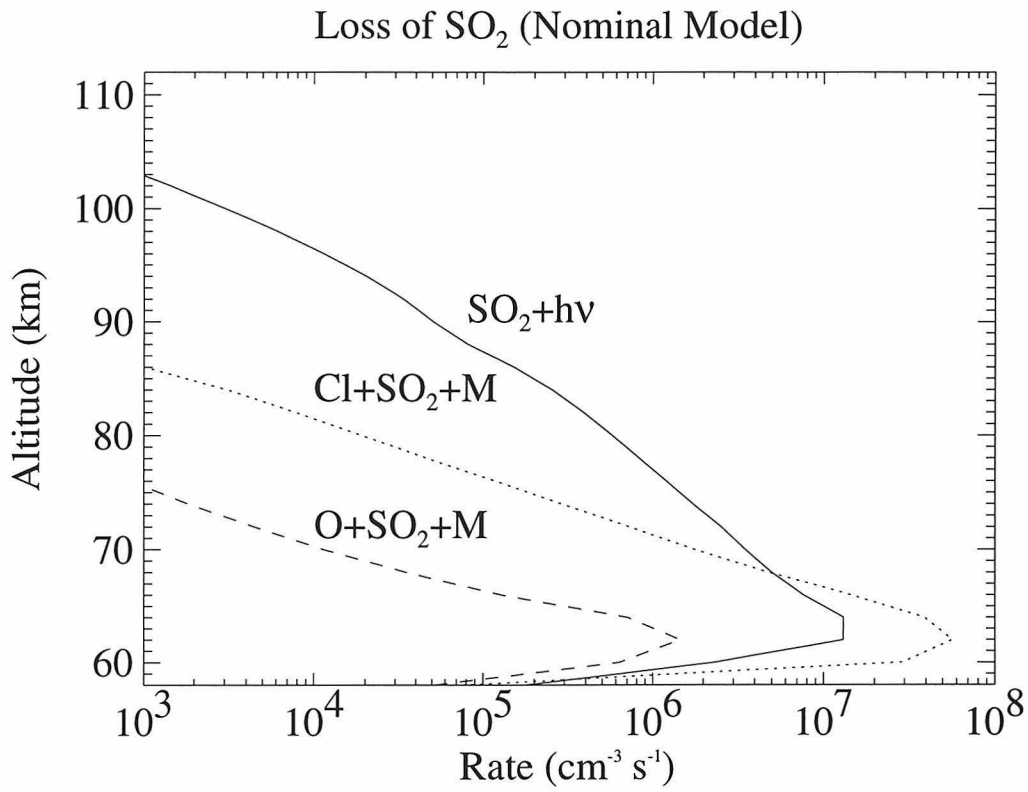

Figure 2.28: Primary reactions destroying SO_2 in the Nominal Model.

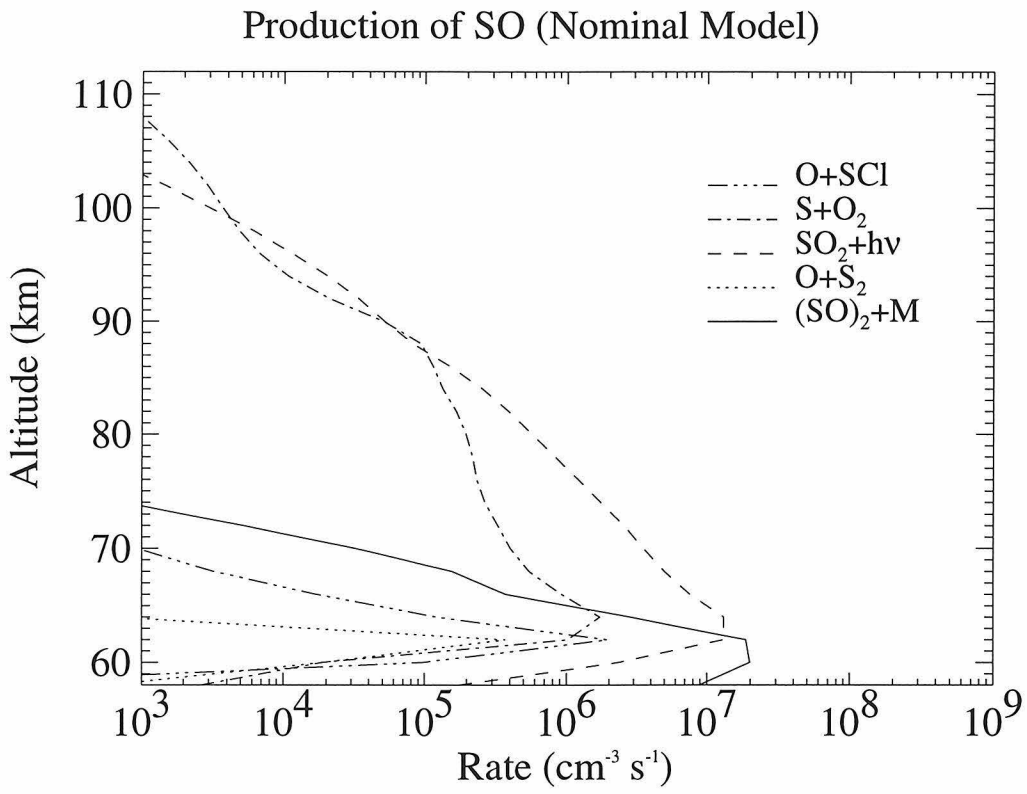

Figure 2.29: Primary reactions producing SO in the Nominal Model.

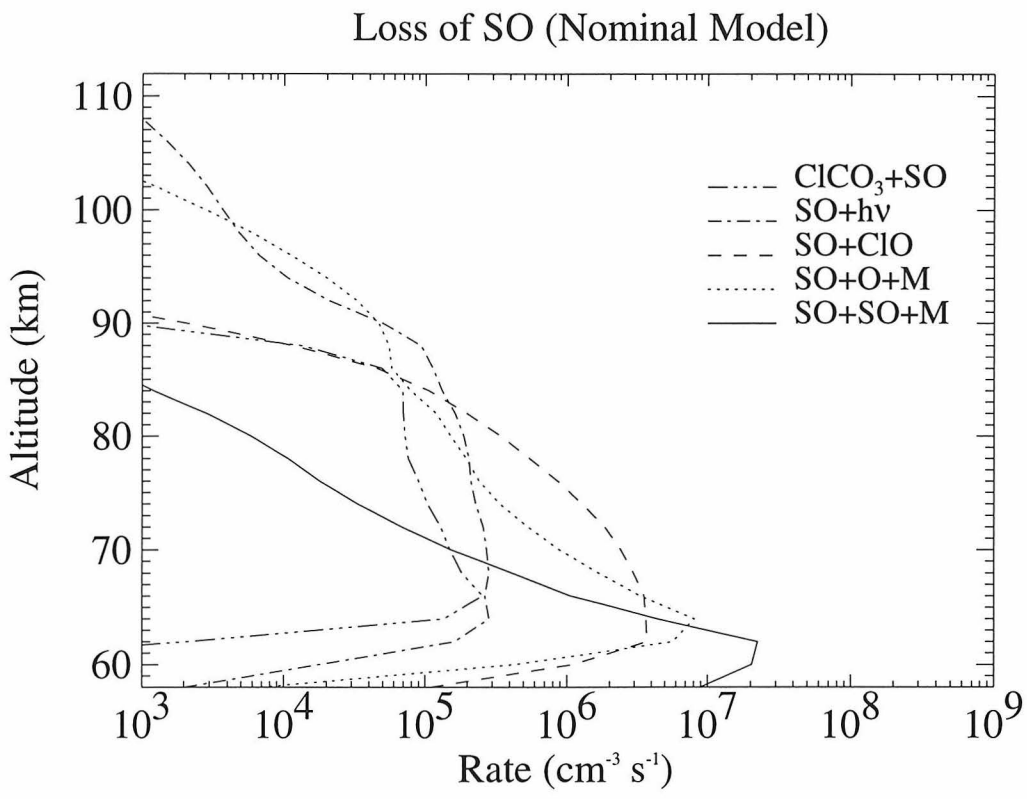

Figure 2.30: Primary reactions destroying SO in the Nominal Model.

A better match to the retrieved SO profile can be obtained if one sums the predicted abundances for SO and $(SO)_2$. Because the nominal value for the $(SO)_2$ equilibrium constant was an estimate, this suggests that plausible empirical adjustments to the enthalpy of reaction may yield a better match between the model predictions for SO and the observations.

The upward fluxes of SO_2 and OCS into the middle atmosphere are calculated to be 8×10^{11} cm^{-2} sec^{-1} and 2×10^{11} cm^{-2} sec^{-1}, respectively. These upward fluxes are balanced in the nominal model by downward fluxes of S_8 and H_2SO_4. The production rates for S_8 and H_2SO_4 in the nominal model are 6×10^{10} cm^{-2} sec^{-1} and 6×10^{11} cm^{-2} sec^{-1}, respectively. These production rates suggest that photolysis of OCS leads almost entirely to production of S_8 and detailed examination of the kinetic paths supports this conclusion. SO_2 that is transported upward from the lower atmosphere is disproportionated into both S_8 and H_2SO_4 with a majority of the SO_2 being oxidized to H_2SO_4.

$SClO_x$ and SCl_x

These two classes of reduced chemical species have not been quantitatively considered in previous Venus photochemical models. The predicted abundances in the nominal model are given in Figure 2.31. With the exception of $ClSO_2$, these species are predicted to exist only within the upper cloud layer.

$ClSO_2$ serves as a buffer for SO_2 (Figures 2.27 and 2.28) which slows the rate at which SO_2 is oxidized to H_2SO_4 as it is transported upward from the lower boundary of the model. This buffering, in combination with the larger eddy diffusion coefficient used in the nominal model, enables the nominal model to have an SO_2 abundance at 70 km altitude that is comparable to that in *Yung and DeMore*'s [1982] model C even though the mixing ratio at 58 km altitude in the nominal model is a factor of 3 smaller than that specified by *Yung and DeMore* [1982].

Most of the reactions involving the SCl_x species are estimated so the results from this aspect of the nominal model are highly speculative. However, the SCl_x species appear to play two roles in the chemistry of the upper cloud layer. First, they provide a minor but important mechanism for splitting Cl_2 at $\lesssim 65$ km altitude which enables

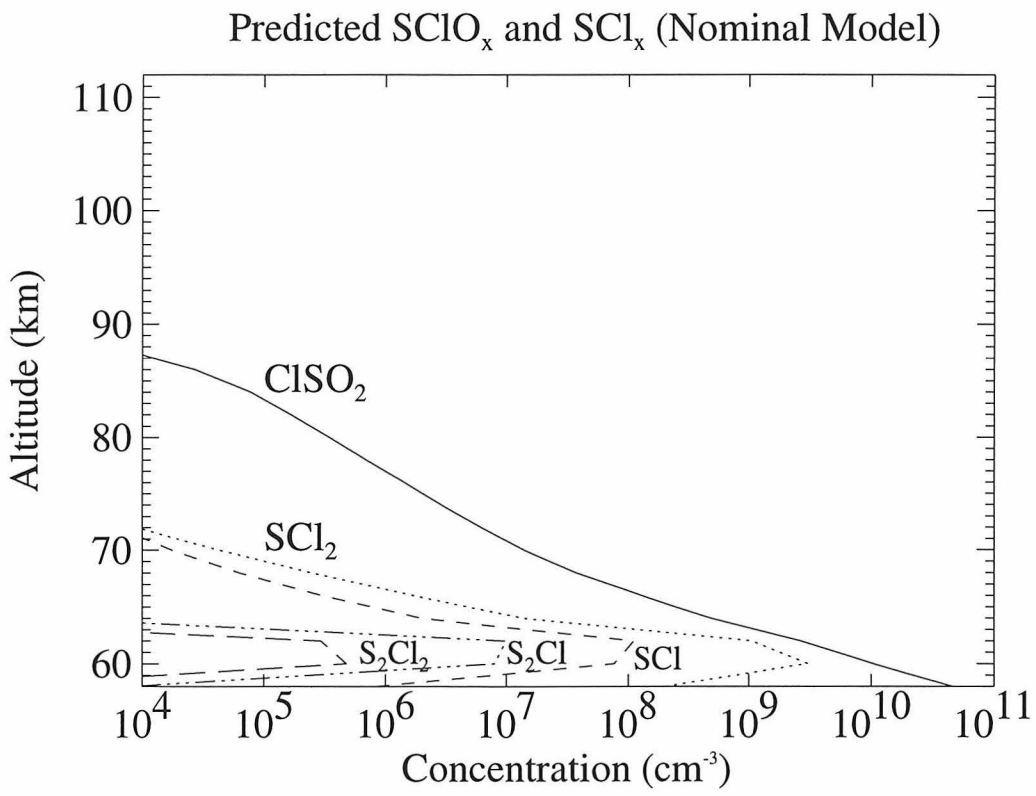

Figure 2.31: Predicted abundances of sulfur-chlorine species in the Nominal Model.

the formation of $ClSO_2$ at those altitudes. Second, the SCl_x species are intermediaries in the process of converting atomic sulfur to S_2 (which eventually becomes S_8 in the model). At 58 km, the primary source of S_2 is Reaction K262, but at higher altitudes, S_2 is primarily formed via Reaction P91. If the proposed reactions involving SCl_x species occur in the Venus upper cloud layer, the actual rates for these reactions may determine the relative rates at which OCS and SO_2 are converted into S_8 and H_2SO_4.

Eddy Diffusion

The eddy diffusion coefficient used for the nominal model is larger than that used in *Yung and DeMore* [1982] and *Krasnopol'sky and Parshev* [1983], but the nominal model's CO profile is within the range of values retrieved by microwave observations (Figure 2.3) suggesting the larger eddy diffusion coefficient may be plausible. In addition, the predicted scale height for SO_2 near 70 km is within the range of values determined by *Na et al.* [1994] from their UV observations (Figure 2.25). As shown in Figure 2.3, there are large diurnal and temporal variations in the CO profile and we are not trying to model the diurnal variations so the degree of agreement achieved by the nominal model is satisfactory given these limitations.

2.3.2 Model Sensitivity Studies

Two types of sensitivity tests were conducted to examine the response of the Nominal Model to changes in input parameters. The first set of tests examined the model's responses to changes in the boundary conditions. These are described in the first part of this section. The second set of tests examined the model's responses to changes in the rates for selected kinetic and photolysis reactions. Those tests are summarized in the second part of this section which describes the results from a model run in which a number of parameters were adjusted simultaneously to minimize the differences between the model predictions and the observations.

Boundary Condition Variations

The upper boundary conditions were varied by the amounts listed in Table 2.7. The amplitudes of the variations were selected based on the estimated uncertainties in these parameters. A similar procedure was followed for the lower boundary conditions but the amplitudes of the variations were based on observations. As noted in Section 2.1.1, interpretation of the HCl observations by *Connes et al.* [1967] depends on the assumed altitude at which the HCl lines form. The 25% variation tested encompasses the smallest value from *Young* [1972] and the results from *Connes et al.* [1967] and *Pollack et al.* [1993]. The larger possible values from *Young* [1972], *Yung and DeMore* [1982], and *Pollack et al.* [1993] lie outside the selected range. The factor of four variation tested for the SO_2 mixing ratio at 58 km altitude is intended to simulate the observed temporal changes in the SO_2 abundance at the cloud top (Figure 2.1). The factor of four variation tested for the OCS mixing ratio at 58 km altitude is an estimate of the uncertainty in this observation. The two alternate H_2O profile tested represent extreme values for this parameter. The case with 1 ppm of H_2 at the lower boundary is based on the *Pioneer Venus* mass spectrometer report of a marginal detection of $\sim$ 1 ppm of H_2S within the cloud layers [*von Zahn et al.* 1983]. If that detection is valid, then H_2S is likely to rapidly photodissociate near the lower boundary of our photochemical model and produce H or H_2 and S. The effects of the additional sulfur produced from photolysis of H_2S can be assessed qualitatively from the OCS and SO_2 boundary condition variation tests. The nominal albedo at the lower boundary was specified to match the measured albedo of the upper cloud layer at $\sim$ 400 nm (Appendix H) but the measured albedo is a function of wavelength. The alternate albedos span the range of possible values for this parameter.

The results from model runs using the alternate boundary conditions are shown in Tables 2.8 and 2.9. For each of these model runs, only the indicated boundary parameter was changed. All other parameters were left at the values described earlier for the Nominal Model. The changes that had the greatest effect on the selected model results have been highlighted in both tables.

Table 2.7: Variations of Boundary Conditions for the Nominal Photochemistry Model

	Lower Boundary		Upper Boundary	
Species	Low	High	Low	High
CO_2	not varied		$\phi = 2.5 \times 10^{11}$	$\phi = 1.0 \times 10^{12}$
CO	not varied		matched to CO_2 flux	
O_2			$\phi = 2.25 \times 10^{8}$	$\phi = 3.6 \times 10^{9}$
HCl	$f = 3.0 \times 10^{-7}$	$f = 5.0 \times 10^{-7}$	$\phi = 2.5 \times 10^{6}$	$\phi = 4.0 \times 10^{7}$
SO_2	$f = 3.0 \times 10^{-7}$	$f = 4.8 \times 10^{-6}$		
O			matched to CO_2 and	O_2 fluxes
Cl			matched to HCl flux	
OCS	$f = 2.5 \times 10^{-8}$	$f = 4.0 \times 10^{-7}$		
H_2O [a]				
H_2		$f = 1.0 \times 10^{-6}$		
Albedo [b]				

Notes: The symbols f and ϕ denote volume mixing ratio and flux (cm^{-2} sec^{-1}), respectively. The sign convention for ϕ is positive for upward flow. The nominal boundary conditions are given in Table 2.2.

[a] The only water present in the low water case was H_2O generated photochemically within the model from photodissociation of HCl. The water vapor mixing ratio at all altitudes was fixed at 1×10^{-6} for the high water case.

[b] Three alternate surface albedos were tested for the lower boundary: 0.0, 0.4, and 0.9.

Table 2.8: Results from Variations of Lower Boundary Conditions

Variation	Flux Down at 58 km (cm^{-2} sec^{-1}) CO	$ClSO_2$	Cl_2	SCl_2	Flux Up at 58 km SO_2	OCS
Nominal [a]	6.9(11)	2.6(9)	2.1(6)	1.2(7)	7.4(11)	2.6(11)
Low HCl conc [b]	8.6(11)	1.8(9)	2.0(6)	9.4(6)	7.5(11)	2.6(11)
High HCl conc	5.7(11)	3.4(9)	2.1(6)	1.3(7)	7.4(11)	2.6(11)
Low SO_2 conc	5.9(11)	3.7(8)	8.5(8)	3.3(8)	3.3(11)	4.2(11)
High SO_2 conc	9.3(11)	2.6(9)	6.9(6)	2.1(7)	2.2(12)	1.5(11)
Low OCS conc	4.9(11)	2.6(9)	3.0(6)	1.1(7)	7.4(11)	6.5(10)
High OCS conc	1.4(12)	2.5(9)	1.7(6)	1.0(7)	7.2(11)	1.0(12)
Low H_2O conc	6.8(11)	2.6(9)	2.1(6)	1.1(7)	2.6(11)	7.3(11)
High H_2O conc	9.7(11)	1.9(9)	1.6(6)	7.3(6)	7.3(11)	2.6(11)
1 ppm H_2	9.0(11)	3.7(7)	7.8(3)	1.7(3)	1.1(12)	2.9(11)
Albedo 0.0	6.2(11)	2.6(9)	3.0(6)	2.4(7)	7.3(11)	1.8(11)
Albedo 0.4	6.6(11)	2.6(9)	2.2(6)	1.5(7)	7.3(11)	2.3(11)
Albedo 0.9	7.5(11)	2.5(9)	2.1(6)	7.6(6)	7.3(11)	3.3(11)

Variation	Concentration at 70 km (cm^{-3}) SO_2	SO	$(SO)_2$	Photolysis Rate at 70 km (sec^{-1}) SO_2	Cl_2	O_3
Nominal [a]	1.8(10)	6.4(8)	3.7(9)	1.9(-4)	5.2(-3)	1.6(-2)
Low HCl conc [b]	1.9(10)	6.2(8)	3.6(9)	1.9(-4)	5.2(-3)	1.6(-2)
High HCl conc	1.7(10)	6.3(8)	3.6(9)	1.9(-4)	5.2(-3)	1.6(-2)
Low SO_2 conc	5.7(9)	2.0(8)	6.2(8)	2.3(-4)	5.3(-3)	1.7(-2)
High SO_2 conc	4.7(10)	1.5(9)	1.1(10)	1.7(-4)	5.2(-3)	1.5(-2)
Low OCS conc	1.8(10)	6.4(8)	3.7(9)	1.9(-4)	5.2(-3)	1.6(-2)
High OCS conc	1.9(10)	6.6(8)	3.9(9)	1.9(-4)	5.2(-3)	1.6(-2)
Low H_2O conc	1.8(10)	6.4(8)	3.7(9)	1.9(-4)	5.2(-3)	1.6(-2)
High H_2O conc	2.1(10)	6.0(8)	3.6(9)	1.9(-4)	5.2(-3)	1.6(-2)
1 ppm H_2	5.5(9)	3.6(8)	1.3(9)	2.2(-4)	5.3(-3)	1.6(-2)
Albedo 0.0	1.8(10)	6.4(8)	3.7(9)	1.9(-4)	5.1(-3)	1.6(-2)
Albedo 0.4	1.8(10)	6.4(8)	3.7(9)	1.9(-4)	5.2(-3)	1.6(-2)
Albedo 0.9	1.8(10)	6.4(8)	3.7(9)	1.9(-4)	5.3(-3)	1.6(-2)

Variation	O_2 Column Abundance (cm^{-2})	Production Rate (cm^{-2} sec^{-1}) S_8	SO_3
Nominal [a]	8.0(18)	4.9(10)	6.1(11)
Low HCl conc [b]	**9.5(18)**	4.3(10)	6.7(11)
High HCl conc	**6.9(18)**	5.4(10)	5.7(11)
Low SO_2 conc	8.3(18)	**6.9(10)**	**2.7(11)**
High SO_2 conc	**7.2(18)**	**7.9(10)**	**1.7(12)**
Low OCS conc	8.0(18)	**2.1(10)**	6.0(11)
High OCS conc	7.9(18)	**1.4(11)**	6.0(11)
Low H_2O conc	7.9(18)	4.8(10)	6.0(11)
High H_2O conc	**1.1(19)**	**3.8(10)**	6.9(11)
1 ppm H_2	**1.5(19)**	**6.5(10)**	**8.5(11)**
Albedo 0.0	8.0(18)	**3.6(10)**	6.1(11)
Albedo 0.4	8.0(18)	4.3(10)	6.1(11)
Albedo 0.9	7.9(18)	**6.0(10)**	6.0(11)

Note: 1.00(13) = 1×10^{13}. [a] Results from Nominal Model described in Section 2.3.1. [b] Results from variations of the lower boundary conditions as described in Table 2.7.

Table 2.9: Results from Variations of Upper Boundary Conditions

Variation	Flux Down at 104 km (cm^{-2} sec^{-1}) CO	O_2	O	Cl	Flux Up at 104 km CO_2	HCl
Nominal [a]	1(12)	3(10)	9(11)	8(7)	1(12)	8(7)
Low CO_2 flux [b]	9(11)	3(10)	9(11)	8(7)	9(11)	8(7)
High CO_2 flux	1(12)	6(10)	1(12)	8(7)	1(12)	8(7)
Low O_2 flux	1(12)	4(10)	1(12)	2(8)	1(12)	8(7)
High O_2 flux	1(12)	3(10)	9(11)	8(7)	1(12)	8(7)
Low HCl flux	1(12)	4(10)	1(12)	8(7)	1(12)	8(7)
High HCl flux	1(12)	3(10)	9(11)	1(8)	1(12)	1(8)

Variation	O_2 Column Abundance (cm^{-2})	Concentration at 104 km (cm^{-3}) CO	O_2	H_2	O_3	ClCO
Nominal [a]	8.0(18)	2(11)	7(10)	3(6)	8(5)	6(1)
Low CO_2 flux [b]	9.4(18)	3(11)	7(10)	3(6)	8(5)	7(1)
High CO_2 flux	8.8(18)	3(11)	8(10)	3(6)	1(6)	6(1)
Low O_2 flux	9.8(18)	3(11)	8(10)	3(6)	1(6)	7(1)
High O_2 flux	8.0(18)	3(11)	8(10)	3(6)	8(5)	6(1)
Low HCl flux	9.8(18)	3(11)	8(10)	3(6)	1(6)	7(1)
High HCl flux	7.9(18)	2(11)	7(10)	3(6)	8(5)	7(1)

Note: $1.00(13) = 1 \times 10^{13}$.

[a] Results from Nominal Model described in Section 2.3.1.

[b] Results from variations of the upper boundary conditions as described in Table 2.7.

Very few of the changes made to the upper boundary conditions had a significant impact on the model results. An interesting exception is that decreasing the upward flux of CO_2, O_2, or HCl increases the column abundance of O_2, but the changes are small compared to the size of the variation in the boundary parameter value.

The lower boundary conditions had greater impact on the model results. A 25% increase in the HCl mixing ratio led to a 15% decrease in the column abundance of O_2. If the photochemical model were to continue to respond linearly for a 100% increase in the HCl mixing ratio (to the 0.8 ppm used by *Yung and DeMore* [1982]), then the O_2 column abundance would decrease by $\sim$ 60%. An increase in the abundance of SO_2 at 58 km also leads to a decrease in the column abundance of O_2, but relative response is much smaller than for HCl. These results suggest that uncertainties and/or variability in the abundances of these species does not have significant impact on the O_2 abundance. However, the O_2 column abundance in the Nominal Model differs by at least an order of magnitude from that in the Venus atmosphere so a "correct" photochemical model might be more sensitive to the HCl and/or SO_2 abundances at the lower boundary.

The high H_2 case confirms one of the results from the *Yung and DeMore* [1982]) model. A large abundance of labile HO_x, such as H_2, near the upper cloud layer can interfere with the chlorine-catalyzed oxidation of CO_2 and increase the abundance of O_2 in the Venus atmosphere. If photochemistry in the atmosphere of Venus today is dominated by chlorine species and if Venus had a much larger abundance of H_2O in the past, then there may have been a period in Venus' history during the transition from hydrogen to chlorine chemistry when the abundance of O_2 may have been much larger than today. The high H_2 case also illustrates the importance of $ClSO_2$ in the transport of SO_2 from the lower boundary of the model to the top of the upper cloud. By increasing the rate at which chlorine in the upper cloud is converted from a labile form, Cl_2, to a relatively unreactive form, HCl, the large abundance of H_2 has decreased the abundance of $ClSO_2$. In addition, the introduction of H_2 increases the production of OH which readily oxidizes SO_2 to SO_3. As a result, SO_2 is converted to S_8 and SO_3 at a faster rate than in the Nominal Model and the gradient of SO_2

concentration versus altitude has become steeper than in the Nominal Model. Thus, the upward flux of SO_2 increased in this test case but the abundances of SO_2, SO, and $(SO)_2$ at 70 km altitude all decreased.

None of the boundary parameter variations altered the SO_2 scale height which is reasonable since this parameter is primarily controlled by photolysis of SO_2 and vertical transport via eddy diffusion.

One-Sigma Model Results

The sensitivity tests we conducted for the kinetic rates indicated the most important parameter governing the column O_2 abundance is the stability of ClCO. Increasing the stability of the equilibrium constant for ClCO by nearly one standard deviation (from *DeMore et al.* [1997]) can reduce the predicted O_2 abundance so that it is compatible with the 2σ upper limit from *Trauger and Lunine* [1983] as will be discussed further in Chapter 3. Other tests we conducted indicated that varying the values for other reactions within the assessed, measured, or estimated uncertainties for the parameters could improve the agreement between the model predictions and existing observations. The changes included in this model are detailed below. The predicted mixing ratios for CO_2, SO_2, and O_2 are shown in Figure 2.32.

ClO_x, $CClO_x$, and O_2

The stability of ClCO is determined by the heat of formation of ClCO and the atmospheric temperature. For this model:

(1) the equilibrium constant for ClCO was changed from curve "JPL97" in Figure 2.4 to be a factor of two smaller than the curve "JPL97 $1-\sigma$";

(2) the CO_2 dissociation cross section at 195 and 200 nm was set to zero at 202 K and the CO_2 dissociation cross section at 200 and 205 nm at 298 K was divided by two (compared to the nominal model) to minimize the production rate for oxygen (Figure 2.33); and

(3) the rate for reaction K178 was increased by a factor of $2\exp(300/T)$ (estimated to be one standard deviation from the nominal value).

As a result of the changes in the stability of ClCO and the reduced photolysis of

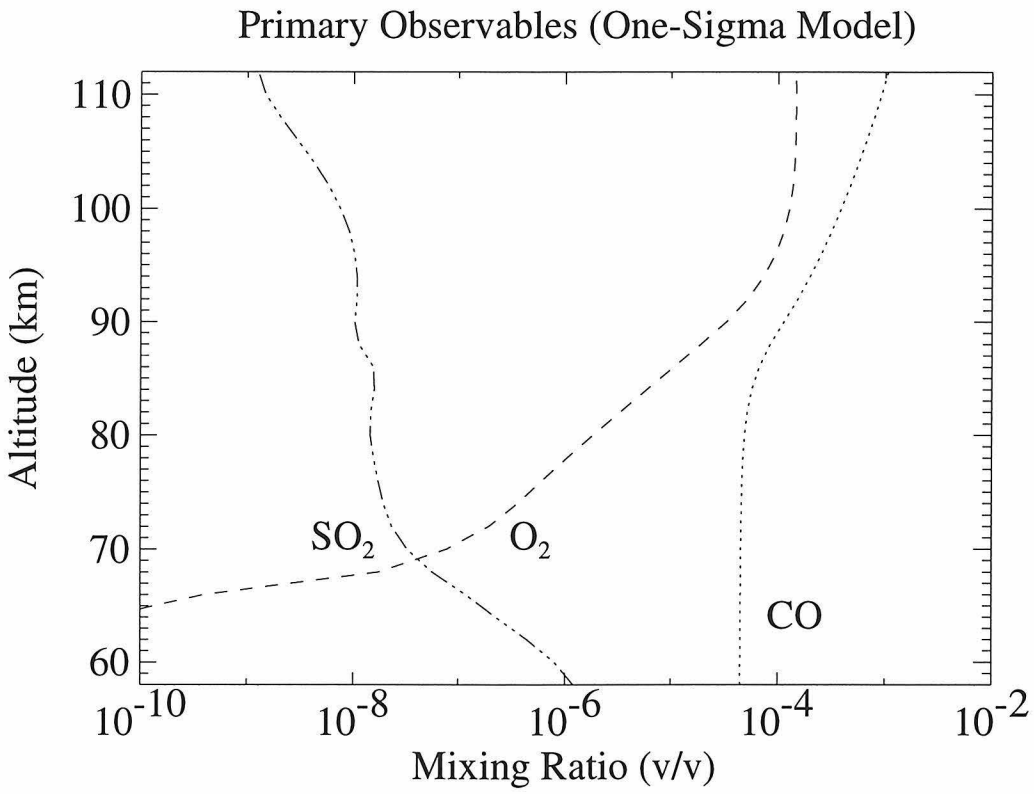

Figure 2.32: Predicted mixing ratios for CO, O_2, and SO_2 from the One-Sigma Model are shown in the dotted, dashed, and dot-dashed lines, respectively.

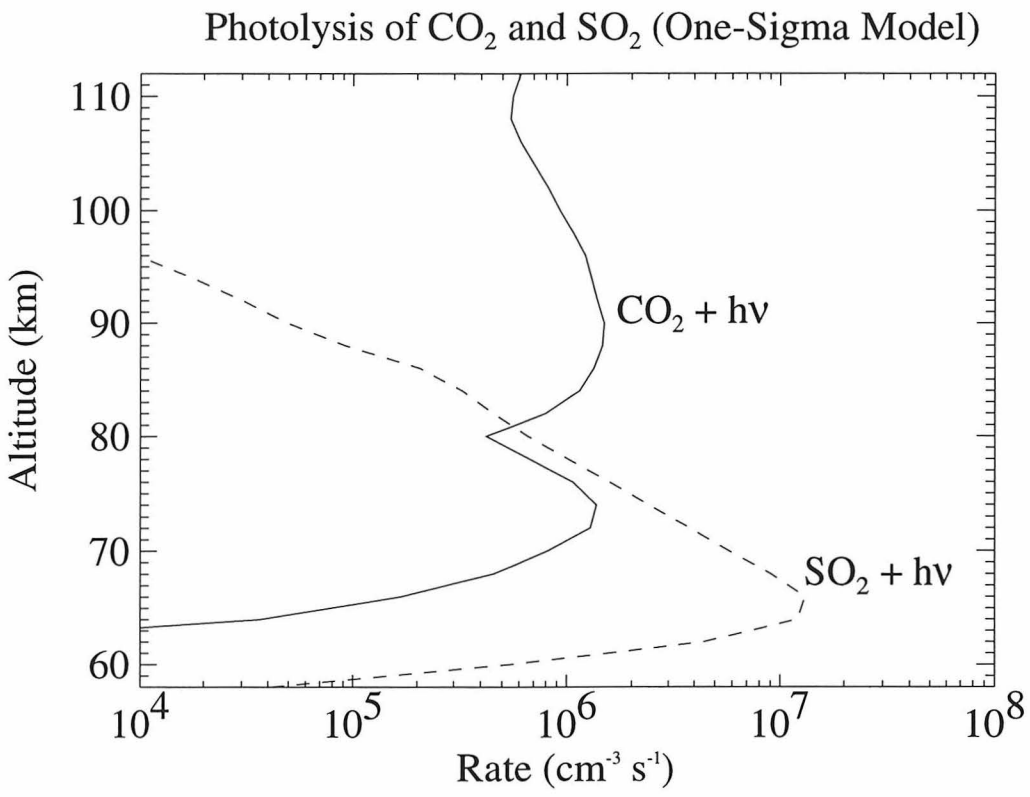

Figure 2.33: Photolysis of CO_2 and SO_2 in the One-Sigma Model.

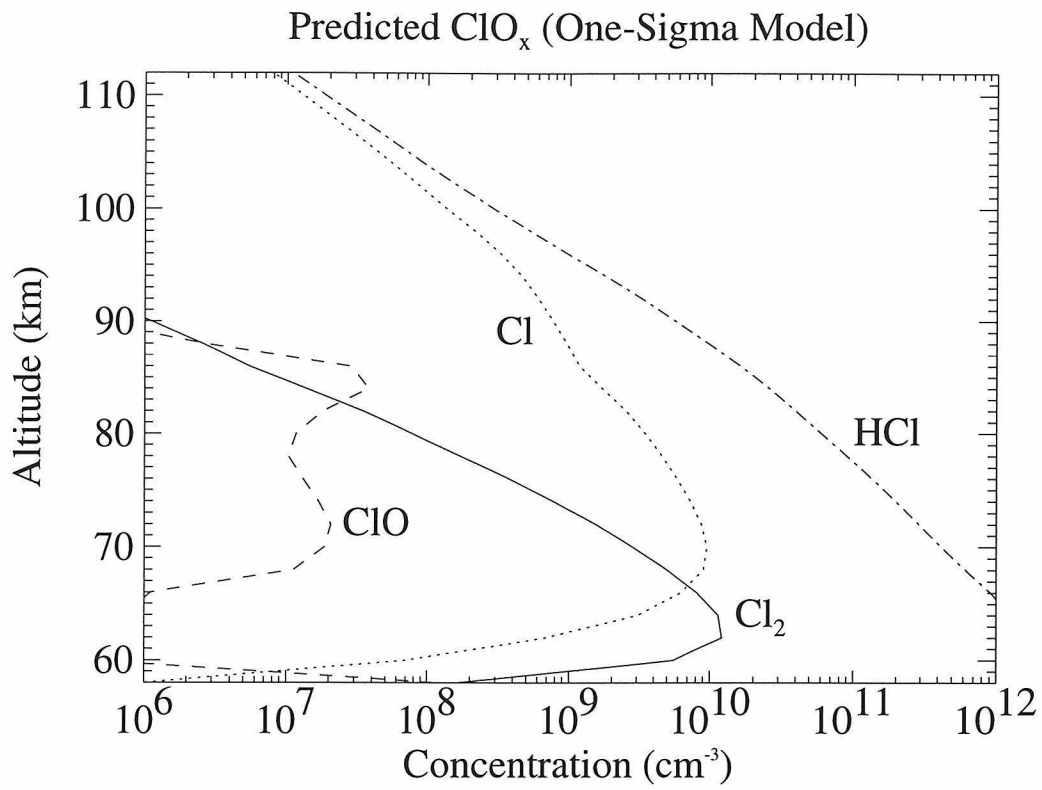

Figure 2.34: Predicted ClO_x abundances in the One-Sigma Model.

CO_2, the ClO abundance in this model (Figure 2.34) is up to a factor of 10 smaller than in the nominal model at 70 – 80 km altitude and has been reduced by several orders of magnitude at 60 – 65 km altitude. The ClCO abundance at 65 – 80 km altitude (Figure 2.35) is a factor of < 2 larger than in the nominal model. At 80 - 90 km altitude, Cl has been shifted from Cl to $ClCO_3$.

These changes in the partitioning of chlorine have three effects on the oxygen budget. First, the smaller abundance of Cl decreases the effectiveness of the Molina-Rowland cycle, Cycle C13, so atomic oxygen is converted to O_2 at a slower rate than in the nominal model (compare Figures 2.15 and 2.36). Second, the larger abundance of $ClCO_3$ increases the rate at which CO is oxidized to CO_2 so oxygen is sequestered in CO_2 at higher altitudes than in the nominal model (compare Figures 2.16 and 2.10

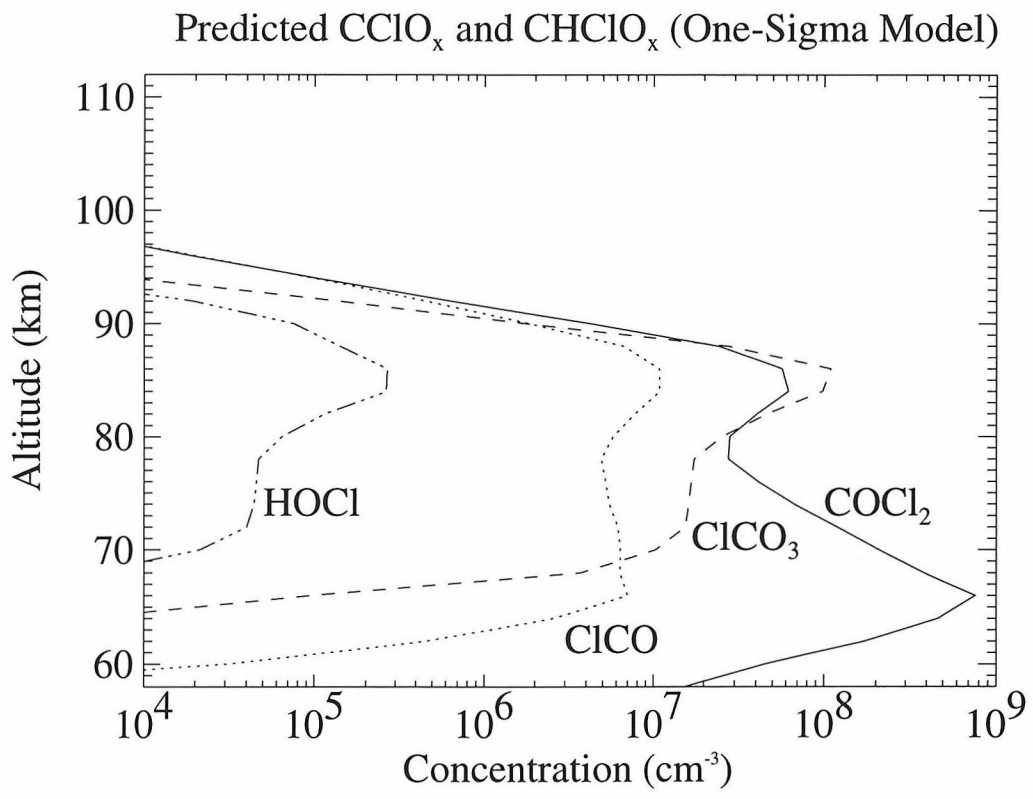

Figure 2.35: Predicted abundances for CClO$_x$) in the One-Sigma Model.

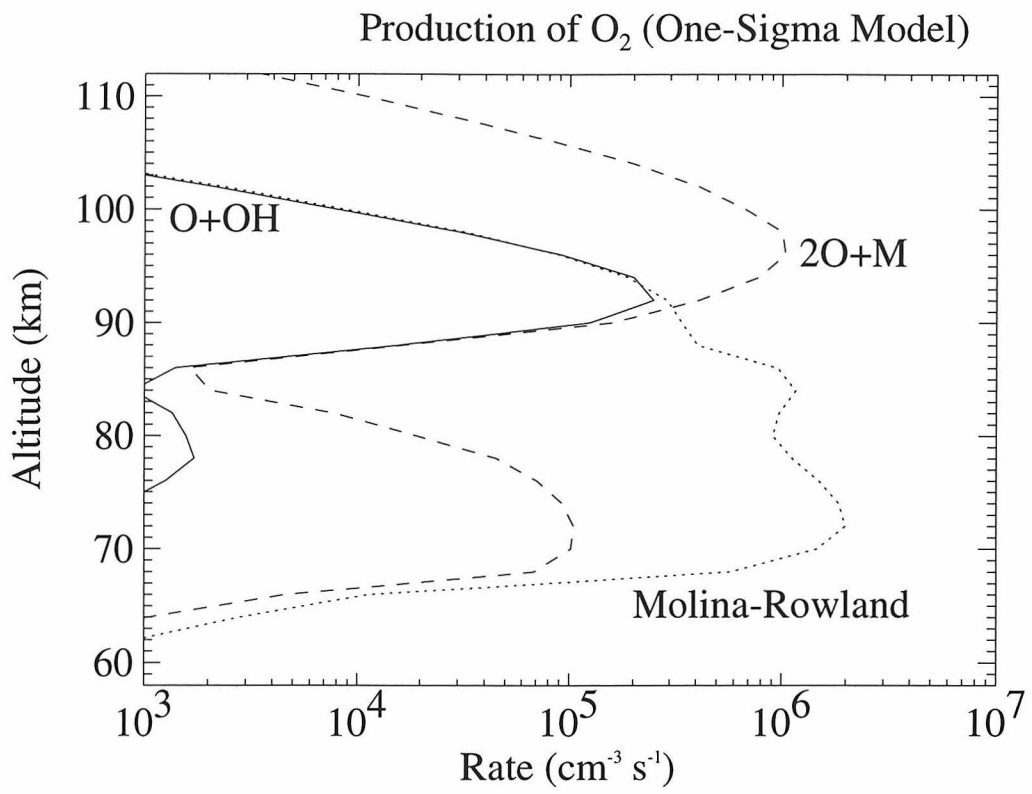

Figure 2.36: Primary reaction producing O_2 in the One-Sigma Model.

to Figures 2.37 and 2.38). Third, the relative importance of Cycle C14 has increased relative to Cycles C15 and C17. The net result is that the abundance of O_2 has decreased by $1-2$ orders of magnitude below that of the Nominal Model at $\lesssim 90$ km altitude. Of particular importance is the sharp decrease in O_2 within the upper cloud layer (< 70 km) since that is the altitude region in which incident sunlight undergoes the greatest amount of multiple scattering off of the aerosol particles.

Setting the CO_2 cross sections at 202 K for 195 and 200 nm to zero decreases the photolysis of CO_2 at 75 - 80 km altitude, Figure 2.33. CO_2 photolysis increases again below 75 km because the atmospheric temperature is above 202 K so the cross sections at 195 and 200 nm are interpolated between the (zero) value at 202 K and the (non-zero) value at 298 K. This change is partly responsible for the decrease in

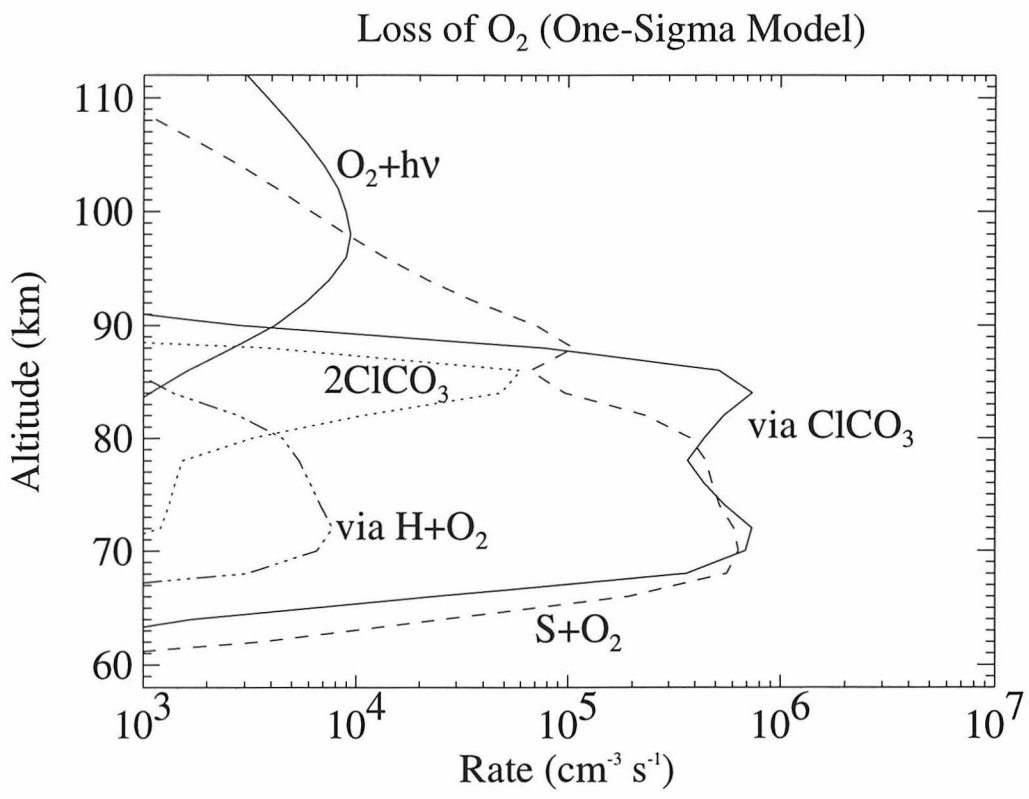

Figure 2.37: Primary reactions destroying O_2 in the One-Sigma Model.

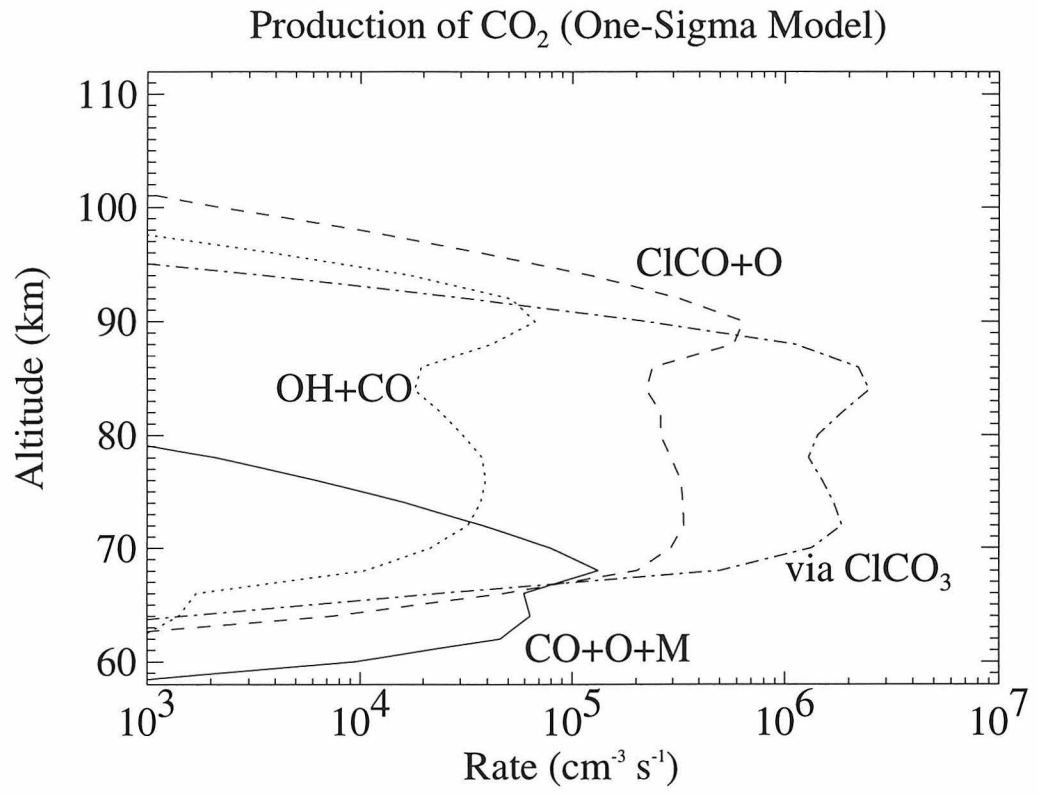

Figure 2.38: Primary reaction producing CO_2 in the One-Sigma Model.

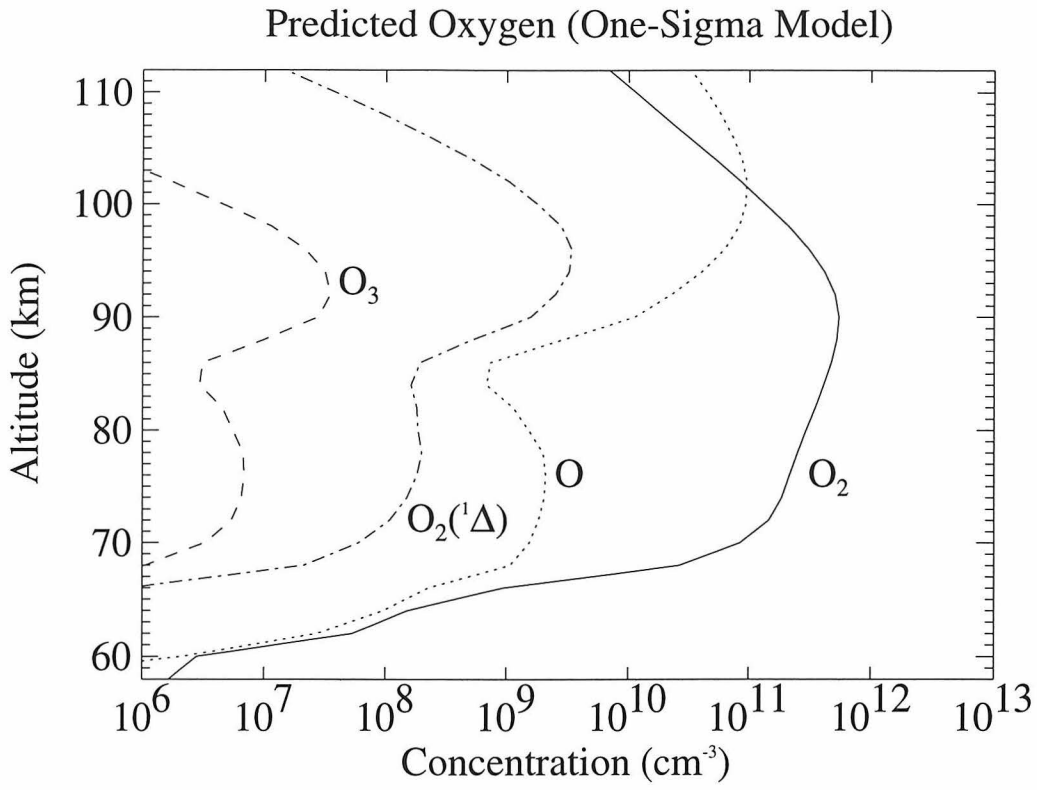

Figure 2.39: Predicted abundances of oxygen species in the One-Sigma Model.

the abundance of O and O_3 at $80 - 85$ km altitude, Figure 2.39.

Comparing these results to those for the nominal model (or those of *Yung and DeMore* [1982]) illustrates key differences between these models. This model accomplishes a larger fraction of the CO oxidation above 80 km altitude so the lower altitudes are so Cycle C17 is less important. This partially decouples the oxidation of CO from the oxidation of SO_2. This also extends the region of sulfate production to higher altitudes than in the Nominal Model (Figures 2.40 and 2.19) and enables the production of polysulfur above 65 km altitude.

$O_2(^1\Delta)$ Airglow

The primary parameters controlling the $O_2(^1\Delta)$ emission rate are (1) the quenching rates for CO_2 and N_2, (2) the lifetime for spontaneous emission of the excited

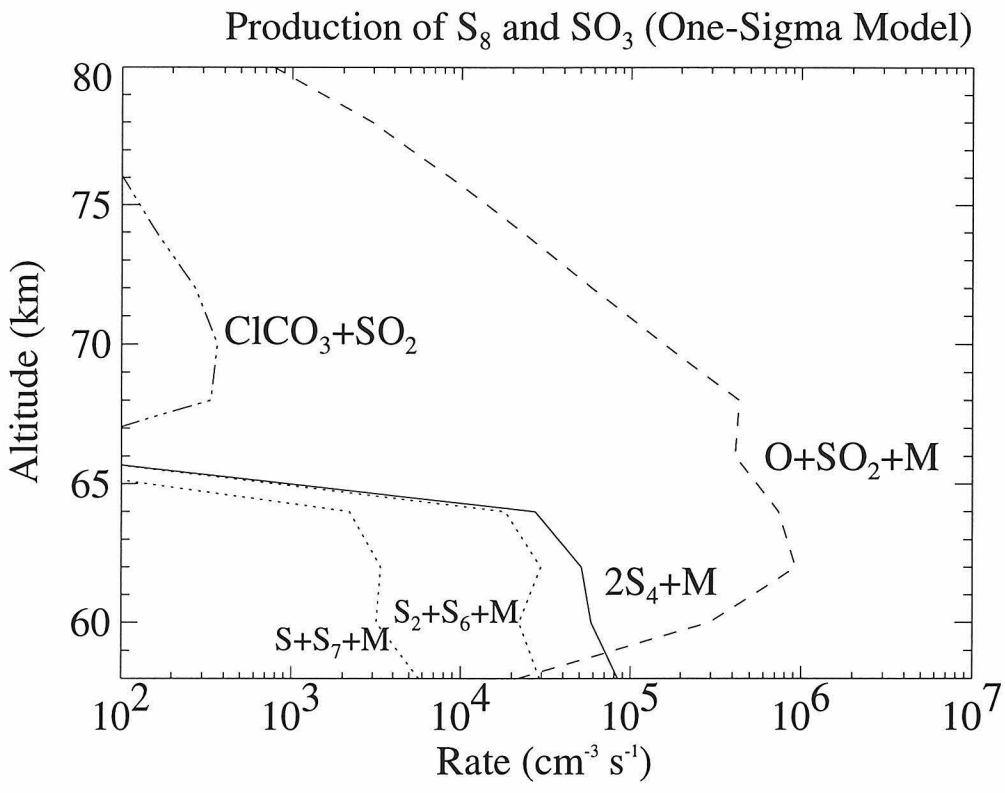

Figure 2.40: Primary reactions producing S_8 and SO_3 in the One-Sigma Model.

state, (3) the rate for Reaction G3, (4) the effective yield for producing the excited $O_2(^1\Delta)$ state from Reaction G3, (5) the relative efficiency for CO_2 as the third-body in Reaction G3, (6) production of $O_2(^1\Delta)$ from photolysis of O_3, (7) the flux of atomic oxygen through the top boundary of the model, and (8) the photolysis rate for CO_2. For this model:

(1) the effective yield of $O_2(^1\Delta)$ from Reactions K99, K98, K101 and K100 was increased to 0.75 (the estimated maximum value),

(2) the rate for Reactions K99 and K98 were increased by a factor of 1.3 (one estimated standard deviation),

(3) the rate for Reactions K101 and K100 were increased by a factor of 1.7 (one estimated standard deviation),

(4) the rates for reactions K202 and K203 were decreased to 2×10^{-21}, and

(5) the lifetime for the $O_2(^1\Delta)$ state was decreased by 10% (less than one standard deviation).

Production of $O_2(^1\Delta)$ via reaction G3 is about 20% larger than in the nominal model at $\gtrsim$ 90 km altitude (compare Figures 2.17 and 2.41). Production of $O_2(^1\Delta)$ via the Molina-Rowland cycle and photolysis of O_3 is significantly smaller than in the nominal model as a result of the smaller O_3 abundance. Collisional quenching of $O_2(^1\Delta)$ has been reduced to 25% of the airglow emission rate (Figure 2.42) and 20% of the collisional quenching is accomplished by atomic oxygen via Reaction K204.

As a result of these changes from the nominal model, the globally-averaged airglow emission rate is 1.1 MR, $\sim$ 15% smaller than the mean of the measured average dayside and nightside emission ($\sim$ 1.3 MR, Section 2.1.1). The airglow emission resulting from photolysis of O_3 in this model is 0.4 MR which is 30% larger than the dayside enhancement found by *Connes et al.* [1979] (0.3 MR).

Hydrogen-containing Species

The rates for the reactions that directly control the abundances of the HO_x species were not changed from the nominal model, but comparison of Figures 2.20 and 2.43 shows the HO_x abundances did change. These changes are largely a result of the smaller abundances of Cl, Cl_2, ClO, and O_2 below 80 km altitude so the HO_x loss

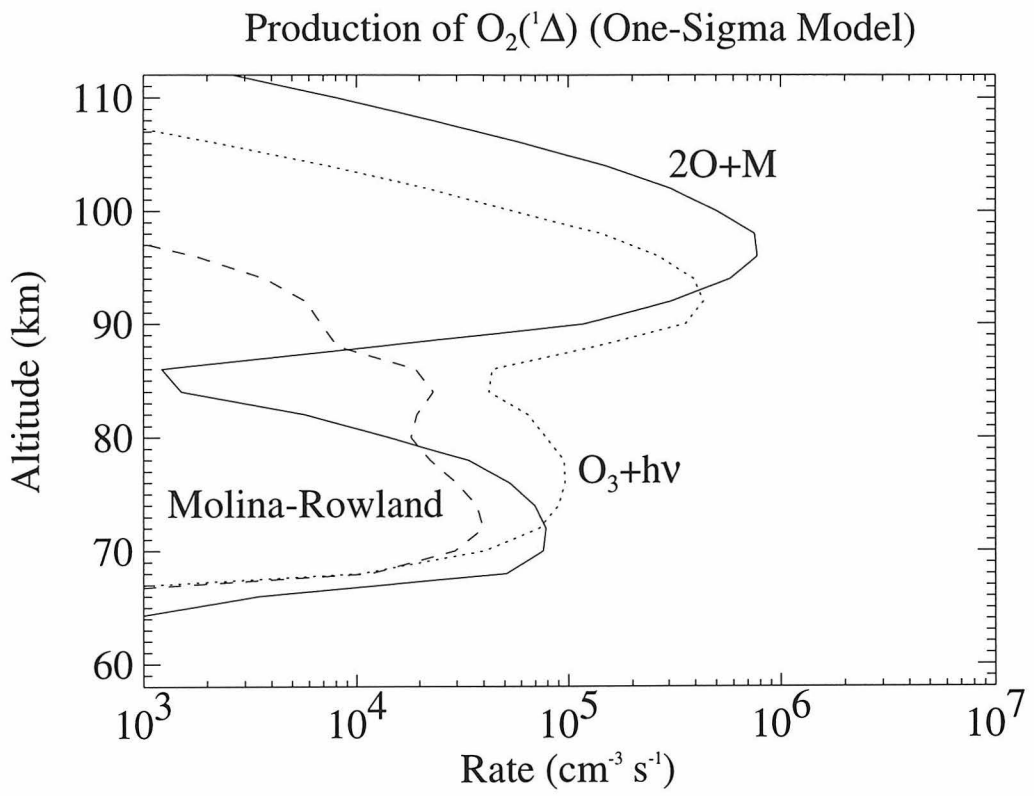

Figure 2.41: Primary reaction producing $O_2(^1\Delta)$ in the One-Sigma Model.

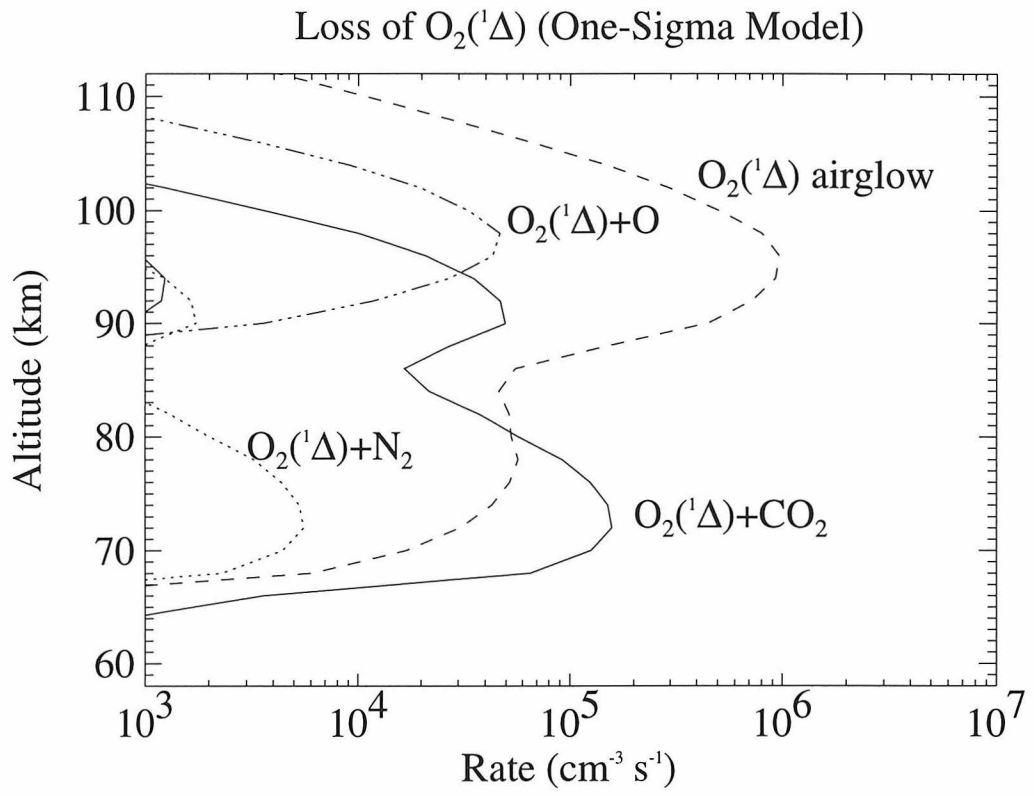

Figure 2.42: Primary reactions destroying $O_2(^1\Delta)$ in the One-Sigma Model.

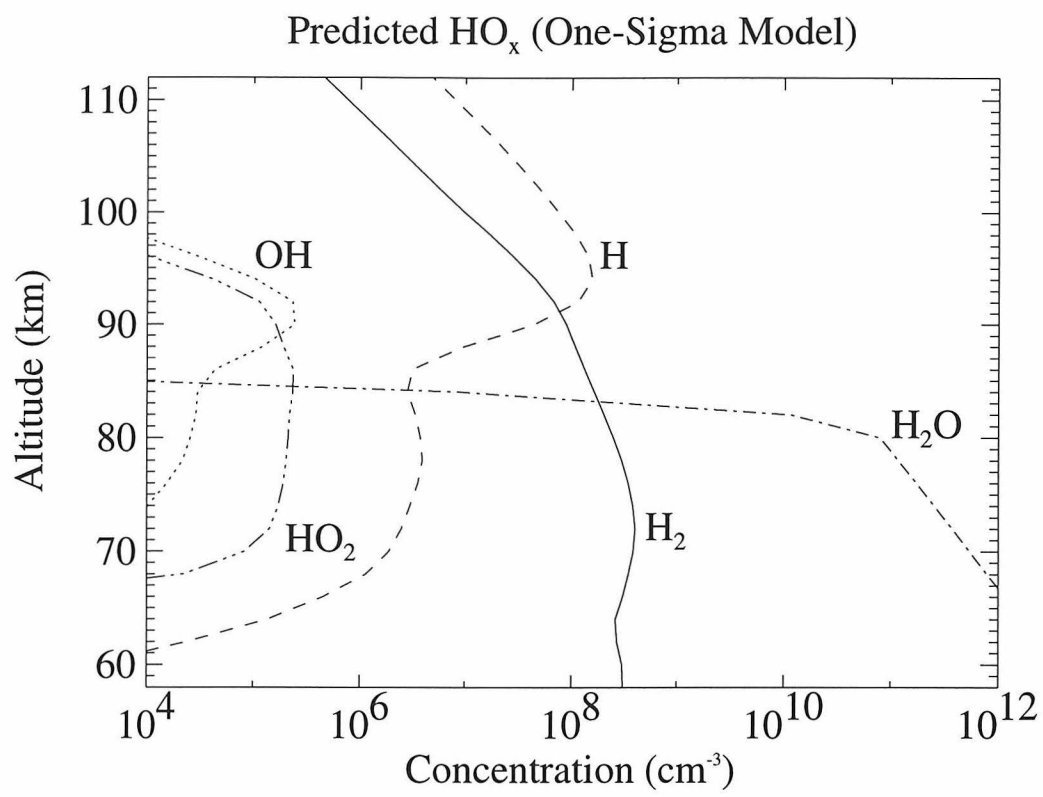

Figure 2.43: Predicted HO_x abundances in the One-Sigma Model.

rate (via conversion of HO_x to HCl) is slower than in the nominal model (Figures 2.44 and 2.22).

In the present model, the total hydrogen atom concentration at 100 km altitude is $\sim 3.8 \times 10^8$ cm^{-3}. Within the uncertainties associated with the previous models [*Krasnopol'sky and Parshev* 1983; *Fox and Bougher* 1991], the total hydrogen abundance at 100 km altitude in this model is consistent with the *Pioneer Venus* observations of H^+ and O^+ above 150 km altitude.

As discussed in Section 2.1.1, the abundance of H_2 in the Venus thermosphere is still not clear. The present model predicts an H_2 mixing ratio of 1×10^{-8} at $100 - 110$ km altitude, a factor of 10 smaller than the upper limit from *Kumar and Taylor* [1985].

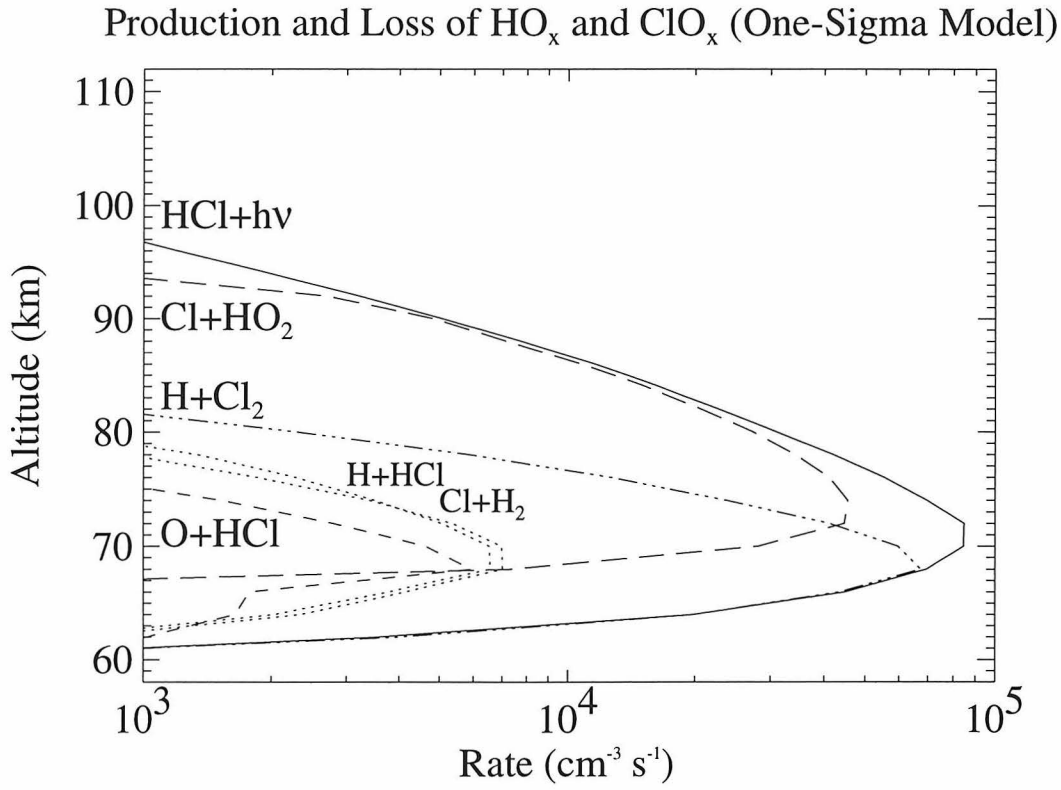

Figure 2.44: Primary reactions producing and destroying HO_x and ClO_x in the One-Sigma Model.

SO_x, OCS, and S_x

Sulfur species can play a significant role in sequestering oxygen via oxidation of SO_2 to SO_3 and subsequent formation of H_2SO_4. They also can play a significant role in splitting the O-O bond in O_2 so that CO can be oxidized to CO_2 via catalytic hydrogen or chlorine cycles. For this model:

(1) the estimated rates for Reactions K193 and K195 were set to 2×10^{-12}, the estimated rate for Reaction K194 was set to 5×10^{-12}, and the estimated rate for Reaction K196 was set to 5×10^{-13};

(2) the rates for reactions K153 and K154 were decreased to be a factor of two smaller than the nominal rate (one estimated standard deviation);

(3) the rate for reaction K160 was increased to be a factor of two larger than the nominal rate (less than one standard deviation);

(4) the estimated rate for Reaction K184 was set to 3×10^{-12}; and

(5) the estimated equilibrium constant for $(SO)_2$ was set to $1 \times 10^{-28} \exp(6000/T)$.

With the exception of doubling the rate for reaction K160, these changes decrease the rate at which SO_2 is oxidized to SO_3 by shifting sulfur from SO_2 to SO and $ClSO_2$. This was done to increase the SO_2 abundance at 70 km altitude. Increasing the mixing ratio for SO_2 at the lower boundary would probably have an equivalent effect. Decreasing the rates for reactions K153 and K154 and decreasing the stability of $(SO)_2$, both increase the SO abundance, particularly at $\sim 65 - 70$ km altitude where the retrieved SO profiles have maximum SO abundance.

Below $\sim$ 80 km altitude, the abundance of SO_2 (Figure 2.45) is controlled by reactions G11, K154, K194, and K168 (Figures 2.46, 2.47). Above 80 km altitude, the predicted SO_2 abundance is similar to that from the Nominal Model, but Reaction K255 has become an important source of SO_2. The importance of Reaction K255 near 85 km altitude also causes a decrease in the SO abundance (Figure 2.45). Above $\sim$ 90 km altitude, the abundance of $ClCO_3$ decreases rapidly and reactions G11 and K154 again become the primary reactions for destroying and producing SO_2. The oxygen in this model below $\sim$ 85 km altitude is depleted compared to the Nominal Model so the abundances of OCS and S_x are higher than in the Nominal Model at $65 - 75$

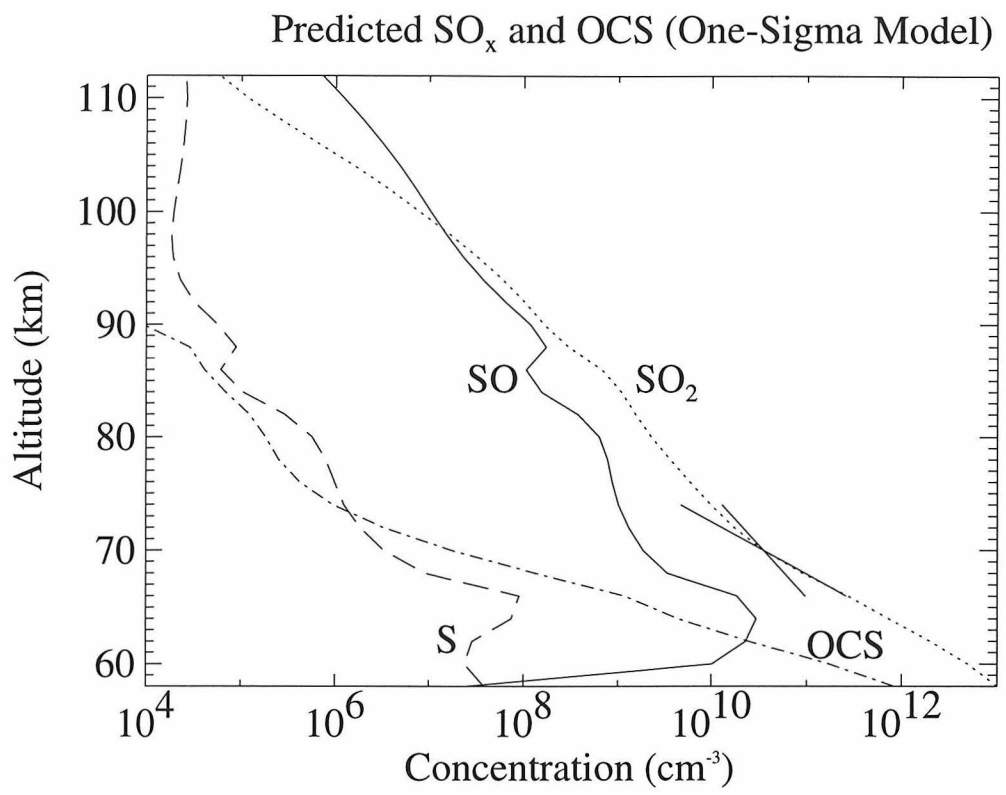

Figure 2.45: Predicted SO_x abundances in the One-Sigma Model. The short bars intersecting the predicted SO_2 profile near 70 km altitude represent the range of SO_2 scale heights inferred by *Na et al.* [1994] from the ultraviolet observations. The concentrations of S_2O and $(SO)_2$ are not shown on this plot because their maximum values in the One-Sigma Model are $\lesssim 5000$ cm^{-3}.

km altitude (Figures 2.45 and 2.48). Production rates for S_8 and SO_3 are shown in Figure 2.40.

The predicted SO profile has a similar shape to those retrieved from ultraviolet observations by *Na et al.* [1990], and *Na et al.* [1994], but the predicted SO abundances are smaller than the retrieved profiles. The predicted SO abundances are within two standard deviations of the retrieved profiles. The SO_2 abundance and scale height at 70 km altitude are within the range reported in *Na et al.* [1994] for the early 1980s (Figure 2.45).

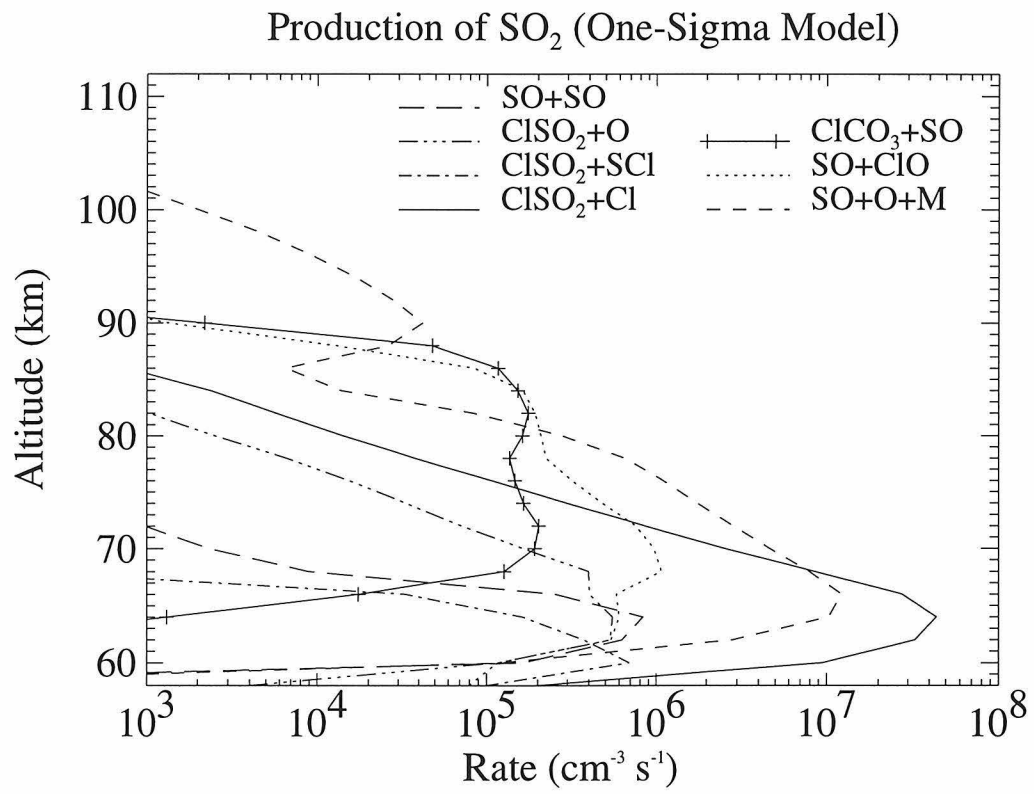

Figure 2.46: Primary reactions producing SO_2 in the One-Sigma Model.

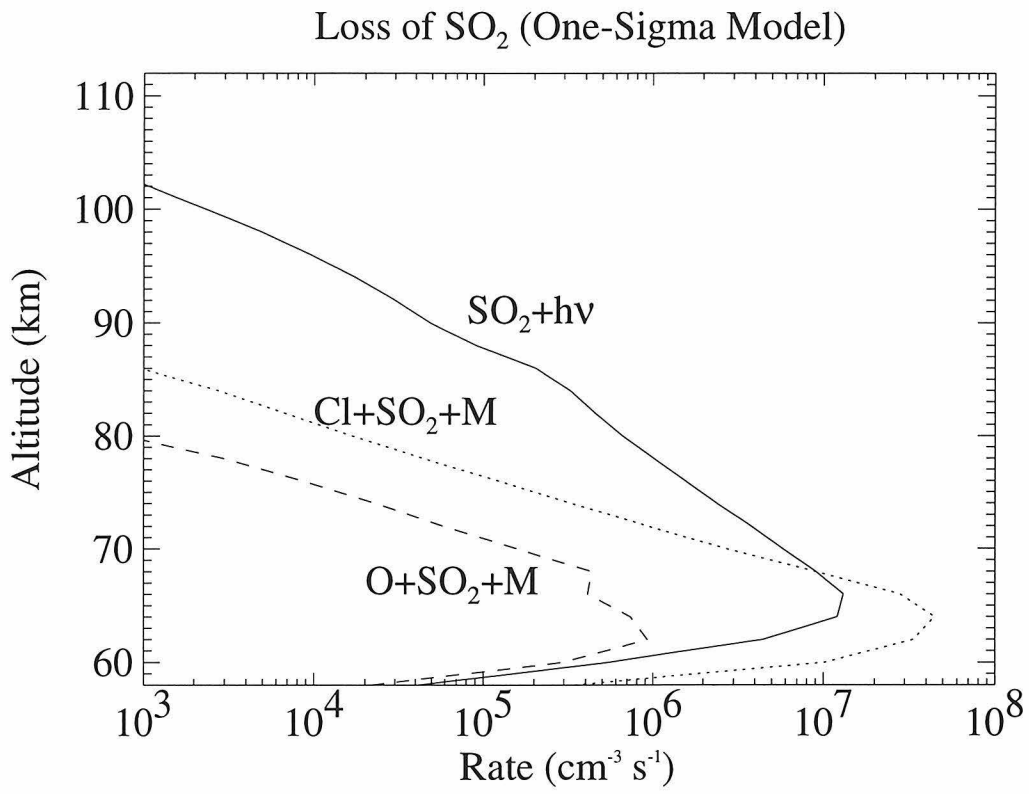

Figure 2.47: Primary reactions destroying SO_2 in the One-Sigma Model.

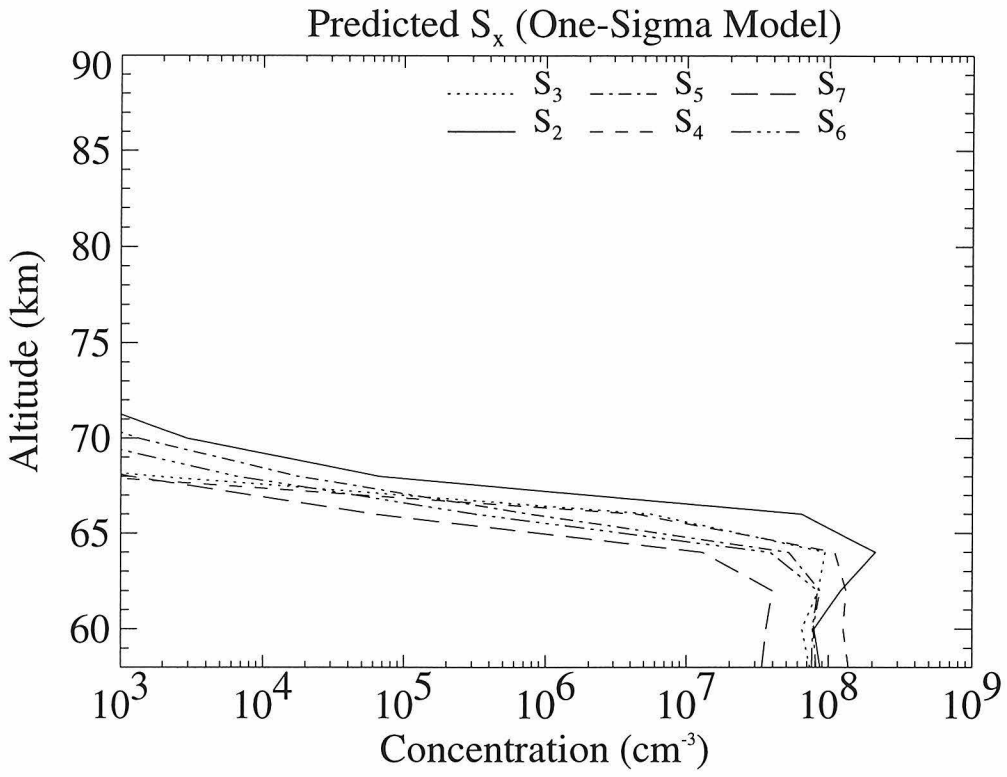

Figure 2.48: Predicted S_x abundances in the One-Sigma Model.

The production rate for SO_3 is $\sim 6 \times 10^{11}$ cm^{-2} s^{-1} which is a factor of $2 - 4$ smaller than in the *Yung and DeMore* [1982] models and is comparable to the SO_3 production rate in the Nominal Model.

The predicted OCS mixing ratio (Figure 2.45) is 2×10^{-11} which is three orders of magnitude smaller than the retrieved value for the cloud top, 10 ppb [*Bezard et al.* 1990]. The OCS transported up from the lower atmosphere is converted to CO and S_8 with a column production rate for S_8 of 6×10^{10} cm^{-2} s^{-1}, comparable to that in the Nominal Model.

Eddy Diffusion

The profile for the eddy diffusion coefficient is curve "Moderate" in Figure 2.8. The predicted CO profile above 95 km and below 80 km altitude is within the observed range although below 80 km altitude the predicted CO mixing ratio does not increase with altitude as in the retrieved profiles. At 80 - 95 km altitude the predicted CO profile is generally smaller than the smallest retrieved profile by one to two times the reported measurement uncertainty. These disagreements suggest the eddy diffusion coefficient below 80 km altitude is too large, but the predicted CO profile's shape lies midway between the average dayside and nightside CO profiles retrieved by *Gurwell et al.* [1995] for their 1988 observations so the predicted CO profile may not be unreasonable as a "global average."

The SO_2 scale height at 68 - 74 km altitude for this model is $\sim 2 - 3$ km (Figure 2.45) which lies within the range derived by *Na et al.* [1994] from UV observations of SO_2, $3(\pm 1)$ km. The predicted SO abundances for this model are generally smaller than the values retrieved from UV observations by *Na et al.* [1990] and *Na et al.* [1994], but the predictions from this model are within two standard deviations of the retrieved profiles.

2.3.3 Highest ClCO Stability Model

Increasing the equilibrium constant for ClCO by one standard deviation (from *DeMore et al.* [1997]) so that ClCO is more stable reduces the predicted O_2 abundance

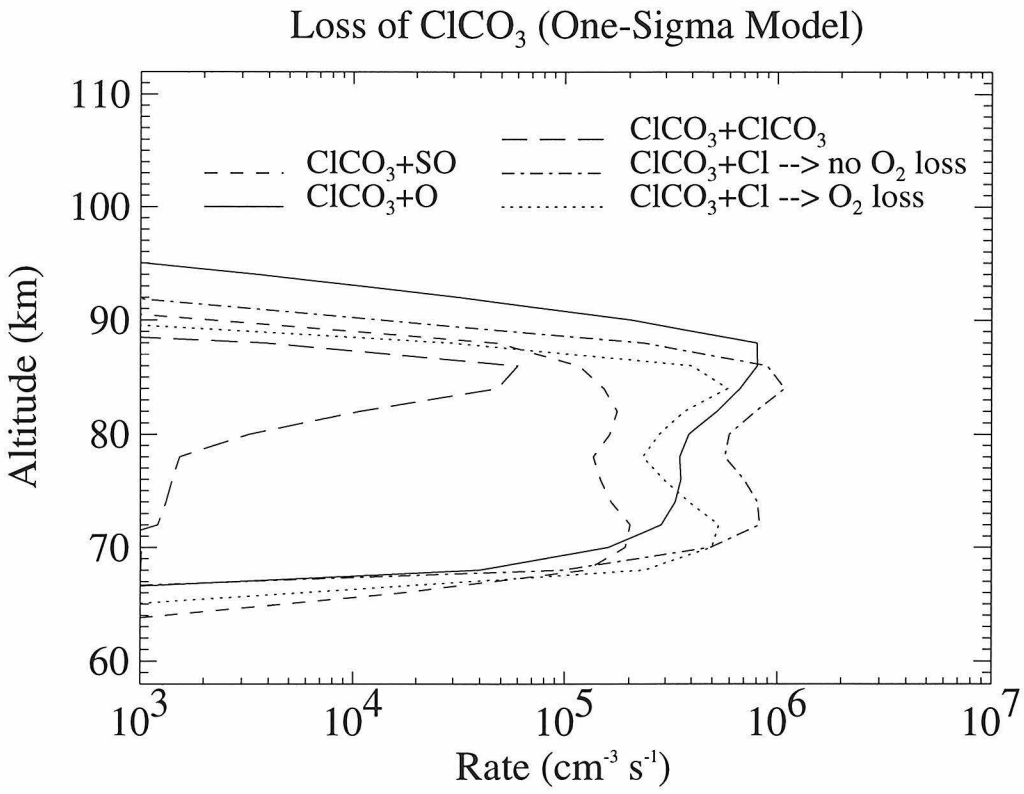

Figure 2.49: Primary reactions destroying $ClCO_3$ in the One-Sigma Model.

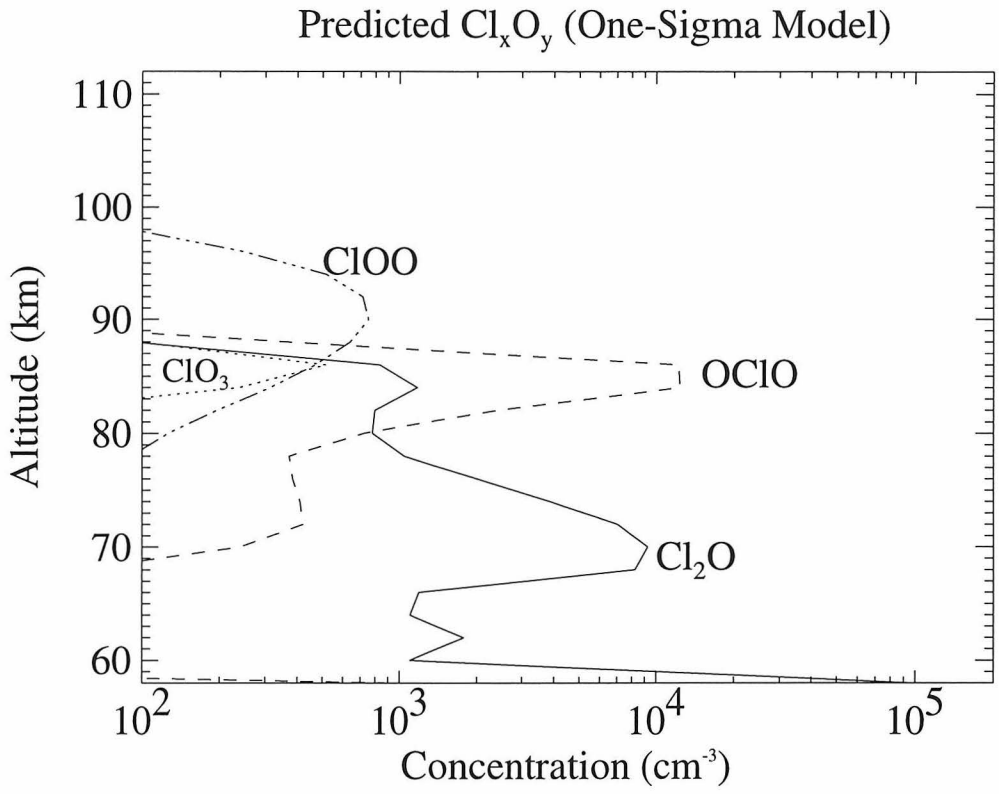

Figure 2.50: Predicted abundances for the higher oxides of chlorine (Cl_xO_y) in the One-Sigma Model.

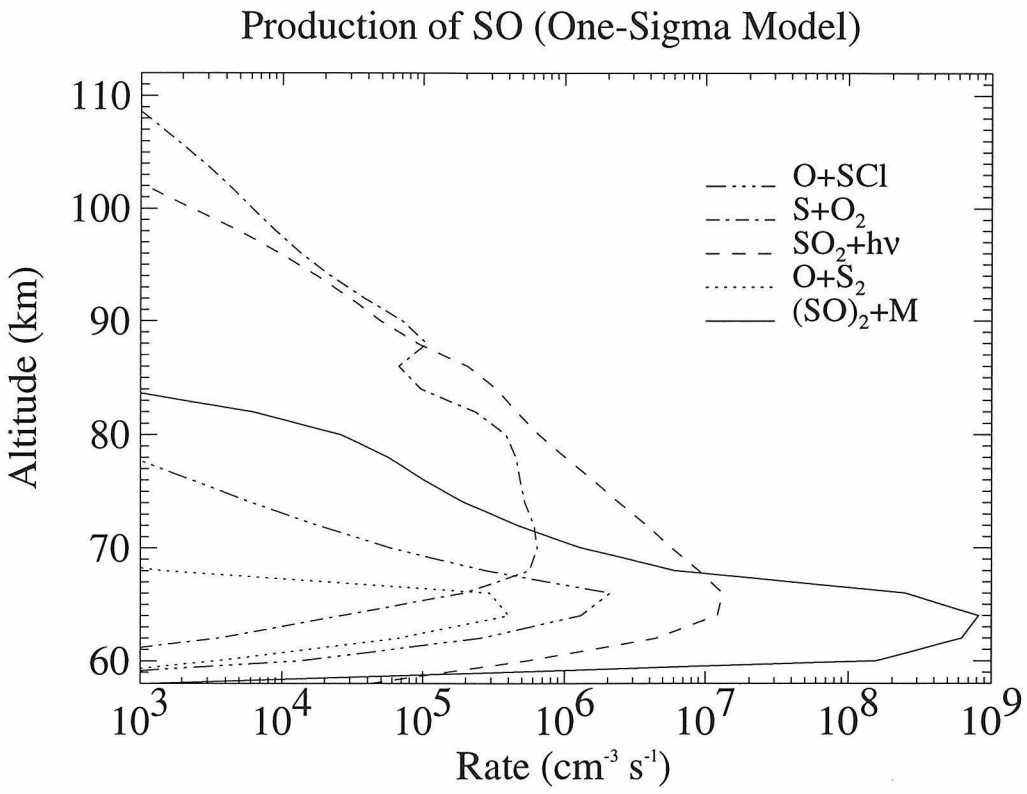

Figure 2.51: Primary reactions producing SO in the One-Sigma Model.

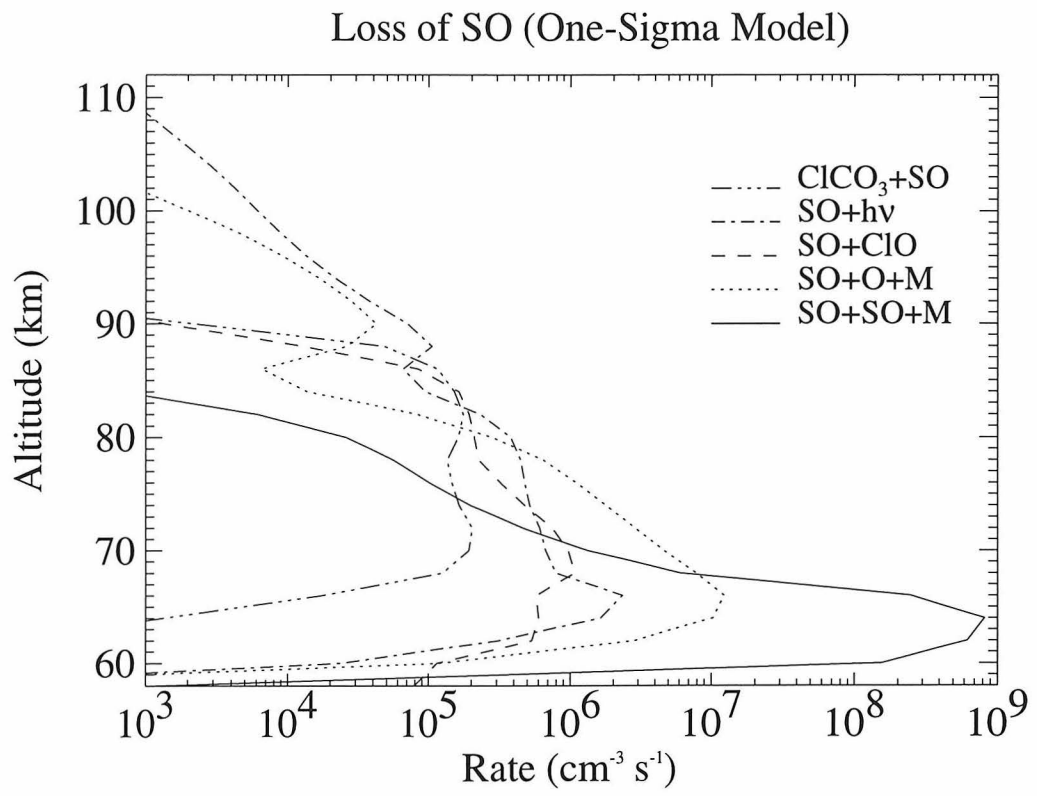

Figure 2.52: Primary reactions destroying SO in the One-Sigma Model.

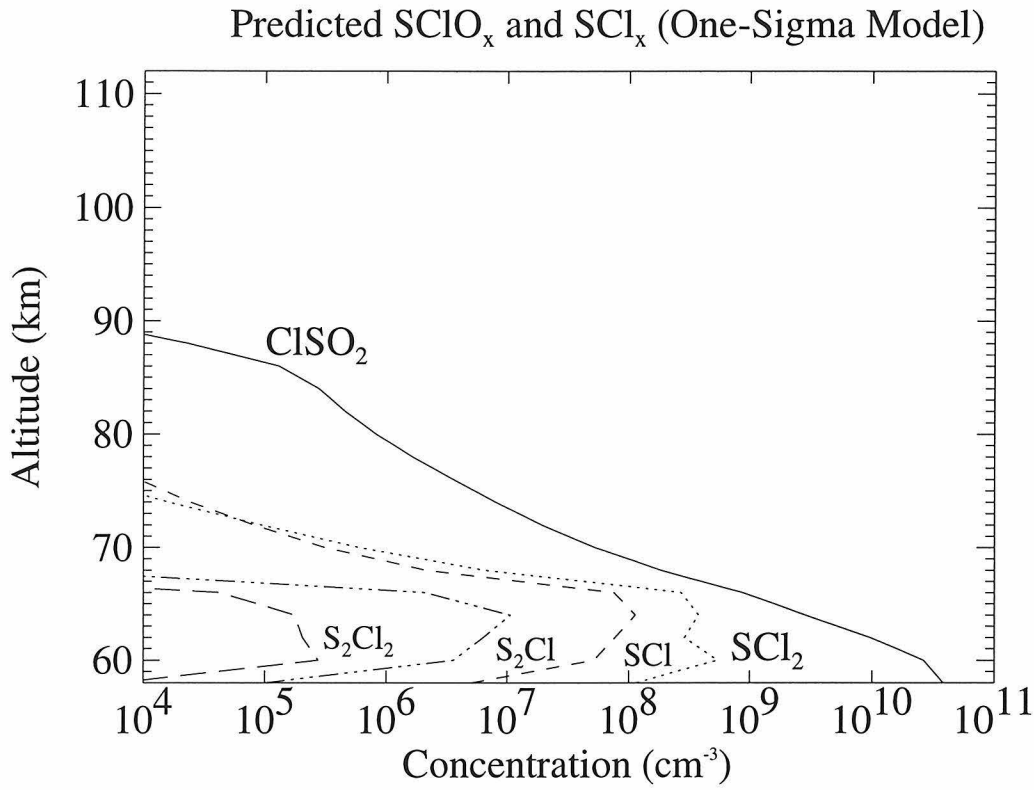

Figure 2.53: Predicted abundances of sulfur-chlorine species in the One-Sigma Model.

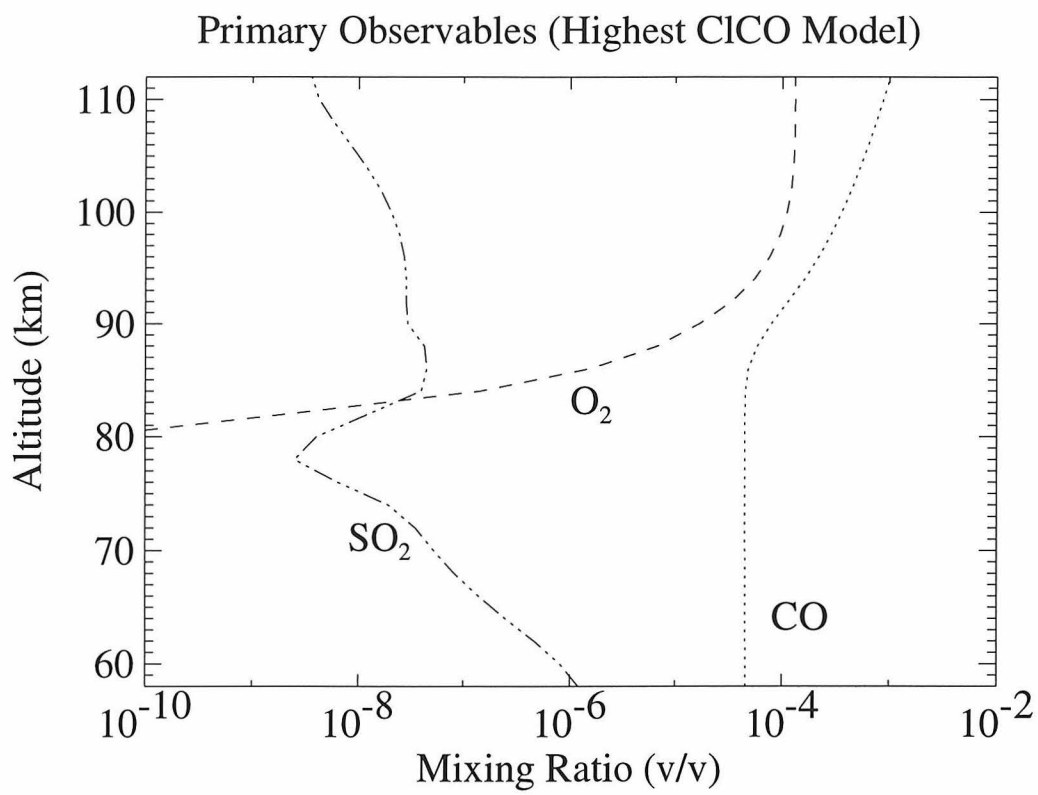

Figure 2.54: Predicted mixing ratios for CO, O_2, and SO_2 from the Highest ClCO Model are shown in the dotted, dashed, and dot-dashed lines, respectively.

compared to the nominal model. However, the column abundance of O_2 is still near the 2σ upper limit obtained by *Trauger and Lunine* [1983]. One method for further decreasing the O_2 abundance is to increase the stability of ClCO by more than one standard deviation. The model described in this section accomplishes this by increasing the equilibrium constant for ClCO by almost three (*DeMore et al.* [1997]) standard deviations and by decreasing the model atmosphere temperatures 10 - 25 K below those of the nominal model (estimated to be a $2 - 3\sigma$ change in the temperatures). This model also implements other changes to bring the predicted $O_2(^1\Delta)$ airglow emission and the predicted SO profile closer to the observed values. The predicted mixing ratios for CO_2, SO_2, and O_2 are shown in Figure 2.54.

ClO_x, $CClO_x$, and O_2

Our sensitivity studies found that the stability of the ClCO molecule has the greatest effect on the rate at which CO is oxidized to CO_2 and the column abundance of O_2. The stability of ClCO is determined by the heat of formation of ClCO and the atmospheric temperature. For this model:

(1) the equilibrium constant for ClCO was changed from curve "JPL97" in Figure 2.4 to curve "Maximum Used" (almost a three *DeMore et al.* [1997] standard deviation change from the *DeMore et al.* [1997] recommendation);

(2) the temperature profile was changed from the nominal value to curve "Cold" in Figure 2.5;

(3) the CO_2 dissociation cross section at 195 and 200 nm was set to zero at 202 K and the CO_2 dissociation cross section at 200 and 205 nm at 298 K was divided by two (compared to the nominal model) to minimize the production rate for oxygen (Figure 2.55); and

(4) the rate for reaction K178 was increased by a factor of 4 $\exp(500/T)$ (estimated to be two standard deviations from the nominal value).

As a result of the changes in the stability of ClCO, the Cl abundance in this model (Figure 2.56) is a factor of 3 smaller than in the nominal model at $70-80$ km altitude and the ClCO abundance at these altitudes (Figure 2.57) is a factor of $\sim$ 50 larger than in the nominal model. At 80 - 90 km altitude, Cl has been shifted by a factor of < 2 from Cl and ClCO to $ClCO_3$.

These changes in the partitioning of chlorine have four effects on oxygen abundances. First, the smaller abundance of Cl decreases the effectiveness of the Molina-Rowland cycle, Cycle C13, so atomic oxygen is converted to O_2 at a slower rate than in the nominal model (compare Figures 2.15 and 2.58). Second, the larger abundances of ClCO and $ClCO_3$ increase the rate at which CO is oxidized to CO_2 so oxygen is sequestered in CO_2 at higher altitudes than in the nominal model (compare Figures 2.16 and 2.10 to Figures 2.59 and 2.60). Third, the dominant mechanism for production of CO_2 has changed so that Cycle C17 is not as important as in the nominal model. Instead, reaction K179 has become important (Figures 2.60 and 2.61).

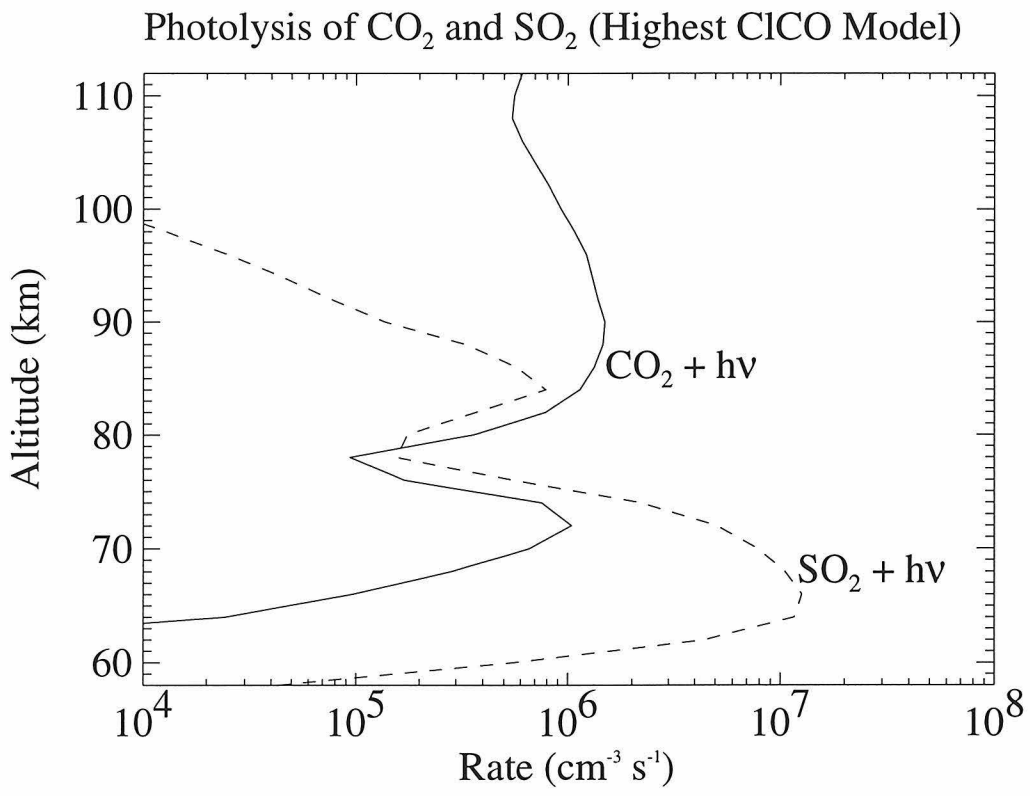

Figure 2.55: Photolysis of CO_2 and SO_2 in the Highest ClCO Model.

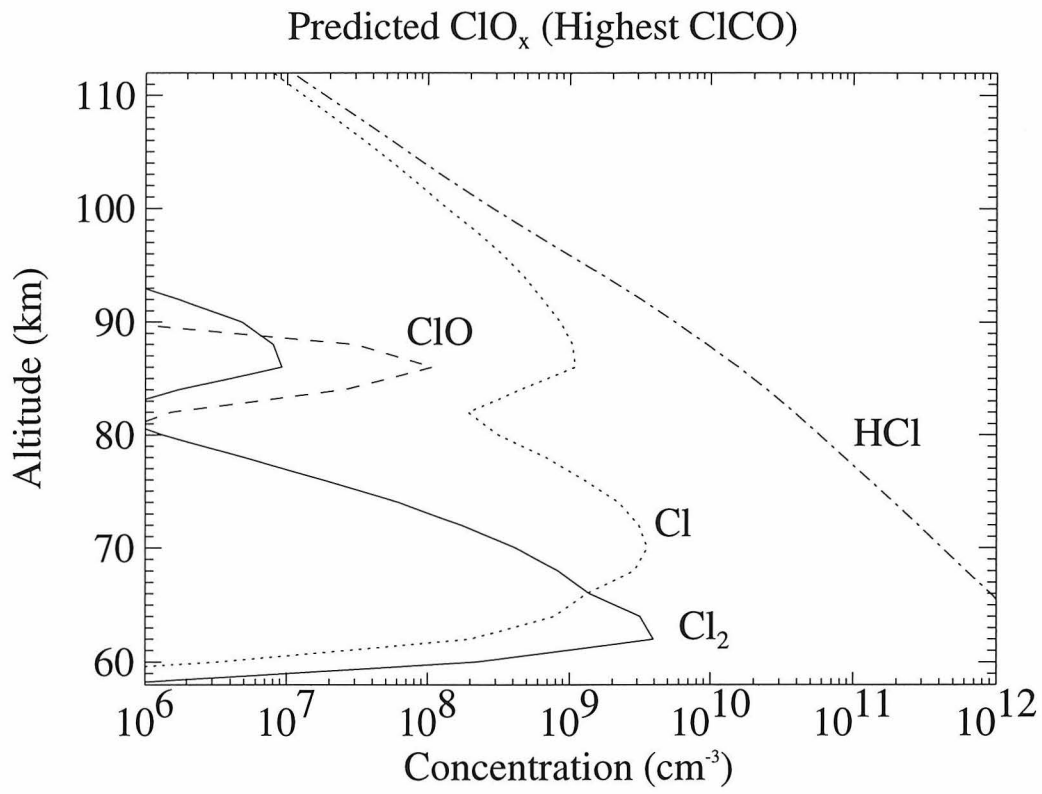

Figure 2.56: Predicted ClO_x abundances in the Highest ClCO Model.

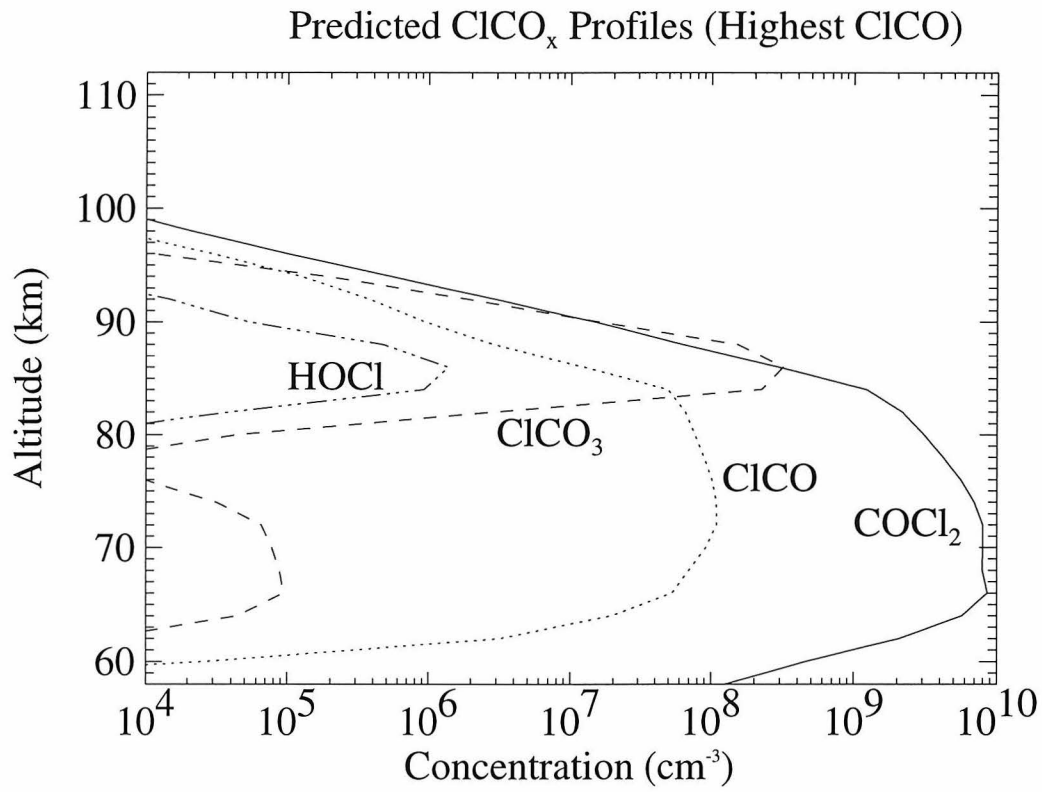

Figure 2.57: Predicted abundances for $CClO_x$) in the Highest ClCO Model.

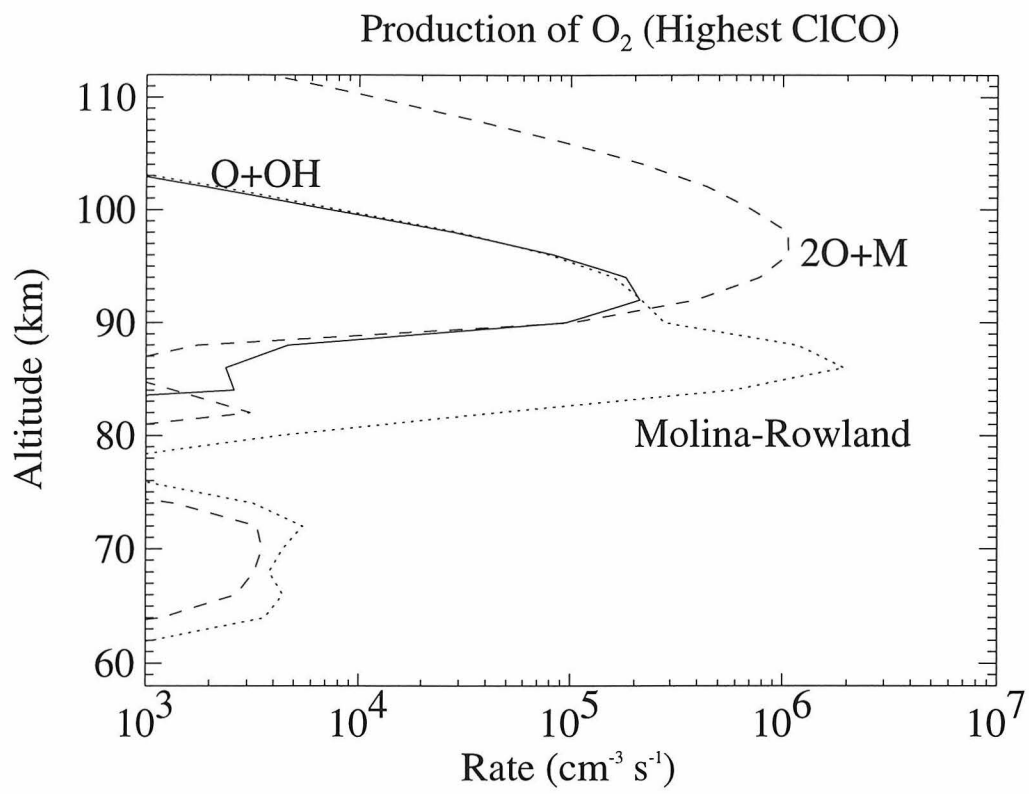

Figure 2.58: Primary reaction producing O_2 in the Highest ClCO Model.

Fourth, production of CO_2 has moved to a sufficiently high altitude that there is a net flux *downward* of CO_2 across the lower boundary.

Setting the CO_2 cross sections at 202 K for 195 and 200 nm to zero decreases the photolysis of CO_2 at 75 - 80 km altitude, Figure 2.55. CO_2 photolysis increases again below 75 km because the atmospheric temperature is above 202 K so the cross sections at 195 and 200 nm are interpolated between the (zero) value at 202 K and the (non-zero) value at 298 K. These changes are also partly responsible for the sharp decrease in the abundance of O_2 at 75 - 80 km altitude, Figure 2.62.

Comparing these results to those for the nominal model (or those of *Yung and DeMore* [1982]) illustrates key differences between these models. This model accomplishes a majority of the CO oxidation above 80 km altitude so the lower altitudes are

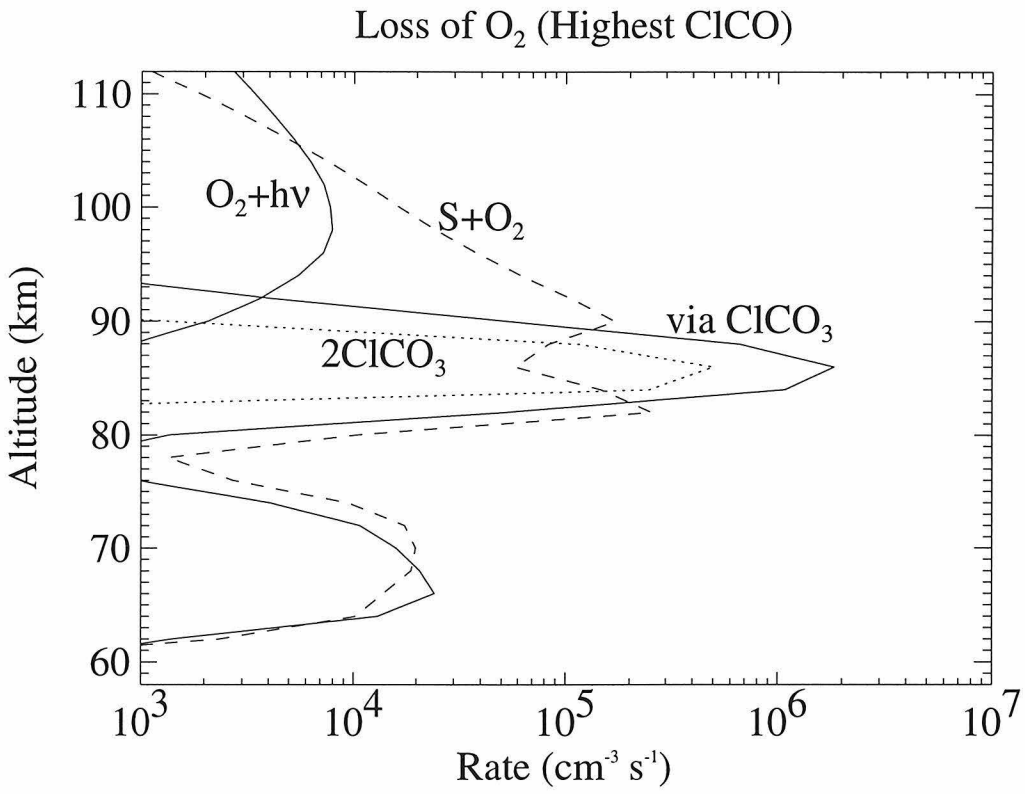

Figure 2.59: Primary reactions destroying O_2 in the Highest ClCO Model.

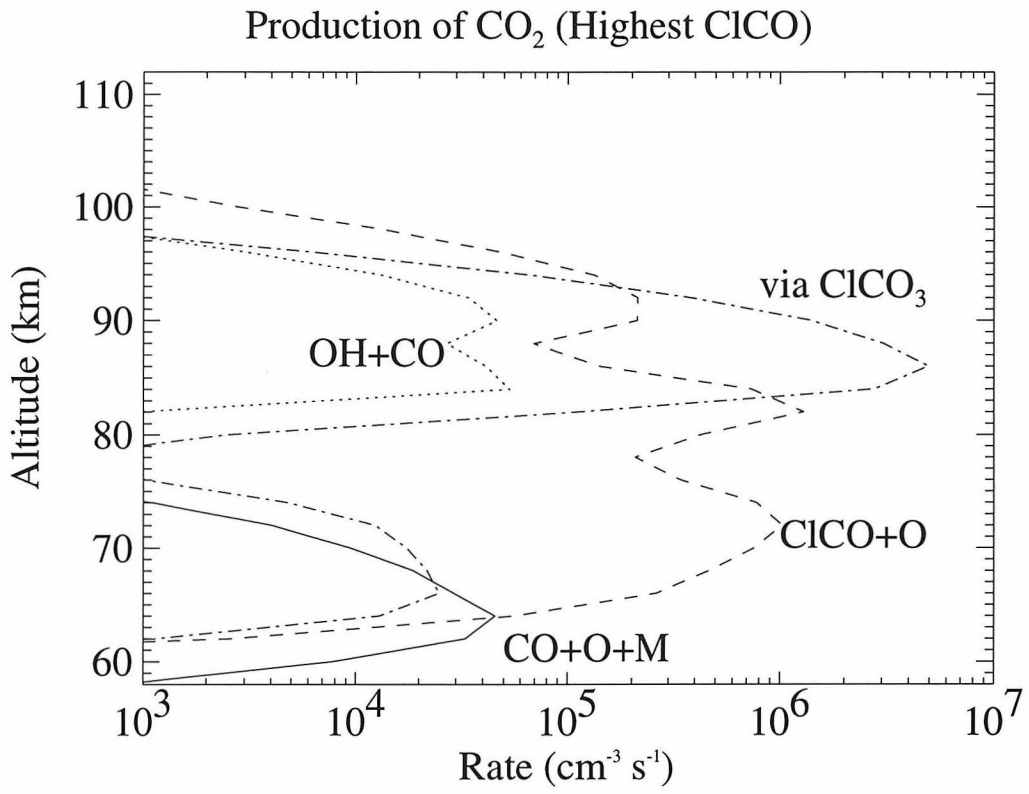

Figure 2.60: Primary reaction producing CO_2 in the Highest ClCO Model.

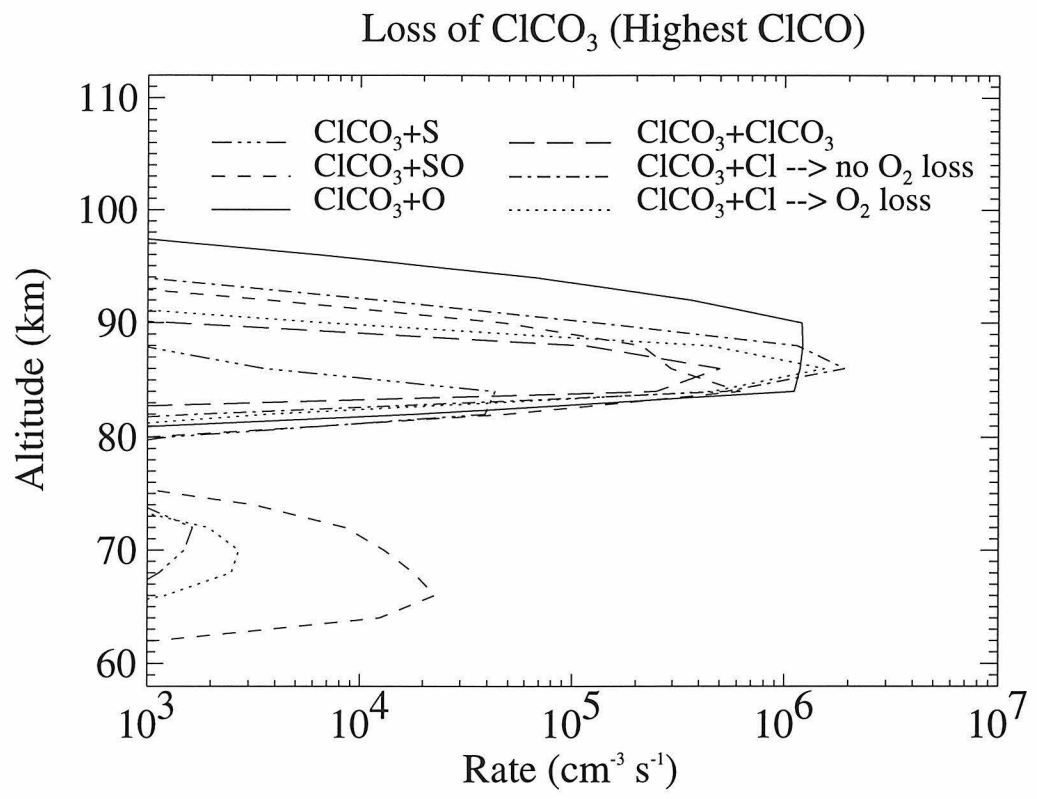

Figure 2.61: Primary reactions destroying $ClCO_3$ in the Highest ClCO Model.

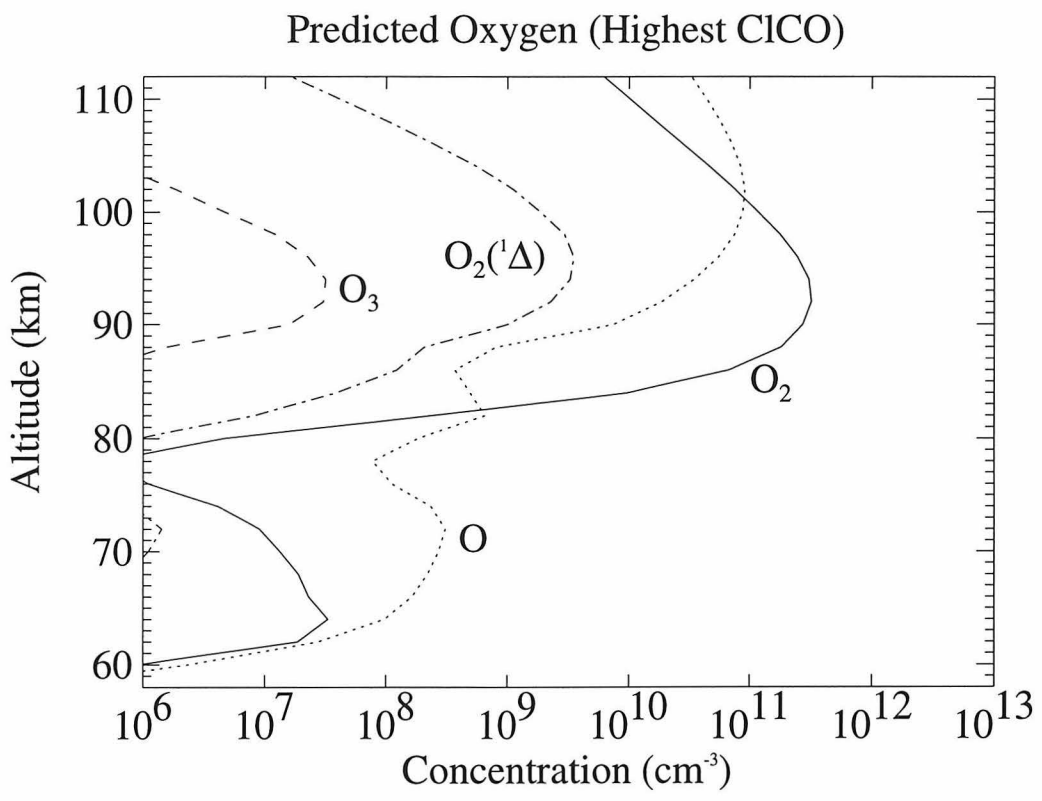

Figure 2.62: Predicted abundances of oxygen species in the Highest ClCO Model.

comparatively reducing. The nominal model (and those of *Yung and DeMore* [1982]) relied heavily on cycle C17 in which oxidation of CO and production of SO_3 are tightly coupled. The actual photochemistry in the Venus middle atmosphere likely lies between these two extremes, but the small upper limit on the abundance of O_2 and the comparatively weak eddy diffusion near the cloud top suggest oxidation of CO to CO_2 occurs predominantly above $\sim$ 75 km altitude.

$O_2(^1\Delta)$ Airglow

The primary parameters controlling the $O_2(^1\Delta)$ emission rate are (1) the quenching rates for CO_2 and N_2, (2) the lifetime for spontaneous emission of the excited state, (3) the rate for Reaction G3, (4) the effective yield for producing the excited $O_2(^1\Delta)$ state from Reaction G3, (5 the relative efficiency for CO_2 as the third-body in Reaction G3, (6) production of $O_2(^1\Delta)$ from photolysis of O_3, (7) the flux of atomic oxygen through the top boundary of the model, and (8) the photolysis rate for CO_2. For this model:

(1) the effective yield of $O_2(^1\Delta)$ from Reactions K99, K98, K101, and K100 was increased to 0.75 (the estimated maximum value),

(2) the rate for Reactions K99 and K98 were increased by a factor of 1.3 (one estimated standard deviation),

(3) the rate for Reactions K101 and K100 were increased by a factor of 1.7 (one estimated standard deviation),

(4) the rates for Reactions K202 and K203 were decreased to 2×10^{-21}, and

(5) the lifetime for the $O_2(^1\Delta)$ state was decreased by 10% (less than one standard deviation).

Production of $O_2(^1\Delta)$ via reaction G3 is a factor of $\lesssim 2$ larger than in the nominal model at $\gtrsim$ 90 km altitude (compare Figures 2.17 and 2.63). Production of $O_2(^1\Delta)$ via the Molina-Rowland cycle and photolysis of O_3 is significantly smaller than in the nominal model as a result of the smaller Cl and O_3 abundances. Collisional quenching of $O_2(^1\Delta)$ has been reduced to 8% of the airglow emission rate (Figure 2.64) and one-half of the collisional quenching is accomplished by atomic oxygen via Reaction K204.

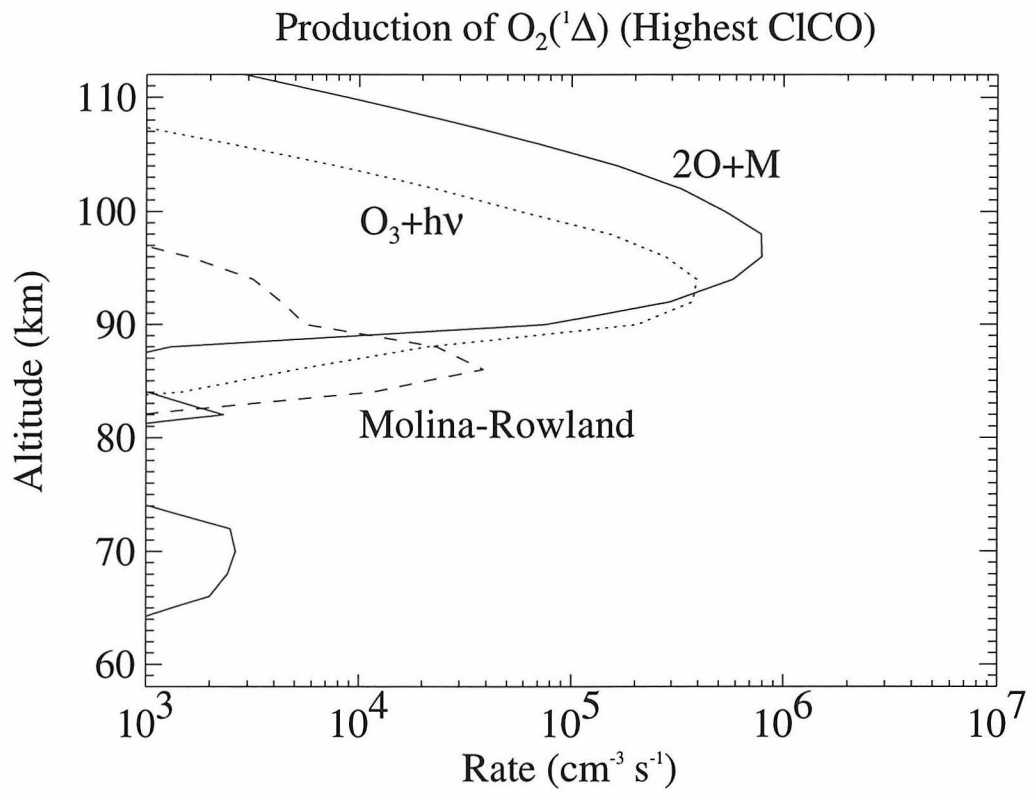

Figure 2.63: Primary reaction producing $O_2(^1\Delta)$ in the Highest ClCO Model.

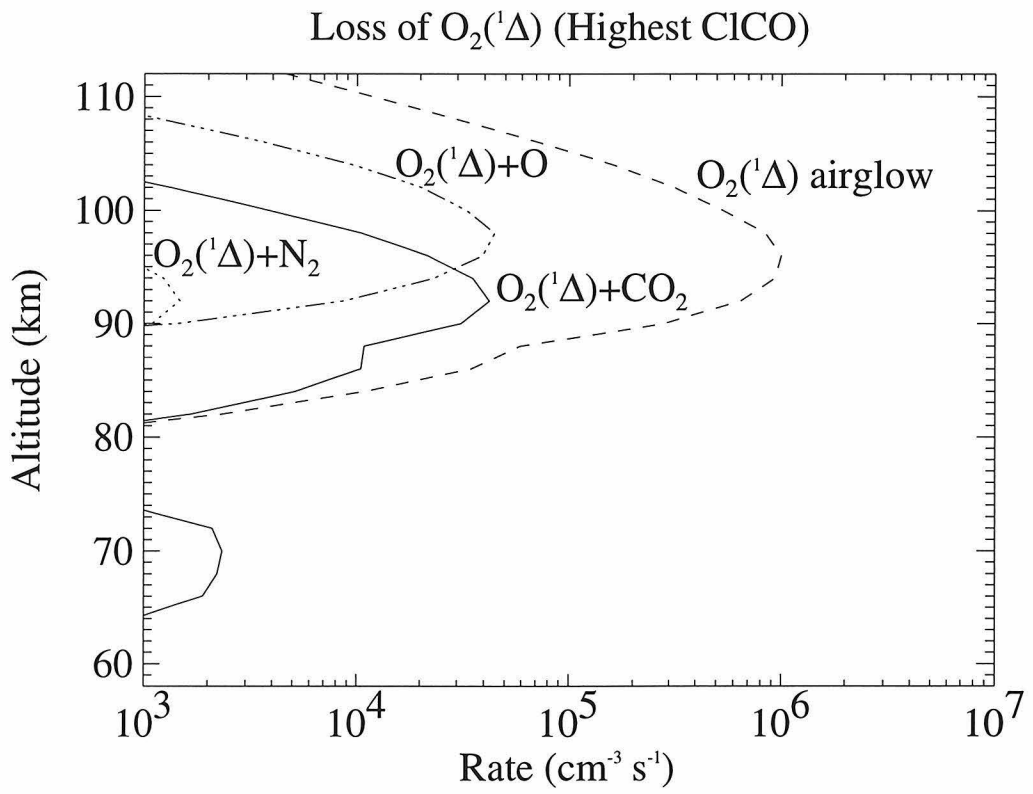

Figure 2.64: Primary reactions destroying $O_2(^1\Delta)$ in the Highest ClCO Model.

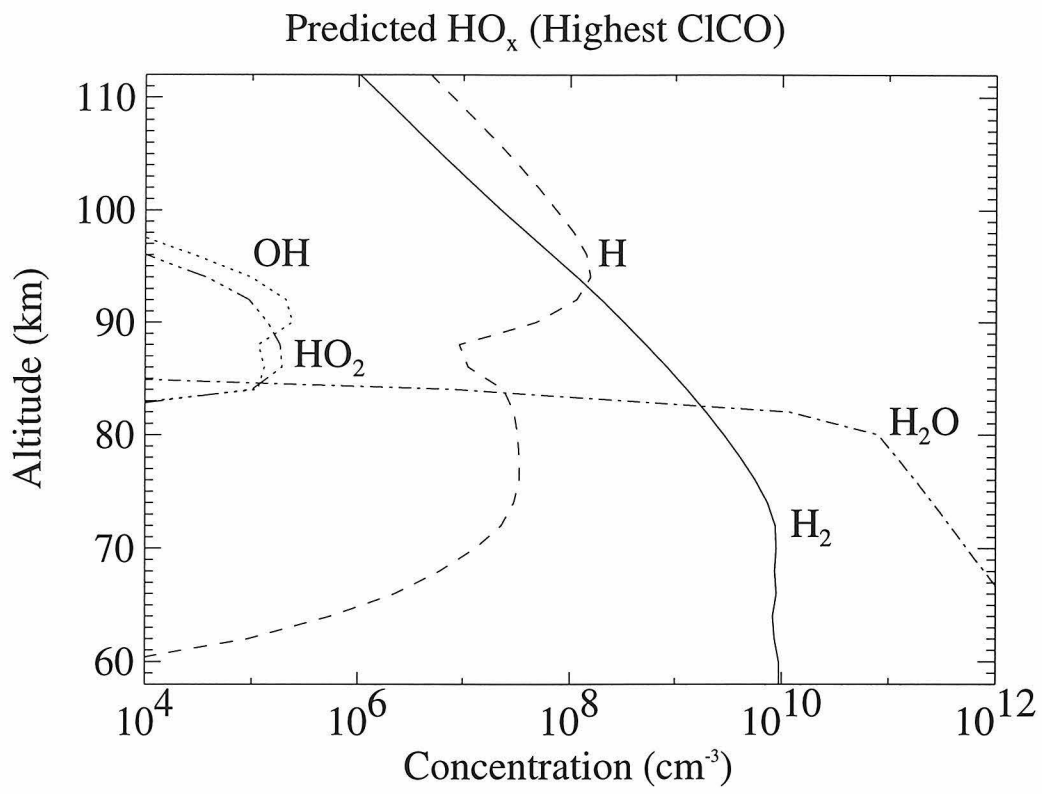

Figure 2.65: Predicted HO_x abundances in the Highest ClCO Model.

As a result of these changes from the nominal model, the globally-averaged airglow emission rate is 1 MR, $\sim$ 25% smaller than the mean of the measured average dayside and nightside emission ($\sim$ 1.3 MR, Section 2.1.1). The airglow emission resulting from photolysis of O_3 in this model is 0.3 MR which agrees with the dayside enhancement found by *Connes et al.* [1979] (0.3 MR).

Hydrogen-containing Species

The rates for the reactions that directly control the abundances of the HO_x species were not changed from the nominal model, but comparison of Figures 2.20 and 2.65 shows the HO_x abundances did change. These changes are largely a result of the smaller abundances of Cl, Cl_2, and O_2 below 80 km altitude so the HO_x loss rate (via conversion of HO_x to HCl) is slower than in the nominal model.

In the present model, the total hydrogen atom concentration at 100 km altitude is $\sim 3.9 \times 10^8$ cm^{-3}. Within the uncertainties associated with the previous models [*Krasnopol'sky and Parshev* 1983; *Fox and Bougher* 1991], the total hydrogen abundance at 100 km altitude in this model is consistent with the *Pioneer Venus* observations of H^+ and O^+ above 150 km altitude.

As discussed in Section 2.1.1, the abundance of H_2 in the Venus thermosphere is still not clear. The present model predicts an H_2 mixing ratio of 2×10^{-8} at $100 - 110$ km altitude, a factor of 5 smaller than the upper limit from *Kumar and Taylor* [1985].

SO_x, OCS, and S_x

Sulfur species can play a significant role in sequestering oxygen via oxidation of SO_2 to SO_3 and subsequent formation of H_2SO_4. They also can play a significant role in splitting the O-O bond in O_2 so that CO can be oxidized to CO_2 via catalytic hydrogen or chlorine cycles. For this model:

(1) the estimated rates for reactions K193 and K195 were set to 2×10^{-12}, the estimated rate for reaction K194 was set to 5×10^{-12}, and the estimated rate for reaction K196 was set to zero;

(2) the rates for reactions K153 and K154 were decreased to a factor of two smaller than the nominal rate (one estimated standard deviation);

(3) the rate for reaction K160 was increased to a factor of two larger than the nominal rate (less than one standard deviation);

(4) the estimated rate for Reaction K184 was set to 3×10^{-12}; and

(5) the estimated equilibrium constant for $(SO)_2$ was set to $1 \times 10^{-28} \exp(6000/T)$.

With the exception of doubling the rate for reaction K160, these changes decrease the rate at which SO_2 is oxidized to SO_3 by shifting sulfur from SO_2 to SO and $ClSO_2$. This was done to increase the SO_2 abundance at 70 km altitude. Increasing the mixing ratio for SO_2 at the lower boundary would probably have an equivalent effect. Decreasing the rates for reactions K153 and K154 and decreasing the stability of $(SO)_2$, both increase the SO abundance, particularly at $\sim 65 - 70$ km altitude where the retrieved SO profiles have maximum SO abundance.

Below $\sim$ 80 km altitude, the abundance of SO_2 (Figure 2.66) is controlled by

reactions G11, K154, K193, K194, and K168 (Figures 2.67, 2.68). Above 80 km altitude, the predicted SO_2 mixing ratio increases significantly as reactions K165 and K255 become important. The importance of reaction K255 at these altitudes also causes a significant decrease in the SO abundance at $\sim 85 - 90$ km altitude (Figure 2.66). Above ~ 90 km altitude, the abundance of $ClCO_3$ decreases rapidly and reactions G11 and K154 again become the primary reactions for destroying and producing SO_2. The oxygen in this model below ~ 85 km altitude is sufficiently depleted that significant abundances of OCS and S_x are predicted (Figures 2.66 and 2.72). Production rates for S_8 and SO_3 are shown in Figure 2.71.

The predicted SO profile is within the range defined by the retrieved SO profiles from *Na et al.* [1990], and *Na et al.* [1994], and the SO_2 abundance and scale height at 70 km altitude are within the range reported in *Na et al.* [1994] for the early 1980s (Figure 2.66).

The production rate for SO_3 is $\sim 4 \times 10^{11}$ cm^{-2} s^{-1} which is a factor of $3 - 5$ smaller than in the *Yung and DeMore* [1982] models and is 70% of the SO_3 production rate in the Nominal Model. This occurs because oxidation of CO to CO_2 occurs at higher altitudes in this model so there is less oxygen available in the upper cloud layer for oxidizing SO_2 to SO_3. As a result of this increase in the effective altitude at which CO is oxidized, the chlorine-catalyzed oxidation of CO and the production of SO_3 are decoupled in the present model.

The predicted OCS abundance (Figure 2.66) is close to the retrieved value for the cloud top, 10 ppb [*Bezard et al.* 1990], but the predicted OCS abundances at higher altitudes are probably larger than would be permitted by the observations. The OCS above 70 km altitude is primarily transported upward from lower altitudes. This suggests the eddy diffusion coefficient at $\lesssim 70$ km altitude may be too large. The OCS transported up from the lower atmosphere is converted to CO and S_8. The column production rate for S_8 is $\sim 1 \times 10^{11}$ cm^{-2} s^{-1}, which is a factor of two larger than in the Nominal Model.

The predicted S_x abundances above 70 km altitude (Figure 2.72) are also probably larger than would be permitted by observations, although there has been no

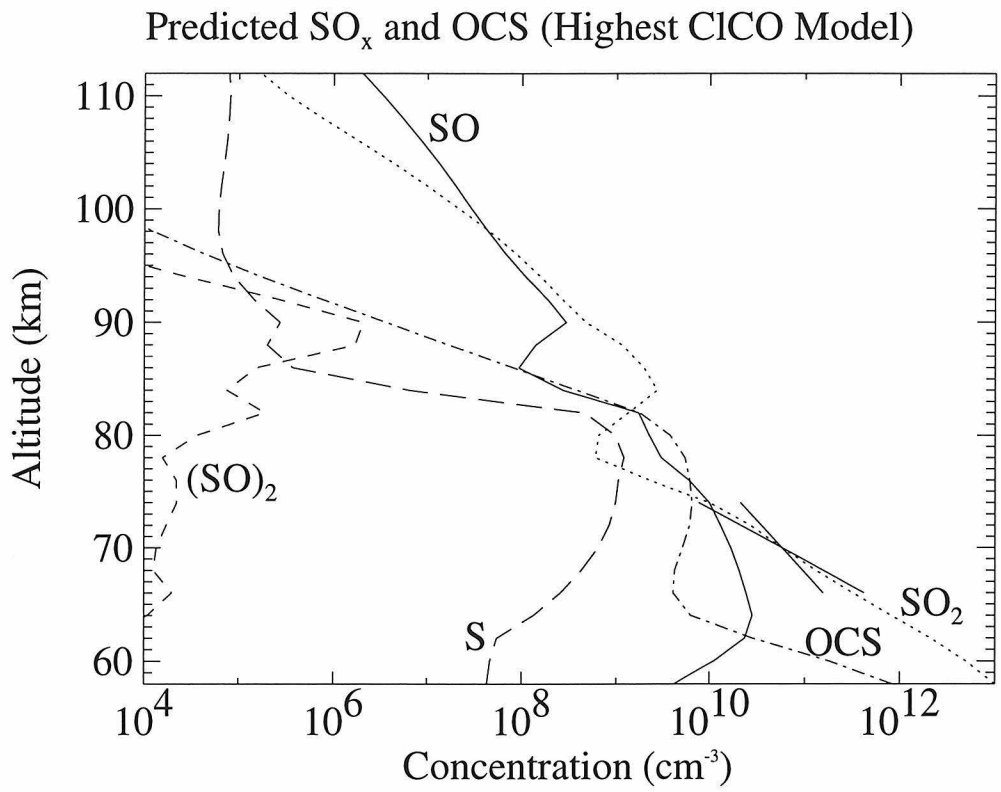

Figure 2.66: Predicted SO_x abundances in the Highest ClCO Model. The short bars intersecting the predicted SO_2 profile near 70 km altitude represent the range of SO_2 scale heights inferred by *Na et al.* [1994] from ultraviolet observations. The concentration of S_2O is not shown on this plot because its maximum value in the Highest ClCO Model is < 5000 cm^{-3}.

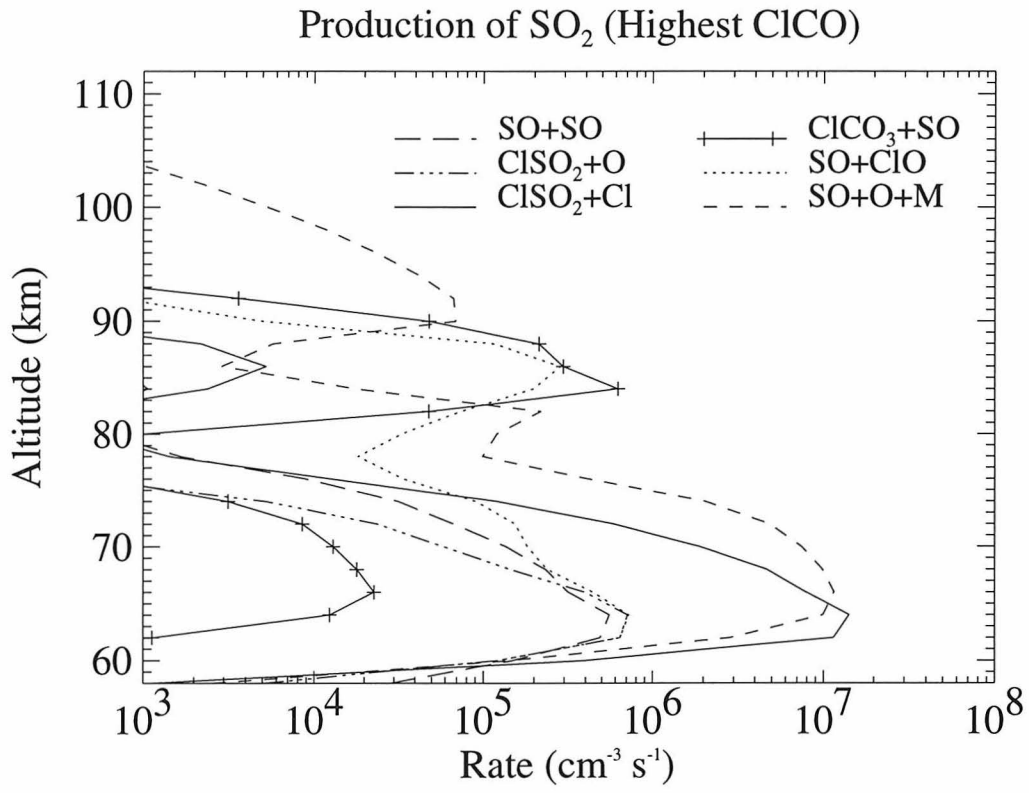

Figure 2.67: Primary reactions producing SO_2 in the Highest ClCO Model.

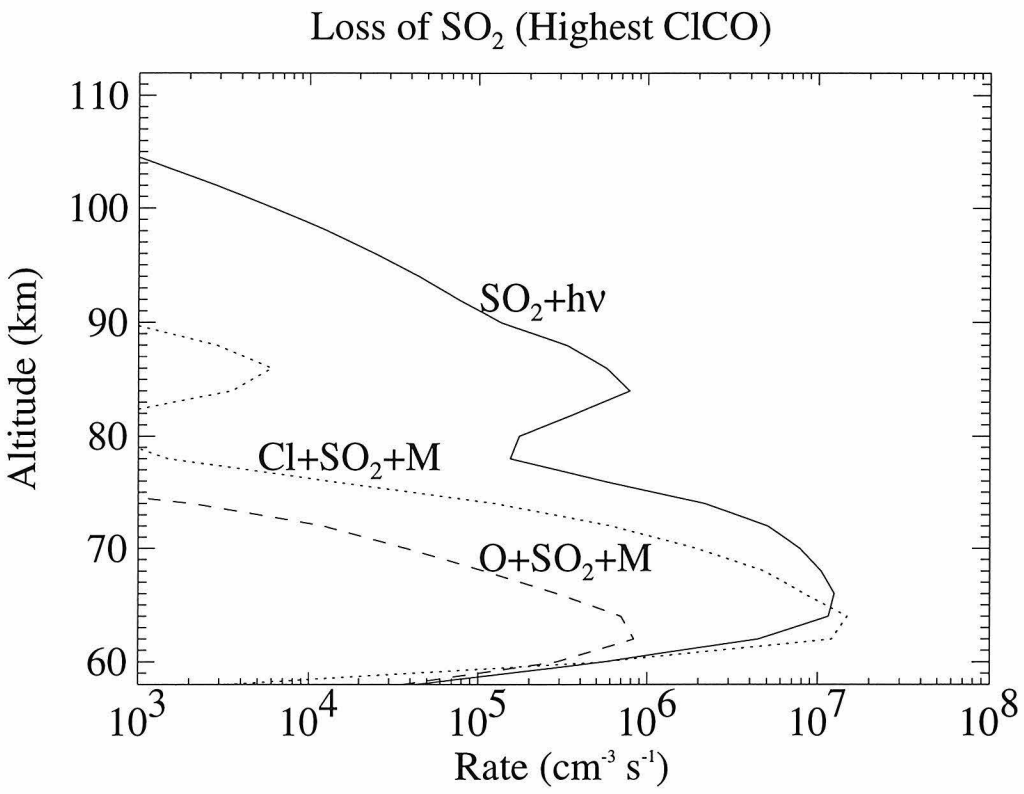

Figure 2.68: Primary reactions destroying SO_2 in the Highest ClCO Model.

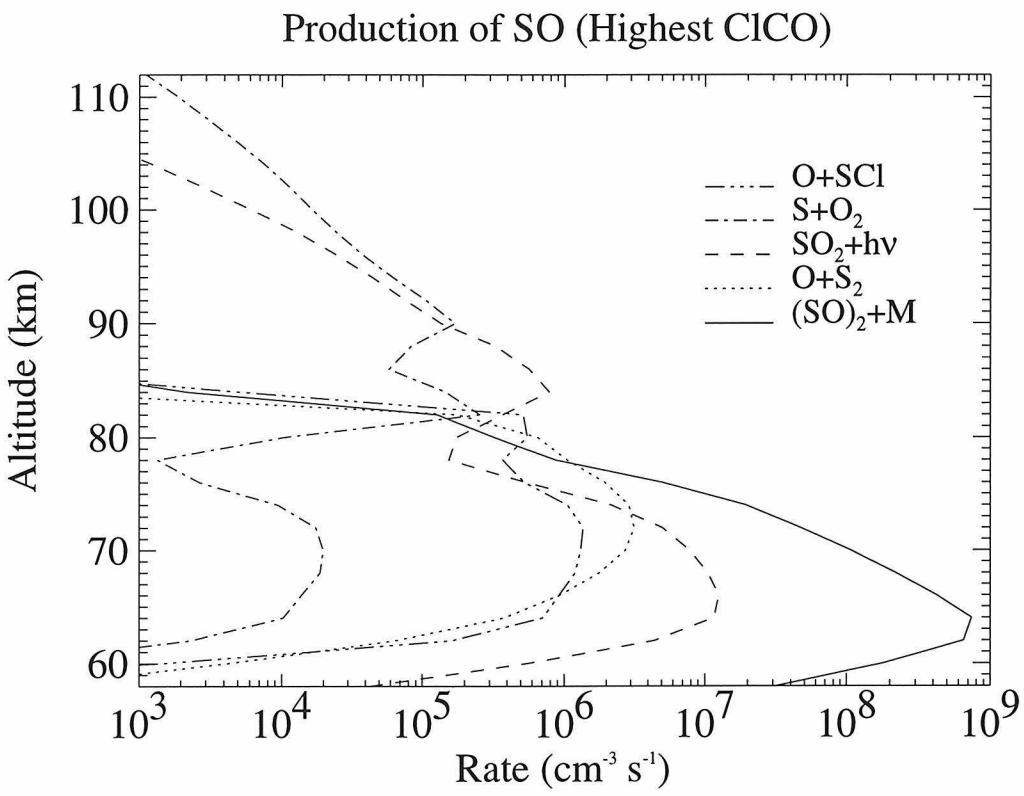

Figure 2.69: Primary reactions producing SO in the Highest ClCO Model.

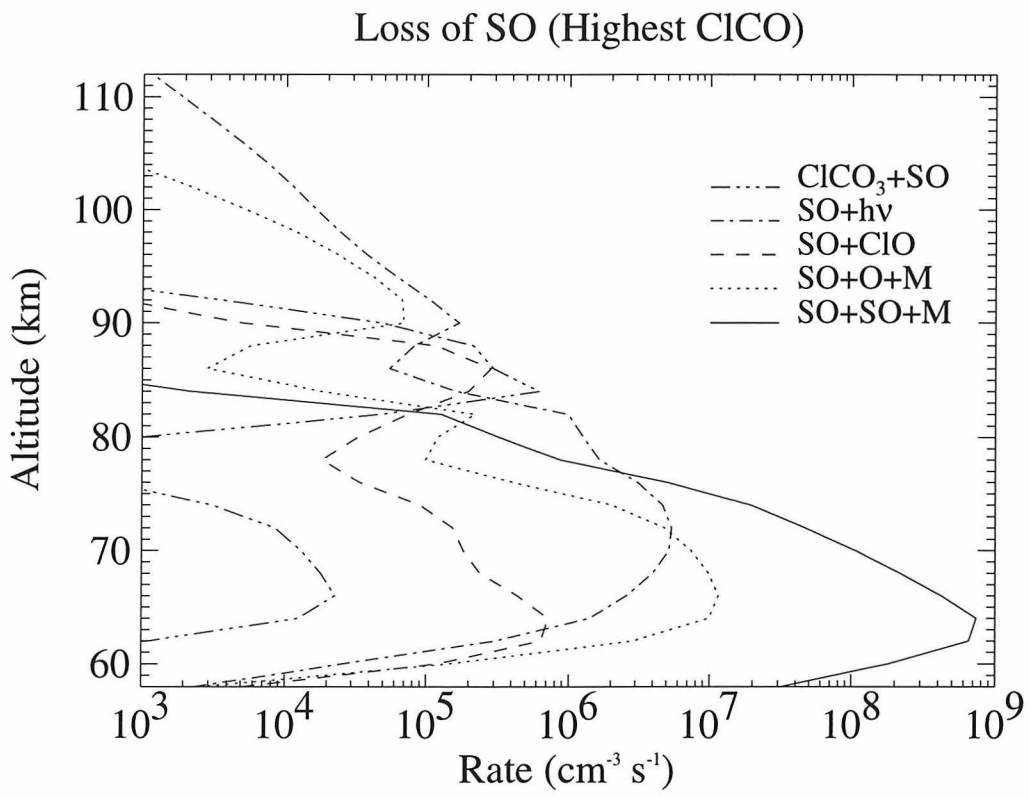

Figure 2.70: Primary reactions destroying SO in the Highest ClCO Model.

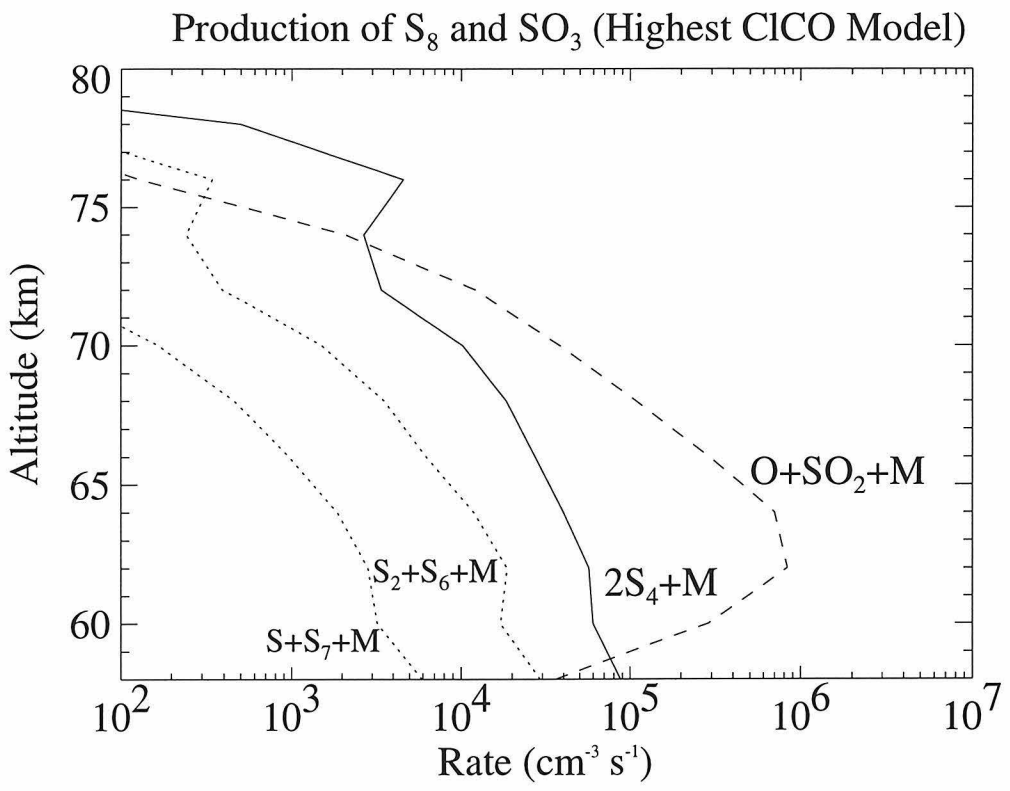

Figure 2.71: Primary reactions producing S_8 and SO_3 in the Highest ClCO Model.

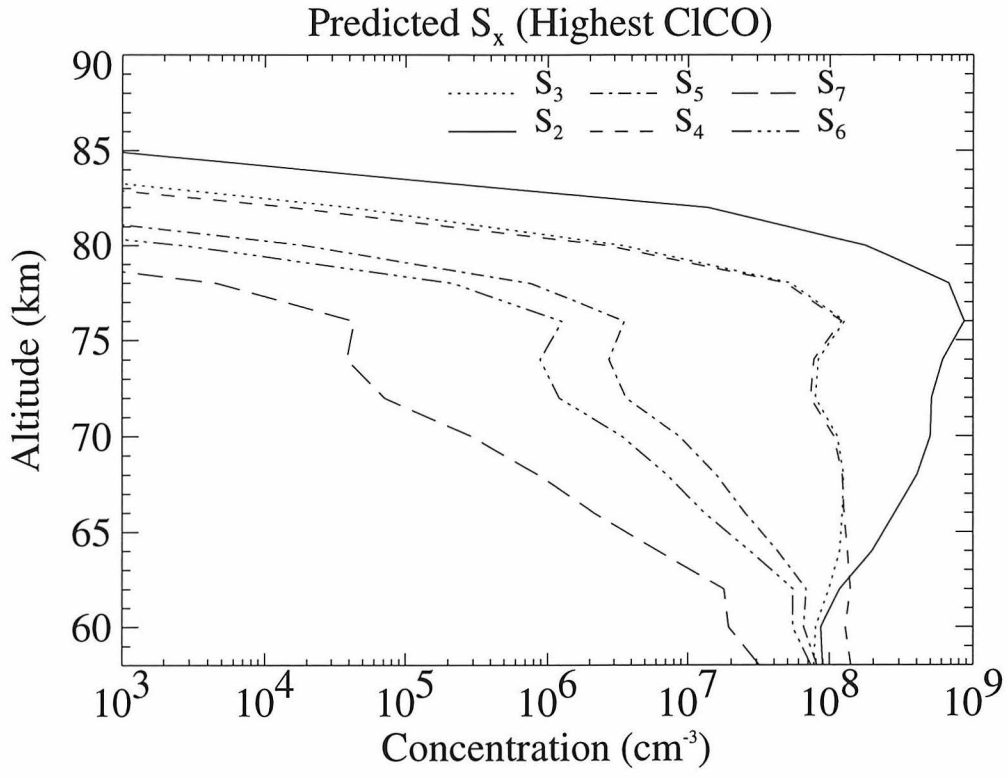

Figure 2.72: Predicted S_x abundances in the Highest ClCO Model.

quantitative attempt to determine an upper limit for *gas-phase* S_x above the clouds. S_x above 70 km altitude is primarily derived from the sulfur produced in photolysis of OCS at these altitudes, so reducing the OCS abundance above 70 km altitude should also make the predicted S_x abundances consistent with the observations.

Comparing the results from this model to those from the nominal model (or the results from *Yung and DeMore* [1982]), one can see that the nature of the chemistry at $\sim 70 - 85$ km altitude is strongly dependent on the oxygen abundance at these altitudes. Increasing the amount of oxygen present at these altitudes would significantly decrease the abundances of OCS and S_x since the presence of oxygen limits the production of S_x.

Eddy Diffusion

The profile for the eddy diffusion coefficient is curve "Coldest" in Figure 2.8. The predicted CO profile above 95 km and below 80 km altitude is within the observed range although below 80 km altitude the predicted CO mixing ratio does not increase with altitude as in the retrieved profiles. At 80 - 95 km altitude the predicted CO profile is generally smaller than the smallest retrieved profile by one to two times the reported measurement uncertainty. These disagreements suggest the eddy diffusion coefficient below 80 km altitude is too large, but the predicted CO profile's shape lies midway between the average dayside and nightside CO profiles retrieved by *Gurwell et al.* [1995] for their 1988 observations so the predicted CO profile may not be unreasonable as a "global average."

The SO_2 scale height at 68 - 74 km altitude for this model is $\sim 2 - 3$ km which lies within the range derived by *Na et al.* [1994] from UV observations of SO_2, $3(\pm 1)$ km. The predicted SO abundances for this model generally lie within one standard deviation of the SO profiles retrieved from UV observations by *Na et al.* [1990] and *Na et al.* [1994].

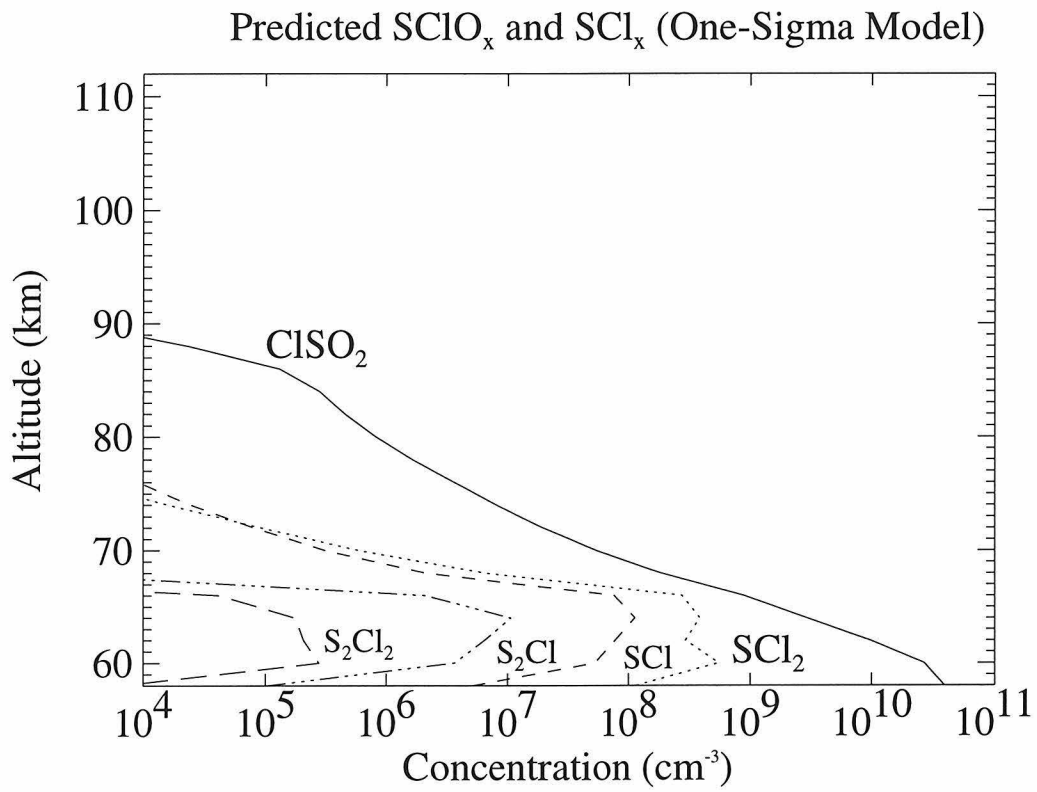

Figure 2.73: Predicted abundances of sulfur-chlorine species in the Highest ClCO Model.

Table 2.10: Comparison of Model Predictions and Observations

	Nominal	One-Sigma	Highest ClCO	*Yung and DeMore* C
k_{K119} (CO + OH) [a]	1×10^{11}	9×10^{10}	4×10^{10}	5×10^{10}
k_{K178} (ClCO + O_2 + M) [a]	5×10^{12}	4×10^{12}	3×10^{12}	5×10^{12}
k_{K179} (ClCO + O) [a]	1×10^{12}	9×10^{11}	1.5×10^{12}	1.2×10^{12}
S_8 Production [a]	5×10^{10}	6×10^{10}	7×10^{10}	
SO_3 Production [a]	6×10^{11}	6×10^{11}	5×10^{11}	1.4×10^{12}
$O_2(^1\Delta)$ Average [a]	9×10^{11}	1.1×10^{12}	1.0×10^{12}	8×10^{11}
$O_2(^1\Delta)$ from O_3 [a][d]	5×10^{11}	4×10^{11}	3×10^{11}	
Φ_{OCS} (58 km) [a]	3×10^{11}	2×10^{11}	2×10^{11}	
Φ_{SO_2} (58 km) [a]	7×10^{11}	8×10^{11}	8×10^{11}	1.4×10^{12}
Φ_{CO_2} (58 km) [a]	4×10^{11}	3×10^{11}	-1×10^{11}	1.4×10^{12}
Φ_{CO} (58 km) [a]	-7×10^{11}	-5×10^{11}	-3×10^{10}	-1.4×10^{12}
Total hydrogen (110 km)[b]	3×10^{7}	3×10^{7}	3×10^{7}	2×10^{8} [c]
H_2 (110 km) [b]	6×10^{5}	8×10^{5}	1.7×10^{6}	8×10^{6} [c]

[a] Units are cm^{-2} sec^{-1}
[b] Units are cm^{-3}
[c] The mixing ratios used to calculated the densities from *Yung and DeMore* [1982] were from 104 km altitude.
[d] Globally-averaged emission in the $O_2(^1\Delta)$ band when the only source for $O_2(^1\Delta)$ was from photolysis of O_3.
The column production rates are integrals from 58 to 112 km.

2.3.4 Comparisons Among Models and Observations

The basic chemistry in all three new models is similar and conceptually simple. CO is oxidized to CO_2 via Reaction K179 or Reaction K178; OCS is photolyzed to produce S_x and CO; and SO_2 is disproportionated to produce S_x and SO_3. The differences among the models lie in the mechanisms by which these processes are accomplished. Some of the major predictions from the models are summarized in Table 2.10.

The fluxes of SO_2 and OCS upward through the lower boundary are the same for all three current models (Table 2.10). These fluxes and the production of SO_3 (and, thus, of H_2SO_4) in all three current models are smaller than in the *Yung and DeMore* [1982] model. The production of SO_3 is smaller because some of the sulfur from SO_2 in the current models is converted to S_x. This channel for loss of sulfur was not available in the *Yung and DeMore* [1982] model. The increased production of S_8 in the Highest ClCO Model, as well as the increased abundances of reduced

sulfur species within the upper cloud layer in that model (Section 2.3.3), suggests that the chemistry occurring within the upper cloud layer is sensitive to the oxygen abundances at these altitudes. The estimated column abundance of S_8 in all three models is $\sim 10^{18}$ cm^{-2} based on the predicted production rates and the eddy diffusion coefficient (which partially controls the rate at which S_8 diffuses through the lower boundary of the model). This is a factor of 3 smaller than the predicted SO_2 column abundance, but the S_8 will likely be in a condensed phase. Assuming the S_8 has density of about 2 g cm^{-3} [*Meyer* 1976], the estimated S_8 abundance is comparable to the estimated total volume of the Mode 1 particles within the upper cloud layer [*Knollenberg and Hunten* 1980]. The predicted sulfur abundance is comparable to that predicted by *Toon et al.* [1982], and the predicted vertical distributions of S_x in the One-Sigma Model are similar to the adjusted profile for amorphous sulfur that *Toon et al.* [1982]. proposed was necessary to match the ultraviolet albedo of Venus.

The SO_2 profiles from all three models (Figure 2.74) are similar, and the predicted scale heights near 70 km altitude agree with the observed value to within the uncertainty of the observations. The SO_2 profile from the Highest ClCO model has a distinctive shape near 80 km, but no vertical profiles have been determined for SO_2 to which this could be compared.

The SO profiles from the three models are similar above 85 km altitude but differ at lower altitudes (Figure 2.75). The SO profile from the Nominal Model lies more than two standard deviations from the observed profiles and gives a worse match to the observations than the *Yung and DeMore* [1982] prediction so the One-Sigma and Highest ClCO Models are better in this respect. This suggests that the equilibrium constant for $(SO)_2$ used in the One-Sigma and Highest ClCO models is more realistic. The differences between the SO profiles from the One-Sigma and Highest ClCO Models are larger than the measurement uncertainty even when combined with the temporal variability, but these differences result from the large differences in the oxygen abundances at $\lesssim 75$ km altitude for these models.

The Nominal Model predicts a CO profile that agrees with the observed profiles to within the observational uncertainty and temporal variability (Figure 2.76). The

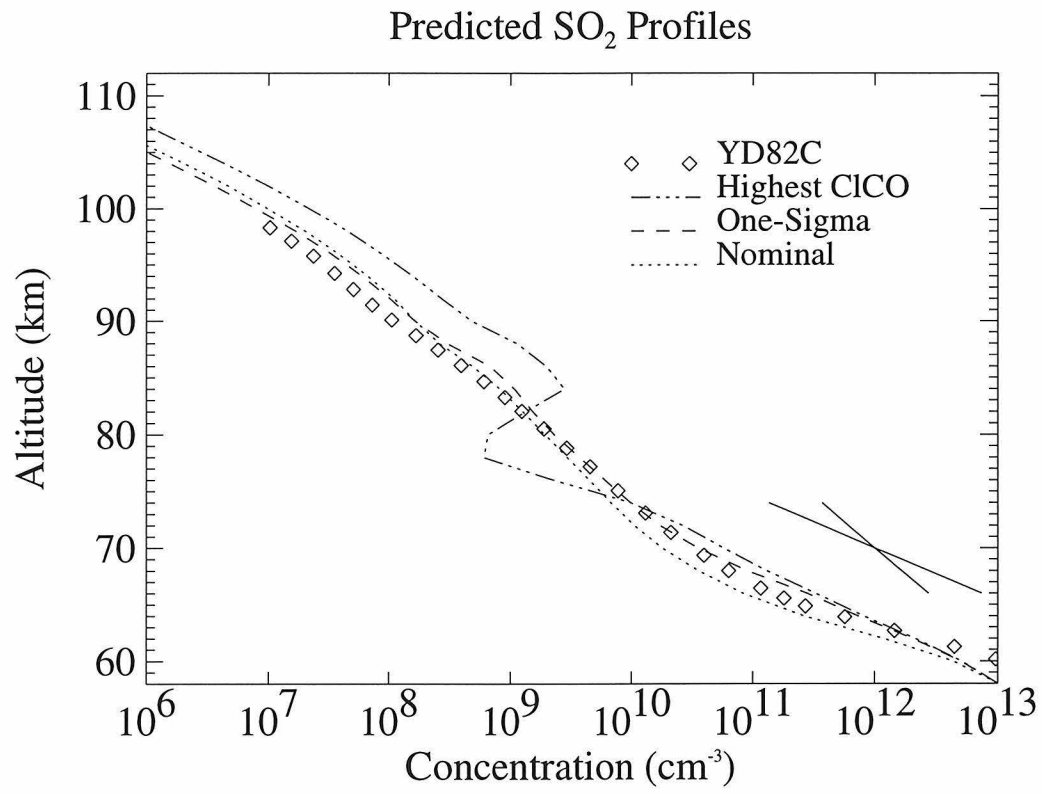

Figure 2.74: Predicted SO_2 abundances from the three current models and from the *Yung and DeMore* [1982] Model C. The range of scale heights observed at the cloud tops by *Na et al.* [1994] is shown as short solid lines.

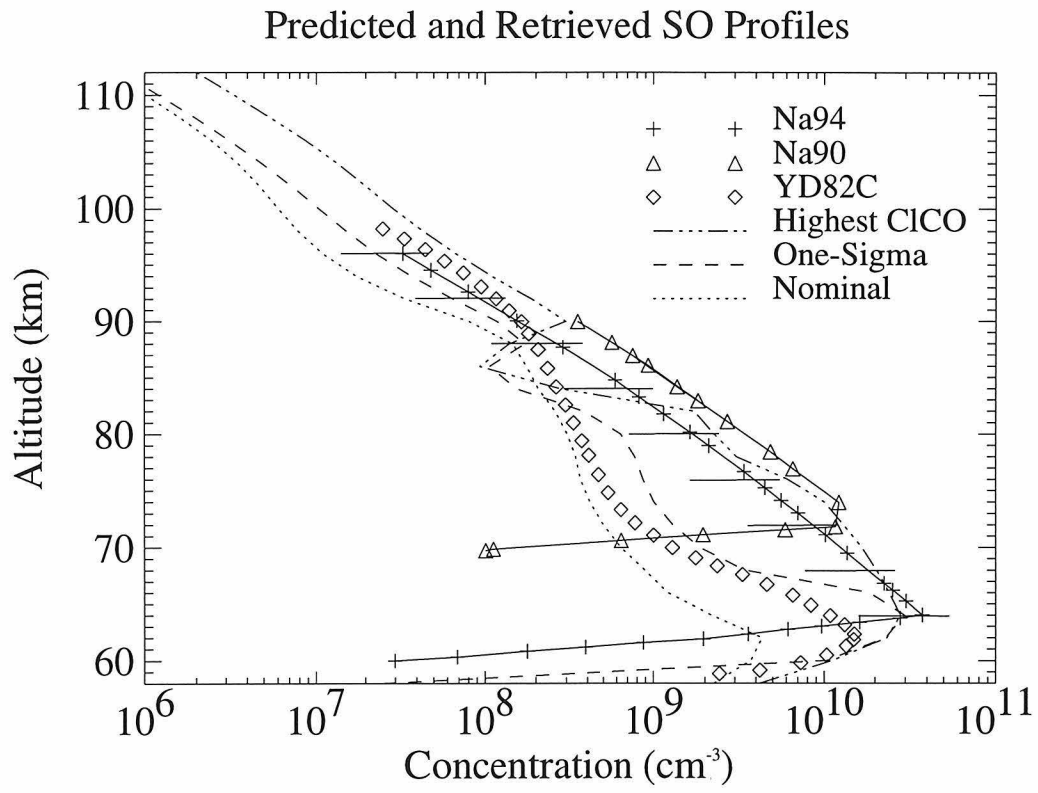

Figure 2.75: Predicted SO abundances from the three current models and from the *Yung and DeMore* [1982] Model C. The SO abundances retrieved from ultraviolet observations by *Na et al.* [1990] and *Na et al.* [1994] are shown along with the stated uncertainties for the 1994 retrieval.

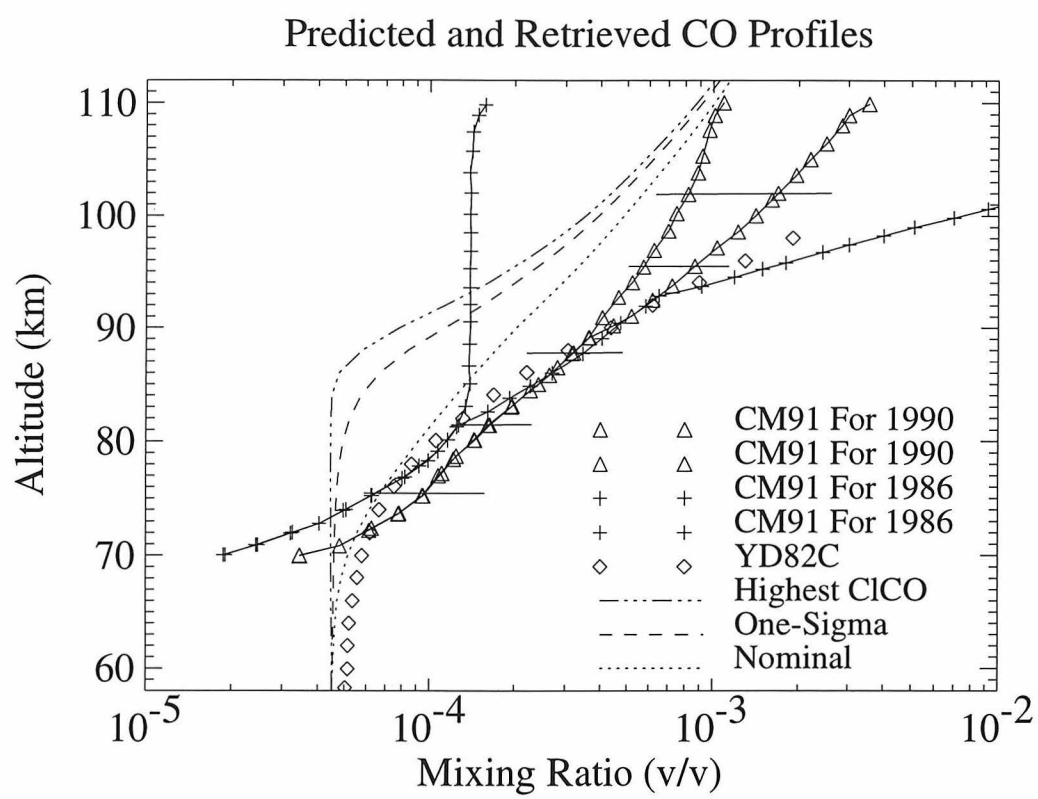

Figure 2.76: Predicted CO mixing ratios from the three current models and from the *Yung and DeMore* [1982] Model C. The CO mixing ratios retrieved from microwave observations by *Clancy and Muhleman* [1991] represent the range of diurnal variations that have been observed.

CO profiles from the One-Sigma and Highest ClCO Models, however, are about three standard deviations from the observed profiles. These differences likely indicate that the eddy diffusion coefficient used in the Nominal Model at $70-85$ km altitude is the maximum that can be used. However, there are large uncertainties in the CO profile near the subsolar point so the "global average" CO profile has greater uncertainty than is shown in Figure 2.76 for the individual measurements.

The greatest differences among the models lie in the abundances of the oxygen species (Figures 2.77 and 2.78). (The oxygen abundances largely determine the differences among the models for the remaining trace species, such as ClO, so the other species will not be discussed separately.) The primary determinant for the difference

in O_2 abundances is the equilibrium constant for ClCO. Based on radiative transfer calculations (Chapter 3), the O_2 profile from the Nominal Model (and that from *Yung and DeMore* [1982]) does not satisfy the upper limit on the abundance of O_2 from *Trauger and Lunine* [1983]; that from the One-Sigma Model is comparable to their 2σ upper limit; and that from the Highest ClCO Model is smaller than their 1σ upper limit. This could indicate that even the One-Sigma model does not satisfy the upper limit on O_2, but a factor of two diurnal or temporal variation could easily exist so the One-Sigma model may be a reasonable representation of the "global average" O_2 abundances. (For comparison, note that the CO mixing ratio varies by several orders of magnitude from the terminator to the antisolar point). The O_3 profiles differ among the current models mainly as a result of the changes in the O_2 abundances. The current model profiles differ from the *Yung and DeMore* [1982] profile because temperature-dependent rates for Reactions K104 and K105 were used in the current models.

The "global average" $O_2(^1\Delta)$ emission rate in the current models is smaller than the observed "global average" by $\sim 20-30\%$. Several possibilities exist for increasing the predicted airglow emission rate: (1) a higher effective yield of $O_2(^1\Delta)$ in Reactions K100 and K101 (*Slanger, T.*, [Personal Communication, 1998] has suggested the yield could be 100%); (2) an larger photolysis rate for CO_2; (3) production of $O_2(^1\Delta)$ in Reaction K197; and (4) production of $O_2(^1\Delta)$ in Reaction G12.

The water vapor profile used in the current models is likely incorrect since it is an extrapolation outside the range of conditions for which it was derived (see Appendix G). The sensitivity studies in Section 2.3.1 found the column O_2 abundance was sensitive to changes in the abundance of water used with the Nominal Model. For this reason, an additional model calculation was performed using the "Alternate" water vapor profile described in Appendix G which gives a reasonable match to the water vapor abundance derived by *Encrenaz et al.* [1995] as shown in Figure 5G.3. All other parameters for the "Alternate" water calculation were the same as for the One-Sigma Model. The O_2 profile derived from the "Alternate" calculation is shown in Figure 2.77. Although the O_2 abundance is larger for the "Alternate" water vapor

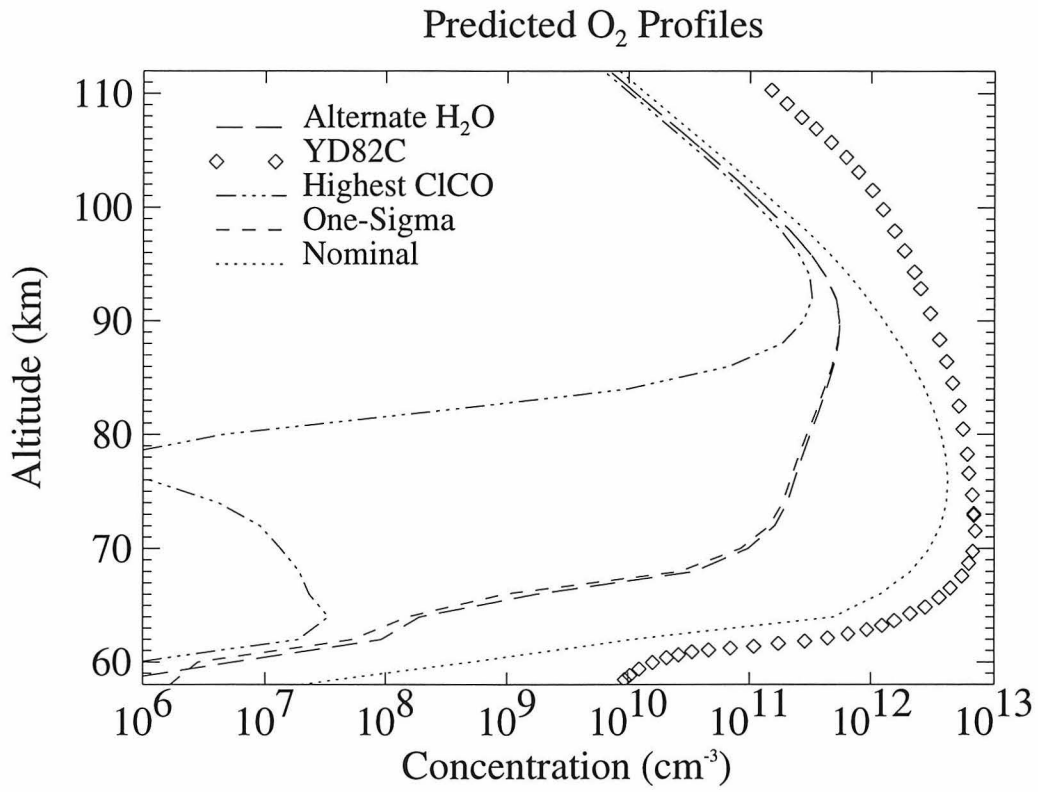

Figure 2.77: Predicted O_2 abundances from the three current models and from the *Yung and DeMore* [1982] Model C.

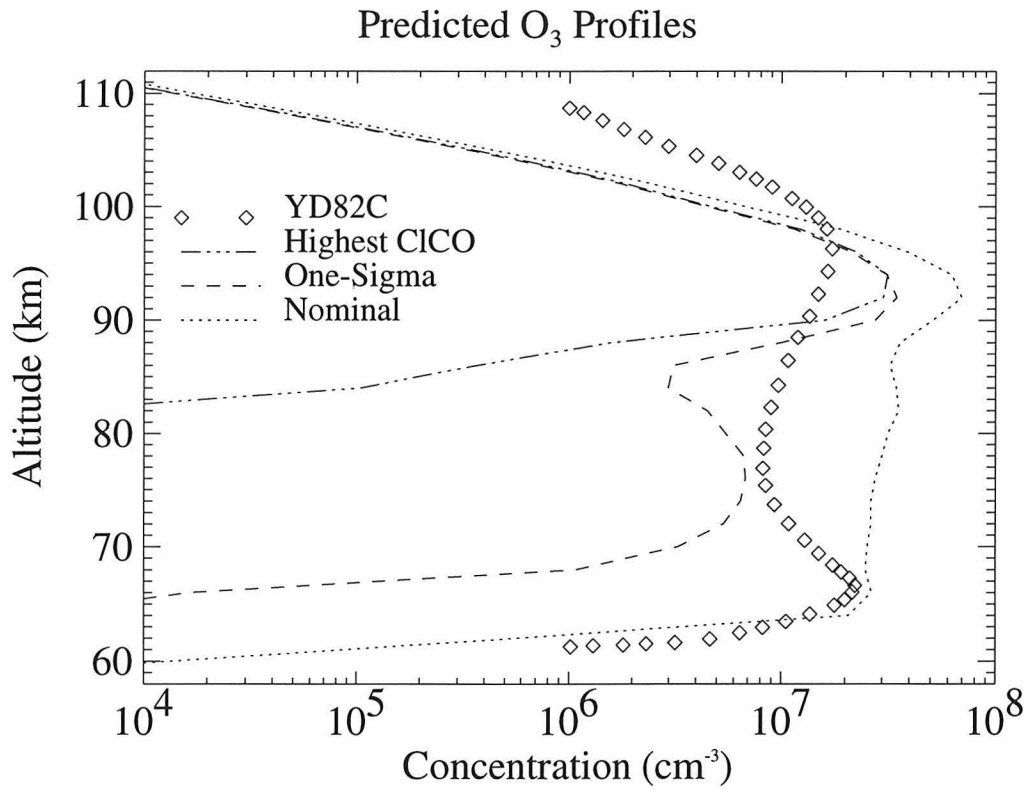

Figure 2.78: Predicted O_3 abundances from the three current models and from the *Yung and DeMore* [1982] Model C. The *Yung and DeMore* [1982] model used a temperature-*independent* rate for Reaction K105. A temperature-*dependent* rate was used for the current models.

profile than it is for the One-Sigma Model, the difference is not significant.

The relative merits of the models and their value in both understanding the chemistry of the Venus middle atmosphere and guiding future research on this subject must be judged by the degree to which the models predictions agree with existing observations (Table 2.1). Predictions from the Nominal Model generally agree better with observations than those from Model C by *Yung and DeMore* [1982]. The two most significant discrepancies between the Nominal Model and the observations are the column O_2 abundance and the SO profile. For these reasons the Nominal Model likely does not give a good representation of the chemistry in the Venus middle atmosphere. Both the One-Sigma and the Highest ClCO Models satisfy most of the existing observations, and, because the abundance of ground-state O_2 has not been determined, it is not possible to use that criterion for rejecting either the One-Sigma or the Highest ClCO Model. The CO profiles from both models, however, may disagree with observations.

A better representation of the chemistry of the Venus middle atmosphere could likely be obtained by using the "Nominal" eddy diffusion profile with most of the modified rates from the One-Sigma Model. The increased abundance of O_2 above 85 km altitude that would result from changing the eddy diffusion profile could be prevented by restoring the rates for Reactions K98, K99, K100, and K101 to near their nominal values. These changes would also increase the production of $O_2(^1\Delta)$ airglow from photolysis of O_3, but an increase in this component of the *dayglow* could be reasonable if the dayglow and nightglow are produced via different mechanisms and the O_2 abundance has a pronounced diurnal variation.

2.4 Discussion

The main objective for the Venus photochemical modeling was to find a plausible solution that is compatible with the existing observational upper limit on the abundance of O_2. Both the One-Sigma and the Highest ClCO Models predict O_2 abundances that are compatible with the 2σ upper limit from *Trauger and Lunine* [1983] (Chap-

ter 3). The changes that were made to the reactions rates, etc., in creating the One-Sigma Model are within the assessed or estimated uncertainties associated with the nominal values. The changes that were made in going from the One-Sigma Model to the Highest ClCO Model, however, are larger than the assessed one standard deviation uncertainties for Reactions K176, K177, and K178. Such large changes are not "statistically" likely in the standard interpretation of measurement uncertainties, but the recommended rates for some reactions that are important in the terrestrial stratosphere have changed by at least twice the assessed uncertainty in response to further laboratory study. For example, the recommended rate for Reaction G14 in *DeMore et al.* [1987] was 1×10^{-11} exp$((2200 \pm 1000)/T)$ with a factor of 10 assessed uncertainty at 298 K. The currently recommended rate for this reaction [*DeMore et al.* 1997] is 1.7×10^{-13} exp$((0 \pm 300)/T)$ with a factor of 3 assessed uncertainty at 298 K. Consequently, the rates used in the Highest ClCO Model may be reasonable, depending on the results from further laboratory study.

Fluorine, Bromine, and Heterogeneous Chemistry Revisited

Three types of chemistry were discarded in Section 2.1.3 as not likely to be important for oxidizing CO in the Venus atmosphere: fluorine, bromine, and heterogeneous chemistry. Based on the results from the current models, we should assess whether our neglect of these three types of chemistry is still reasonable.

The primary reservoir for fluorine is probably HF based on studies of the terrestrial atmosphere, and HF has been detected in the Venus atmosphere (Table 2.1). Because the threshold for photodissociating HF is near 170 nm and CO_2 absorbs strongly at the same wavelengths, direct photodissociation of HF below 110 km altitude will be small. That leaves two possible sources for creating labile fluorine in the $60 - 110$ km altitude region: transport down from above 110 km and transport upward from the surface in a form that can be photodissociated more easily than HF. Above 110 km, the photodissociation rate for HF will increase so fluorine could be transported down from higher altitudes into the middle atmosphere. The distance the fluorine is transported will depend on the relative timescales for transport versus fluorine's lifetime against reaction with H_2 to form HF. For the Nominal Model, the transport

timescale at 110 km altitude is $\sim 10^4$ sec. The photochemical lifetime for fluorine is $\lesssim 10^5$ sec near 110 km altitude because the concentration of H_2 is 10^6 cm^{-3} and the rate constant for Reaction G15 is $1.4 \times 10^{-10} \exp(-500/T)$ [*DeMore et al.* 1997]. The photochemical lifetime for fluorine below 100 km altitude, though, is $\lesssim 10^4$ sec because the concentration of H_2 increases to $> 10^7$ cm^{-3}. These comparisons indicate a significant fraction of the total fluorine might be in labile form at $\gtrsim 100$ km altitude. If the labile fluorine is to be important in the oxidation of CO, the equilibrium constant for FCO would have to be at least two orders of magnitude larger than that for ClCO to compensate for the smaller abundance of HF. The reaction enthalpy for forming FCO is 34 kcal/mol while that for ClCO is $\sim$ 8 kcal/mol so the thermal dissociation rate for FCO is orders of magnitude smaller than that for ClCO and might have some impact on the oxidation of CO at > 100 km altitude. *Parisot and Moreels* [1984] examined the chemistry of fluorine-oxides and, in agreement with our general arguments, found fluorine was not important in the chemistry of the middle atmosphere. *Parisot and Moreels* [1984] predicted a maximum abundance of 20 cm^{-3} for F which is much smaller than the Cl abundance in all three current models. The creation of other fluorine compounds at the surface of Venus is possible, but their concentrations are likely to be much smaller than those of the analogous chlorine compounds based on the observed relative abundances of HF and HCl. In addition, the thresholds for photodissociation of the fluorine compounds will be at higher energy than those for the analogous chlorine compounds. Consequently, fluorine compounds do not seem likely to play important roles in the oxidation of CO below 100 km altitude unless a mechanism is found that very effectively shields fluorine from reacting with H or H_2 to form HF.

The role of bromine in the Venus atmosphere has much greater uncertainties than for fluorine. First, bromine has never been detected in the Venus atmosphere. Second, bromine compounds are generally less stable than the analogous chlorine compounds so it is not clear whether BrCO could even exist. If bromine is present in the Venus atmosphere, it is not likely to be in the form of Br_2 which is the only bromine species for which a published upper limit exists (mixing ratio $< 2 \times 10^{-10}$ [*von Zahn et al.*

1983]). The heat of formation for Br_2 is 7.4 kcal/mol versus -9 kcal/mol for HBr and Br_2 photodissociates readily. HBr is weakly bound and Reaction G16 would be sufficiently rapid in the Venus atmosphere based on the results from the current models that the dominant form would likely be BrO.

Bromine compounds could play two roles in the Venus atmosphere. The first, conversion of O and O_3 to O_2, has been found to be important in the Earth's atmosphere [*McElroy et al.* 1986; *Anderson et al.* 1989]. The second potential role is in the oxidation of CO to CO_2. The abundance of bromine is unknown, but if its abundance is similar to that for HCl in the Venus atmosphere, then Reaction G17 would be important in the production of O_2. The yields of $O_2(^1\Delta)$ from these bromine reactions have not been measured but, if they are $\gtrsim$ 10%, then they could be minor but important sources for producing $O_2(^1\Delta)$. On the nightside, Reaction G12 could also be an important source for producing $O_2(^1\Delta)$. Studies of the terrestrial atmosphere [*Anderson et al.* 1989] have found that a significant fraction of the BrO and ClO produced during sunlit hours are converted at night to BrCl and O_2 via Reaction G12. If the BrO abundance in the Venus atmosphere is comparable to the HCl abundance and if the yield of $O_2(^1\Delta)$ from Reaction G12 is $\gtrsim$ 10%, then this reaction could contribute an important fraction of the observed Venus nightglow.

The importance of bromine in the oxidation of CO depends on the stability of BrCO. $COBr_2$, FBrCO, and HBrCO have been observed [e.g., *Parkington et al.* 1997; *Patty and Lagemann* 1953; *Niki et al.* 1985, respectively], but BrCO is believed to be unstable. *Walker and Prophet* [1966] estimated the bond dissociation energy in BrCO as -10 kcal/mol, implying it would not be stable at any temperature. If BrCO is stable at < 170 K, then this could be a viable pathway for oxidizing CO, but unless the abundance of bromine is much larger than that of HCl, this pathway for oxidizing CO does not appear to be important. Bromine could be important as a stabilizing buffer for COCl if reactions producing and destroying COClBr occurred on timescales comparable to the loss timescale for COCl in the current models. Due to the uncertainties involved, further examination of the potential role of bromine compounds in the Venus atmosphere is deferred to a subsequent research project.

By analogy to the Antarctic stratosphere, it has been suggested that heterogeneous chemistry might be very important in the Venus atmosphere [e.g., *Leu, M-T., and Y.L. Yung*, Personal Communication, 1995]. (Heterogeneous chemistry, in this case, refers to a reaction that occurs on or within a liquid aerosol particle between two species that are predominantly found in the gas phase and whose products are also predominantly found in the gas phase. In essence, the aerosol particle serves as a catalyst for the equivalent gas-phase reaction.) Even though heterogeneous chemistry has been shown to be important in the terrestrial atmosphere [e.g., review by *Ravishankara* 1997], there are three problems with directly transferring the terrestrial results to the Venus atmosphere. First, the most important heterogeneous reactions in the terrestrial atmosphere involve nitrogen species. As discussed in Section 2.1.2, there is no clear evidence that photochemically active nitrogen is present in significant amounts in the Venus atmosphere. Consequently, the only heterogeneous reaction that has been suggested for Venus is Reaction G10. The second difference between Venus and the Earth is that on Venus the labile chlorine (i.e., Cl_2) produced in Reaction G10 is needed at $\gtrsim 75$ km for the oxidation of CO, but the largest abundance of aerosols is found at $\lesssim 70$ km altitude. Thus, vertical transport would be required. However, the photochemical loss lifetime for Cl_2 in the current models is more than two orders of magnitude smaller than the transport lifetime. The third difficulty with invoking significant rates for heterogeneous chemistry in the Venus atmosphere is that HCl is only weakly soluble in concentrated sulfuric acid. If Reaction G10 is to increase the local production rate of Cl_2 by more than 10%, then the reactive uptake coefficient (γ) for Reaction G10 would have to be > 0.2 *and* the aerosol number density at 90 km would have to be an order of magnitude larger than that determined by *Lane and Opstbaum* [1983]. Based on the the analysis of Reaction G10 by *Donaldson et al.* [1997], this requires a sulfuric acid concentration < 55 wt% near 90 km altitude. Current polarimetry measurements do not have sufficient resolution to exclude this possibility but the aerosol scattering characteristics are consistent with 75 wt% H_2SO_4 ($+10, -5$ wt% H_2SO_4 [*Hovenier, J.*, Personal Communication, 1997]). Other heterogeneous reactions that could be important for the Venus atmosphere and that

have received some laboratory study are Reactions G18, G19, and G20. The first two are believed to produce HCl while the third produces BrCl [*DeMore et al.* 1997]. Based on current laboratory measurements and observations, heterogeneous reactions are not likely to be important at low latitudes but they might be important near the poles where the haze layer is thicker and extends to higher altitudes.

Comparison to Terrestrial Atmospheric Chemistry

The chemistry cycles for oxidation of CO in the current Venus models are not important in the terrestrial atmosphere due to the differing oxidizing states of the two atmospheres. These CO oxidation cycles are also not important in the Martian atmosphere due to the much smaller (or not detected) abundance of chlorine compounds in the Martian atmosphere. Some elements of the chlorine and sulfur chemistry that have been explored in this modeling, however, are important in Antarctic regions that have been denitrified, in volcanic plumes, and in sulfate-rich layers within the terrestrial stratosphere. These are active areas of research so future developments in terrestrial studies may provide additional insight into the processes occurring in the Venus atmosphere.

Reaction G3 is important in the upper mesosphere of the Earth, Venus, and Mars. As noted by *Slanger and Osterbrock* [1998], the higher excited states of O_2 that are produced in this reaction are difficult to study in the laboratory and are quenched rapidly by the O_2 in the terrestrial atmosphere. CO_2, however, seems to be much less efficient than O_2 at collisionally quenching the higher excited states of O_2 [*Bloemink et al.* 1998] so detailed studies of the O_2 airglow on Venus and Mars may provide information that cannot easily be obtained in any other manner.

The Second Ultraviolet Absorber

Another criterion for the results from photochemical models is that they should be consistent with the requirements from radiative transfer models for the Venus clouds. The upper cloud layer on Venus is distinguished by dark markings (areas of low albedo) that are readily apparent in ultraviolet images. *Pollack et al.* [1980] showed that SO_2 was the primary species responsible for the UV absorption and dark markings, but they found that SO_2 could not explain the low albedo of Venus at

320 – 400 nm. To explain the low albedo in this wavelength region, a multitude of possible "second absorbers" has been proposed. The primary contenders at the moment are sulfur allotropes [*Toon et al.* 1982], Cl_2 [*Pollack et al.* 1980], S_2O [*Hapke and Graham* 1989; *Na and Esposito* 1997], and croconic acid [*Hartley et al.* 1989].

Yung and DeMore [1982] found the column abundance of Cl_2 (10^{17} cm^{-2}) in their Model C was consistent with the absorption required in the *Pollack et al.* [1980] radiative transfer model. However, the column abundance of Cl_2 in the Nominal and One-Sigma Models is 10^{16} and is 2×10^{15} in the Highest ClCO Model, thus reducing the support for the *Pollack et al.* [1980] proposal. Likewise, the S_2O abundances predicted in the current models are several orders of magnitude smaller than those derived by *Na and Esposito* [1997]. This reduces the support for this species, but the differences between the models result from two estimated reaction rates so there are no conclusive grounds for preferring either model (Appendix L).

The production of sulfur allotropes (S_x) within the upper cloud in the current model suggests they could be important absorbers but their cross sections are largely unknown. S_2 has a strong absorption band at < 320 nm, but appears to have only weak absorption at longer wavelengths (see Appendix B). S_3 has a strong absorption band in the 350 – 470 nm wavelength region so it could provide part of the observed absorption. However, the predicted absorption for S_3 in the One-Sigma Model is comparable to the predicted absorption for Cl_2, so the prediction absorption for S_3 is a factor of ~ 10 smaller than the required absorption from *Pollack et al.* [1980]. In the Highest ClCO Model, the prediction absorption for S_3 is a factor of 3 larger than in the Nominal Model, but this is still smaller than required. The only known absorption band for gaseous S_4 is at 430 – 570 nm which does not match the requirements derived by *Pollack et al.* [1980]. No gas-phase spectra were found for S_x compounds with $x > 4$ so it is not possible to provide quantitative assessments of those compounds. Due to the low vapor pressure of S_8, it will probably rapidly condense into a solid or liquid state. The absorption by S_8 in a liquid solution with benzene or methanol [*Bartlett et al.* 1958; *Steudel et al.* 1988, respectively] decreases by two orders of magnitude from 300 to 370 nm which does not agree with the required absorption. However, the

absorption by irradiated sulfur in a benzene solution decreases by less than one order of magnitude from 300 to 370 nm [*Bartlett et al.* 1958], and the absorption by S_{12} in a liquid solution with methylcyclohexane is approximately constant for 300 – 340 nm. Consequently, some form of sulfur in the solid or liquid state *could* possibly have the proper spectral shape in the 300 – 400 nm wavelength range [*Toon et al.* 1982]. The estimated S_8 abundance given in Section 2.3.4 for the photochemical models is comparable to the sulfur abundance that *Toon et al.* [1982] calculated, and the predicted vertical distribution of S_x in the One-Sigma Model is similar to the distribution that *Toon et al.* [1982] believed would give a satisfactory fit to the ultraviolet albedo of Venus. It is not clear from existing laboratory spectra [*Bartlett et al.* 1958; *Steudel et al.* 1988], however, whether the amorphous sulfur that was proposed by *Toon et al.* [1982] is compatible with the ultraviolet albedo of Venus at 200 – 300 nm.

Two new possibilities for the second absorber are suggested by the current models: $ClSO_2$ and SCl_x. Both will be correlated with SO_2 and will have peak abundances in the upper cloud layer and short photochemical lifetimes above the clouds, as required [*Pollack et al.* 1980]. Some of the SCl_x have measured absorption in the 320 – 400 nm region (Appendix B), but the predicted abundances would produce less absorption than the predicted Cl_2 in this wavelength region. The cross section for $ClSO_2$ has not been measured, but if it is similar to that for SO_2 with a shift to longer wavelengths due to the difference in the ionization potentials for the two species, then $ClSO_2$ would absorb strongly in the 320 – 400 nm wavelength region. The predicted abundances, however, would produce less absorption than the predicted Cl_2 in this wavelength region for the assumed $ClSO_2$ cross section.

2.4.1 Implications for the Chemistry in the Lower Atmosphere

Our modeling does not extend below the cloud layers into the lower atmosphere. The derived fluxes through our lower boundary, however, can be used to assess whether

the solution we have obtained for the upper atmosphere chemistry is reasonable. The calculated production rates for S_8 and SO_3 in our model are shown in Table 2.10 along with the required fluxes at the lower boundary for CO, SO_2, OCS, and CO_2. Based on these fluxes, the net chemistry required in the lower atmosphere for the Nominal and One-Sigma Models is

$$8CO + S_8 \rightarrow 8OCS$$

$$CO + SO_3 \rightarrow CO_2 + SO_2$$

$$16SO_3 + S_8 \rightarrow 24SO_2$$

The conversion of CO and S_8 to OCS as these species are diffusively transported toward the surface is consistent with the observed increase in OCS abundance at lower altitudes [*Pollack et al.* 1993] and the observed decrease in CO abundance below the lower cloud [*von Zahn et al.* 1983]. The thermal stability of S_8 decreases rapidly with increasing temperature so it is very likely that SO_3 would readily react with the S_2 produced from thermal dissociation of S_8 to form the required amounts of SO_2.

The total production of S_8 and SO_3 is consistent with the order of magnitude estimate in *Yung and DeMore* [1982] of the H_2SO_4 production rate (10^{12} cm^{-2} sec^{-1}). Their estimate was based on the observed aerosol particle sizes in the cloud layers and the Stokes fall velocity for a particle of radius 1 micrometer. The estimate in *Yung and DeMore* [1982] was used by *Krasnopol'sky and Pollack* [1994] in their modeling of the vertical profile of H_2SO_4 and H_2O in the lower and middle cloud layers.

We have not attempted to solve for the abundance of H_2O in our model, but since the dominant source of HO_x in our model is from HCl, the required upward flux of H_2O should be equal to the production rate of SO_3. The mixing ratio of H_2 that we predict at 60 km is 3×10^{-11} in the Nominal Model and 5×10^{-11} in the One-Sigma

Model. This mixing ratio is much smaller than the mixing ratio of H_2 ($10^{-9} - 10^{-8}$) predicted from thermochemical equilibrium at $\sim$ 20 km altitude [*Yung and DeMore* 1982].

The upward flux of HCl required at 60 km is 3×10^9 cm^{-2} sec^{-1} in the Nominal and One-Sigma Models. This is much smaller than the calculated production rate of SO_3. The downward chlorine flux required to maintain chemical equilibrium is carried downward by $ClSO_2$. This species is likely to decompose rapidly at the temperatures found in the lower atmosphere so the chlorine will rapidly react with hydrogen to form HCl.

The results from the case in which oxygen was most depleted (the Highest ClCO Model) suggest the lower atmosphere could be more reducing than has been considered in previous studies [e.g., *Yung and DeMore* [1982]]. The standard presumption has been that some of the CO which is produced in the middle atmosphere from photolysis of CO_2 is transported downward, then oxidized to CO_2 in or below the lower cloud layer. The oxygen for oxidizing CO is supplied by thermal dissociation of H_2SO_4 at the elevated temperatures found in the lower atmosphere. However, if ClCO is effectively much more stable at $65 - 75$ km altitude than presently believed (as was proposed in the Highest ClCO Model), then the oxidation of CO at these altitudes will be so efficient that OCS diffusing upward from the lower atmosphere effectively will be converted into CO_2 and S_8. This would require that the lower atmosphere convert some of the downward flux of CO_2 into CO. The extremely high stability of ClCO at 65 km altitude is not physically reasonable given the measured temperatures within the upper cloud layer, but the results from the Highest ClCO Model suggest that oxidation of CO to CO_2 can be accomplished almost entirely within the Venus middle atmosphere. Furthermore, if the "global-average" O_2 abundance in the middle atmosphere is more than a factor of three smaller than the current upper limit, then the results from the Highest ClCO Model suggest there may be a downward flux of CO_2 through the base of the upper cloud.

2.4.2 Evolution of the Venus Atmosphere

The boundary parameter variations for the Nominal Model in Table 2.7 indicate the O_2 abundance in the Venus middle atmosphere is not sensitive to large changes in the abundance of SO_2. For those tests, a factor of 8 increase in the SO_2 abundance at 70 km altitude led to a factor of 7 increase in the upward flux of SO_2 through the lower boundary of the model but produced only a 15% decrease in the column abundance of O_2. Tests were not conducted for the conditions in the *Yung and DeMore* [1982] model, but the factors that are primarily responsible for limiting the magnitude of the response by O_2 to such a large change in the SO_2 abundance were not present in the *Yung and DeMore* [1982] model. The oxidation of CO was largely decoupled from the oxidation of SO_2 in even the Nominal Model so the increased influx of SO_2 is disproportionated into S_8 and SO_3. Only a small fraction of the increased SO_2 flux reaches a sufficiently high altitude that it can serve as a sink for oxygen that had been oxidizing CO. This can be seen in the increase in the magnitude of the downward flux of CO for the high SO_2 case.

The results obtained here give a better match to the existing observations than those obtained by *Yung and DeMore* [1982]. Even if further study validates the importance of the chlorine chemistry examined in this work for the current Venus atmosphere, the results from the *Yung and DeMore* [1982] study should not be disregarded. Oxidation via hydrogen catalytic cycles may have been more important in previous epochs if the abundance of water was much larger than it is today. The boundary parameter variation tests with large abundances for H_2 and H_2O suggest that the hydrogen and chlorine cycles can mutually annihilate each other when they are of roughly equal importance. If there was a transition epoch in Venus' history when the chemistry changed from hydrogen-dominated to chlorine-dominated, then the abundance of oxygen species in the middle atmosphere might have been much larger than it is today.

2.5 References

Ackerman, M., Ultraviolet Solar Radiation Related to Mesospheric Processes, in *Mesospheric Models and Related Experiments*, ed. G. Fiocco, Proceedings of the Fourth ESRIN-ESLAB Symposium held 6-10 July 1970, (D. Reidel Publishing, Dordrecht, The Netherlands), 149-159, 1971.

Ahmed, S.M., and V. Kumar, Quantitative Photoabsorption and Fluorescence Spectroscopy of SO_2 at 188 - 231 and 278.7 - 320 nm, *J. Quant. Spectrosc. Radiat. Transfer* **47**, 359-373, 1992.

Alexander, M., Mechanism for the Venus Thermospheric Superrotation, *Geophys. Res. Lett.* **19**, 2207-2210, 1992.

Allen, C.W., *Astrophysical Quantities*, (Athlone Press, London, UK, 310 pp.), 1976.

Allen, M.A., and J.E. Frederick, Effective Photodissociation Cross Sections for Molecular Oxygen and Nitric Oxide in the Schumann-Runge Bands, *J. Atmos. Sci.* **39**, 2066-2075, 1982.

Allen, M., Y.L. Yung, and J.W.Waters, Vertical Transport and Photochemistry in the Terrestrial Mesosphere and Lower Thermosphere (50 - 120 km), *J. Geophys. Res.* **86**, 3617-3627, 1981.

Amimoto, S.T., A.P. Force, and J.R. Wiesenfeld, Ozone Photochemistry: Production and Deactivation of $O_2(^1D_2)$ Following Photolysis at 248 nm, *Chem. Phys. Lett.* **60**, 40-43, 1978.

Anbar, A.D., M. Allen, and H.A. Nair, Photodissociation in the Atmosphere of Mars: Impact of High Resolution, Temperature-Dependent CO_2 Cross-section Measurements, *J. Geophys. Res.* **98**, 10925-10931, 1993.

Anderson, S.M., and K. Mauersberger, Laser Measurements of Ozone Absorption Cross Sections in the Chappuis Band, *Geophys. Res. Lett.* **19**, 933-936, 1992.

Anderson, J.G., W.H. Brune, S.A. Lloyd, D.W. Toohey, S.P. Sander, W.L. Starr, M. Lowenstein, and J.R. Podolske, Kinetics of O_3 Destruction by ClO and BrO Within the Antarctic Vortex: An Analysis Based on in Situ ER-2 Data, *J. Geophys. Res.* **94**, 11480-11520, 1989.

Aref'eva, R.G., V.G. Samoilovich, and Y.V. Filippov, Discharge in an Ozonizer as a Source of Atomic Oxygen, *Vestn. Mosk. Univ. Ser. 2 Khim.* **18**, 400, 1978.

Arnold, I., and F.J. Comes, Temperature Dependence of the Reactions $O(^3P) + O_3 \rightarrow 2O_2$ and $O(^3P) + O_2 + M \rightarrow O_3 + M$, *Chem. Phys.* **42**, 231-239, 1979.

Atkinson, R., D.L. Baulch, R.A. Cox, R.F. Hampson, Jr., J.A. Kerr, and J. Troe, Evaluated Kinetic and Photochemical Data for Atmospheric Chemistry Supplement IV, *J. Phys. Chem. Ref. Data* **21**, 1125-1568, 1992.

Badger, R.M., A.C. Wright, and R.F. Whitlock, Absolute Intensities of the Discrete and Continuous Absorption Bands of Oxygen Gas at 1.26 and 1.065 μm and the Radiative Lifetime of the $^1\Delta_g$ Oxygen State, *J. Chem. Phys.* **43**, 4345-4350, 1965.

Baer, S., H. Hippler, R. Rahn, M. Siefke, N. Seitzinger, and J.Troe, Thermodynamic and Kinetic Properties of the Reaction $Cl + O_2 + M \rightleftharpoons ClOO + M$ in the Range 160-300 K and 1-1000 Bar, *J. Chem. Phys.* **95**, 6463-6470, 1991.

Ball, M.J., and F.S. Larkin, Determination of the Rates of Atomic Reactions by the Discharge-flow Method, *Nature Physic. Sci.* **245**, 63-64, 1973.

Barker, E., Detection of SO_2 in the UV Spectrum of Venus, *Geophys. Res. Lett.* **6**, 117, 1979.

Barnes, R., and A. Sinha, Photodissociation and Unimolecular Dissociation of HOCl, 14th Informal Symposium on Kinetics and Photochemistry in the Atmosphere, (San Diego, CA, February 19), 1997.

Bartlett, P.D., G. Lohaus, and C.D. Lewis, Reactions of Elemental Sulfur. III. A Preliminary Study of the Conversion of Hexatomic to Octatomic Sulfur, *J. Am. Chem. Soc.* **80**, 5064-5069, 1958.

Basco, N., and S.K. Dogra, Reactions of Halogen Oxides Studied by Flash Photolysis I. The Flash Photolysis of Chlorine Dioxide, *Proc. Roy. Soc. London A* **323**, 29, 1971.

Basco, N., and R.D. Morse, Reaction of Halogen Oxides Studied by Flash Photolysis IV. Vacuum Ultraviolet Kinetic Spectroscopy Studies on Chlorine Dioxide, *Proc. R. Soc. Lond. A* **336**, 495-505, 1974.

Basco, N., and A.E. Pearson, Reactions of Sulphur Atoms in Presence of Carbon Disulphide, Carbonyl Sulphide, and Nitric Oxide, *Trans. Faraday Soc.* **63**, 2684-2694, 1967.

Baulch, D.L., D.D. Drysdale, D.G. Horne, and A.C. Lloyd, *Evaluated Kinetic Data for High Temperature Reactions, Volume 1: Homogeneous Gas Phase Reactions of the H_2-O_2 System*, (CRC Press, Boca Raton, FL), 1972.

Baulch, D.L., D.D. Drysdale, J. Duxbury, and S.J. Grant, *Evaluated Kinetic Data for High Temperature Reactions, Volume 3: Homogeneous Gas Phase Reactions of the O_2-O_3 System, the CO-O_2-H_2 System, and of sulphur-containing species*, (CRC Press, Boca Raton, FL) 1976.

Baulch, D.L., R.A. Cox, R.F. Hampson, Jr., J.A. Kerr, J. Troe, and R.T. Watson, Evaluated Kinetic and Photochemical Data for Atmospheric Chemistry, *J. Phys. Chem. Ref. Data* **9**, 295-386, 1980.

Baulch, D.L., J. Duxbury, S.J. Grant, and D.C. Montague, *Evaluated Kinetic Data for High Temperature Reactions, Volume 4: Homogeneous Gas Phase Reactions of halogen- and cyanide-containing species*, (American Chemical Society), 1981.

Baulch, D.L., C.J. Cobos, R.A. Cox, C. Esser, P. Frank, Th. Just, J.A. Kerr, M.J. Pilling, J. Troe, R.W. Walker, and J. Warnatz, Evaluated Kinetic Data for Combustion Modeling, *J. Phys. Chem. Ref. Data* **21**, 411-734, 1992.

Belton, M.J.S., Theory of the Curve of Growth and Phase Effects in a Cloudy Atmosphere: Application to Venus, *J. Atmos. Sci.* **25**, 596-609, 1968.

Bertaux, J.L., and J.T. Clarke, Deuterium Content of the Venus Atmosphere, *Nature* **338**, 567-568, 1989.

Bevan, P.L.T., and G.R.A. Johnson, *J.C.S. Faraday I* **69**, 922, 1973.

Bezard, B., C. deBergh, D. Crisp, and J-P Maillard, The Deep Atmosphere of Venus Revealed by High-Resolution Nightside Spectra, *Nature* **345**, 508-511, 1990.

Billmers, R.I., and A.L. Smith, Ultraviolet-Visible Absorption Spectra of Equilibrium Sulfur Vapor: Molar Absorptivity Spectra of S_3 and S_4, *J. Phys. Chem.* **95**, 4242-4245, 1991.

Black, G., and G. Porter, Vacuum Ultra-violet Flash Photolysis of Water Vapour, *Proc. Roy. Soc. A* **266**, 185-197, 1962.

Black, G., R.L. Sharpless, T.G. Slanger, and M.R. Taherian, The 1150-1300 Angstrom Absorption Spectrum of O_2 at 930 K, *Chem. Phys. Lett.* **113**, 311-313, 1985.

Bloemink, H.I., R.A. Copeland, and T.G. Slanger, Collisional Removal of Vibrationally Excited O_2(b) by O_2, N_2, and CO_2, *J. Chem. Phys., in press*, 1998.

Bodenstein, M., S. Lenher, and C. Wagner, Die Photochemische Bildung von Phosgen. IV, *Z. Phys. Chem. Abt. B* **3**, 459-478, 1929.

Borrell, P., C.J. Cobos, A.E. Croce de Cobos, H.Hippler, K. Luther, A.R. Ravishankara, and J. Troe, Radical Association Reactions in Gases at High Pressures, *Ber. Bunsenges. Phys. Chem.* **89**, 337-339, 1985.

Borucki, W.J., J.W. Dyer, J.R. Phillips, and P. Pham, *Pioneer Venus* Orbiter Search for Venusian Lightning, *J. Geophys. Res.* **96**, 11033-11043, 1991.

Brahan, K.M., A.D. Hewitt, G.D. Boone, and S.A. Hewitt, Rate Constant for the Reaction of Cl with $CHCl_3$, *Int. J. Chem. Kin.* **28**, 397-404, 1996.

Breckenridge, W.H., and H. Taube, Some Reactions of Ground-state (^{3}P) and Electronically Excited (^{1}D) Sulfur Atoms, *J. Chem. Phys.* **53**, 1750, 1970.

Burkholder, J.B., and R.K. Talukdar, Temperature Dependence of the Ozone Absorption Spectrum Over the Wavelength Range 410 to 760 nm, *Geophys. Res. Lett.* **21**, 581-584, 1994.

Burns, W.G., and F.S. Dainton, The Determination of the Equilibrium and Rate Constants of the Chain Propagation and Termination Reactions in the Photochemical Formation of Phosgene, *Trans. Faraday Soc.* **48**, 39-52, 1952.

CIAP Monograph, *The Natural Stratosphere of 1974*, 5-184, 1975.

Carver, J.H., H.P. Gies, T.I. Hobbs, B.R. Lewis, and D.G. McCoy, Temperature Dependence of the Molecular Oxygen Photoabsorption Cross Section Near the H Lyman α Line, *J. Geophys. Res.* **82**, 1955-1960, 1977.

Chang, W.D., S.B. Karra, and S.M. Senkan, A Computational Study of Chlorine Inhibition of CO Flames, *Combustion and Flame* **69**, 113-122, 1987.

Chase, M.W., Jr., C.A. Davies, J.R. Downey, Jr., D.J. Frurip, R.A. McDonald, and A.N. Syverud, *JANAF Thermochemical Tables*, Third Edition, *J. Phys. Chem. Ref. Data* **14**, Supplement 1, 1985.

Chiu, C-L., Photodissociation of Gas Phase Dichlorodisulfane: Its Products and Rate Law, *Proc. Natl. Sci. Counc. B. ROC* **7(2)**, 123-130, 1983.

Chiu, C-L., and H. Chang, Observation of Photodissociation of S_2Cl_2 and Resonance Raman and Fluorescence Spectra of S_2Cl Under 514.5 nm Radiation, *Spectrochim. Acta A* **50**, 2239-2248, 1994.

Chiu, C.L., S.C. Pan, and C.K. Ni, Recognition of the Violet System of S_2Cl in the Pyrolysis of S_2Cl_2, *J. Chem. Phys.* **85**, 10-12, 1986.

Choo, K.Y., and M-T Leu, Determination of $O_2(^1\Sigma_g^+)$ and $O_2(^1\Delta_g)$ Yields in Cl + O_2 and Cl + O_3 Reactions, *J. Phys. Chem.* **89**, 4832-4837, 1985.

Clancy, R. and D. Muhleman, Chemical-dynamical Models of the Venus Mesosphere Based Upon Diurnal Microwave CO Variations, *Icarus* **64**, 183-204, 1985.

Clancy, R. and D. Muhleman, Long-term (1979-1990) Changes in the Thermal, Dynamical, and Compositional Structure of the Venus Mesosphere as Inferred from Microwave Spectral Line Observations of ^{1}2CO, ^{1}3CO, and C^{1}8O, *Icarus* **89**, 129-146, 1991.

Clancy, R.T., D.O. Muhleman, and G.L. Berge Mesospheric Photochemistry and Circulation from CO Microwave Measurements, in *An International Conference on the Venus Environment*, (NASA Ames Research Center), 21, 1981.

Clark, T.C., M.A.A. Clyne, and D.H. Stedman, Mechanism of Formation of Triatomic Molecules in Atomic Combination Reactions, *Trans. Faraday Soc.* **62**, 3354-3365, 1966.

Clegg, S.L., and P. Brimblecombe, Application of a Multicomponent Thermodynamic Model to Activities and Thermal Properties of 0 - 40 mol kg^{-1} Aqueous Sulfuric Acid from $<$ 200 K to 328 K, *J. Chem. Eng. Data* **40**, 43-64, 1995.

Cloutier, P.A., L. Kramer, and H.A. Taylor, Jr., Observations of the Nightside Venus Ionosphere: Final Encounter of the *Pioneer Venus* Orbiter Ion Mass Spectrometer, *Geophys. Res. Lett.* **20**, 2731-2734, 1993.

Cobos, C.J., H. Hippler, and J. Troe, Falloff Curves of the Recombination Reaction O + SO $+M \rightarrow SO_2 + M$ in a Variety of Bath Gases, *J. Phys. Chem.* **89**, 1778-1783, 1985.

Colin, R., Spectrum of SO: Analysis of the $B^3\Sigma^-$ - $X^3\Sigma^-$ and $A^3\Pi$ - $X^3\Sigma^-$ Band Systems, *Can. J. Phys.* **47**, 979-994, 1969.

Colton, R.J., and J.W. Rabalais, Photoelectron and Electronic Absorption Spectra of SCl_2, S_2Cl_2, S_2Br_2, and $(CH_3)_2S_2$, *J. Electr. Spectr. Rel. Phenom.* **3**, 345-357, 1974.

Connes, P., J. Connes, L. Kaplan, and W. Benedict, Traces of HCl and HF in the Atmosphere of Venus, *Ap. J.* **147**, 1230-1237, 1967.

Connes, P., J. Connes, L.D. Kaplan, and W.S. Benedict, Carbon Monoxide in the Venus Atmosphere, *Ap. J.* **152**, 731-743, 1968.

Connes, P., J. Connes, F. Noxon, W. Traub, and N. Carlton, $O_2(^1\Delta)$ Emission in the Day & Night Airglow of Venus, *Ap. J.* **233**, L29-L32, 1979.

Conway, R.R., R.P. McCoy, C.A. Barth, and A.L. Lane, IUE Detection of Sulfur Dioxide in the Atmosphere of Venus, *Geophys. Res. Lett.* **6**, 629-631, 1979.

Crisp, D., Radiative Forcing of the Venus Mesosphere I: Solar Fluxes and Heating Rates, *Icarus* **67**, 484-514, 1986.

Crisp, D., D. Allen, D. Grinspoon, and J. Pollack, The Dark Side of Venus: Near-Infrared Images and Spectra from the Anglo-Australian Observatory, *Science* **253**, 1263-1266, 1991.

Crisp, D., V.S. Meadows, B. Bezard, C. de Bergh, J-P Maillard, and F.P. Mills, Ground-based Near-Infrared Observations of the Venus Night Side: Near-Infrared $O_2(^1\Delta)$ Airglow from the Upper Atmosphere, *J. Geophys. Res.* **101**, 4577-4593, 1996.

Croce de Cobos, A.E., and J. Troe, High-pressure Range of the Recombination O + $O_2 = O_3$, *Int. J. Chem. Kin.* **16**, 1519-1529, 1984.

Dahneke, B., Simple Kinetic Theory of Brownian Diffusion in Vapors and Aerosols, in *Theory of Dispersed Multiphase Flow*, ed. R.E. Meyer, (Academic Press, New York), 97-133, 1983.

Davenport, J., B. Ridley, H.I. Schiff, and K.H. Welge, General Discussion regarding Reactions of Excited Species in the Photolysis of Ozone, *Far. Disc. of the Chem. Soc.* **53**, 230-231, 1972.

Davis, D.D., W. Wong, and J. Lephardt, A Laser Flash Photolysis-Resonance Fluorescence Kinetic Study: Reaction of $O(^3P)$ with O_3, *Chem. Phys. Lett.* **22**, 273-278, 1973.

de Bergh, C., B. Bezard, T. Owen, D. Crisp, J-P Maillard, and B.L. Lutz, Deuterium on Venus: Observations from Earth, *Science* **251**, 547-549, 1991.

DeMore, W.B., and E. Tschuikow-Roux, Ultraviolet Spectrum and Chemical Reactivity of the ClO Dimer, *J. Phys. Chem.* **94**, 5856-5860, 1990.

DeMore, W.B., M-T. Leu, R.H. Smith, and Y.L. Yung, Laboratory Studies on the Reactions Between Chlorine, Sulfur Dioxide, and Oxygen: Implications for the Venus Stratosphere, *Icarus* **63**, 347-353, 1985.

DeMore, W., M. Molina, S. Sander, D. Golden, R. Hampson, M. Kurylo, C. Howard, and A. Ravishankara, *Chemical Kinetics and Photochemical Data for Use in Stratospheric Modeling: Evaluation number 8*, Jet Propulsion Laboratory Publication 87-41, 1987.

DeMore, W., S. Sander, D. Golden, M. Molina, R. Hampson, M. Kurylo, C. Howard, and A. Ravishankara, *Chemical Kinetics and Photochemical Data for Use in Stratospheric Modeling: Evaluation number 9*, Jet Propulsion Laboratory Publication 90-1, 1990.

DeMore, W., S. Sander, D. Golden, R. Hampson, M. Kurylo, C. Howard, A. Ravishankara, C. Kolb, and M. Molina, *Chemical Kinetics and Photochemical Data*

for Use in Stratospheric Modeling: Evaluation number 10, Jet Propulsion Laboratory Publication 92-20, 1992.

DeMore, W.B., S.P. Sander, D.M. Golden, R.F. Hampson, M.J. Kurylo, C.J. Howard, A.R. Ravishankara, C.E. Kolb, and M.J. Molina, *Chemical Kinetics and Photochemical Data for Use in Stratospheric Modeling Evaluation 11*, Jet Propulsion Laboratory Publication 94-26, 1994.

DeMore, W.B., S.P. Sander, D.M. Golden, R.F. Hampson, M.J. Kurylo, C.J. Howard, A.R. Ravishankara, C.E. Kolb, and M.J. Molina, *Chemical Kinetics and Photochemical Data for Use in Stratospheric Modeling Evaluation 12*, Jet Propulsion Laboratory Publication 97-4, 1997.

Ditchburn, R.W., and P.A. Young, The Absorption of Molecular Oxygen Between 1850 and 2500 Angstrom, *J. Atmos. Terr. Phys.* **24**, 127-139, 1962.

Donahue, T.M., Deuterium on Venus, *Nature* **340**, 513-514, 1989.

Donaldson, D.J., A.R. Ravishankara, and D.R. Hanson, Detailed Study of HOCl + HCl $\rightarrow$ Cl_2+ H_2O in Sulfuric Acid, *J. Phys. Chem. A* **101**, 4717-4725, 1997.

Donovan, R.J., D. Husain, and P.T. Jackson, Spectroscopic and Kinetic Studies of the SO Radical and the Photolysis of Thionyl Chloride, *Trans. Faraday Soc.* **65**, 2930-2940, 1969.

Dubey, M.K., and G.P. Smith, Model Sensitivity-Uncertainty Analysis and Elementary Rate Theory Calculations Applied to Stratospheric ClO/HCl, 14th Informal Symposium on Kinetics and Photochemistry in the Atmosphere, (San Diego, February 19), 1997.

Ebata, T., O. Nakazawa, and M. Ito, Rovibrational Dependences of the Predissociation in the C^1B_2 State of SO_2, *Chem. Phys. Lett.* **143**, 31-37, 1988.

Edlen, B., The Refractive Index of Air, *Metrologia* **2**, 71-80, 1966.

Effenhauser, C.S., P. Felder, and J.R. Huber, Two-Photon Dissociation of Sulfur Dioxide at 248 and 308 nm, *Chem. Phys.* **142**, 311-320, 1990.

Eibling, R.E., and M. Kaufman, Kinetics Studies Relevant to Possible Coupling Between the Stratospheric Chlorine and Sulfur Cycles, *Atmos. Environ.* **17**, 429-431, 1983.

Ellis, D.M., J.J. McGarvey, and W.D. McGrath, Reaction of O(3P) Atoms with Ozone, *Nature Physical Science* **229**, 153-154, 1971.

Encrenaz, Th., E. Lellouch, G. Paubert, and S. Gulkis, First Detection of HDO in the Atmosphere of Venus at Radio Wavelengths – An Estimate of the H_2O Vertical Distribution, *Astron. Astrophys.* **246**, L63-L66, 1991.

Encrenaz, Th., E. Lellouch, J. Cernicharo, G. Paubert, S. Gulkis, and T. Spilker, The Thermal Profile and Water Abundance in the Venus Mesosphere from H_2O and HDO Millimeter Observations, *Icarus* **117**, 162-172, 1995.

Fair, R.W., and B.A. Thrush, Mechanism of S_2 Chemiluminescence in the Reaction of Hydrogen Atoms with Hydrogen Sulphide, *Trans. Faraday Soc.* **65**, 1208-1218, 1969.

Feautrier, P., Sur la Rèsolution Numèrique de l'*È*quation de Transfert, *C. R. Acad. Sci. Paris* **258**, 3139-3194, 1964.

Feher, F., and H. Munzner, Ultraviolett-Absorptionsspektren Kettenformiger Schwefelverbindungen, *Chemische Berichte* **96**, 1131-1149, 1963.

Felder, P., C.S. Effenhauser, B.M. Haas, and J.R. Huber, Photodissociation of Sulfur Dioxide at 193 nm, *Chem. Phys. Lett.* **148**, 417-422, 1988.

Fink, E.H., K.D. Setzer, and J. Wildt, Collision-induced Emission of $O_2(b^1\Sigma_g^+ \rightarrow a^1\Delta_g)$ in the Gas Phase, *Int. J. Quant. Chem.* **39**, 287-298, 1991.

Flesca, N.G., A-M. Diamy, R.I. Ben-Aim, Contribution a l'Etude de la Chimionisation dans une Flamme de Propane et d'Oxygene Soumis a une Decharge Microondes, *J. Chim. Phys.* **76**, 681-686, 1979.

Fowles, P., J. deSorgo, A.J. Yarwood, O.P. Strausz, and H.E. Gunning, The Reactions of Sulfur Atoms. IX. The Flash Photolysis of Carbonyl Sulfide and the Reactions of S(^{1}D) Atoms with Hydrogen and Methane, *J. Amer. Chem. Soc.* **89**, 1352-1362, 1967.

Fox, J., and S. Bougher, Structure, Luminosity, and Dynamics of the Venus Thermosphere, *Space Science Reviews* **55**, 357-489, 1991.

Francisco, J.S., and A.N. Goldstein, The Structure and Dissociation Energetics of Low-lying States of the Chloroformyl Radical, ClCO, *Chem. Phys.* **128**, 367-372, 1988.

Freeman, D.E., K. Yoshino, J.R. Esmond, and W.H. Parkinson, High Resolution Absorption Cross-section Measurements of Ozone at 195 K in the Wavelength Region 240 - 350 nm, *Planet. Space Sci.* **32**, 239-248, 1984a.

Freeman, D.E., K. Yoshino, J.R. Esmond, and W.H. Parkinson, High Resolution Absorption Cross-section Measurements of SO_2 at 213 K in the Wavelength Region 172 - 240 nm, *Planet. Space Sci.* **32**, 1125-1134, 1984b.

Gamache, R.R., A. Goldman, and L.S. Rothman, Improved Spectral Parameters for the Three Most Abundant Isotopomers of the Oxygen Molecule, *J. Quant. Spectrosc. Radiat. Transfer* **59**, 495-509, 1998.

Gel'man, B.G., V.G. Zolotukhin, N.I. Lamonov, B.V. Levchuk, A.N. Lipatov, L.M. Mukhin, D.F. Nenarokov, V.A. Rotin, and B.P. Okhotnikov, Analysis of Chemical Composition of Venus Atmosphere by Gas Chromatograph on *Venera 12*, *Kosmich. Issled.* **17**, 708-713, 1979. (English translation, *Cosmic Res.* **17**, 585-589, 1980)

Giauque, W.F., E.W. Hornung, J.E. Kunzler, and T.R. Rubin, The Thermodynamic Properties of Aqueous Sulfuric Acid Solutions and Hydrates from 15 to 300 K, *J. Am. Chem. Soc.* **82**, 62-70, 1960.

Gibson, S.T., H.P.F. Gies, A.J. Blake, D.G. McCoy, and P.J. Rogers, Temperature Dependence in the Schumann-Runge Photoabsorption Continuum of Oxygen, *J. Quant. Spectrosc. Radiat. Transfer* **30**, 385-393, 1983.

Gmitro, J.I., and T. Vermeulen, Vapor-Liquid Equilibria for Aqueous Sulfuric Acid, *A.I.Ch.E. Journal* **10**, 740-746, 1964.

Goody, R.M., and Y.L. Yung, *Atmospheric Radiation Theoretical Basis*, (Oxford University Press, Oxford, 519 pp.), 1989.

Greenwood, N.N., and A. Earnshaw, *Chemistry of the Elements*, (Pergamon Press, Oxford, 1542 pp.), 1984.

Griggs, M., Absorption Coefficients of Ozone in the Ultraviolet and Visible Regions, *J. Chem. Phys.* **49**, 857-859, 1968.

Gurnett, D.A., W.S. Kurth, A. Roux, R.Gendrin, C.F. Kennel, and S.J. Bolton, Lightning and Plasma-wave Observations from the *Galileo* Flyby of Venus, *Science* **253**, 1522-1525, 1991.

Gurwell, M., D. Muhleman, K. Shah, G. Berge, D. Rudy, and A. Grossman, Observations of the CO Bulge on Venus and Implications for Mesospheric Winds, *Icarus* **115**, 141-158, 1995.

Hampson, R.F., *Chemical Kinetic and Photochemical Data Sheets for Atmospheric Reactions*, Federal Aviation Administration Report FAA-EE-80-17, 1980.

Hansell, S.A., W.K. Wells, and D.M. Hunten, Optical Detection of Lightning on Venus, *Icarus* **117**, 345-351, 1995.

Hansen, J.E., and J.W. Hovenier, Interpretation of the Polarization of Venus, *J. Atmos. Sci.* **31**, 1137-1160, 1974.

Hapke, B., and F. Graham, Spectral Properties of Condensed Phases of Disulfur Monoxide, Polysulfur Oxide, and Irradiated Sulfur, *Icarus* **79**, 47-55, 1989.

Hartle, R.E., and H.A. Taylor, Identification of Deuterium Ions in the Ionosphere of Venus, *Geophys. Res. Lett.* **10**, 965-968, 1983.

Hartley, K.K., A.R. Wolff, and L.D. Travis, Croconic Acid: An Absorber in the Venus Clouds?, *Icarus* **77**, 382-390, 1989.

Hearn, C.H., and J.A. Joens, The Near UV Absorption Spectrum of CS_2 and SO_2 at 300 K, *J. Quant. Spectrosc. Radiat. Transfer* **45**, 69-75, 1991.

Heicklen, J., Gas Phase Oxidation of Perhalocarbon, *Advan. Photochem.* **7**, 57, 1969.

Henyey, L.C., and J.L. Greenstein, Diffuse Radiation in the Galaxy, *Ap. J.* **93**, 70-83, 1941.

Herron, J.T., and R.E. Huie, Rate Constants at 298 K for the Reactions SO + SO $+M \rightarrow (SO)_2 + M$ and SO + $(SO)_2 \rightarrow SO_2$+ S_2O, *Chem. Phys. Lett.* **76**, 322-324, 1980.

Hewitt, A.D., K.M. Brahan, G.D. Boone, and S.A. Hewitt, Kinetics and Mechanism of the Cl + CO Reaction in Air, *Int. J. Chem. Kin.* **28**, 763-771, 1996.

Hildebrandt, B., H. Vanni, and H. Heydtmann, Infrared Chemiluminescence in the Reactions of 0.45 eV Hydrogen Atoms with Cl_2, SCl_2, and PCl_3, *Chem. Phys.* **84**, 125-137, 1984.

Hochanadel, C.J., J.A. Ghormley, and J.W. Boyle, Vibrationally Excited Ozone in the Pulse Radiolysis and Flash Photolysis of Oxygen, *J. Chem. Phys.* **48**, 2416-2420, 1968.

Hoffman, J.H., V.I. Oyama, and U. von Zahn, Measurements of the Venus Lower Atmosphere Composition: A Comparison of Results, *J. Geophys. Res.* **85**, 7871-7881, 1979.

Hogan, L.G., and D.S. Burch, A Measurement of the Rate Constant for the Reaction $O + O_2 + O_2 \rightarrow O_3 + O_2$, *J. Chem. Phys.* **65**, 894-900, 1976.

Hopkins, A.G., S-Y. Tang, and C.W. Brown, Infrared and Raman Spectra of the Low-Temperature Produts from Discharged Sulfur Dioxide, *J. Am. Ch. Soc.* **95**, 3486-3490, 1973.

Howe, J.D., M.N.R. Ashford, R.A. Morgan, C.M. Western, W.J. Buma, J.B. Milan, and C.A. de Lange, Observation of the SCl Radical by Resonance-enhanced Multiphoton Ionisation Spectroscopy, *J. Chem. Soc. Faraday Trans.* **91**, 773-780, 1995.

Hsu, Y.T., Y.P. Lee, and J.F. Ogilvie, Intensities of Lines in the Band $a^1\Delta_g(v'=0) \rightarrow X^3\Sigma_g(v''=0)$ of $^{16}O_2$ in Absorption, *Spectrochim. Acta* **48**, 1227-1230, 1992.

Huder, K.J., and W.B. DeMore, Absorption Cross-sections of the ClO Dimer, *J. Phys. Chem.* **99**, 3905-3908, 1995.

Hui, M-H., and S.A. Rice, Decay of Fluorescence from Single Vibronic States of SO_2, *Chem. Phys. Lett.* **17**, 474-478, 1972.

Huie, R.E., J.T. Herron, and D.D. Davis, Absolute Rate Constants for the Reaction $O + O_2 + M \rightarrow O_3 + M$ over the Temperature Range 200-346 K, *J. Phys. Chem.* **76**, 2653-2658, 1972.

Hunten, D.M., Venus Lightning: Pros and Cons, *Adv. Space Res.* **15(4)**, 109-112, 1995.

Hunten, D.M., T.M. Donahue, J.C.G. Walker, and J.F. Kasting, Escape of Atmospheres and Loss of Water, in *Origin and Evolution of Planetary and Satellite Atmospheres*, (Univ. of Arizona Press, Tucson, AZ), 396, 1989.

Inn, E.C.Y., Rate Constant for the Reaction $CO(^1\Sigma^+) + O(^3P) + CO_2 \rightarrow 2CO_2$, *J. Chem. Phys.* **59**, 5431-5433, 1973.

Inn, E.C.Y., Rate of Recombination of Oxygen Atoms and CO at Temperatures Below Ambient, *J. Chem. Phys.* **61**, 1589-1590, 1974.

Intezarova, E.I., and V.N. Kondrat'ev, Thermal Decomposition of Ozone, *Izvest. Akad. Nauk USSR, Ser. Khim.* **11**, 2440-2446, 1967. (English translation, *Bulletin of the Academy of Sciences ofthe USSR, Division of Chemical Sciences* **11**, 2326-2331, 1967)

Jacox, M.E., and D.E. Milligan, Matrix Isolation Study of the Reaction of Cl Atoms with CO. The Infrared Spectrum of the Free Radical ClCO, *J. Chem. Phys.* **43**, 866-870, 1965.

Jakubowski, E., M.G. Ahmed, E.M. Lown, H.S. Sandhu, R.K. Gosavi, and O.P. Strausz, Sulfur Atom Abstraction from Episulfides and Carbonyl Sulfide by Methyl Radicals, *J. Am. Chem. Soc.* **94**, 4094-4101, 1972.

Johnston, H.S., M. Paige, and F. Yao, Oxygen Absorption Cross Sections in the Herzberg Continuum and Between 206 and 327 K, *J. Geophys. Res.* **89**, 11661-11665, 1984.

Jones, A.V., Infra-red and Ultraviolet Spectra of Sulphur Monoxide, *J. Chem. Phys.* **18**, 1263-1268, 1950.

Kaufman, F., Elementary Gas Reactions, in *Annual Review of Physical Chemistry 20*, (Annual Review, Palo Alto, CA), 45-90, 1969.

Kaufman, F., and J.R. Kelso, Rate Constant of the Reaction $O + 2O_2 \rightarrow O_3 + O_2$, *Disc. Faraday Soc.* **37**, 26-37, 1964.

Kaufman, F., and J.R. Kelso, M Effect in the Gas-phase Recombination of O with O_2, *J. Chem. Phys.* **46**, 4541-4543, 1967.

Kawasaki, M., and H. Sato, Photodissociation of Molecular Beams of SO_2 at 193 nm, *Chem. Phys. Lett.* **139**, 585-588, 1987.

Keating, G.M., J.L. Bertaux, S.W. Bougher, T.E. Cravens, R.E. Dickinson, A.E. Hedin, V.A. Krasnopol'sky, A.F. Nagy, J.Y. Nicholson, III, L.J. Paxton, and U. von Zahn, Models of Venus Neutral Upper Atmosphere: Structure and Composition, *Adv. Space Res.* **5**, 117, 1986.

Keyser, L.F., Absolute Rate-constant and Branching Fractions for the H and HO_2 Reaction from 245-K to 300-K, *J. Phys. Chem.* **90**, 2994-3003, 1986.

Kita, D., and D.H. Stedman, Kinetic Studies of Reactions of Hydrogen Atoms with HCl, Cl_2, and NOCl, and Chlorine Atoms with H_2 and NOCl, *J. Chem. Soc. Faraday Trans. II* **78**, 1249-1259, 1982.

Klais, O., P.C. Anderson, and M.J. Kurylo, A Reinvestigation of the Temperature Dependence of the Rate Constant for the Reaction $O + O_2 + M \rightarrow O_3 + M$ (for M = O_2, N_2, and Ar) by the Flash Photolysis Resonance Fluorescence Technique, *Int. J. Chem. Kin.* **12**, 469-490, 1980.

Klemm, R.B., and D.D. Davis, A Flash Photolysis-Resonance Fluorescence Kinetics Study of the Reaction $S(^3P)$ + OCS, *J. Phys. Chem.* **78**, 1137-1140, 1974.

Kley, D., Ly (α) Absorption Cross-section of H_2O and O_2, *J. Atmos. Chem.* **2**, 203-210, 1984.

Knollenberg, R.G., and D.M. Hunten, The Microphysics of the Clouds of Venus: Results of the *Pioneer* Venus Particle Size Spectrometer Experiment, *J. Geophys. Res.* **85**, 8039-8058, 1980.

Knollenberg, R., L. Travis, M. Tomasko, P.Smith, B. Ragent, L. Esposito, D. McCleese, J. Martonchick, and R. Beer, The Clouds of Venus: A Synthesis Report, *J. Geophys. Res.* **85**, 8059-8081, 1980.

Kondrat'yev, V.N., *The Rate Constants of Gas-Phase Reactions*, (Nanka, Moscow), 1971.

Krasnoperov, L.N., E.N. Chesnokov, and V.N. Panfilov, The Time-resolved LMR Method as used to Measure Elementary Reaction Rates of Cl Atoms and SiH_3 Radicals in Pulse Photolysis of S_2Cl_2 in the Presence of SiH_4, *Chem. Phys.* **89**, 297-305, 1984.

Krasnopol'sky, V. and V. Parshev, *Kosmich. Issled.* **19**, 87, *Cosmic Res.* **19**, 261-278, 1981.

Krasnopol'sky, V.A., and V.A. Parshev, Photochemistry of the Venus Atmosphere, in *Venus*, ed. Hunten, D.M., L. Colin, T.M. Donohue, and V.I. Moroz, (Univ. of Arizona Press, Tucson, AZ), 431-458, 1983.

Krasnopolsky, V.A., and J.B. Pollack, H_2O–H_2SO_4 System in Venus' Clouds and OCS, CO, and H_2SO_4 Profiles in Venus' Troposphere, *Icarus* **109**, 58-78, 1994.

Ksanfomaliti, L.V., Lightning in the Cloud Layer of Venus, *Kosm. Issled.* **17**, 747, 1979.

Ksanfomality, L.V., F.L. Scarf, and W.W.L. Taylor, The Electrical Activity of the Atmosphere of Venus, *Venus*, ed. Hunten, D.M., L. Colin, T.M. Donohue, and V.I. Moroz, (Univ. of Arizona Press, Tucson, AZ), 565-603, 1983.

Kumar, S. and H. Taylor, Jr., Deuterium on Venus: Model Comparisons with *Pioneer Venus* Observations of the Predawn Bulge Ionosphere, *Icarus* **62**, 494-504, 1985.

Kumar, S., D. Hunten, and H. Taylor, Jr., H_2 Abundance in the Atmosphere of Venus, *Geophys. Res. Lett.* **8**, 237-240, 1981.

Lakshminarayana, G., Ultraviolet Band Systems of S_2O, *J. Molec. Spectrosc.* **55**, 141-150, 1975.

Lalo, C., and C. Vermeil, Photolysis of SO_2 at 123.6 nm in the presence of H_2, *J. Photochem.* **1**, 321-325, 1972.

Lalo, C., and C. Vermeil, Photochemistry of SO_2 in the Vacuum-UV II. Luminescence Studies, *J. Photochem.* **3**, 441-454, 1974.

Lane, W.A., and R. Opstbaum, High Altitude Venus Haze from Pioneer Venus Limb Scans, *Icarus* **54**, 48-58, 1983.

Langford, R.B., and G.A. Oldershaw, Mechanism of Sulphur Formation in the Flash Photolysis of Carbonyl Sulphide, *J.C.S. Faraday I* **69**, 1389-1397, 1973.

Laszlo, B., and S.P. Sander, Kinetics Studies of the HO_2 + ClO Reaction, 14th Informal Symposium on Kinetics and Photochemistry in the Atmosphere, (San Diego, CA, February 19), 1997.

Lawrence, G.M., Production of $O(^1S)$ from Photodissociation of CO_2, *J. Chem. Phys.* **57**, 5616-5617, 1972.

Lee, L.C., and M. Suto, Quantitative Photoabsorption and Fluorescence Study of H_2O and D_2O at 50-190 nm, *Chem. Phys.* **110**, 161-169, 1986.

Lee, L.C., T.G. Slanger, G. Black, and R.L. Sharpless, Quantum Yields for the Production of $O(^1D)$ from Photodissociation of O_2 at 1160-1770 Angstrom, *J. Chem. Phys.* **67**, 5602-5606, 1977.

Lee, Y.R., C.L. Chiu, and S.M. Lin, Photodissociation of S_2Cl_2 at 308 nm by Translational Spectroscopy, *Chem. Phys. Lett.* **216**, 209-214, 1993.

Leen, T.M., and M.M. Graff, Oxygen Chemistry of Shocked Interstellar Clouds 3. Sulfur and Oxygen Species in Dense Clouds, *Ap. J.* **325**, 411-416, 1988.

Leroy, B., P.Rigaud, J.L. Jourdain, and G. LeBras, Spectres d-Absorption dans le Proche Ultraviolet de CS_2 et SO_2 Entre 200 et 300 K, *The Moon and the Planets* **29**, 177-183, 1983.

Leu, M-T., Rate Constants for the Reaction of OH with SO_2 at Low Pressure, *J. Phys. Chem.* **86**, 4558-4562, 1982.

Leu, M-T., and Y.L. Yung, Determination of $O_2(a^1\Delta_g)$ and $O_2(b^1\Sigma_g^+)$ Yields in the Reaction O + ClO $\rightarrow$ Cl + O_2: Implications for Photochemistry in the Atmosphere of Venus, *Geophys. Res. Lett.* **9**, 949-952, 1987.

Lewis, B.R., and J.H. Carver, Temperature Dependence of the Carbon Dioxide Photoabsorption Cross Section Between 1200 and 1970 Angstrom, *J. Quant. Spectrosc. Radiat. Transfer* **30**, 297-309, 1983.

Lewis, B.R., S.T. Gibson, M. Emami, and J.H. Carver, Resonances in the Photodissociation of Isotopic Molecular Oxygen I. The Longest Band, *J. Quant. Spectrosc. Radiat. Transfer* **40**, 1-13, 1988a.

Lewis, B.R., S.T. Gibson, M. Emami, and J.H. Carver, Resonances in the Photodissociation of Isotopic Molecular Oxygen II. The Second and Third Bands, *J. Quant. Spectrosc. Radiat. Transfer* **40**, 469-477, 1988b.

Libuda, H.G., F. Zabel, E.H. Fink, and K.H. Becker, Formyl Chloride: UVAbsorption Cross Sections and Rate Constants for the Reactions with Cl and OH, *J. Phys. Chem.* **94**, 5860-5865, 1990.

Lin, C.L., and M-T. Leu, Temperature and Third-body Dependence of the Rate Constant for the Reaction O + O_2 + $M \rightarrow O_3 + M$, *Int. J. Chem. Kin.* **14**, 417-434, 1982.

Lin, L-B., Y-P. Lee, and J.F. Ogilvie, Linestrengths of the Band $a^1\Delta_g(v\prime = 0)$ – $X^3\Sigma_g(v\prime\prime = 0)$ of $^{16}O_2$, *J. Quant. Spectrosc. Radiat. Transfer* **39**, 375-380, 1988.

Logan, J.A., M.J. Prather, S.C. Wofsy, and M.B. McElroy, Atmospheric Chemistry: Response to Human Influence, *Phil. Trans. R. Soc. London* **290**, 187-234, 1978.

London, J., G.J. Rottman, T.N. Woods, and F. Wu, Time Variations of Solar UV Irradiance as Measured by the SOLSTICE (UARS) Instrument, *Geophys. Res. Lett.* **20**, 1315-1318, 1993.

Mallard, W.G., F. Westley, J.T. Herron, and R.F. Hampson, NIST Chemical Kinetics Database version 6.0, National Institute of Standards and Technology Standard Reference Data, (Gaithersburg, MD), 1994.

Manatt, S.L., and A.L. Lane, A Compilation of the Absorption Cross-sections of SO_2 from 106 to 403 nm, *J. Quant. Spectrosc. Radiat. Transfer* **50**, 267-276, 1993.

Marshall, T.C., Studies of Atomic Recombination of Nitrogen, Hydrogen, and Oxygen by Paramagnetic Resonance, *Physics of Fluids* **5**, 743-753, 1962.

Marshall, S.A., M. Steinberg, and D.S. Hacker, *Bull. Amer. Physic. Soc.* **5**, 380, 1960.

Martinez, R.I., and J.T. Herron, Methyl Thiirane: Kinetic Gas-phase Titration of Sulfur Atoms in S_xO_y Systems, *Int. J. Chem. Kin.* **15**, 1127, 1983.

Martinez, R.D., and J.A. Joens, SO_2 Absorption Cross-section Measurements from 197 nm to 240 nm, *Geophys. Res. Lett.* **19**, 277-279, 1992.

Massucci, M., S.L. Clegg, and P.Brimblecombe, Equilibrium Vapor Pressure of H_2O Above Aqueous H_2SO_4 at Low Temperature, *J. Chem. Eng. Data* **41**, 765-778, 1996.

Mathias, A., and H.I. Schiff, Mass Spectrometric Studies of Atom Reactions, *Disc. Faraday Soc.* **37**, 38-45, 1964.

McElroy, M.B., and T.M. Donahue, Stability of the Martian Atmosphere, *Science* **177**, 986-988, 1972.

McElroy, M.B., N.D. Sze, and Y.L. Yung, Photochemistry of the Venus Atmosphere, *J. Atmos. Sci.* **30**, 1437-1447, 1973.

McElroy, M.B., M.J. Prather, and J.M. Rodriguez, Escape of Hydrogen from Venus, *Science* **215**, 1614-1615, 1982.

McElroy, M.B., R.J. Salawitch, S.C. Wofsy, and J.A. Logan, Reductions of Antartic Ozone due to Synergistic Interactions of Chlorine and Bromine, *Nature* **321**, 759-762, 1986.

McGee, T.J., and J.R. Burris, Jr., SO_2 Absorption Cross Sections in the Near UV, *J. Quant. Spectrosc. Radiat. Transfer* **37**, 165-182, 1987.

Meier, R.R., G.P. Anderson, C.A. Cantrell, L.A. Hall, J. Lean, K. Minschwaner, R.E. Shetter, E.P. Shettle, and K. Stamnes, Actinic Radiation in the Terrestrial Atmosphere, *J. Atmos. Solar-Terrestrial Phys.* **59**, 2111-2157, 1997.

Meschi, D.J., and R.J. Myers, The Microwave Spectrum, Structure, and Dipole Moment of Disulfur Monoxide, *J. Molec. Spectrosc.* **3**, 405-416, 1959.

Meyer, B., Elemental Sulfur, *Chem. Rev.* **76**, 367-388, 1976.

Michelangeli, D.V., M. Allen, Y.L. Yung, R-L. Shia, D. Crisp, and J. Eluszkiewicz, Enhancement of Atmospheric Radiation by an Aerosol Layer, *J. Geophys. Res.* **97**, 865-874, 1992.

Michelsen, H.A., R.J. Salawitch, P.O. Wennberg, and J.G. Anderson, Production of $O(^1D)$ from Photolysis of O_3, *Geophys. Res. Lett.* **21**, 2227-2230, 1994.

Miller, J.C., and R.J. Gordon, Kinetics of the Cl-H_2 System I. Detailed Balance in the Cl + H_2 Reaction, *J. Chem. Phys.* **75**, 5305-5310, 1981.

Mills, C.T., and L.F. Phillips, Photo-oxidation of CO in a Sulphuric Acid Aerosol, *J. Photochem. Photobiol. A: Chem.* **74**, 7-9, 1993.

Mills, C.T., and L.F. Phillips, Quantum Yields of CO_2 and SO_2 Formation from 193 nm Photooxidation of CO, *J. Photochem. Photobiol. A: Chem.* **93**, 83-87, 1996.

Mlynczak, M.G., and D.J. Nesbitt, The Einstein Coefficient for Spontaneous Emission of the $O_2(a^1\Delta_g)$ state, *Geophys. Res. Lett.* **22**, 1381-1384, 1995.

Molina, L.T., and M.J. Molina, Absolute Absorption Cross Sections of Ozone in the 185- to 350-nm Wavelength Range, *J. Geophys. Res.* **91**, 14501-14508, 1986.

Molina, M.J., and F.S. Rowland, Stratospheric Sink for Chlorofluoromethanes: Chlorine-atom Catalyzed Destruction of Ozone, *Nature* **249**, 810-812, 1974.

Molina, L.T., J.J. Lamb, and M.J. Molina, Temperature Dependent UV Absorption Cross Sections for Carbonyl Sulfide, *Geophys. Res. Lett.* **8**, 1008-1011, 1981.

Morgan, J.E., and H.I. Schiff, Recombination of Oxygen Atoms in the Presence of Inert Gases, *J. Chem. Phys.* **38**, 1495-1500, 1963.

Moroz, V.I. Magnitude and Albedo Data of Venus, *Venus*, ed. Hunten, D.M., L. Colin, T.M. Donohue, and V.I. Moroz, (Univ. of Arizona Press, Tucson, AZ), 27-35, 1983.

Mount, G.H., G.J. Rottman, and J.G. Timothy, The Solar Spectral Irradiance 1200 - 2550 Angstrom at Solar Maximum, *J. Geophys. Res.* **85**, 4271-4274, 1980.

Mozurkewich, M., and S.W. Benson, Self-Reaction of HO_2 and DO_2: Negative Temperature Dependence and Pressure Effects, *Int. J. Chem. Kin.* **17**, 787-807, 1985.

Mukhin, L.M., B.G. Gel'man, N.I. Lamonov, V.V. Mel'nikov, D.F. Nenarokov, B.P. Okhotnikov, V.A. Rotin, and V.N. Khokhlov, Gas-Chromatograph Analysis of the Chemical Composition of the Atmosphere of Venus by the Landers of the *Venera 13* and *Venera 14* Spacecraft, *Kosmich. Issled.* **21**, 225-230, 1983. (English translation, *Cosmic Res.* **21**, 168-172, 1983)

Murray, J.T., W.A. Little, Jr., Q. Williams, and T.L. Weatherly, Molecular Constants of Sulfur Dichloride from Microwave Spectrum Analysis, *J. Chem. Phys.* **65**, 985, 1976.

Murrells, T.P., Elementary Reactions of the SCl Radical Part I., *J. Chem. Soc. Faraday Trans. II* **84**, 67-83, 1988a.

Murrells, T.P., Elementary Reactions of the SCl Radical Part II., *J. Chem. Soc. Faraday Trans. II* **84**, 85-94, 1988b.

Myer, J.A., and J.A.R. Samson, Vacuum Ultraviolet Absorption Cross Sections of CO, HCl, and ICN Between 1050 and 2100 Angstrom, *J. Chem. Phys.* **52**, 266-271, 1970.

Na, C.Y., and L.W. Esposito, UV Observations of Venus with HST, American Astronomical Society Division of Planetary Sciences Conference, (Mauna Lani, HI, October 1995), 1995.

Na, C.Y., and L.W. Esposito, Is Disulfur Monoxide a Second Absorber on Venus?, *Icarus* **125**, 364-368, 1997.

Na, C.Y., L.W. Esposito, and T.E. Skinner, International Ultraviolet Explorer Observation of Venus SO_2 and SO, *J. Geophys. Res.* **95**, 7485-7491, 1990.

Na, C.Y., L.W. Esposito, W.E. McClintock, and C.A. Barth, Sulfur Dioxide in the Atmosphere of Venus, *Icarus* **112**, 389-395, 1994.

Nair, H., M. Allen, A.D. Anbar, and Y.L. Yung, A Photochemical Model of the Martian Atmosphere, *Icarus* **111**, 124-150, 1994.

Neckel, H., and D. Labs, The Solar Radiation Between 3300 and 12500 Angstrom, *Solar Physics* **90**, 205-258, 1984.

Nee, J.B., and L.C. Lee, Vacuum Ultraviolet Photoabsorption Study of SO, *J. Chem. Phys.* **84**, 5303-5307, 1986.

Nicholas, J.E., C.A. Amodio, and M.J. Baker, Kinetics and Mechanism of the Decomposition of H_2S, CH_3SH and $(CH_3)_2S$ in a Radio-frequency Pulse Discharge, *J. Chem. Soc. Faraday Trans. I* **75**, 1868-1875, 1979.

Nicolet, M., The Solar Spectral Irradiance and its Action in the Atmospheric Photodissociation Processes, *Planet. Space Sci.* **29**, 951-974, 1981.

Nicovich, J., K. Kreutter, and P. Wine, Kinetics and Thermochemistry of ClCO Formation from the Cl+CO Association Reaction, *J. Chem. Phys.* **92**, 3539-3544, 1990.

Niki, H., P.D. Maker, C.M. Savage, and L.P. Breitenbach, An FTIR Spectroscopic Study of the Reactions Br + $CH_3CHO \rightarrow$ HBr + CH_3CO and $CH_3C(O)OO$ + NO_2 – Reversible $CH_3C(O)OONO_2$ (PAN), *Int. J. Chem. Kin.* **17**, 525-534, 1985.

Ogawa, S., and M. Ogawa, Absorption Cross Sections of $O_2(a^1\Delta_g)$ and $O_2(X^3\Sigma_g^-)$ in the Region from 1087 to 1700 Angstrom, *Can. J. Phys.* **53**, 1845-1852, 1975.

Ohta, T., Mechanism of Chlorine Catalytic Oxidation of CO in the Gas Phase, *Bull. Chem. Soc. Jpn.* **5**, 869-872, 1983.

Okabe, H., *Photochemistry of Small Molecules*, (Wiley, New York, 431 pp.), 1978.

Old, J.G., K.L. Gentili, and E.R. Peck, Dispersion of Carbon Dioxide, *J. Opt. Soc. Am.* **61**, 89-90, 1971.

Oommen, *Spectra and Reactions of Elemental Sulfur*, Ph.D. Dissertation, University of Washington, (Seattle, WA, 214 pp.), 1970.

Oyama, V.I., G.C. Carle, F. Woeller, J.B. Pollack R.T. Reynolds, and R.A. Craig, *Pioneer Venus* Gas Chromatography of the Lower Atmosphere of Venus, *J. Geophys. Res.* **85**, 7891-7902, 1980.

Parisot, J-P., and G. Moreels, Photochemistry of Fluorine in the Mesosphere of Venus, *Icarus* **59**, 69-73, 1984.

Park, J., Y. Lee, and G.W. Flynn, Tunable Diode Laser Probe of Chlorine Atoms Produced from the Photodissociation of a Number of Molecular Precursors, *Chem. Phys. Lett.* **186**, 441-449, 1991.

Parkington, M.J., T.A. Ryan, and K.R. Seddon, Carbonyl Dibromide: A Novel Reagent for the Synthesis of Metal Bromides and Bromide Oxides, *J. Chem. Soc. Dalton Trans.*, 257-261, 1997.

Parkinson, T.M., and D.M. Hunten, Spectroscopy and Aeronomy of O_2 on Mars, *J. Atmos. Sci.* **29**, 1380-1390, 1972.

Patty, R.R., and R.T. Lagemann, The Infrared Spectrum and Molecular Structure of Carbonylbromofluoride, *Spectrochim. Acta* **15**, 60-63, 1959.

Phillips, L., Absolute Absorption Cross Sections for SO Between 190 and 235 nm, *J. Phys. Chem.* **85**, 3994-4000, 1981.

Pollack, J., O. Toon, R. Whitten, R. Boese, B. Ragent, M. Tomasko, L. Esposito, L. Travis, and D. Wiedeman, Distribution and Source of the UV Absorption in Venus' Atmosphere, *J. Geophys. Res.* **85**, 8141-8150, 1980.

Pollack, J.B., J.B. Dalton, D. Grinspoon, R.B. Wattson, R. Freedman, D. Crisp, D.A. Allen, B. Bezard, C. deBergh, L.P. Giver, Q. Ma, and R. Tipping, Near-Infrared Light from Venus' Nightside: A Spectroscopic Analysis, *Icarus* **103**, 1-42, 1993.

Poulet, G., G. Laverdet, and G. Le Bras, *J. Phys. Chem.* **90**, 159-165, 1986.

Prasad, S.S., and T.J. Lee, Atmospheric Chemistry of the Reaction $ClO + O_2 \leftrightarrow ClO \cdot O_2$: Where it Stands, What Needs to Be Done, and Why?, *J. Geophys. Res.* **99**, 8225-8230, 1994.

Prather, M.J., Solution of the Inhomogeneous Rayleigh Scattering Atmosphere, *Ap. J.* **192**, 787-792, 1976.

Prinn, R.G., Photochemistry of HCl and Other Minor Constituents in the Atmosphere of Venus, *J. Atmos. Sci.* **28**, 1058-1068, 1971.

Prinn, R.G., Venus: Chemical and Dynamical Processes in the Stratosphere and Mesosphere, *J. Atmos. Sci.* **32**, 1237-1247, 1975.

Prinn, R.G., Venus: Chemistry of the Lower Atmosphere Prior to the *Pioneer Venus* Mission, *Geophys. Res. Lett.* **5**, 973-976, 1978.

Ragent, B., and J. Blamont, The Structure of the Clouds of Venus: Results of the Pioneer Venus Nephelometer Experiment, *J. Geophys. Res.* **85**, 8089-8106, 1980.

Rau, H., T.R.N. Kutty, and J.R.F. Guedes de Carvalho, Thermodynamics of Sulphur Vapour, *J. Chem. Thermodynamics* **5**, 833-844, 1973.

Ravishankara, A.R., Heterogeneous and Multiphase Chemistry in the Troposphere, *Science* **276**, 1058-1065, 1997.

Robie, D.C., S. Arepalli, N. Presser, T. Kitsopoulos, and R.J. Gordon, The Intramolecular Kinetic Isotope Effect for the Reaction $O(^3P)$ + HD, *J. Chem. Phys.* **92**, 7382-7393, 1990.

Rothman, L.S., R.R. Gamache, R.H. Tipping, C.P. Rinsland, M.A.H. Smith, D.Chris Benner, V. Malathy Devi, J-M. Flaud, C. Camy-Peyret, A. Perrin, A. Goldman, S.T. Massie, L.R. Brown, and R.A. Toth, The HITRAN Molecular Database: Editions of 1991 and 1992, *J. Quant. Spectrosc. Radiat. Transfer* **48**, 469-507, 1992.

Samuel, R., The Dissociation Spectra of Covalent Polyatomic Molecules, *Rev. Modern Phys.* **18**, 103-147, 1946.

Sander, S.P., R.R. Friedl, and Y.L. Yung, Rate of Formation of the ClO Dimer in the Polar Stratosphere: Implications for Ozone Loss, *Science* **245**, 1095-1098, 1989.

Sandor, B.J., R.T. Clancy, D.W. Rusch, C.E. Randall, R.S. Eckman, D.S. Siskind, and D.O. Muhleman, Microwave Observations and Modeling of $O_2(^1\Delta_g)$ and O_3 Diurnal Variation in the Mesosphere, *J. Geophys. Res.* **102**, 9013-9028, 1997.

Sato, T., T. Kinugawa, T. Arikawa, and M. Kawasaki, Two-photon Dissociation of SO_2 in the Ultraviolet Region, *Chem. Phys.* **165**, 173-182, 1992.

Sato, M., L.D. Travis, and K. Kawabata, Photopolarimetry Analysis of the Venus Atmosphere in Polar Regions, *Icarus* **124**, 569-585, 1996.

Schloerb, F.P., S.E. Robinson, and W.M. Irvine, Observations of CO in the Stratosphere of Venus via its $J = 0 \rightarrow 1$ rotation transition. *Icarus* **43**, 121-127, 1980.

Schurgers, M., and K.H. Welge, Absorptionskoeffizient von H_2O_2 und N_2H_4 zwichen 1200 und 2000 Angstrom, *Z. Naturforsch A* **23**, 1508-1510, 1968.

Seeley, J.V., J.T. Jayne, and M.J. Molina, High Pressure Fast-Flow Technique for Gas Phase Kinetics Studies, *Int. J. Chem. Kin.* **25**, 571-594, 1993.

Seiff, A., Models of Venus's Atmospheric Structure, in *Venus*, ed. Hunten, D.M., L. Colin, T.M. Donohue, and V.I. Moroz, (Univ. of Arizona Press, Tucson, AZ), 1045-1048, 1983.

Seinfeld, J.H., *Atmospheric Chemistry and Physics of Air Pollution*, (John Wiley & Sons, New York, 738 pp.), 1986.

Shemansky, D.E., CO_2 Extinction Coefficient 1700 - 3000 Angstrom, *J. Chem. Phys.* **56**, 1582-1587, 1972.

Silvente, E., R.C. Richter, M. Zheng, E.S. Saltzman, and A.J. Hynes, Relative Quantum Yields for $O(^1D)$ Production in the Photolysis of Ozone Between 301 and 336 nm: Evidence for the Participation of a Spin-forbidden Channel, *Chem. Phys. Lett.* **264**, 309-315, 1997.

Singleton, D.L., and R.J. Cvetanovic, Evaluated Chemical Kinetic Data for the Reactions of Atomic Oxygen $O(^3P)$ with Sulfur Containing Compounds, *J. Phys. Chem. Ref. Data* **17**, 1377-1437, 1988.

Siskind, D.E., B.J. Connor, R.S. Eckman, E.E. Remsberg, J.J. Tsou, and A. Parrish, An Intercomparison of Model Ozone Deficits in the Upper Stratosphere and Mesosphere from Two Data Sets, *J. Geophys. Res.* **100**, 11191-11201, 1995.

Slanger, T.G., and G. Black, CO_2 Photolysis Revisited, *J. Chem. Phys.* **68**, 1844-1849, 1978.

Slanger, T.G., and G. Black, Photodissociative Channels at 1216 Angstrom for H_2O, NH_3, and CH_4, *J. Chem. Phys.* **77**, 2432-2437, 1982.

Slanger, T.G., and D.E. Osterbrock, Aeronomy-Astronomy Collaboration Focuses on Nighttime Terrestrial Atmosphere, *Eos (Transactions of the American Geophysical Union)* **79**, 149 and 154, 1998.

Slanger, T.G., B.J. Wood, and G. Black, Kinetics of $O(^3P)$+ CO $+M$ Recombination, *J. Chem. Phys.* **57**, 233-238, 1972.

Snelling, D.R., The Ultraviolet Flash Photolysis of Ozone and the Reactions of $O(^1D)$ and $O_2(^1\Sigma_g^+)$, *Can. J. Chem.* **52**, 257-270, 1974.

Spence, J.W., E.O. Edney, and P.L. Hanst, Peroxychloroformyl Nitrate: Synthesis and Thermal Stability, *Chem. Phys. Lett.* **56**, 478-483, 1978.

Sprague, K.E., and J.A. Joens, SO_2 Absorption Cross-section Measurements from 320 nm to 405 nm, *J. Quant. Spectrosc. Radiat. Transfer* **53**, 349-352, 1995.

Steele, H.M., and P. Hamill, Effects of Temperature and Humidity on the Growth and Optical Properties of Sulfuric Acid-Water Droplets in the Stratosphere, *J. Aerosol Sci.* **12**, 517-528, 1981.

Steudel, R., D. Jensen, P. Gobel, and P. Hugo, Optical-absorption Spectra of the Homocyclic Sulfur Molecules S_n (6, 7, 8, 9, 10, 12, 15, 20) in Solution, *Ber. Bunsenges. Phys. Chem.* **92**, 118-122, 1988.

Stief, L.V., W.A. Payne, and R.B. Klemm, A Flash Photolysis-resonance Fluorescence Study of the Formation of $O(^1D)$ in the Photolysis of Water and the Reaction of $O(^1D)$ with H_2, Ar, and He, *J. Chem. Phys.* **62**, 4000-4008, 1975.

Strattan, L.W., R.E. Eibling, and M. Kauffman, Rate Constant of the Reaction Between Chlorine Atoms and Sulfur Dioxide and its Significance for Stratospheric Chlorine Chemistry, *Atmos. Environ.* **13**, 175-177, 1979.

Stuhl, F., and H. Niki, Measurements of Rate Constants for Termolecular Reactions of $O(^3P)$ with NO, O_2, CO, N_2, and CO_2 Using a Pulsed Vacuum-UV Photolysis-Chemiluminescent Method, *J. Chem. Phys.* **55**, 3943-3953, 1971.

Sung, J.P., and D.W. Setser, Comparisons of Energy Disposal by the Reactions of H Atoms with Cl_2, SCl_2, S_2Cl_2, $SOCl_2$, and SO_2Cl_2, from Observation of HCl Infrared Chemiluminescence, *Chem. Phys. Lett.* **58**, 98-103, 1978.

Suto, M., R.L. Day, and L.C. Lee, Fluorescence Yields from Photodissociation of SO_2 at 1060 - 1330 Angstrom, *J. Phys. B.: At. Mol. Phys.* **15** 4165-4174, 1982.

Sze, N., and M. McElroy, Some Problems in Venus Aeronomy, *Planet. Space Sci.* **23**, 763-786, 1975.

Tabazadeh, A., O.B. Toon, S.L. Clegg, and P.Hamill, A New Parameterization of H_2SO_4/H_2O Aerosol Composition: Atmospheric Implications, *Geophys. Res. Lett.* **24**, 1931-1934, 1997.

Taherian, M.R., and T.G. Slanger, Products and Yields from O_3 Photodissociation at 1576 Angstrom, *J. Chem. Phys.* **83**, 6246-6250, 1985.

Takacs, G.A., Heats of Formation and Bond Dissociation Energies of Some Simple Sulfur- and Halogen-containing Molecules, *J. Chem. Eng. Data* **23**, 174-175, 1978.

Takahashi, K., M. Kishigami, Y. Matsumi, M. Kawasaki, and A.J. Orr-Ewing, Observation of the Spin-forbidden $O(^1D) + O_2(X^3\Sigma)$ Channel in the 317 - 327 nm Photolysis of Ozone, *J. Chem. Phys.* **105**, 5290-5293, 1996.

Tanaka, Y., E.C.Y. Inn, and K. Watanabe, Absorption Coefficients of Gases in the Vacuum Ultraviolet. Part IV. Ozone, *J. Chem. Phys.* **21**, 1651-1653, 1953.

Taylor, F., R. Beer, M. Chahine, d. Diner, L. Elson, R. Haskins, D. McCleese, J. Martonchik, P. Reichley, S. Bradley, J. Delderfield, J. Schofield, C. Farmer, L. Froidevaux, J. Leung, M. Coffey, and J. Gille, Structure and Meteorology of the Middle Atmosphere of Venus: Infrared Remote Sensing from the Pioneer Orbiter, *J. Geophys. Res.* **85**, 7963-8006, 1980.

Thompson, B.A., P. Harteck, and R.R. Reeves, Ultraviolet Absorption Coefficients of CO_2, CO, O_2, H_2O, N_2O, NH_3, NO, SO_2, and CH_4 Between 1850 and 4000 Angstrom, *J. Geophys. Res.* **68**, 6431-6436, 1963.

Tiemann, E., H. Kanamori, and E. Hirota, Infrared Diode Laser Spectroscopy of SCl Generated by The Photolysis of S_2Cl_2 and SCl_2, *J. Molec. Spectrosc.* **137**, 278-285, 1989.

Tokue, I., A. Hiraya, and K. Shobotake, Photoabsorption Spectra and Photodissociation of S_2Cl_2 in the Vacuum Ultraviolet, *Chem. Phys. Lett.* **153**, 346-350, 1988.

Toon, O.B., R.P. Turco, and J.B. Pollack, The Ultraviolet Absorber on Venus: Amorphous Sulfur, *Icarus* **51**, 358-373, 1982.

Traub, W.A., and N.P. Carleton, Observation Of O_2, H_2O, and HD in Planetary Atmospheres, in *Exploration of the Planetary System*, ed. A. Woszczyk and C. Iwaniszewska, (Reidel, Dordrecht, The Netherlands), 223-228, 1974.

Trauger, J., and J. Lunine, Spectroscopy of Molecular Oxygen in the Atmospheres of Venus and Mars, *Icarus* **55**, 272-281, 1983.

Tsang, W., and R.F. Hampson, Chemical Kinetic Data Base for Combustion Chemistry. Part I. Methane and Related Compounds, *J. Phys. Chem. Ref. Data* **15**, 1087-1279, 1986.

Turnipseed, A.A., G.L. Vaghjiani, T. Gierczak, J.E. Thompson, and A.R. Ravishankara, The Photochemistry of Ozone at 193 and 222 nm, *J. Chem. Phys.* **95**, 3244-3251, 1991.

van de Hulst, H.C., *Multiple Light Scattering*, vols. I and II, (Academic, San Diego, CA), 1980.

Venkitachalam, T., and R. Bersohn, Two-photon Dissociation of SO_2 in the Region 285 - 311 nm, *J. Photochem.* **26**, 65-67, 1984.

von Zahn, U., K.H. Fricke, D.M. Hunten, D. Krankowsky, K. Mauersberger, and A.O. Nier, The Upper Atmosphere of Venus During Morning Conditions, *J. Geophys. Res.* **85**, 7829-7840, 1980.

von Zahn, U., S. Kumar, H. Niemann, and R. Prinn, Composition of the Venus Atmosphere, in *Venus*, ed. Hunten, D.M., L. Colin, T.M. Donohue, and V.I. Moroz, (Univ. of Arizona Press, Tucson, AZ), 299-430, 1983.

WMO (World Meteorological Organization), *Atmospheric Ozone 1985*, Global Ozone Research and Monitoring Project Report 16, 1985.

Walker, L.C., and H. Prophet, Enthalpy of Formation of Oxalyl Chloride and the COCl Radical, *Trans. Faraday Soc.* **63**, 879-882, 1966.

Wang, J., D.G. McCoy, A.J. Blake, and L. Torop, Effects of the Close Approach of Potential Curves in Photoabsorption by Diatomic Molecules II. Temperature Dependence of the O_2 Cross Section in the Region 130-160 nm, *J. Quant. Spectrosc. Radiat. Transfer* **38**, 19-27, 1987.

Washida, N., H. Akimoto, and M. Okuda, *Bull. Chem. Soc. Japan* **53**, 3496-3503, 1980.

Watanabe, K., and M. Zelikoff, Absorption Coefficients of Water Vapor in the Vacuum Ultraviolet, *J. Opt. Soc. Amer.* **43**, 753-755, 1953.

Watanabe, K., E.C.Y. Inn, and M. Zelikoff, Absorption Coefficients of Oxygen in the Vacuum Ultraviolet, *J. Chem. Phys.* **21**, 1026-1030, 1953.

Watkins, I.W., Three Electronic Transitions of Sulfur Dioxide in the Vacuum Ultraviolet, *J. Molec. Spectrosc.* **29**, 402-409, 1969.

Watson, R.T., Rate Constants for Reactions of ClO_x of Atmospheric Interest, *J. Phys. Chem. Ref. Data* **6**, 871-917, 1977.

Wayne, R.P., Reactions of Excited Species in the Photolysis of Ozone, *Far. Disc. of the Chem. Soc.* **53**, 172-181 and 230, 1972.

Wayne, R.P., Singlet Oxygen in the Environmental Sciences, *Res. Chem. Intermed.* **20**, 395-422, 1994.

Welge, K.H., Photolysis of O_x, HO_x, CO_x, and SO_x Compounds, *Can. J. Chem.* **52**, 1424-1435, 1974.

Weng, C-J., T-I. Ho, T-M. Su, Laser Photolysis Study of the Recombination Reactions of Atomic Chlorine in Inert Gases, *J. Phys. Chem.* **91**, 5235-5238, 1987.

Wildt, J., G. Bednarek, and E.H. Fink, Laser Excitation of $O_2(b^1\Sigma_g^+, v = 0, 1, 2)$–Rates and Channels of Energy Transfer and Quenching, *Chem. Phys.* **122**, 463-470, 1988.

Wilson, W.J., M.J. Klein, R.K. Kakar, S. Gulkis, E.T. Olsen, and P.T.P. Ho, Venus I. Carbon Monoxide Distribution and Molecular Line Searches, *Icarus* **45**, 624-637, 1981.

Wilson, M.W., M. Rothschild, D.F. Muller, and C.K. Rhodes, Multiphoton Photofragmentation of SO_2 at 248 nm, *J. Chem. Phys.* **77**, 1837-1841, 1982.

Wine, P.H., J.M. Nicovich, and A.R. Ravishankara, Kinetics of the Reations of $O(^3P)$ and $O(^1D)$ with Cl_2, *J. Phys. Chem.* **89**, 3914, 1985.

Wine, P.H., J.R. Wells, and A.R. Ravishankara, Channel Specific Rate Constants for Reactions of O^1D with HCl and HBr, *J. Chem. Phys.* **84**, 1349-1354, 1986.

Winick, J.R., and A.I. Stewart, Photochemistry of SO_2 in Venus' Upper Cloud Layers, *J. Geophys. Res.* **85**, 7849-7860, 1980.

Woo, R., and A. Ishimaru, Eddy Diffusion Coefficient for the Atmosphere of Venus from Radio Scintillation Measurements, *Nature* **289**, 383-384, 1981.

Woods, T.N., D.K. Prinz, G.J. Rottman, J. London, P.C. Crane, R.P. Cebula, E. Hilsenrath, G.E. Brueckner, M.D. Andrews, O.R. White, M.E. VanHoosier, L.E. Gloyd, L.C. Herring, B.G. Knapp, C.K. Pankratz, and P.A. Reiser, Validation of the UARS Solar Ultraviolet Irradiances: Comparison with the ATLAS 1 and 2 Measurements, *J. Geophys. Res.* **101**, 9541-9569, 1996.

Yoshino, K., D.E. Freeman, J.R. Esmond, and W.H. Parkinson, Absolute Absorption Cross-section Measurements of Ozone in the Wavelength Region 238 - 335 nm and the Temperature Dependence, *Planet. Space Sci.* **36**, 395-398, 1988a.

Yoshino, K., A.S-C. Cheung, J.R. Esmond, W.H. Parkinson, D.E. Freeman, S.L. Guberman, A. Jenouvrier, B. Coquart, and M.F. Merienne, Improved Absorption Cross-sections of Oxygen in the Wavelength Region 205-240 nm of the Herzberg Continuum, *Planet. Space Sci.* **36**, 1469-1475, 1988b.

Yoshino, K., J.R. Esmond, A.S-C. Cheung, D.E. Freeman, and W.H. Parkinson, High Resolution Absorption Cross Sections in the Transmission Window Region of the Schumann-Runge Bands and Herzberg Continuum of O_2, *Planet. Space Sci.* **40**, 185-192, 1992.

Yoshino, K., J.R. Esmond, D.E. Freeman, and W.H. Parkinson, Measurements of Absolute Absorption Cross Sections of Ozone in the 185- to 254-nm Wavelength

Region and the Temperature Dependence, *J. Geophys. Res.* **98**, 5205-5211, 1993.

Young, A.T., Revised Depolarization Corrections for Atmospheric Extinction, *Appl. Opt.* **19**, 3427-3428, 1980.

Young L.D.G., High Resolution Spectrum of Venus–A Review, *Icarus* **17**, 632-658, 1972.

Yung, Y., and W. DeMore, Photochemistry of the Stratosphere of Venus: Implications for Atmospheric Evolution, *Icarus* **51**, 199-247, 1982.

Zhang, Q., P. Dupre, B. Grzybowski, and P.H. Vacarro, Laser-induced Fluorescence Studies of Jet-cooled S_2O: Axis-switching and Predissociation Effects, *J. Chem. Phys.* **103**, 67-79, 1995.

Chapter 3

Comparisons of the Photochemical Modeling to Observations

Two approaches have been taken in this attempt to understand the dominant photochemical processes in the Venus middle atmosphere. The results from a new spectroscopic attempt to detect molecular oxygen were presented in Chapter 1. The results from a new one-dimensional photochemical model were described in Chapter 2. Most of the predictions from the photochemical model were compared to the extant, published observations in Sections 2.3.4 and 2.4. A quantitative comparison of the molecular oxygen abundances predicted in Chapter 2, however, was deferred to this chapter because the comparison directly links the modeling from Chapter 2 to the observations and radiative transfer modeling described in Chapter 1. The remainder of this chapter outlines the major conclusions from this combined observational and numerical study of the Venus atmosphere and recommends future studies that are needed to understand the chemistry of the Venus middle atmosphere.

3.1 Radiative Transfer Modeling of the Photochemical Model Predictions for O_2

The column O_2 abundances predicted in the three current models are 8×10^{18}, 1×10^{18}, and 4×10^{17} cm^{-2} for the Nominal, One-Sigma, and Highest ClCO Models, respectively. The 2σ upper limit on the column O_2 abundance from the observation by *Trauger and Lunine* [1983] is 1.5×10^{18} cm^{-2} (above 58 km altitude) or 2×10^{18} cm^{-2} (above 68 km altitude which is approximately optical depth unity), assuming the

mixing ratio of O_2 is the same at all altitudes. The distribution of O_2 predicted by photochemical models, however, is not uniform (Figure 3.1). Because the photochemical models predict that O_2 is concentrated above the upper cloud layer where there are fewer aerosol particles and thus less scattering by the particles, the absorption produced by the predicted O_2 profiles will be smaller than for the uniform profile that was assumed in Chapter 1. In addition, the absorption may be a stronger function of the viewing zenith than was true for the uniform profiles (Table 1.3). Similar effects were noted in comparing the absorption by ozone in the terrestrial troposphere and stratosphere by *Jiang et al.* [1997].

The predicted O_2 profiles from model C of *Yung and DeMore* [1982], the One-Sigma Model, and the Highest ClCO Model were used in the radiative transfer model described in Chapter 1 to provide a quantitative comparison against the observational upper limit. The results for the nominal cloud model that was described in Chapter 1 are shown in Figure 3.2 and Table 3.1. Comparing Tables 1.3 and 3.1, the calculated absorption for the One-Sigma Model is comparable to that for the 2σ observational upper limit (which is equivalent to a uniform mixing ratio of 3×10^{-7}) while the calculated absorption for the Highest ClCO Model is smaller than the 1σ upper limit.

The radiative transfer calculation for the O_2 profile from the Highest ClCO Model was repeated for three alternate cloud models. One was constructed to be similar to that used by *Trauger and Lunine* [1983]. One used the optical depths, cloud scale heights, and particle size distributions from *Knibbe et al.* [1998], *Grinspoon et al.* [1993], and *Pollack et al.* [1993]. The third alternate cloud model was the same as the second, but used the upper haze particle size distribution from *Grinspoon et al.* [1993], and *Pollack et al.* [1993] in lieu of that from *Knibbe et al.* [1998]. The results were within 20% of those obtained using the nominal cloud model.

The O_2 profiles from the photochemical models stop at 58 km altitude because that is the lower boundary for the models. Lacking better information, the O_2 abundance below 58 km altitude was set to zero for the radiative transfer model calculations whose results are presented in Tables 1.3 and 3.1. Two additional calculations were performed in which the O_2 mixing ratio below 58 km was specified to be 1.4×10^{-5}

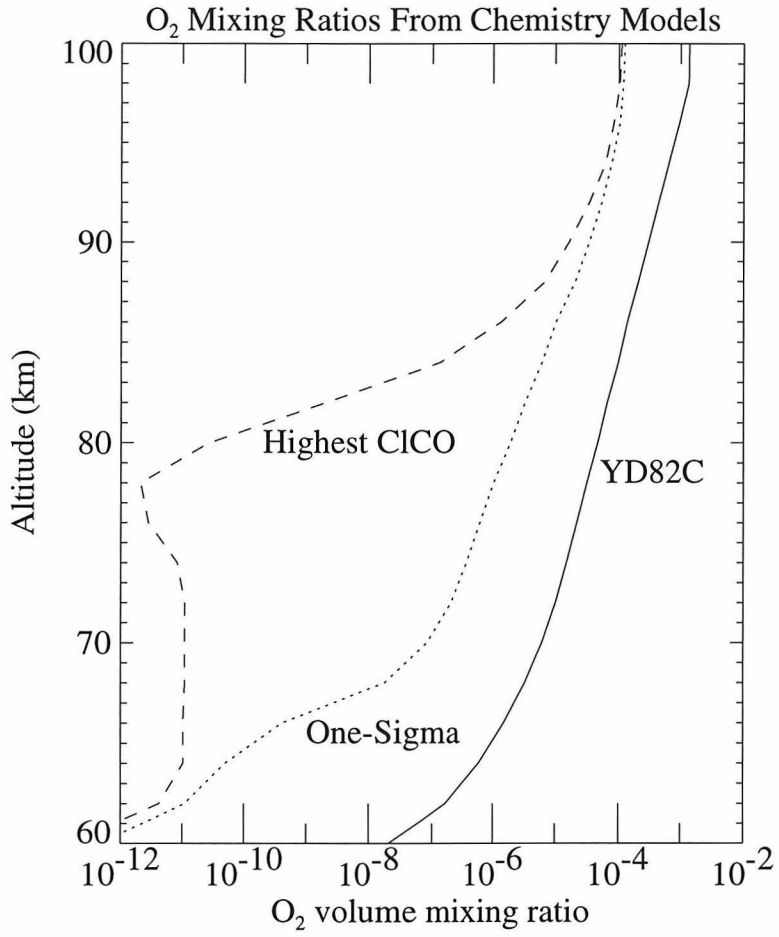

Figure 3.1: Predicted O_2 profiles from three photochemical models. "YD82C" is the O_2 profile from Model C by *Yung and DeMore* [1982]. "One-Sigma" is from the One-Sigma Model described in Chapter 2. "Highest ClCO" is from the Highest ClCO Model described in Chapter 2.

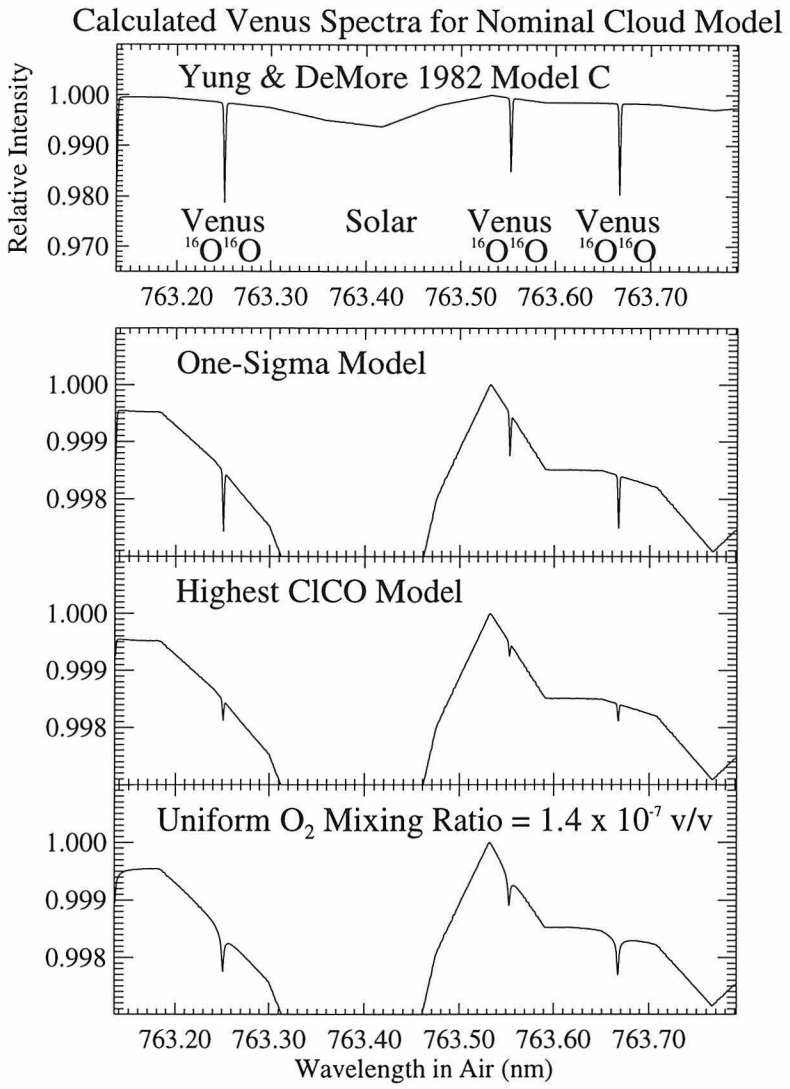

Figure 3.2: Synthetic spectra of the Venus atmosphere for three O_2 profiles from photochemical models. The spectra in these figures were calculated for an incident solar zenith angle of 40 degrees, a viewing zenith angle of 44 degrees, and a relative viewing azimuth angle of 180 degrees. The synthetic spectra have been converted to wavelength in air, Doppler-shifted by the appropriate amount, and convolved with a triangle kernel filter (simulating the UHRF spectrometer response function) to the wavelength resolution and sampling of the UHRF data. The 1σ upper limit on the column abundance is represented by the bottom spectrum. Note the factor of five change in vertical scale between the upper plot and the three lower plots.

Table 3.1: $(\delta I/I)$ for Calculated Spectra for Predicted O_2 Profiles

O_2 Model Profile [a]	Viewing [b] Zen Angle	$10^3 \times (\delta I/I)$ Averaged Over FWHM (pixels) 2	3	4	5	Equivalent Width (nm)
YD82C	29	10	8	7	5	$\sim 1.5 \times 10^{-5}$
	34	10	8	7	5	
	44	10	8	7	5	
	54	10	8	7	5	
One-Sigma	29	0.5	0.4	0.3	0.3	$\sim 7 \times 10^{-7}$
	34	0.5	0.4	0.3	0.3	
	44	0.5	0.4	0.3	0.3	
	54	0.5	0.4	0.3	0.3	
Highest ClCO	29	0.2	0.1	0.1	0.08	$\sim 2 \times 10^{-7}$
	34	0.2	0.1	0.1	0.08	
	44	0.2	0.1	0.1	0.08	
	54	0.2	0.1	0.1	0.08	
A [c]	29	5	4	4	3	
	34	4	4	4	3	
	44	4	4	4	3	
	54	4	4	4	3	
B [d]	29	0.7	0.6	0.5	0.4	
	34	0.7	0.6	0.6	0.5	
	44	0.7	0.6	0.6	0.5	
	54	0.7	0.6	0.6	0.5	

[a] O_2 Model Profiles are shown in Figure 3.2

[b] Viewing zenith angle is given in table. The incident solar zenith angle was 84– (viewing zenith angle). The relative viewing azimuth angle was 180 degrees.

[c] O_2 from Highest ClCO Model was used for $\geq$ 58 km altitude. A uniform mixing ratio of 1.4×10^{-5} was used at lower altitudes.

[d] O_2 from Highest ClCO Model was used for $\geq$ 58 km altitude. A uniform mixing ratio of 1.4×10^{-6} was used at lower altitudes.

and 1.4×10^{-6} while the O_2 mixing ratio at higher altitudes was taken from the Highest ClCO Model. The results are presented in Table 3.1 as Models A and B. The calculated absorptions for Models A and B are larger than those for the Highest ClCO Model indicating some of the scattered sunlight received at the Earth has passed through at least the middle cloud layer, $51 - 57$ km altitude. These calculations indicate the spectroscopic non-detection of O_2 by *Trauger and Lunine* [1983] conflicts with the marginal detection of O_2 at 52 km altitude by *Pioneer Venus* (mixing ratio of $(44 \pm 25) \times 10^{-6}$ [*Oyama et al.* 1980]). This implies either an error in one of the measurements or significant variability (temporally or spatially) in the O_2 abundance within the cloud layers. These calculations confirm the suggestion by *Young* [1972] that spectroscopic measurements of Venus using reflected sunlight can be sensitive to greater pressures than previously believed.

3.2 Conclusions

The long-term evolution (or stability) of the atmosphere of Venus is one of the major unresolved questions within planetary science. A preliminary step that must be solved before we can properly examine the evolution of the Venus atmosphere is to determine the primary photochemical processes within the current epoch. None of the previous photochemical models have been able to find a range of plausible parameters for which the model predictions were within the observational constraints. The work described in Chapters 2 and 3 has shown, for the first time, that the observational constraints may be satisfied if key parameters are adjusted within their assessed or estimated uncertainties. The major conclusions from this observational and numerical study of the Venus atmosphere are outlined in the following paragraphs.

The results from the current study suggest that CO in the Venus atmosphere is primarily oxidized via chlorine catalytic chemistry. *Yung and DeMore* [1982] found that the stability of CO_2 in the Venus atmosphere could be maintained via catalytic chemistry involving hydrogen, nitrogen, or chlorine compounds. However, neither the hydrogen nor the nitrogen dominated catalytic chemistry studied in their mod-

els provided a satisfactory solution that is within the observational constraints that presently exist. Changes have occurred in our understanding of hydrogen and nitrogen chemistry since 1982, but the primary processes governing oxidation of CO have not changed by significant amounts. The results from the current models show that a range of parameters exists in which chlorine-dominated chemistry can satisfy the existing observational constraints if the stability of ClCO is increased by its assessed one standard deviation uncertainty from *DeMore et al.* [1997]. Equivalently, the proposed increase in the stability of ClCO could be due to some other mechanism, such as temperatures below 150 K in the $85 - 90$ km altitude region or the presence of another species that interacts with ClCO on the timescale of ~ 1 second to increase the effective photochemical lifetime of ClCO.

The current observational limit on absorption by O_2 in the Venus middle atmosphere can be reconciled with the predictions from photochemical models if the distribution of O_2 from the photochemical models is compared to the observational limit with the aid of a radiative transfer model. The observational upper limit on absorption by O_2 in the Venus atmosphere when combined with the observed airglow intensities in the $O_2(a^1\Delta)$ band place tight constraints on the amount of O_2 present within and above the cloud layers, the vertical distribution of the O_2, and the mechanism(s) by which it is formed. It is not possible to present a completely satisfactory explanation of the oxygen budget in the Venus atmosphere due to the large uncertainties that exist in observational and laboratory data. The observations and modeling results in Chapters 1, 2, and 3 suggest, though, that (1) O_2 is depleted (mixing ratio $\lesssim 10^{-7}$) within the middle and upper cloud layers ($50-70$ km altitude); (2) the O_2 abundance is largest at $80-100$ km altitude; (3) the production of O_2 via Reaction G3 ($2O + M \rightarrow O_2 + M$) is comparable to the photolysis rate of CO_2 above 90 km altitude; and (4) the effective yield of $O_2(a^1\Delta)$ from Reaction G3 is $\gtrsim 75\%$ in the Venus atmosphere. The intense airglow in the $O_2(a^1\Delta)$ band may have different production mechanisms on the dayside and nightside depending on the interaction between the three-dimensional dynamics and the chemistry. This cannot be studied properly with a one-dimensional "globally-averaged" photochemical model.

The current photochemical model cannot explain the localized regions of intense airglow emission seen in the $O_2(a^1\Delta)$ band ($> 5 \times 10^{12}$ cm^{-2} sec^{-1} [*Crisp et al.* 1996]). Localized phenomena such as this must be studied in the context of either a Chemical Transport Model (in which the dynamics are specified based on external sources of information) or a General Circulation Model (in which the dynamics are calculated internally) such as the Venus Thermospheric GCM [e.g., *Zhang et al.* 1996].

The O_2 abundance in the Venus atmosphere is predicted to be roughly constant over the past 15 years despite the large observed changes in the abundance of SO_2 and SO at the cloud tops. The oxidation of CO to CO_2 appears to control the column abundance of O_2 and the oxidation of CO occurs predominantly above 75 km altitude in the current models. Thus, the oxidation of CO in the current models has been decoupled from the oxidation of SO_2 and the observed changes in the abundances of SO_2 and SO do not produce large changes in the O_2 abundance. This differs from the results obtained by *Yung and DeMore* [1982] because they had only one path, H_2SO_4, by which sulfur could be transported from the middle atmosphere downward to lower altitudes. The current models predict that the observed changes in the abundances of SO_2 and SO should produce large changes in the relative production rates of S_8 and H_2SO_4 within the upper cloud layer.

The upper limit on the absorption due to O_2 in the Venus middle atmosphere derived from new observations is $< 3 \times 10^{-6}$, if the molecular oxygen is uniformly mixed throughout the Venus atmosphere. This is consistent with the upper limit (3×10^{-7}) obtained by *Trauger and Lunine* [1983]. The sensitivity of the new observation, however, was not sufficient to exclude the possibility that the O_2 abundance in the Venus atmosphere is now larger than the upper limit from *Trauger and Lunine* [1983].

The water vapor abundance, at least above $\sim$ 85 km altitude, derived from microwave studies [*Encrenaz et al.* 1995] is consistent with the equilibrium vapor pressure over 75 wt% H_2SO_4 extrapolated from the relations given in *Tabazadeh et al.* [1997]. This agrees with the conclusion from polarimetry studies [*Hansen and Hovenier* 1974] that the composition of the aerosols is consistent with concentrated sulfuric acid, but the uncertainties in both the water vapor observation and the extrapolation

of the equilibrium vapor pressure to conditions for which it has not been measured are too large to quantitatively exclude other proposed alternatives (e.g., formation of water ice).

Heterogeneous chemistry does not appear to be required to explain the oxidation of CO to CO_2. Furthermore, based on existing information heterogeneous chemistry does not appear to be an important element of the chemistry of the Venus middle atmosphere despite the large abundance of aerosol particles that are present. The effectiveness of heterogeneous chemistry is primarily limited by the low predicted abundances of HOCl in the Venus atmosphere and the low solubility of HCl in concentrated sulfuric acid. The presence of reactive nitrogen compounds (such as NO) might change this conclusion because heterogeneous reactions involving nitrogen compounds are more efficient than those involving solely HCl and HOCl in sulfuric acid.

The sulfur abundance and vertical distribution predicted in the current models are comparable to the abundance and distribution for amorphous sulfur that *Toon et al.* [1982] proposed as an explanation for the ultraviolet albedo of Venus. This is the first time that the predictions from a detailed photochemical model calculation may have been reconciled with the required radiative properties of the Venus clouds. Two major problems remain before amorphous sulfur can be confidently regarded as the second ultraviolet absorber. First, the vertical distribution of sulfur below the base of the upper cloud layer needs to be reconciled with the solar flux attenuation observed by the *Pioneer Venus* probes. Second, the spectral characteristics of amorphous sulfur at < 300 nm may not be consistent with the existing observations.

The photochemical modeling presented in Chapter 2 outlines the first quantitative assessment of the roles that SCl_x and $SClO_x$ compounds may play in the chemistry within the upper cloud layer. The results suggest that SCl_x and $SClO_x$ compounds may be viable alternative candidates for the second ultraviolet absorber and that these compounds may regulate the disproportionation of SO_2 and OCS into S_8 and H_2SO_4.

Spectroscopic studies of the Venus atmosphere using reflected sunlight as the source for illumination can be sensitive to the presence of species below the base of

the upper cloud ($\sim$ 58 km altitude). This occurs for a weakly-absorbing molecule due to the strong peak in the forward scattering direction for the Venus aerosols.

The results obtained in this study are necessarily limited by the degree to which a one-dimensional "global-average" model can simulate phenomena that may be complex functions of geographic location, time of day, etc. Pending a detection of absorption by O_2, the progress that may be made via further photochemical modeling is limited. However, a photochemical model that considers diurnally-varying chemistry is needed to clarify many of the issues associated with oxygen in the Venus atmosphere. Such a model would also be useful when designing a new attempt to detect O_2 since it could provide a more realistic estimate of the sensitivity that would be required. Additional suggestions for future work are outlined in Section 3.3.

3.3 Future Research

The research presented in this dissertation would not have been possible without the referenced observational, laboratory, and modeling studies. Further advances in all three areas are required to reduce the existing uncertainties in the photochemical models. A recommended list of observations and laboratory experiments is summarized in Table 3.2.

Observations

The O_2 column abundance *relative to* CO_2 is the most critical parameter required. This relative abundance is one of the first-order requirements that a photochemical model must predict correctly in order to have confidence in the model's other predictions. The relative intensities of the dayside and nightside airglow emission in the $O_2(a^1\Delta)$ band need to be measured again. This relative intensity in combination with the diurnal modeling proposed below constrains the abundance and vertical profile of O_3 on the dayside of the Venus atmosphere. Only one measurement currently exists [*Connes et al.* 1979] and there are large uncertainties associated with it. The $O_2(a^1\Delta)$ vertical profile can provide a wealth of information and, based on calculations for the proposed *VESPER* Discovery-class mission, will be easier to measure than that for

Table 3.2: Recommended List of Future Observations and Chemical Kinetics Experiments

Observations
Spectroscopic detection of O_2
Confirmation of H_2 versus D in thermosphere
Relative intensities of $O_2(a^1\Delta)$ dayside and nightside airglow
Vertical profiles for $O_2(a^1\Delta)$
Spectroscopic detections of O_3, ClO, NO or NO_2, BrO, H_2S, and $ClSO_2$
Vertical profile for OCS
Simultaneous retrieval of CO mixing ratios and temperatures as a function of local time

Laboratory Experiments
Equilibrium constant for ClCO at < 200 K
Determination of k_{K179} and k_{K180} (ClCO + O)
Effective yield for $O_2(a^1\Delta)$ from $2O + CO_2$
Radiative lifetime for $O_2(a^1\Delta)$
Determination of k_{K203} ($O_2(a^1\Delta)+ CO_2$)
Quantum yield for $O_2(a^1\Delta)$ from BrO + ClO (see text)
Chemistry of $(SO)_2$
Existence of BrCO at < 200 K
Determination of k_{K194} ($ClSO_2+$ Cl)
Ultraviolet absorption cross sections for S_2O, $ClSO_2$, and S_2

ground-state O_2 [*Chin, G.*, Personal Communication, 1998]. The $O_2(a^1\Delta)$ profile should disclose the mechanism(s) by which O_2 is produced, tightly constrain the vertical profile for ground-state O_2, and give valuable information on the dynamics of the atmosphere above 85 km altitude. The profile, in combination with numerical modeling, may also provide a more sensitive test of the collisional quenching for Reaction K203 than may be feasible in the laboratory [*Slanger, T.*, Personal Communication, 1998].

Simultaneous retrievals of CO mixing ratios and temperature as a function of local time are needed to reduce the uncertainties in the distribution of CO and the temperatures in the $80 - 95$ km altitude region. Temperatures in this altitude region partially determine the stability of ClCO and, thus, regulate the effectiveness of the chlorine catalytic cycles examined in the current photochemical models. This can be accomplished via nearly-simultaneous interferometric maps of ^{12}CO and ^{13}CO.

Detections of ClO, BrO, NO or NO_2, H_2, and H_2S (or smaller upper limits on their abundances) are required to clarify which of the several proposed types of chemistry are most important in the Venus atmosphere. Detection of $ClSO_2$ and/or observations of the OCS profile would constrain the eddy diffusion near the top of the upper cloud and would constraint the chemistry occurring within the upper cloud. Detection of O_3 would provide valuable information on the odd oxygen abundance and, together with a detection of O_2, would constrain the oxygen budget of the middle atmosphere very tightly.

One problem with the extant observations is the large temporal separation between some of the most important ones, such as those for HCl and H_2O. After the abundance of O_2 has been determined, additional observations of HCl, H_2O, SO_2, and SO will be needed to establish the conditions that existed at the time of the O_2 observation.

Laboratory Experiments

The recommendations for future laboratory experiments focus on the oxygen budget and the proposed cloud-level chemistry. The uncertainty in the equilibrium constant for ClCO at < 200 K needs to be reduced by at least a factor of two. The rates for Reactions K179 and K180 with uncertainties of less than a factor of five

are needed to verify the plausibility of these proposed reactions. Theoretical and/or laboratory studies are required to assess whether BrCO would be stable at $\sim$ 150 K. If not, then bromine compounds do not play direct roles in the oxidation of CO.

The effective yield of $O_2(a^1\Delta)$ from Reaction K101 will determine the contribution of this source to the observed airglow. The radiative lifetime of the $O_2(a^1\Delta)$ state is needed to within $\sim$ 3% uncertainty. The uncertainty in the *Badger et al.* [1965] measurement is $10-15\%$, but *Gamache et al.* [1998] cited unpublished results indicating the lifetime is $\sim$ 15% smaller than the value from *Badger et al.* [1965]. A 15% decrease in the lifetime is a larger change in the desired direction than was done for the One-Sigma Model and the Highest ClCO Model. The collisional quenching rate for Reaction K203 is needed, or at least verification is needed that the rate is $\lesssim 2 \times 10^{-21}$ as proposed in the One-Sigma and Highest ClCO Models. This is an order of magnitude smaller than the current upper limit. If the abundance of BrO in the Venus atmosphere is comparable to that of HCl, then Reaction G12 becomes a potentially important source for $O_2(a^1\Delta)$.

The chemistry of $(SO)_2$ has received little study since *Yung and DeMore* [1982] and their modeling of it was largely based on estimated rates. Laboratory studies are also needed for other reduced sulfur and sulfur chlorine species to determine whether the proposed species could contribute to the ultraviolet absorption at $300-400$ nm.

Modeling

Three useful assessments can be conducted with small modifications to the existing one-dimensional "global average" model. Bromine chemistry can be evaluated to quantify what abundances are required for bromine to affect the oxygen budget in the middle atmosphere. Fluorine chemistry should be examined above 100 km altitude to determine whether oxidation of FCO can be an important pathway for oxidizing CO at those altitudes. Fluorine chemistry is not likely to impact the overall rate of oxidation for CO, but it may be occur at altitudes where the the total density is too small for chlorine-catalyzed oxidation. A new assessment of nitrogen chemistry is needed that includes potential heterogeneous reactions among nitrogen and chlorine species. This will quantify the abundance of reactive nitrogen that is required for

nitrogen chemistry to affect the overall chemistry of the middle atmosphere.

Further advances in photochemical modeling for the Venus atmosphere require consideration of at least diurnal effects. This is possible with slight modifications to the existing model and would provide good initial comparisons against the existing diurnal CO and $O_2(a^1\Delta)$ data. Subsequent investigations are likely to require at least a two-dimensional Chemical Transport Model. If any of the proposed Discovery-class missions to Venus are selected, development of such a two-dimensional model will be needed for a full analysis of the measurements.

Finally, a new study of the radiative characteristics of the Venus middle atmosphere is needed to assess the predictions from the current photochemical models.

3.4 References

Badger, R.M., A.C. Wright, and R.F. Whitlock, Absolute Intensities of the Discrete and Continuous Absorption Bands of Oxygen Gas at 1.26 and 1.065 μm and the Radiative Lifetime of the $^1\Delta_g$ Oxygen State, *J. Chem. Phys.* **43**, 4345-4350, 1965.

Connes, P., J. Connes, F. Noxon, W. Traub, and N. Carlton, O_2 ($^1\Delta$) Emission in the Day & Night Airglow of Venus, *Ap. J.* **233**, L29-L32, 1979.

Crisp, D., V.S. Meadows, B. Bezard, C. de Bergh, J-P Maillard, and F.P. Mills, Ground-based Near-Infrared Observations of the Venus Night Side: Near-Infrared O_2 ($^1\Delta$) Airglow from the Upper Atmosphere, *J. Geophys. Res.* **101**, 4577-4593, 1996.

DeMore, W.B., S.P. Sander, D.M. Golden, R.F. Hampson, M.J. Kurylo, C.J. Howard, A.R. Ravishankara, C.E. Kolb, and M.J. Molina, *Chemical Kinetics and Photochemical Data for Use in Stratospheric Modeling Evaluation 12*, Jet Propulsion Laboratory Publication 97-4, 1997.

Encrenaz, Th., E. Lellouch, J. Cernicharo, G. Paubert, S. Gulkis, and T. Spilker, The Thermal Profile and Water Abundance in the Venus Mesosphere from H_2O and HDO Millimeter Observations, *Icarus* **117**, 162-172, 1995.

Gamache, R.R., A. Goldman, and L.S. Rothman, Improved Spectral Parameters for the Three Most Abundant Isotopomers of the Oxygen Molecule, *J. Quant. Spectrosc. Radiat. Transfer* **59**, 495-509, 1998.

Grinspoon, D.H., J.B. Pollack, and B.R. Sitton, Probing Venus Cloud Structure with *Galileo* NIMS, *Planet. Space Sci.*, **41**, 515-542, 1993.

Hansen, J.E., and J.W. Hovenier, Interpretation of the Polarization of Venus, *J. Atmos. Sci.* **31**, 1137-1160, 1974.

Jiang, Y.B., Y.L. Yung, and S.P. Sander, Detection of Tropospheric Ozone by Remote-sensing from the Ground, *j. Quant. Spectrosc. Rad. Transfer* **57**, 811-818, 1997.

Knibbe, W.J.J., J.F. de Haan, J.W. Hovenier, and L.D. Travis, Analysis of Temporal Variations of the Polarization of Venus Observed by *Pioneer Venus* Orbiter, *J. Geophys. Res.* **103**, 8557-8574, 1998.

Oyama, V.I., G.C. Carle, F. Woeller, J.B. Pollack R.T. Reynolds, and R.A. Craig, Pioneer Venus Gas Chromatography of the Lower Atmosphere of Venus, *J. Geophys. Res.* **85**, 7891-7902, 1980.

Pollack, J.B., J.B. Dalton, D. Grinspoon, R.B. Wattson, R. Freedman, D. Crisp, D.A. Allen, B. Bezard, C. de Bergh, L.P. Giver, Q. Ma, and R. Tipping, Near-Infrared Light from Venus' Nightside: A Spectroscopic Analysis, *Icarus* **103**, 1-42, 1993.

Tabazadeh, A., O.B. Toon, S.L. Clegg, and P.Hamill, A New Parameterization of H_2SO_4/H_2O Aerosol Composition: Atmospheric Implications, *Geophys. Res. Lett.* **24**, 1931-1934, 1997.

Trauger, J., and J. Lunine, Spectroscopy of Molecular Oxygen in the Atmospheres of Venus and Mars, *Icarus* **55**, 272-281, 1983.

Young L.D.G., High Resolution Spectrum of Venus–A Review, *Icarus* **17**, 632-658, 1972.

Yung, Y., and W. DeMore, Photochemistry of the Stratosphere of Venus: Implications for Atmospheric Evolution, *Icarus* **51**, 199-247, 1982.

Zhang, S., S.W. Bougher, and M.J. Alexander, The Impact of Gravity-waves on the Venus Thermosphere and O_2 IR Nightglow, *J. Geophys. Res.* **101**, 23195-23205, 1996.

Chapter 4

Thermal Infrared Spectroscopy of Europa and Callisto

Franklin P. Mills and Michael E. Brown

Division of Geological and Planetary Sciences

California Institute of Technology

Pasadena, CA 91125

Submitted in modified form to

Journal of Geophysical Research

Contribution Number 5766 of the

Division of Geological and Planetary Sciences

California Institute of Technology

Abstract

The trailing hemispheres of Europa and Callisto were observed and a $9-13$ μm spectrum of Europa with better spectral resolution and better signal-to-noise than was previously possible has been derived. The ratio spectrum of the two satellites has a signal-to-noise ratio of approximately 30 and spectral resolving power of approximately 50. The ratio spectrum was combined with the average Voyager 1 spectrum of Callisto from *Spencer* [1987a] to obtain a $9-13$ μm spectrum of Europa with signal-to-noise that is a factor of 10 better than that in the average Voyager spectrum of Europa in *Spencer* [1987a]. No emissivity features due to water ice are apparent at the 3% level in our Europa spectrum. The disk-integrated, effective color temperature ratio for the two satellites is consistent with previous ground-based, broadband, thermal infrared photometry. One possible explanation for the absence of features in the thermal infrared spectra of Europa (at the 3% level) and Callisto (at the 1% level) is if the surfaces of both satellites have significant abundances of small particles ($\lesssim$ 50 micrometer in size). This explanation is consistent with most of the published observations by *Galileo*.

4.1 Introduction

This work presents the results from new observations in the thermal infrared ($7-14$ μm wavelength region) to determine if thermal infrared spectra with better signal-to-noise than could previously be obtained could discriminate among the proposed models for the surfaces of Callisto and Europa.

Previous spectral studies of the icy Galilean satellites have focused primarily on the $0.4-3$ μm wavelength range and have led to the development of several competing models for the surface properties of the satellites. None of the published models explains all spectral features observed for Europa or Callisto in the $0.4-3$ μm wavelength region. The four published models that give the best fits to the observed $0.4-3$ μm spectra for Callisto are (1) small ($\sim 5-30$ micrometer in size) particles of water

ice intimately mixed with small chondritic or phyllosilicate particles and (poorly constrained size) particles of a dark, spectrally neutral material (e.g., magnetite) [*Roush et al.* 1990]; (2) segregated regions of ice/frost and chondritic material in particles that are of unstated size [*Spencer* 1987b]; (3) medium to large (of order hundreds of micrometers to centimeters in size) particles of ice intimately mixed with (indeterminate size) chondritic or phyllosilicate particles [*Calvin et al.* 1995]; and (4) very fine ($\lesssim$ 1 micrometer in size) surface roughness or frost overlying larger particles or sheets of ice [*Clark et al.* 1986]. The estimated surface composition for Callisto is (1) $\sim 25 - 45$ wt% water ice [*Roush et al.* 1990]; (2) $\sim 3 - 10$ wt% water ice [*Spencer* 1987b]; (3) $\sim 20 - 45$ wt% water ice [*Calvin et al.* 1995]; and (4) "abundant" (up to 70% according to *Calvin et al.* [1995]) water ice [*Clark et al.* 1986]. The identity of the remaining component(s) is unknown. The model that gives the best fit to the observed $0.4 - 3$ μm spectra for Europa has medium to large (of order hundreds of micrometers to centimeters in size) particles of ice [*Calvin et al.* 1995]. *Calvin et al.* [1995] did not estimate the fraction of Europa's surface that was ice, but *Clark et al.* [1986] concluded Europa's surface was $\gtrsim$ 95 wt% ice. Earlier studies for Callisto and Europa are reviewed in *Johnson and Pilcher* [1977] and *Clark et al.* [1986].

Thermal infrared observations have the potential to discriminate among the proposed models for the surfaces of Callisto and Europa. Both water ice and silicates have distinctive emissivity features in the thermal infrared when the materials are in medium-to-large ($\gtrsim$ 75 micrometer in size) particles: water ice near $11 - 12$ μm [*Warren* 1984; *Spencer* 1987a] and silicates in the $7.5 - 9.5$ μm region [references in *Nash et al.* 1993]. Consequently, if Callisto's surface is dominated by medium-to-large size particles of silicate and Europa's is not, then a ratio of the two spectra should contain distinctive emissivity features in the $7.5 - 9.5$ μm region. Similarly, if Europa's surface is dominated by medium-to-large size particles of ice and Callisto's surface is not, then the ratio spectrum should contain distinctive emissivity features in the $11 - 12$ μm region. If no significant features are found, then the simplest explanations are that both surfaces have (1) similar composition and particle size; (2) thermal emission spectra that are dominated by emission from small ($\lesssim$ 50 microme-

ter in size) particles; (3) surfaces that are rough on length scales of $\lesssim 50$ micrometer; (4) ice and non-ice particles interspersed in a manner that suppresses the thermal infrared signatures of both ice and silicates; (5) a sufficient amount of a spectrally neutral material to suppress the thermal infrared signatures of both ice and silicates; or (6) silicates are not present on Callisto's surface in spectrally significant amounts.

Ground-based observations of the icy Galilean satellites in the 1970s measured only broadband brightness temperatures [reviewed in *Morrison* 1977]. Since then, no ground-based thermal emission spectra have been published although there have been significant improvements in instrumentation. *Hanel et al.* [1979] found "contrast differences on the order of 1 percent or less" in Voyager 1 spectra of Europa and Callisto. *Spencer* [1987a] also concluded there were no unambiguous spectral features in the Voyager spectra of Europa and Callisto. However, the Voyager spectra were relatively noisy for wavelengths $\lesssim 13$ μm for Europa and for wavelengths $\lesssim 8$ μm for Callisto so Voyager might not have been able to detect features due to water ice on Europa or silicates on Callisto. We have combined our ratio spectrum with the average Voyager 1 spectrum of Callisto from *Spencer* [1987a] to produce a spectrum of Europa that has better signal-to-noise by about a factor of 10 in the $9 - 13$ μm wavelength region than that collected by Voyager at Europa.

4.2 Background

Four primary variables govern the appearance of a planetary surface in the infrared when the planet has little or no atmosphere: the composition of the surface particles, the relative abundance of each component, the size of the particles, and the manner in which particles of differing composition are interspersed. One diagnostic feature for composition is the wavelengths at which the molecular vibration bands (reststrahlen bands) are located. Strong reststrahlen bands for most silicates and for water ice lie within the thermal infrared region [*Farmer* 1974, *Warren* 1984, *Elachi* 1987]. Consequently, thermal infrared spectra are being used for compositional mapping of the Earth [e.g., *Bartholomew et al.* 1989] and will be used for Mars [*Christensen et*

al. 1992]. A primary concern for observing the thermal infrared reststrahlen bands is that the observed intensity of these bands decreases at small particle sizes [*Lyon* 1964, *Hunt and Logan* 1972, and *Salisbury and Wald* 1992]. Figure 4.1 shows calculated emissivities for water ice particles as a function of the particle radius. For loosely packed lunar soil samples, whose emission is dominated by emission from particles $\lesssim$ 5 micrometer in size, [*Salisbury, J.*, Personal Communication, 1997] has found the silicate reststrahlen bands are only $\sim$ 2% deep. Other factors that can affect thermal infrared spectra are spatial inhomogeneities in composition and near surface temperature gradients. However, *Thomson and Salisbury* [1993] have shown that spectra of silicate particles in the 75-250 micrometer size range behave as linear mixtures (by volume) of the component materials, and *Henderson and Jakosky* [1994] showed that the spectral contrast in the reststrahlen bands *increases* as a result of the thermal gradient present on a body with no atmosphere when the surface is heated from below. This can happen when the surface is more translucent at visual wavelengths than at thermal wavelengths, has been observed in studies of terrestrial snow, and has been proposed for the icy Galilean satellites [*Urquhart and Jakosky* 1996 and references therein].

4.3 Observations and Processing

Callisto and Europa were observed on July 1, 1996, from 6:30 - 11:30 UT from Palomar Observatory using the 5-meter Hale Telescope and SpectroCam-10 [*Hayward et al.* 1993]. SpectroCam-10 was used in its low-resolution spectrographic mode where it uses 128 spectral $\times$ 64 spatial pixels of the 128 $\times$ 128 Si:As BIBIB detector. The spectral resolving power was $\sim$ 50 with a $2'' \times 16''$ slit, and spectra were collected at three grating positions to provide complete coverage of the $8 - 14$ μm region. The angular resolution is $0.25''$ per pixel in the spatial direction.

SpectroCam-10 acquires data in a sequence of nods (moving the entire telescope) and chops (moving the secondary mirror) on and off the object. These nods and chops are arranged to permit proper removal of background radiance (such as that

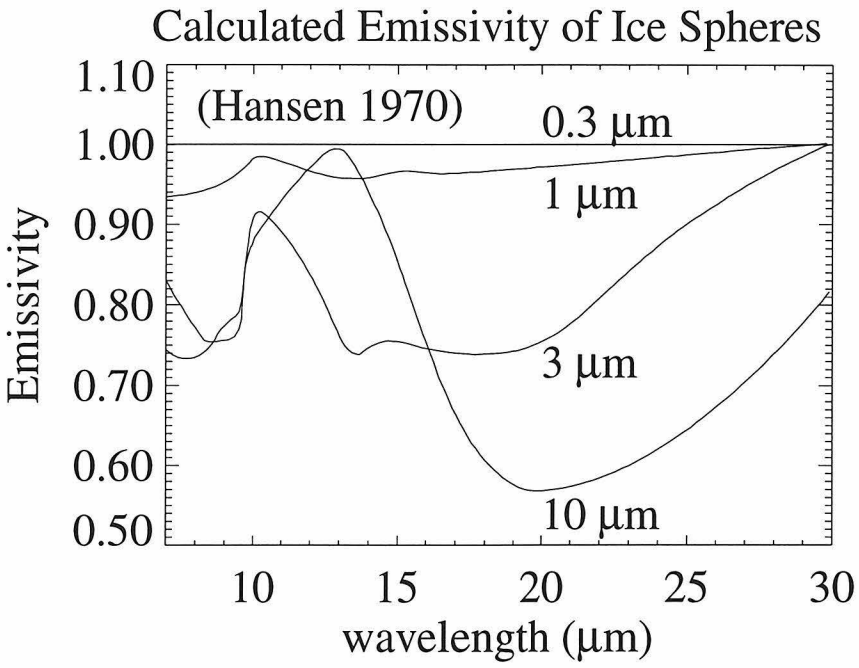

Figure 4.1: "Calculated emissivity of ice spheres with radii r = 0.3, 1, 3, and 10 micrometer, as a function of wavelength." [*Hansen* 1972]

from the earth's atmosphere and the telescope) from the measured thermal emission for an object. In the simplest case, that for spectra of an extended source that fills over half of the field of view of SpectroCam-10, the object is included in only one of the four beams:

$$F_{oo} = O + A_{obj} + T_{on} \tag{4.3.0.1}$$

$$F_{oc} = A_{off} + T_{off} \tag{4.3.0.2}$$

$$F_{no} = A_{off} + T_{on}. \tag{4.3.0.3}$$

$$F_{nc} = A_{off} + T_{off}. \tag{4.3.0.4}$$

where O is the radiance emitted by the object, A_{obj} is the radiance emitted by the intervening atmosphere when viewing the object, A_{off} is the radiance emitted by the atmosphere when not viewing the object, T_{on} is the radiance emitted by the telescope when looking along the telescope axis, and T_{off} is the radiance emitted by the telescope when looking off the telescope axis. The desired radiance from the object is given by $O = F_{oo} - F_{oc} - (F_{no} - F_{nc})$, assuming that the atmospheric emission is the same for all positions. The angular separation between the positions is small and the time separation is sufficiently small so that this approximation is true to sufficiently high accuracy. If the object is sufficiently small that it fills less than half of the field of view of SpectroCam-10, then the nod and chop distances and directions can be adjusted to improve the observing efficiency while still properly characterizing the atmosphere and telescope emission.

The chopping frequency for measuring telluric emission near the objects was 4.75 Hz, and both the nodding and chopping used separations of approximately 8″. The on-source integration time for individual object and sky spectra was 60 seconds; Callisto and Europa were observed, alternately, for intervals of 15 minutes each. The

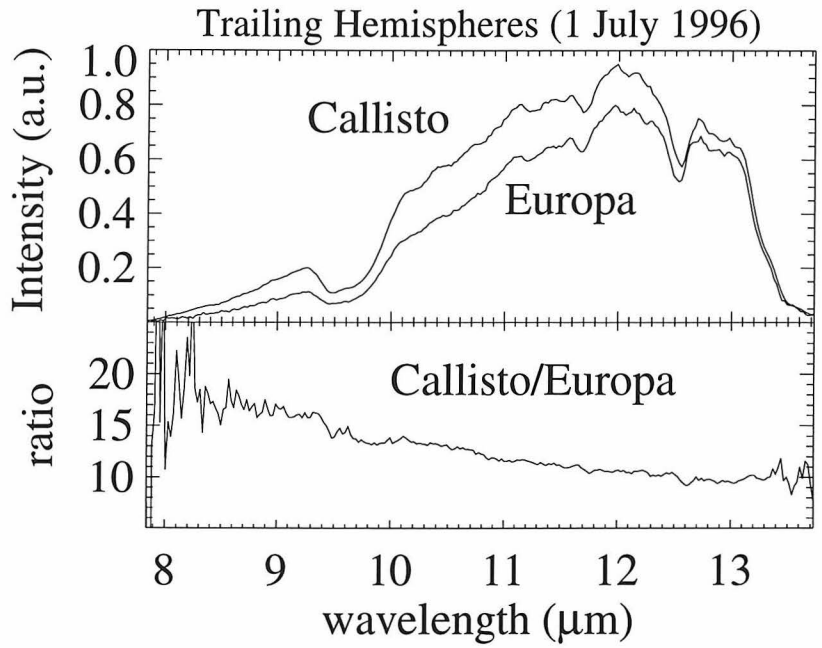

Figure 4.2: (a) Disk-integrated thermal emission spectra of the trailing hemispheres of Callisto and Europa measured with SpectroCam-10 at Palomar Observatory. Collected on 1 July 1996. (b) Ratio of Callisto and Europa thermal emission spectra from (a).

flat-fielded spectra were wavelength-calibrated by comparing the prominent telluric emission features in each recorded spectrum to a synthetic telluric emission spectrum. A zero-point wavelength shift was determined for each recorded spectrum then the wavelength-shifted spectra were added to produce Figure 4.2a. Figure 4.2b shows the ratio of the averaged spectra for the two objects (Callisto/Europa).

The solar phase angle was approximately 0.7°. The trailing hemisphere of Callisto was observed at orbital longitudes $280 - 290°$, and the trailing hemisphere of Europa was observed at orbital longitudes $210 - 230°$. Airmass ranged from 1.8 to 2.7 and typical seeing was $1''$. Observing conditions were non–photometric; Palomar had been closed the preceding 36 hours due to ash from surrounding forest fires and residual smoke from those fires was present at the time of our observations. Thermal emission

from the smoke should have been removed by the nodding and chopping on and off target sequence. Assuming the smoke concentration varied slowly with time, the effects of scattering by the smoke particles should not be present in the ratio spectrum we derive because scattering by the smoke would have the same effect on both the Europa and the Callisto spectra. In addition, the visual optical depth of the smoke was small based on daytime observations.

4.4 Results

Figure 4.2b has several features, but all lie at the wings of telluric absorption bands so they are likely due to incomplete cancellation of the telluric bands as a result of the non- photometric conditions. Our signal level is sufficiently poor at wavelengths less than 9 μm and greater than 13 μm that features outside this range should not be considered significant. The absence of significant features in Figure 4.2b is consistent with previous findings [*Hanel et al.* 1979; *Spencer* 1987a].

The dominant source of "noise" in our measurement at approximately $9-13$ μm is incomplete cancellation of telluric emission and transmission features. A reasonable estimate of the noise level at these wavelengths is given by the RMS deviation, $\sim 3\%$, of our ratio spectrum from the ratio of a 151 K and a 130 K blackbody as shown in Figure 4.3. (See Appendix A for discussion of the ratio of the effective temperatures of the satellites.) At shorter wavelengths, our noise level is determined by the relatively low flux from Europa. At longer wavelengths, relatively poor transmission through the earth's atmosphere limits our sensitivity.

We combined our ratio spectrum, Figure 4.2b, with the average spectrum of Callisto collected by Voyager 1 (digitized from *Spencer* 1987a] to synthesize a spectrum of Europa, the upper curve in Figure 4.4. (For details on how the Europa spectrum was synthesized, interested readers may consult Appendix B.) The noise level in our synthesized Europa spectrum represents solely the noise from our ratio spectrum. We find no significant features, at our 3% noise level, at the expected locations of water ice features, 10.9 and 12.2 μm [*Warren* 1984; *Spencer* 1987a], in our synthesized

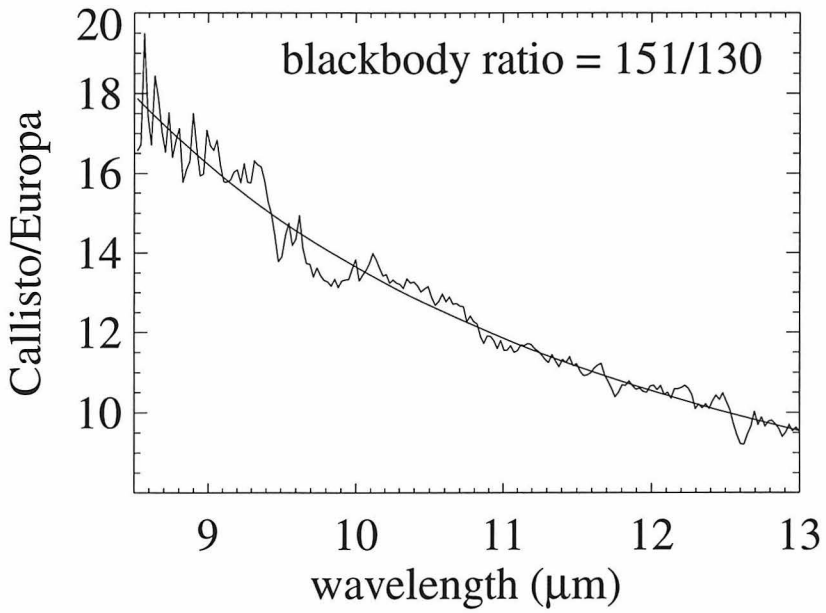

Figure 4.3: Comparison of our ratio spectrum for Callisto and Europa to the ratio spectrum for a pair of blackbodies. The curve is the ratio of a 151 K and a 130 K blackbody. RMS deviation from this curve is 3% for the $8.5 - 13$ μm region.

spectrum of Europa. The absence of water ice features in our synthesized Europa spectrum is consistent with the analysis by *Spencer* [1987a] of the noisier average Voyager spectrum of Europa, the lower curve in Figure 4.4. However, our lower noise level decreases the upper limit on water ice features by about a factor of 10.

4.5 Discussion

We find no significant emission features at the 3% level that are indicative of surface composition in a $9 - 13$ μm spectrum of Europa. The lack of water ice features in the synthesized Europa spectrum, Figure 4.4, is consistent with the thermal emission from Europa's surface being dominated by emission from small particles ($\lesssim$ 50 micrometer in size). The *Galileo* NIMS spectrum of the northern polar region of Europa in *Carlson et al.* [1996] for the $1 - 3\mu$m wavelength region is consistent with this interpretation as are disk-integrated spectra of the trailing hemisphere of Europa [*Calvin et al.* 1995]. The preferred interpretation in both of those studies for the features in the $1 - 3\mu$m wavelength region spectra is that they are produced by a thin layer of fine-grained frost overlying ice. These results from infrared spectra are consistent with thermal inertia models of Europa and visual photometry. *Orton et al.* [1996] found that the measured temperature variation from the subsolar point to the evening terminator required a surface thermal inertia for Europa that is one-third as large as that determined for Ganymede and one-half as large as that determined for Callisto [*Spencer* 1987a; *Urquhart and Jakosky* 1996]. *Buratti*'s [1995] models of the visual surface reflectivity of Europa found the upper regolith of Europa could be either extremely uncompacted or the most compacted surface of all the Galilean satellites.

A second possible explanation for the lack of features in the ratio spectrum is that both Europa and Callisto have water ice features in their spectra and those features cancel in the ratio spectrum we obtained. However, there are no water ice features at the $< 1\%$ level in the average Voyager 1 spectrum of Callisto [*Hanel et al.* 1979, *Spencer* 1987a, this work].

A third possible explanation for the lack of water ice features in the derived Europa

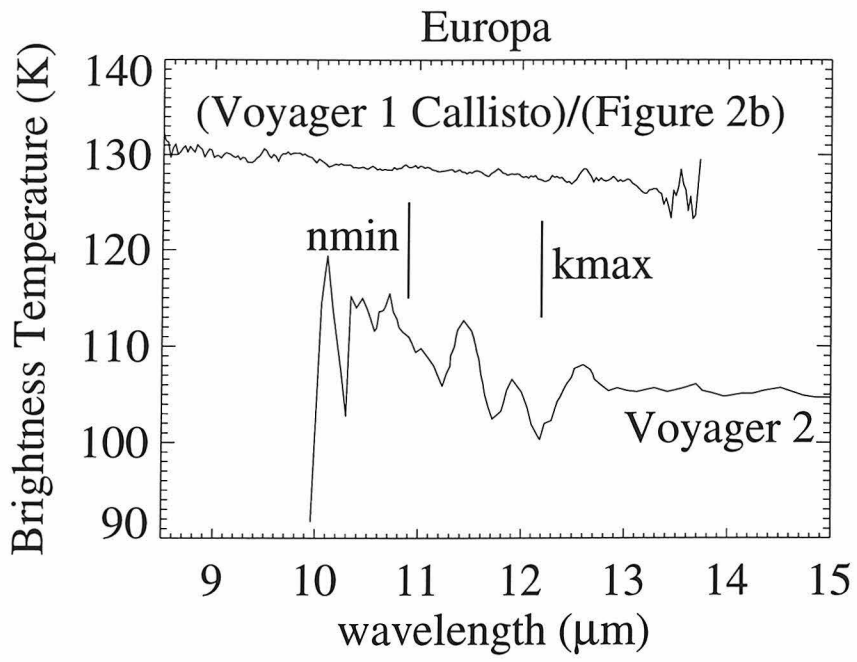

Figure 4.4: The lower curve is the average Voyager 2 spectrum of Europa from *Spencer* [1987a]. It is an average of all spectra with 22–μm brightness temperature warmer than 90 K, a total of 53 spectra. The spectrum was smoothed by Spencer with a boxcar filter of width 14 cm^{-1}. The labels 'kmax' and 'nmin' indicate the locations where water ice features would be expected. [*Warren* 1984; *Spencer* 1987a] The upper curve is the Europa spectrum derived from combining the ratio spectrum in Figure 2b with the average Voyager 1 spectrum of Callisto from Spencer as discussed in Appendix B. No features are found above our 3% noise level at the locations marked 'kmax' and 'nmin'. (The temperature offset between our derived spectrum and that obtained by Voyager 2 for Europa arises because we have used Voyager 1 spectra from the relatively warm afternoon quadrant of Callisto to scale our ratio spectrum whereas the Voyager 2 spectra of Europa were collected closer to Europa's relatively cool evening terminator.)

spectrum is that the features are below the noise level for the spectrum. *Dozier and Warren* [1982] calculated the expected hemispherically-averaged emissivity for snow, as shown in Figure 4.5. However, those calculations were done for a typical terrestrial snow in which air is intermixed with spheres of ice and for the porosities typically found in terrestrial snow. As a result, those calculations may not apply to the conditions present on the surface of Europa. *Dozier and Warren* [1982] used a "delta-Eddington" approximation for multiple scattering together with Mie theory for single scattering. They also showed that there are significant differences between the calculated emissivities from this model and a more accurate doubling model at viewing angles of $\gtrsim$ 75 degrees. Figure 4.6 from *Salisbury et al.* [1994] shows that measured spectra for natural terrestrial snow have larger emissivity variations than predicted by the numerical calculations. Further modeling and laboratory studies are required to quantify the constraints that thermal infrared observations can place on the surface characteristics of the Galilean satellites.

Our ratio spectrum, Figure 4.2b, is too noisy at < 8.5 μm to place a significant constraint on possible silicate reststrahlen bands in Callisto's spectrum. The average Voyager 1 spectrum of Callisto [*Spencer* 1987a], however, shows no evidence for emission features at the 1% level in the $8 - 14\mu$m wavelength range [*Hanel et al.* 1979, *Spencer* 1987a, this work]. The lack of features at these wavelengths in the Voyager spectrum of Callisto is consistent with at least three scenarios. In the first two scenarios, the surface of Callisto is segregated into regions that are ice-rich with high albedo and regions that are ice-poor with low albedo [*Spencer* 1987c]. In this case, most of the thermal emission from Callisto's surface would be from the ice-poor areas due to their higher temperatures. The lack of spectral features in the $8 - 14\mu$m wavelength region then implies that either the surface of Callisto has abundant small particles ($\lesssim$ 50 micrometer in size) or is composed of materials that have no spectral features in the measured wavelength region. *Spencer* [1987b] found that spectra of Callisto could be matched reasonably well with small amounts ($\sim 3 - 10\%$) of water ice. In that work, the strong $3 - \mu$m absorption band had a large contribution from water of hydration in the non-ice component of the surface. More recently, *Galileo* NIMS

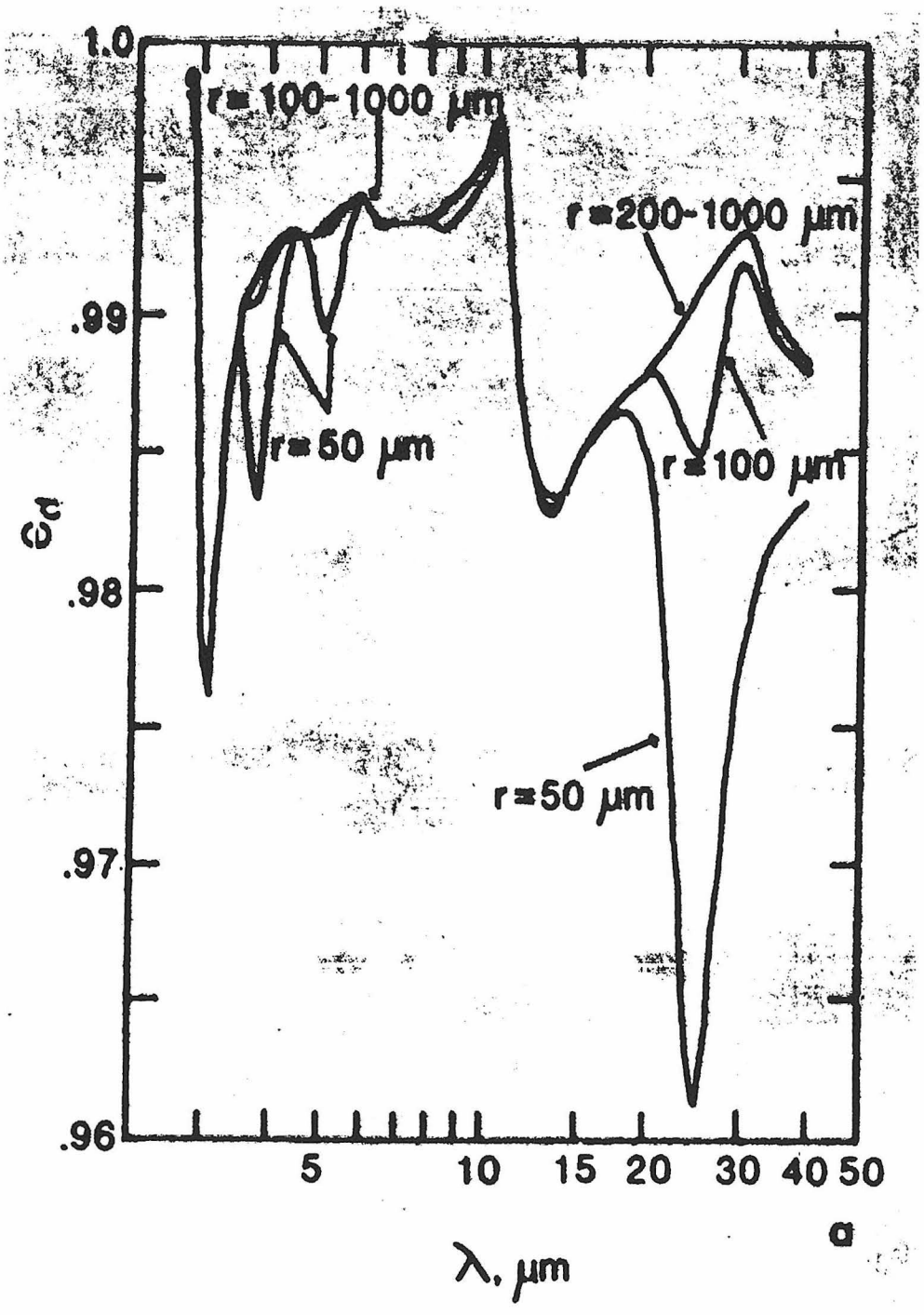

Figure 4.5: Calculated hemispherically averaged emissivity of snow for grain radii from 50 to 1000 μm from *Dozier and Warren* [1982].

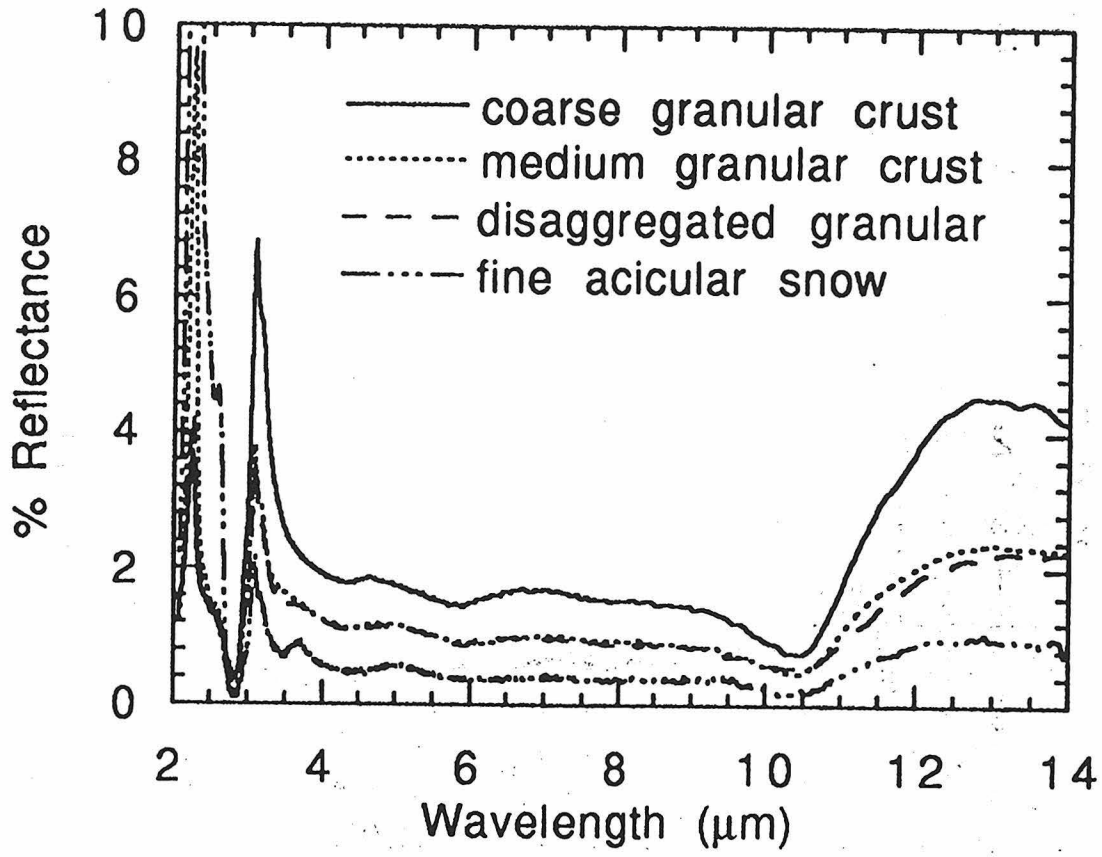

Figure 4.6: "Directional hemispherical reflectance of fine, acicular, dry snow ... compared to spectra of medium and coarse granular snow crusts, and to disaggregated coarse granular snow. The fine, acicular snow grains were typically 40-80 micrometer in diameter and 240-480 micrometer long; the grain size of the medium granular snow crust was typically 330-500 micrometer; and that of the coarse granular snow crust was typically 1000-2000 micrometer. The disaggregated snow grains were typically 600-1400 micrometer in diameter." [*Salisbury et al.* 1994]

spectra of Callisto revealed an absorption feature at 4.25μm that has been attributed to hydrated or hydroxylated minerals or CO_2 (possibly in a clathrate form) [*Carlson et al.* 1996]. A third possible scenario is that the surface of Callisto is composed primarily of ice, including abundant small particles.

Relatively small particle sizes on the surface of Callisto would be consistent with thermal inertia because they require a thin, low inertia layer above a thicker, higher inertia layer [*Spencer* 1987a and *Veverka* 1986]. Small particle sizes would also be consistent with the numerical modeling by *Roush et al.* [1990]. They found reasonable fits to a $1-5$ μm spectrum of Callisto with mixtures of ice, magnetite, and serpentine in which the ice particles were $\sim 10-30$ micrometers in diameter and the serpentine particles were $\sim 5-15$ micrometer in diameter. Finally, *Buratti*'s [1995] models of the visual surface reflectivities of Callisto found the compaction state of Callisto's surface is similar to that of the Moon.

One argument against small particle sizes for water ice on both satellites is that fine ice grains will grow relatively rapidly into larger particles [*Clark et al.* 1986] as a result of the constant migration of water molecules in the vapor phase and the preferential loss of smaller ice grains via sputtering. *Carlson et al.* [1996] find that the surface ice grain properties on *Ganymede* are fairly uniform in the icy areas that have been mapped. However, they find that the $1.04-\mu$m water ice absorption band is stronger near the equator, suggesting the grain sizes are larger at the equator. They state, though, that O_2 also absorbs at $1.05-\mu$m so there are uncertainties in their interpretation.

4.6 Conclusion

We find no definite features at the 3% level in a $9-13\mu$m spectrum of Europa. *Spencer* [1987a] and *Hanel et al.* [1979] similarly found no definite spectral features at the 1% level in $8-14$ μm spectra of Callisto. This lack of features suggests the surfaces of both satellites could contain abundant particles that are $\lesssim 50$ micrometer in size. The lack of features in this wavelength region is consistent with spectra of lunar soil samples

[*Salisbury et al.* 1997; *Salisbury, J.*, Personal Communication, 1997] and implies that current thermal emission spectra do not place any constraint on the identity of the non-ice material on Callisto or Europa. Future thermal infrared emission studies of the icy Galilean satellites will likely need to locate the Christiansen wavelengths of the surface materials to determine the surface compositions of the satellites.

4.7 References

Bartholomew, M.J., A.B. Kahle, and G. Hoover, Infrared Spectroscopy (2.3 – 20 μm) for the Geological Interpretation of Remotely Sensed Multispectral Mid-infrared Data, *Int. J. Remote Sens.* **10**, 529-544, 1989.

Buratti, B.J., Photometry and Surface Structure of the Icy Galilean Satellites, *J. Geophys. Res.* **100**, 19061-19066, 1995.

Calvin, W.M., R.N. Clark, R.H. Brown, and J.R. Spencer, Spectra of the Icy Galilean Satellites from 0.2 to 5 μm: A Compilation, New Observations, and a Recent Summary, *J. Geophys. Res.* **100**, 19041-19048, 1995.

Carlson, R., W. Smythe, K. Baines, E. Barbinis, K. Becker, R. Burns, S. Calcutt, W. Calvin, R. Clark, G. Danielson, A. Davies, P. Drossart, T. Encrenaz, F. Fanale, J. Granahan, G. Hansen, P. Herrera, D. Hibbitts, J. Hui, P. Irwin, T. Johnson, L. Kamp, H. Kieffer, F. Leader, E. Lellouch, R. Lopes-Gautier, D. Matson, T. McCord, R. Mehlman, A. Ocampo, G. Orton, M. Roos-Serote, M. Segura, J. Shirley, L. Soderblom, A. Stevenson, F. Taylor, J. Torson, A. Weir, and P. Weissman, Near-Infrared Spectroscopy and Spectral Mapping of Jupiter and the Galilean Satellites: Results from Galileo's Initial Orbit, *Science*, **274**, 385-388, 1996.

Christensen, P.R., D.L. Anderson, S.C. Chase, R.N. Clark, H.H. Kieffer, M.C. Malin, J.C. Pearl, J. Carpenter, N. Bandiera, F.G. Brown, and S. Silverman, Thermal Emission Spectrometer Experiment: Mars Observer Mission,*J. Geophys. Res.* **97**, 7719-7734, 1992.

Clark, R.N., F.P. Fanale, and M.J. Gaffey, Surface Composition of Satellites, in *Satellites*, ed. J.A. Burns and M.S. Matthews, (University of Arizona Press, Tucson, AZ), 463-472, 1986.

Conel, J.E., Infrared Emissivities of Silicates: Experimental Results and a Cloudy Atmosphere Model of Spectral Emission from Condensed Particulate Mediums,

J. Geophys. Res. **74**, 1614-1634, 1969.

Dozier, J., and S.G. Warren, Effect of Viewing Angle on the Infrared Brightness Temperature of Snow, *Water Resources Research* **18**, 1424-1434, 1982.

Elachi, C., *Introduction to the Physics and Techniques of Remote Sensing*, 133-137, (John Wiley and Sons), 1987.

Farmer, V.C., *Infrared Spectra of Minerals*, (Mineralogical Society, London, 539 pp.), 1974.

Gillett, F.C., K.M. Merrill, and W.A. Stein, Albedo and Thermal Emission of Jovian Satellites I - IV, *Astrophys. Lett.* **6**, 247-249, 1970.

Hanel, R., B. Conrath, M. Flasar, V. Kunde, P. Lowman, W. Maguire, J. Pearl, J. Pirraglia, and R. Samuelson, Infrared Observations of the Jovian System from Voyager 1, *Science* **204**, 972-976, 1979.

Hansen, O.L., *Thermal Radiation from the Galilean Satellites Measured at 10 and 20 microns*, Ph.D. Dissertation, California Institute of Technology, Pasadena, CA, 1972.

Hayward, T.L, J.W. Miles, J.R. Houck, G.E. Gull, and J. Schoenwald, SpectroCam-10: A 10-micron Spectrograph/Camera for the Hale Telescope, *Proc. of the SPIE* **1946**, 334-340, 1993.

Henderson, B.G., and B.M. Jakosky, Near-surface Thermal Gradients and Their Effects on Mid-infrared Emission Spectra of Planetary Surfaces, *J. Geophys. Res.* **99**, 19063-19073, 1994.

Johnson, T.V., and C.B. Pilcher, Satellite Spectrophotometry and Surface Compositions, in *Planetary Satellites*, ed. J.A. Burns, (University of Arizona Press, Tucson, AZ), 232-252, 1977.

Lyon, R.J.P., *Evaluation of Infrared Spectrophotometry for Compositional Analysis of Lunar and Planetary Soils, Part 2: Rough and Powdered Surfaces*, Final Report, NASA Rep. CR-100, (115 pp.), 1964.

Morrison, D., Radiometry of Satellites and of the Rings of Saturn, in *Planetary Satellites*, ed. J.A. Burns, (University of Arizona Press, Tucson, AZ), 269-291, 1977.

Nash, D.B., J.W. Salisbury, J.E. Conel, P.G. Lucey, and P.R. Christensen, Evaluation of Infrared Emission Spectroscopy for Mapping the Moon's Surface Composition from Lunar Orbit, *J. Geophys. Res.* **98**, 23535-23552, 1993.

Orton, G.S., J.R. Spencer, L.D. Travis, T.Z. Martin, and L.K. Tamppari, Galileo Photopolarimeter-Radiometer Observations of Jupiter and the Galilean Satellites, *Science* **274**, 389-391, 1996.

Roush, T.L., J.B. Pollack, F.C. Witterborn, J.D. Bregman, and J.P. Simpson, Ice and Minerals on Callisto: A Reassessment of the Reflectance Spectra, *Icarus* **86**, 355-382, 1990.

Salisbury, J.W., and A. Wald, The Role of Volume Scattering in Reducing Spectral Contrast of Reststrahlen Bands in Spectra of Powdered Minerals, *Icarus* **96**, 121-128, 1992.

Salisbury, J.W., D.M. D'Aria, and A. Wald, Measurements of Thermal Infrared Spectral Reflectance of Frost, Snow, and Ice, *J. Geophys. Res.* **99**, 24235-24240, 1994.

Salisbury, J.W., A. Basu, and E.M. Fischer, Thermal Infrared Spectra of Lunar Soils, *Icarus* **130**, 125-139, 1997.

Spencer, J.R., *The Surfaces of Europa, Ganymede, and Callisto: An Investigation Using Voyager IRIS Thermal Infrared Spectra*, Ph.D. Dissertation, The University of Arizona, Tucson, AZ, 1987a.

Spencer, J.R., Icy Galilean Satellite Reflectance Spectra: Less Ice on Ganymede and Callisto?, *Icarus* **70**, 99-110, 1987b.

Spencer, J.R., Thermal Segregation of Water Ice on the Galilean Satellites, *Icarus* **69**, 297-313, 1987c.

Thomson, J.L., and J.W. Salisbury, The Mid-infrared Reflectance of Mineral Mixtures ($7 - 14$ μm), *Remote Sens. Environ.* **45**, 1-13, 1993.

Urquhart, M.L., and B.M. Jakosky, Constraints on the Solid-State Greenhouse-Effect on the Icy Galilean Satellites, *J. Geophys. Res.* **101**, 21169-21176, 1996.

Veverka, J., P. Thomas, T.V. Johnson, D. Matson, and K. Housen, The Physical Characteristics of Satellite Surfaces, in *Satellites*, ed. J.A. Burns and M.S. Matthews, (University of Arizona Press, Tucson, AZ), 342-402, 1986.

Warren, S.G., Optical Constants of Ice from the Ultraviolet to the Microwave, *Appl. Opt.* **23**, 1206-1225, 1984.

A Effective, Disk-Integrated Color Temperatures

Figure 4.2b can also be used to constrain the ratio between the disk-integrated, effective, color temperatures of Callisto and Europa. Figure 4.3 shows our measured ratio spectrum with a blackbody ratio spectrum plotted over it. The blackbody ratio spectrum has been scaled to account for such factors as the difference in projected area and difference in observing time of the two satellites. This scaling would also account for any differences in flux produced by temporal variations in the observing conditions. The best-fit temperatures for the two satellites are given by the solid line in Figure 4A.1. (The temperature ratio is not constant because the Planck function is not linearly self-similar as a function of temperature.) The RMS deviation of our ratio spectrum from the 151/130 blackbody ratio spectrum shown in Figure 4.3 is $\sim 3\%$. All points along the best-fit curve in Figure 4A.1 are statistically equivalent in terms of agreement with the measured ratio spectrum. The color temperature ratio we derive is consistent with previous ground-based brightness temperatures derived from broadband photometry within the $8 - 12$ μm wavelength region, the data with error bars in Figure 4A.1. However, as noted in *Morrison* [1977], there may be a bias in earlier brightness temperatures [*Gillett et al.* 1970] due to incorrect estimations of the satellite diameters and/or calibration procedures. (The data from *Gillett et al.* [1970] are the two points that lie farthest from our best-fit color temperature ratio.) As shown in Figure 4A.1, our ratio spectrum places a tight constraint on the second satellite's effective temperature if one satellite's effective temperature is known. The RMS deviation of the blackbody ratios 147/130 and 155/130 was used to estimate the uncertainty in the effective color temperature ratio. These uncertainties are shown as dashed lines in Figure 4A.1.

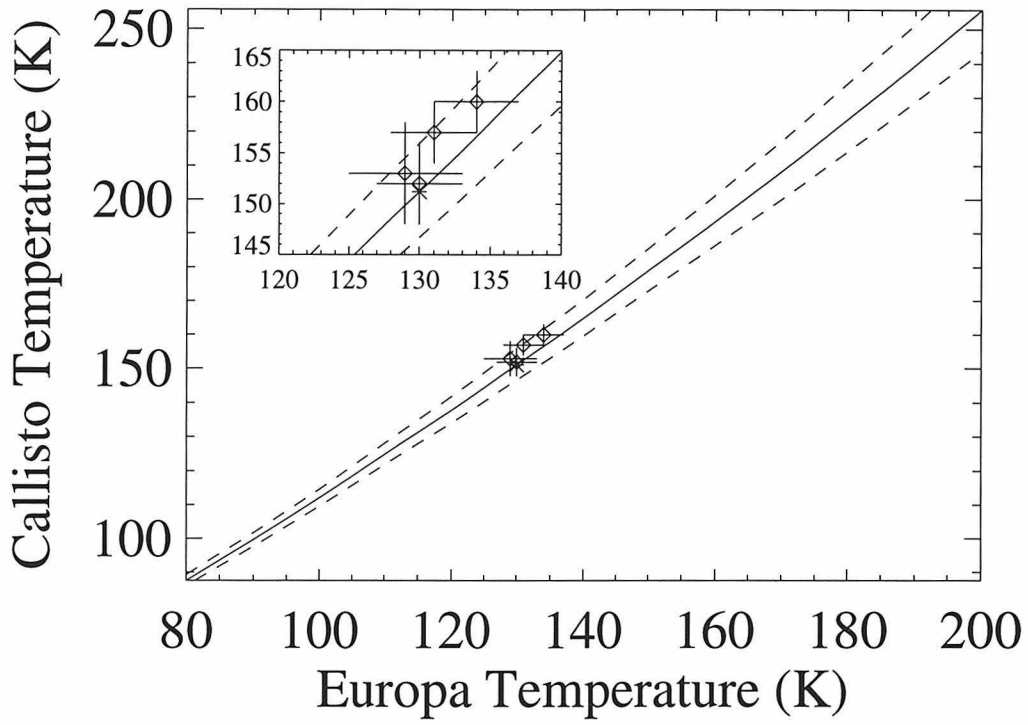

Figure 4A.1: The solid line is the effective temperature for Callisto that gives the best fit to the measured ratio spectrum as a function of the effective temperature for Europa. The diamonds (with error bars) are the broadband brightness temperatures from ground-based thermal infrared photometry as reviewed in *Morrison* [1977]. The color temperature ratio used for comparison to the ratio spectrum in Figure 3 is marked with an asterisk. All points along the solid line are statistically equivalent in terms of the quality of the fit to the measured ratio spectrum, Figure 6a. The dashed lines are the estimated uncertainty in the effective color temperature ratio. The RMS deviations from the measured ratio spectrum for the blackbody ratios in Figure 7 were used as the thresholds for the estimated uncertainty.

B Synthesis of the Europa Spectrum

Spencer [1987a] derived an average spectrum of Callisto from Voyager 1 data by averaging all spectra that had a brightness temperature at 22μm that was warmer than 130 K, a total of 90 spectra. Spencer then smoothed the average spectrum with a boxcar filter of width 14 cm^{-1} to create his Figure 4. We digitized the average Callisto spectrum from Spencer's Figure 4 then fit a second-order polynomial through the digitized points to remove the ($< 1\%$) instrument and digitization noise since the noise level in our ratio spectrum ($\sim 3\%$) was significantly larger than the noise in the average Voyager 1 spectrum of Callisto. Consequently, the noise level in our Europa spectrum includes only noise from our ratio spectrum. The Voyager brightness temperature for Callisto at every wavelength in our ratio spectrum was converted into radiance, divided by the value of our ratio spectrum at that wavelength, then converted into brightness temperatures to create the upper curve in our Figure 4.4 (effectively giving $[Voyager\ Callisto]/[\{Palomar\ Callisto\}/\{Palomar\ Europa\}]$).

The lower curve in our Figure 4.4 was digitized from the average Voyager 2 spectrum of Europa in Spencer's Figure 4. Spencer averaged 53 spectra, all of which had a 22 μm brightness temperature that was warmer than 90 K then smoothed the average spectrum with a boxcar filter of width 14 cm^{-1}. The temperature offset between the two curves in our Figure 4.4 arises because the Voyager Europa spectra were collected at its terminator whereas the Voyager Callisto spectra were collected at its warmer afternoon quadrant.

Chapter 5

Appendices for the Photochemical Modeling in Chapter 2

A Photolysis Reactions

Table 5A.1: Photolysis Reactions in Nominal Photochemical Model (part 1)

	Reaction			Rate at 70, 112 km	Reference
P14	$S_3 + h\nu$	$\rightarrow$	S_3		†$F0$
P15	$S_4 + h\nu$	$\rightarrow$	S_4		†$F0$
P57	$CO_2 + h\nu$	$\rightarrow$	$CO + O$	1.1×10^{-12}, 6.8×10^{-9}	$M42F0$
P58	$CO_2 + h\nu$	$\rightarrow$	$CO + O(^1D)$	0 , 6.8×10^{-9}	$M42F0$
P59	$O_2 + h\nu$	$\rightarrow$	$2\ O$	1.1×10^{-9}, 1.0×10^{-7}	$F0$
P60	$O_2 + h\nu$	$\rightarrow$	$O + O(^1D)$	0 , 3.4×10^{-8}	$F0$
P61	$O_3 + h\nu$	$\rightarrow$	$O_2 + O$	2.6×10^{-3}, 2.5×10^{-3}	$M02M9$
P62	$O_3 + h\nu$	$\rightarrow$	$O_2(^1\Delta) + O(^1D)$	1.3×10^{-2}, 1.3×10^{-2}	$M02M9$
P63	$O_3 + h\nu$	$\rightarrow$	$3\ O$	1.1×10^{-9}, 1.4×10^{-6}	$M02M9$
P64	$O_3 + h\nu$	$\rightarrow$	$O_2 + O(^1D)$	1.4×10^{-6}, 1.2×10^{-6}	$M02M9$
P65	$O_3 + h\nu$	$\rightarrow$	$O_2(^1\Delta) + O$	1.4×10^{-6}, 1.2×10^{-6}	$M02M9$
P66	$H_2O + h\nu$	$\rightarrow$	$H + OH$	1.0×10^{-12}, 4.3×10^{-6}	$F0$
P67	$H_2O + h\nu$	$\rightarrow$	$H_2 + O(^1D)$	0 , 1.1×10^{-7}	$F0$
P68	$H_2O + h\nu$	$\rightarrow$	$2\ H + O$	0 , 1.3×10^{-7}	$F0$
P69	$H_2O_2 + h\nu$	$\rightarrow$	$2\ OH$	1.7×10^{-4}, 1.8×10^{-4}	$F0$
P70	$HCl + h\nu$	$\rightarrow$	$H + Cl$	2.1×10^{-7}, 2.7×10^{-6}	$M0$
P71	$ClO + h\nu$	$\rightarrow$	$Cl + O$	1.1×10^{-2}, 1.1×10^{-2}	$A0$
P72	$SO + h\nu$	$\rightarrow$	$S + O$	4.3×10^{-4}, 6.2×10^{-4}	$M4$
P73	$SO_2 + h\nu$	$\rightarrow$	$SO + O$	1.9×10^{-4}, 3.1×10^{-4}	$M42M9$
P74	$SO_2 + h\nu$	$\rightarrow$	$S + O_2$	6.8×10^{-7}, 2.4×10^{-6}	$M42M9$
P75	$SO_2 + h\nu$	$\rightarrow$	$S + 2\ O$	0 , 0	$M42M9$
P76	$Cl_2 + h\nu$	$\rightarrow$	$2\ Cl$	5.2×10^{-3}, 4.7×10^{-3}	$C0$
P77	$COCl_2 + h\nu$	$\rightarrow$	$ClCO + Cl$	8.7×10^{-5}, 9.1×10^{-5}	$F0$
P78	$HOCl + h\nu$	$\rightarrow$	$OH + Cl$	9.9×10^{-4}, 9.1×10^{-4}	$M0$
P79	$S_2 + h\nu$	$\rightarrow$	$2\ S$	6.6×10^{-3}, 6.4×10^{-3}	$M5$
P80	$S_2O + h\nu$	$\rightarrow$	$SO + S$	9.0×10^{-2}, 8.8×10^{-2}	$M5$
P81	$OCS + h\nu$	$\rightarrow$	$CO + S$	4.8×10^{-5}, 4.8×10^{-5}	$E02M0$
P82	$ClOO + h\nu$	$\rightarrow$	$ClO + O$	1.8×10^{-2}, 1.7×10^{-2}	$B0$
P83	$OClO + h\nu$	$\rightarrow$	$ClO + O$	1.6×10^{-1}, 1.4×10^{-1}	$A0$
P84	$ClO_3 + h\nu$	$\rightarrow$	$ClO + O_2$	4.3×10^{-2}, 4.0×10^{-2}	$F0$

Table 5A.1: Photolysis Reactions in Nominal Photochemical Model (part 2)

	Reaction			Rate Coefficient	Reference
P85	$Cl_2O + h\nu$	$\rightarrow$	$Cl + ClO$	7.3×10^{-3}, 7.0×10^{-3}	$B0$
P86	$Cl_2O_2 + h\nu$	$\rightarrow$	$Cl + ClOO$	1.2×10^{-2}, 1.1×10^{-2}	$C0$
P87	$Cl_2O_3 + h\nu$	$\rightarrow$	$ClO + ClOO$	3.8×10^{-2}, 3.6×10^{-2}	$B0$
P88	$SCl + h\nu$	$\rightarrow$	$S + Cl$	5.3×10^{-2}, 4.7×10^{-2}	$M9$
P89	$SCl_2 + h\nu$	$\rightarrow$	$SCl + Cl$	4.5×10^{-3}, 4.1×10^{-3}	$M4M9$
P90	$SCl_2 + h\nu$	$\rightarrow$	$S + 2\ Cl$	3.3×10^{-4}, 4.5×10^{-4}	$M4M9$
P91	$S_2Cl + h\nu$	$\rightarrow$	$S_2 + Cl$	1.4×10^{-1}, 1.2×10^{-1}	$M9$
P92	$S_2Cl + h\nu$	$\rightarrow$	$SCl + S$	3.7×10^{-4}, 3.4×10^{-4}	$M9$
P93	$S_2Cl_2 + h\nu$	$\rightarrow$	$2\ SCl$	2.1×10^{-2}, 2.0×10^{-2}	$M4M9$
P94	$S_2Cl_2 + h\nu$	$\rightarrow$	$S_2 + 2\ Cl$	2.2×10^{-2}, 2.1×10^{-2}	$M4M9$
P95	$S_2Cl_2 + h\nu$	$\rightarrow$	$S_2Cl + Cl$	2.7×10^{-2}, 2.6×10^{-2}	$M4M9$

† Reactions P14 and P15 represent photoabsorption opacity due to these molecules. Hence, the product molecules are the same as the photoabsorbing molecules.

Photoabsorption reactions R1 - R13 and R16 - R56, not shown above, represent the atmospheric opacity resulting from the photolysis reactions that are included in this table. The photoabsorption opacity reactions also include the opacity produced by the molecules at wavelengths that are larger than the photodissociation threshold.

Units are s^{-1}. Solar flux is the high solar flux data from Table 2.5. Photolysis rate coefficients are given at 70 km ($\sim$ cloud top altitude) and at the top of the model atmosphere (112 km).

Reference Codes: First letter is reference for photodissociation cross section, second letter is reference for branching ratio, if applicable. The numbers after each letter describe the type of information used to determine the rate.

References: (A) *DeMore et al.* [1990], (B) *DeMore et al.* [1992], (C) *DeMore et al.* [1994], (D) *DeMore et al.* [1997], (E) *Molina et al.* [1981], (F) *Allen, M.A.,* [Personal Communication, 1995] compilation from multiple sources (see Appendix 5B), (M) estimated for this study (see Appendix 5B).

Data types: (0) Measured or critically evaluated cross section, (2) Linearly interpolated between measured temperature dependent cross sections, (4) Scaled based on comparisons of published absolute cross sections, (5) Scaled from measured relative cross section, (9) Estimate.

B Sources of Photoabsorption and Photodissociation Data

This appendix describes the sources from which the data used for the photolysis reactions were obtained. For each molecule, it provides the source(s) for the photoabsorption cross section at $\sim$ 298 K, the source(s) for the photodissociation quantum yields and branching ratios, and the source(s) for photoabsorption cross sections at other temperatures. If data at multiple temperatures was available, the photoabsorption cross section at the specified atmospheric temperature was determined by linear interpolation between the nearest temperatures at which the cross section had been measured. If quantitative laboratory measurements were not available and values were required for model calculations, the values have been estimated. The information presented here was used for the nominal model calculations. The nominal values were modified for the calculations described in Sections 2.3.2 and 2.3.3 as described in those sections.

CO_2:

The photoabsorption cross section at 298 K from *Lewis and Carver* [1983] was used for 120.0 - 197.0 nm. For 197.25 - 203.75 nm at 298 K, the photoabsorption cross section was taken from *Shemansky* [1972]. The 298 K cross section was extrapolated to be zero at 204.0 nm. No correction was made for the Rayleigh scattering cross section at these wavelengths. The cross section at 298 K at $>$ 204.0 nm was approximated as zero based on the assessment by *Shemansky* [1972] that approximately all extinction by CO_2 at these longer wavelengths could be attributed to Rayleigh scattering. The energetic threshold for photodissociation of CO_2 is near $224.5 - 227.5$ nm [*DeMore et al.* 1994 and *Okabe* 1978, respectively].

Photodissociation branching ratios for $120-125$ nm were estimated based on *Lawrence* [1972] and *Slanger and Black* [1978]. For $125 - 160$ nm, branching ratios were based on *Slanger and Black* [1978]. For $>$ 160 nm, the branching ratios were based on *Okabe* [1978]. The photoabsorption cross section at 202 K from *Lewis and Carver* [1983] was

used for 120.0 - 197.0 nm. For 197.25 - 200.0 nm at 202 K, the photoabsorption cross section was estimated to be a factor of three smaller than that measured by *Shemansky* [1972] at 298 K. The factor of three was selected to match the difference between the 202 K and 298 K cross sections near 197 nm [*Lewis and Carver* 1983]. The 202 K cross section was estimated to be zero at 200.25 nm. No correction was made for the Rayleigh scattering cross section at these wavelengths. The cross section at 202 K at $>$ 200.25 nm was approximated as zero based on the assessment by *Shemansky* [1972] noted above.

O_2:

The photoabsorption cross section for $120 - 250$ nm is a composite based on multiple measurements. The data used for creating the cross section are from *Ogawa and Ogawa* [1975], *Lewis et al.* [1988a], *Lewis et al.* [1988b], *Carver et al.* [1977], *Kley* [1984], *Wang et al.* [1987], *Black et al.* [1985], *Gibson et al.* [1983], *Ackerman* [1971], *Allen and Frederick* [1982], *Yoshino et al.* [1992], *Yoshino et al.* [1988b], *Ditchburn and Young* [1962], and *Johnston et al.* [1984].

The photodissociation branching ratios from *Lee et al.* [1977] were used for $120 - 180$ nm. For $190 - 250$ nm the photodissociation quantum yield was assumed to be 1.0.

O_3:

The photoabsorption cross section digitized from figures in *Tanaka et al.* [1953] was used for 120.0 - 183.9 nm. These data were converted from absorption coefficient (cm^{-1}) to cross section (cm^2) assuming the absorption coefficient had been reported in units of cm^{-1} atm^{-1} at 273 K (base e). The *Tanaka et al.* [1953] were then multiplied by 0.98 and shifted to smaller wavelengths by 0.4 nm. This unit conversion, scaling factor, and wavelength shift minimized the RMS difference between the *Tanaka et al.* [1953] data and the *Yoshino et al.* [1993] data at 185 - 220 nm. The scaling factor and wavelength shift are within the stated uncertainty for the *Tanaka et al.* [1953] data and could arise in part from the digitization process. The photoabsorption cross section at 184.9 - 253.8 nm for 295 K was taken from *Yoshino et al.* [1993]. For 254.0 - 350.0, the photoabsorption cross section at 298 K from *Molina and Molina* [1986] was multiplied by 0.966. This scaling factor minimized the RMS difference between the

Molina and Molina [1986] data and the measurements at Hg I wavelengths by *Yoshino et al.* [1988a] at 295 K (their Table 2). For 407.2 - 758.9 nm, the photoabsorption cross section at 298 K digitized from *Burkholder and Talukdar* [1994] was shifted to larger wavelengths by 0.1 nm. This wavelength shift is within the stated uncertainty for the *Burkholder and Talukdar* [1994] data, and minimized the RMS difference between the *Burkholder and Talukdar* [1994] data and the results from *Anderson and Mauersberger* [1992] for 480 - 760 nm. The data from *Griggs* [1968] for $\sim$ 30 C at 761.6 – 852.8 nm was digitized then scaled and shifted to larger wavelengths by 1.8 nm. The scaling and wavelength shift minimized the RMSdifference between the *Griggs* [1968] data and that from *Burkholder and Talukdar* [1994] and *Anderson and Mauersberger* [1992].

The branching ratios used in the model are given in Table 5B.1. The branching ratios are temperature- dependent for 305.0 - 325.0 nm. At other wavelengths, the branching ratios were presumed to be independent of temperature. The effective branching ratios for $<$ 200 nm are based on measurements by *Taherian and Slanger* [1985] and *Turnipseed et al.* [1991]. The effective branching ratios were calculated from the measured direct branching ratios at $<$ 200 nm by assuming that 90% of the $O_2(b^1\Sigma)$ produced would be collisionally quenched to $O_2(a^1\Delta)$ and 10% would be collisionally quenched to $O_2(X^3\Sigma)$ (see Appendix 5D). Those for 200 – 271 nm are based on the analysis by *Michelsen et al.* [1994]. Those for 271 – 305 nm are based on *Michelsen et al.* [1994] and *DeMore et al.* [1997]. For $>$ 305 nm, the branching ratios are primarily from *DeMore et al.* [1997]. The yields for the spin-forbidden channels in Table 5B.1 for 310 – 411 nm are an estimate based on *Silvente et al.* [1997] and *Takahashi et al.* [1996].

The photoabsorption cross sections from *Yoshino et al.* [1993] were used for 184.9 - 253.8 nm at 228 and 195 K. The cross section from *Freeman et al.* [1984a] for 153.8 - 349.7 nm at 195 K was scaled to match the revised absolute cross sections given in *Yoshino et al.* [1988a] at Hg I wavelengths. The cross section from *Molina and Molina* [1986] for 254.0 - 350.0 nm at 228 K was multiplied by 0.966 (described above). The cross section from *Molina and Molina* [1986] for 240.5 - 350.0 nm at 263

Table 5B.1: Branching Ratios for Photolysis of O_3

[a] Wavelength	$O_2(X^3S)$ $+O(^3P)$	$O_2(a^1\Delta)$ $+O(^1D)$	$O_2(X^3\Sigma)$ $+O(^1D)$	$O_2(a^1\Delta)$ $+O(^3P)$	3O
120.0	0.0	[b] 0.50	0.0	[b] 0.05	0.45
160.0	0.0	[b] 0.50	0.0	[b] 0.05	0.45
160.00001	0.0	[b] 0.45	0.0	[b] 0.05	0.50
199.70	0.50	[b] 0.45	0.0	[b] 0.05	0.0
199.70001	0.13	0.87	0.0	0.0	0.0
271.0	0.13	0.87	0.0	0.0	0.0
305.0	[c]T	T	0.0	0.0	0.0
311.0	T	T	0.01	0.01	0.0
325.0	T	T	0.01	0.01	0.0
325.00001	0.98	0.0	0.01	0.01	0.0
411.0	0.98	0.0	0.01	0.01	0.0
411.00001	1.0	0.0	0.0	0.0	0.0
611.0	1.0	0.0	0.0	0.0	0.0
611.00001	1.0	0.0	0.0	0.0	0.0
850.0	1.0	0.0	0.0	0.0	0.0

[a] Wavelengths are in nanometers. [b] Branching ratios are effective branching ratios following collisional quenching of $O_2(b^1\Sigma)$ (Appendix 5D). [c] T means the branching ratios are dependent on temperature as described in the text.

K was multiplied by 0.966 (described above). No measurements were reported by *Molina and Molina* [1986] at 263 K for 185.0 - 240.0 nm so the scaled cross sections reported at 226 and 298 K were averaged. This was done to simplify the program which interpolates between the measured cross sections to the specified atmospheric temperatures. The cross section for O_3 was assumed to be independent of temperature for $350.0 < \lambda < 407.0$ nm. The relative cross section data from *Burkholder and Talukdar* [1994] for 407.0 - 852.8 nm at 220 - 280 K was digitized, shifted to larger wavelengths by 0.1 nm, and multiplied by the $\sim 298 - 303$ K cross section.

H_2O:

The photoabsorption cross section for $120 - 180$ nm was digitized from *Lee and Suto* [1986]. For $180 - 185$ nm the cross section was digitized from *Watanabe and Zelikoff* [1953], and for $190 - 195$ the cross section was digitized from *Thompson et al.* [1963].

The photodissociation branching ratios were based on measurements by *Slanger and Black* [1982] and *Stief et al.* [1975].

H_2O_2:

The photoabsorption cross section for $120 - 175$ nm was taken from *Schurgers and Welge* [1968]. For $180 - 190$ nm, that from *CIAP* [1975] was used. For $190 - 350$ nm, the cross section from *DeMore et al.* [1990] was used.

The photodissociation quantum yield was assumed to by 1.0 at all wavelengths.

HCl:

The photoabsorption cross section for $120.0 - 139.9$ nm was digitized from *Myer and Samson* [1970]. For $140.0 - 220.0$ nm, the cross section was taken from *Watson* [1977].

The photodissociation quantum yield was assumed to be 1.0 at all wavelengths based on the assessment in *Myer and Samson* [1970].

ClO:

The photoabsorption cross section for $230 - 325$ nm was taken from *DeMore et al.* [1990].

The photodissociation quantum yield was assumed to be 1.0 at all wavelengths.

SO:

The photoabsorption cross section for 120.0 – 133.45 nm was scaled from that in *Nee and Lee* [1986]. The scaling factor was (0.88)(8.875)/(9.0) based on the following three items. *Nee and Lee* [1986] assumed the cross section for SO at 190.0 nm was 9.0×10^{-18} based on the measurements by *Phillips* [1981]. The value digitized from *Phillips* [1981] at 190.0 nm was 8.875×10^{-18} [*Manatt, S.*, Personal Communication, 1993]. Later work [*Phillips, L.F.*, Personal Communication, 1992] suggested a multiplicative correction factor of 0.88 for the SO cross sections in *Phillips* [1981]. The estimated upper-limit cross section from *Nee and Lee* [1986] for 135.0 – 180.0 nm was scaled by the same factor described above. For 190.1 – 235.1 nm, the data from *Phillips* [1981] was multiplied by 0.88 as described above then the wavelengths were shifted by 0.11 nm to larger wavelengths based on the comparisons in *Manatt and Lane* [1993]. This wavelength shift is consistent with the differences between the band head locations in *Phillips* [1981] and *Colin* [1969].

Photodissociation quantum yields were assumed to be 1.0 for 120.5 – 232.0 nm.

SO_2:

The photoabsorption cross section for 120.0 – 132.22 nm was digitized from *Suto et al.* [1982] then shifted to smaller wavelengths by 0.063 nm to match the peak positions given in Table 1 of *Suto et al.* [1982]. This wavelength shift could arise from the digitization process. For 132.32 – 136.62 nm, the photoabsorption cross section from *Manatt and Lane* [1993] was shifted to larger wavelengths by 0.2162nm. This wavelength shift gave the best match to the (wavelength-shifted) positions of the peaks at 131.5339 and 131.9985 nm in the *Suto et al.* [1982] data. The photoabsorption cross section from *Manatt and Lane* [1993] was used for 136.70 - 196.90 nm with no wavelength shift. For 196.92 - 227.74 nm, the photoabsorption cross section from *Martinez and Joens* [1992] was used. The wavelength positions for the *Martinez and Joens* [1992] and *Hearn and Joens* [1991] data for 227.76 - 231.80 nm were recalibrated based on more precise measurements made in 1994 [*Joens, J.A.*, Personal Communication, 1994]. The recalibrated data from the two studies were then averaged and used for this wavelength region. For 231.82 - 323.06 nm, the data from *Hearn and Joens* [1991] were used as originally published. For 323.08 - 406.0 nm, the data from

Sprague and Joens [1995] were used.

The branching ratios used in the model are given in Table 5B.2. The branching ratios were presumed to be independent of temperature at all wavelengths. The branching ratios for $\leq$ 165 nm are estimates based on fluorescence measurements [*Suto et al.* 1982], qualitative measurements of relative yields for each branch [*Sato et al.* 1992; *Effenhauser et al.* 1990; *Venkitachalam and Bersohn* 1984; *Wilson et al.* 1982; *Lalo and Vermeil* 1974; *Lalo and Vermeil* 1972], limited information on which vibrational modes are likely to be excited in this wavelength region [*Watkins* 1969], and the review by *Welge* [1974]. The relative branching ratios for $165 < \lambda < 210$ nm are based on measurements by *Felder et al.* [1988], *Kawasaki and Sato* [1987], and *Ebata et al.* [1988]. These measurements have shown the primary products of photolysis in this wavelength region are SO and O but have not excluded a small yield of S and O_2. The total photodissociation yields for $>$ 200 nm are based on measurements of the fluorescence yield in *Ahmed and Kumar* [1992] and *Hui and Rice* [1972].

A photoabsorption cross section was compiled for 171 – 320 nm at an effective temperature of $\sim$ 213 K. For 171.02 – 239.79 nm, the cross sections from *Freeman et al.* [1984b] were used after converting the wavenumber ordinate to wavelength in standard air using the index of refraction for standard air from *Edlen* [1966]. For 281.5 – 291.5 nm, the data at 295, 263, and 218 K in *Leroy et al.* [1983] were digitized then linearly extrapolated using a least-squares fit at each wavelength to 213 K. For 299.97 – 320.37 nm, the cross section at 213 K was derived by linearly interpolation between the data at 295 and 210 K in *McGee and Burris* [1987]. Prior to this interpolation, the *McGee and Burris* [1987] data were shifted to smaller wavelengths by 0.03 nm based on the comparisons by *Manatt and Lane* [1993].

Cl_2:

The photoabsorption cross section for 240 - 475 nm at 298 K was taken from *DeMore et al.* [1997].

The quantum yield for photodissociation was assumed to be 1.0 at all wavelengths.

$COCl_2$:

Table 5B.2: Branching Ratios for Photolysis of SO_2

[a] Wavelength	SO+O	$S+O_2$	S+2O
120.0	0.7	0.3	0
130.0	0.7	0.3	
130.00001	0.95	0.05	
165.0	0.95	0.05	
165.00001	0.99	0.01	
195.0	0.99	0.01	
200.0	0.98	0.0099	
200.83	0.97897	0.00989	
203.93	0.97949	0.00989	
205.33	0.97998	0.0099	
207.15	0.97525	0.00985	
208.64	0.96108	0.00971	
210.1	0.9568	0.00966	
210.10001	0.96647	0	
210.17	0.96627		
212.02	0.95348		
213.18	0.97109		
214.99	0.96786		
215.75	0.97954		
216.58	0.91978		
217.99	0.89342		
218.78	0.849		
220.3	0.42751		
220.30001	0		

[a] Wavelengths are in nanometers.

The photoabsorption cross section for 182.5 - 232.5 nm at 298 K was taken from *DeMore et al.* [1992]. The photoabsorption cross section for 232.5 - 285.0 nm at 298 K was taken from *Baulch et al.* [1980].

The quantum yield for photodissociation was assumed to be 1.0 at all wavelengths.

HOCl:

The photoabsorption cross section for 200.0 – 380.0 nm was taken from *DeMore et al.* [1994]. For 396.0 – 530.0 nm, the photoabsorption cross section was from *Barnes and Sinha* [1997].

The photodissociation quantum yield was assumed to be 1.0 at all wavelengths.

S_2:

The photoabsorption cross section was estimated. The estimate was based, primarily, on the discussion in *Oommen* [1970]. For 156 – 185 nm, the cross section for O_2 from *Watanabe et al.* [1953] was shifted to larger wavelengths by the difference between the measured ionization potentials for O_2 and S_2. The shifted O_2 cross section was then multiplied by 0.1 to minimize the disagreement between it and that derived from CS_2 as will be discussed in the next couple sentences. For 187 – 230 nm, the cross section for CS_2 from *Hearn and Joens* [1991] was first multiplied by 10^{-3} based on the relative optical depths for CS_2 and S_2 in this wavelength region digitized from *Oommen* [1970]. Then, the scaled CS_2 cross section was multiplied by 10 to minimize the disagreement between it and the shifted O_2 cross section. Thus, the CS_2 cross section was, effectively, multiplied by 10^{-2}. For 232 – 315 nm, the cross section for S_2 that was digitized from *Oommen* [1970] was scaled so that the maximum cross section was $\sim 10^{-17}$ based on *Oommen*'s [1970] comparison of the S_2 and SO_2 cross sections in this wavelength region. For 316 – 335 nm, the cross section for O_2 from *Watanabe et al.* [1953] was shifted to larger wavelengths by the difference between the measured ionization potentials for O_2 and S_2. The shifted O_2 cross section was then multiplied by 0.1 for the reason given above. The S_2 cross section at 360 nm was estimated to be $\sim 10^{-25}$ and that at > 360 nm was estimated to be zero based on *Okabe*'s [1978] assessment that absorption by S_2 began at near 360 nm.

The photodissociation quantum yield was assumed to be 1.0 at all wavelengths.

S_2O:

The photoabsorption cross section for 260 – 340 nm was estimated as 30 times the SO_2 cross section at these wavelengths based on the discussion in *Jones* [1950]. *Jones* [1950] estimated the absorption cross section for 260 – 340 was $\sim$ 10 – 100 times larger than the SO_2 cross section at these wavelengths. *Jones* [1950] attributed this absorption to $(SO)_2$, but later studies [*Lakshminarayana* 1975; *Hopkins et al.* 1973; *Meschi and Myers* 1959] suggest the species formed is S_2O.

The photodissociation quantum yields are based on measurements by *Zhang et al.* [1995] who found rapid predissociation in the band whose origin is at 319.4 nm and slow predissociation in the band whose origin is at 332.2 nm.

OCS:

The photoabsorption cross section at 295 K for 185.0 – 300.0 nm was taken from *Molina et al.* [1981].

The photodissociation quantum yield was assumed to be 0.72 for wavelengths $\leq$ 285.3 nm based on the recommendation in *DeMore et al.* [1994].

The photoabsorption cross section at 225 K for 185.0 – 296.0 nm was taken from *Molina et al.* [1981].

ClOO:

The photoabsorption cross section for 220 – 280 nm was taken from *DeMore et al.* [1992].

The photodissociation quantum yield was assumed to be 1.0 at all wavelengths.

OClO:

The photoabsorption cross section for 150 – 185 nm was taken from *Basco and Morse* [1974]. That for 250 – 430 was taken from *DeMore et al.* [1990].

The photodissociation quantum yield was assumed to be 1.0 at all wavelengths.

ClO_3:

The photoabsorption cross section for 200 – 350 nm was taken from *DeMore et al.* [1990].

The photodissociation quantum yield was assumed to be 1.0 at all wavelengths.

Cl_2O:

The photoabsorption cross section for 200 – 500 nm was taken from *DeMore et al.* [1992].

The photodissociation quantum yield was assumed to be 1.0 at all wavelengths.

Cl_2O_2:

The photoabsorption cross section for 190 – 450 nm was taken from *DeMore et al.* [1994] as modified by *Huder and DeMore* [1995].

The photodissociation quantum yield was assumed to be 1.0 at all wavelengths.

Cl_2O_3:

The photoabsorption cross section for 220 – 320 nm was taken from *DeMore et al.* [1992].

The photodissociation quantum yield was assumed to be 1.0 at all wavelengths.

SCl:

The photoabsorption cross section was estimated by scaling and shifting the ClO spectrum. The ClO spectrum was shifted to larger wavelengths based on the difference between the measured ionization potential for ClO and the calculated ionization potential for SCl. The magnitude of the ClO spectrum was multiplied by a factor of 0.1 based on comparisons between the absorption cross sections of $SOCl_2$ and S_2Cl_2 and between those of Cl_2O and SCl_2. This scaling factor is plausible (or possibly an upper limit) since SCl has never been clearly identified in spectra and the scaled cross section is a factor of 10 larger than the cross section of S_2Cl_2.

The photodissociation quantum yield was assumed to be 1.0 at all wavelengths.

SCl_2:

The photoabsorption cross section for 190.7 – 500.0 nm was taken from *Colton and Rabalais* [1974]. The contribution of S_2Cl_2 to this spectrum was approximately removed by multiplying the S_2Cl_2 spectrum by a factor of 0.01 and subtracting it from the measured SCl_2 spectrum.

Table 5B.3: Branching Ratios for Photolysis of SCl_2

[a] Wavelength	SCl+Cl	S+2Cl
182.50	0.	1.0
190.70	0.	1.0
230.00	0.25	0.75
230.00001	1.0	0.
460.00	1.0	0.
460.00001	0.	0.

[a] Wavelengths are in nanometers.

The photodissociation branching ratios (Table 5B.3) were estimated based on the energy required to produce the possible products of the photodissociation reaction and qualitative observations. *Tiemann et al.* [1989] and *Howe et al.* [1995] observed production of SCl from photolysis of SCl_2 at 248, and 340−346 nm. *Samuel* [1946] had assigned the absorption band near 400 nm to the SCl + Cl channel, the absorption band near 270 nm to the S + 2Cl channel, and the absorption band near 230 nm to the $S(^1D)$ + 2Cl channel.

S_2Cl:

The photoabsorption cross section was estimated by scaling and shifting the ClOO spectrum. The ClOO spectrum was shifted to larger wavelengths based on the difference between the measured ionization potential for ClOO and the calculated ionization potential for S_2Cl. The magnitude of the ClOO spectrum was multiplied by a factor of 0.1 based on comparisons between the absorption cross sections of $SOCl_2$ and S_2Cl_2 and between those of Cl_2O and SCl_2. This scaling factor is plausible (or possibly an upper limit) since *Chiu et al.* [1986] indicated they had difficulty measuring the S_2Cl spectrum due to the strong absorption by S_2Cl_2. The scaled cross section is a factor of 100 larger than the cross section of S_2Cl_2.

The photodissociation branching ratios (Table 5B.4) were estimated based on the energy required to produce the possible products of the photodissociation reaction and qualitative observations. *Lee et al.* [1993] interpreted their results as implying

Table 5B.4: Branching Ratios for Photolysis of S_2Cl

[a] Wavelength	SCl+S	S_2+Cl
320.00	0.1	0.9
340.80	0.1	0.9
340.80001	0.	1.0
500.00	0.	1.0
500.00001	0.	0.

[a] Wavelengths are in nanometers.

that photolysis of S_2Cl at 308 nm predominantly produced S_2 + Cl.

S_2Cl_2:

The photoabsorption cross section for 120 – 172.9 nm was digitized from *Tokue et al.* [1988]. The photoabsorption cross section for 186.8 – 421.1 nm was digitized from *Colton and Rabalais* [1974]. The wavelengths for the digitized data at 236.3 – 244.8 nm were multiplied by 1.016 to create a smooth curve through this wavelength region, as was measured by *Chiu* [1983]. For 439.8 – 479.8 nm, the photoabsorption cross section was digitized from *Feher and Munzner* [1963]. The *Feher and Munzner* [1963] data were acquired for S_2Cl_2 in solution with cyclo-hexane, but their measurements agree reasonably well with those by *Colton and Rabalais* [1974] at shorter wavelengths. Gas-phase study by *Chiu* [1983] shows that S_2Cl_2 does have detectable absorption in the gas- phase for 400 – 480 nm.

The photodissociation branching ratios in Table 5B.5 were estimated. The wavelength boundaries were chosen to match either the minima between absorption bands or energetic thresholds for a proposed branch. *Tokue et al.* [1988] assigned the absorption peaks in their spectrum at < 200 nm to the S_2 + 2Cl channel. *Samuel* [1946] assigns the absorption band near 260 nm to the S_2 + 2Cl channel, but *Tiemann et al.* [1989] detection weak production of SCl in photolysis at 248 nm. *Chiu* [1983] interpret their measurements as indicating the primary photodissociation products are 2SCl at wavelengths > 300 nm, but *Lee et al.* [1993] found that photolysis at 308 nm leads

Table 5B.5: Branching Ratios for Photolysis of S_2Cl_2

[a] Wavelength	S_2Cl+Cl	$S-2+2Cl$	$2SCl$
120.00	0.	1.0	0.
180.00	0.	1.0	0.
180.00001	0.	0.5	0.5
230.00	0.	0.5	0.5
230.00001	0.15	0.75	0.1
280.00	0.15	0.75	0.1
280.00001	0.75	0.	0.25
308.70	0.75	0.	0.25
308.70001	1.0	0.	1.0
385.80	1.0	0.	1.0
385.80001	0.	0.	0.

[a] Wavelengths are in nanometers.

almost exclusively to production of S_2Cl + Cl. *Chiu and Chang* [1994] found that S_2Cl_2 did no photodissociate at 514.5 nm even though it is energetically feasible. The results from *Park et al.* [1991] were disregarded since they seem to conflict with all other studies.

S_3:

The photoabsorption cross section for $350 - 600$ nm was digitized from *Billmers and Smith* [1991]. Their data were based on analyses of spectra of sulfur vapor at 723 and 843 K.

The photodissociation quantum yield for these wavelengths was assumed to be 0.0.

S_4:

The photoabsorption cross section for $350 - 600$ nm was digitized from *Billmers and Smith* [1991]. Their data were based on analyses of spectra of sulfur vapor at 723 and 843 K.

The photodissociation quantum yield for these wavelengths was assumed to be 0.0.

C Kinetic Reactions

Table 5C.1: Reactions Referenced in Text

	Reaction		
G1	$CO_2 + h\nu$	$\rightarrow$	$CO + O$
G2	$CO + O + M$	$\rightarrow$	$CO_2 + M$
G3	$2\ O + M$	$\rightarrow$	$O_2 + M$
G4	$ClOO + CO$	$\rightarrow$	$ClO + CO_2$
G5	$ClOO + M$	$\rightarrow$	$Cl + O_2 + M$
G6	$ClCO + O_2$	$\rightarrow$	$ClO + CO_2$
G7	$Cl + CO + M$	$\rightarrow$	$ClCO + M$
G8	$ClCO + M$	$\rightarrow$	$Cl + CO + M$
G9	$NO + HO_2$	$\rightarrow$	$NO_2 + OH$
G10	$HCl + HOCl + \text{aerosol}$	$\rightarrow$	$H_2O + Cl_2 + \text{aerosol}$
G11	$SO_2 + h\nu$	$\rightarrow$	products
G12	$BrO + ClO$	$\rightarrow$	$BrCl + BrCl$
G13	$S_2O + H_2O$	$\rightarrow$	$H_2S_2O_2$
G14	$O + HOCl$	$\rightarrow$	$OH + ClO$
G15	$F + H_2$	$\rightarrow$	$HF + H$
G16	$O + HBr$	$\rightarrow$	$OH + Br$
G17	$Br + O_3$	$\rightarrow$	$BrO + O_2$
G18	$Cl + \text{aerosol}$	$\rightarrow$	$HCl + \text{aerosol}$
G19	$ClO + \text{aerosol}$	$\rightarrow$	$HCl + \text{aerosol}$
G20	$HCl + HOBr + \text{aerosol}$	$\rightarrow$	$H_2O + BrCl + \text{aerosol}$

The photolysis reactions listed in this table are included in the photochemical model (see Appendix A), but a separate reaction was included for each of the possible product combinations in the actual model calculations. The generic reaction listed here refers to all possible products and is referenced in the text for ease of explanation.

The reactions with M in this table are included for ease of explanation in the text. Separate reactions with M replaced by CO_2 and N_2 were included in the photochemical model as noted in the remainder of Table C.1.

The remaining reactions are referenced in the text but were *not* included in the photochemical model.

Table 5C.2: Kinetic Reactions in Nominal Photochemical Model (part 1)

	Reaction	Rate Coefficient	Reference
K96	$CO + O + N_2 \rightarrow CO_2 + N_2$	$3.4 \times 10^{-33}\ e^{-2180/T}$	$M2$
K97	$CO + O + CO_2 \rightarrow 2\ CO_2$	$4.0 \times 10^{-33}\ e^{-1940/T}$	$M3$
K98	$2\ O + N_2 \rightarrow O_2(^1\Delta) + N_2$	$1.7 \times 10^{-28}\ T^{-2.0}$	$E0M9$
K99	$2\ O + N_2 \rightarrow O_2 + N_2$	$2.6 \times 10^{-28}\ T^{-2.0}$	$E0$
K100	$2\ O + CO_2 \rightarrow O_2(^1\Delta) + CO_2$	$7.7 \times 10^{-28}\ T^{-2.0}$	$E4M9$
K101	$2\ O + CO_2 \rightarrow O_2 + CO_2$	$5.2 \times 10^{-28}\ T^{-2.0}$	$E4$
K102	$2\ O + O_2 \rightarrow O_2(^1\Delta) + O_2$	$5.7 \times 10^{-29}\ T^{-2.0}$	$E4M9$
K103	$2\ O + CO \rightarrow O_2(^1\Delta) + CO$	$2.7 \times 10^{-28}\ T^{-2.0}$	$E5M9$
K104	$O + O_2 + N_2 \rightarrow O_3 + N_2$	$k_0 = 5.6 \times 10^{-34}\ (T/300)^{-2.5}$	$M3$
		$k_\infty = 2.8 \times 10^{-12}$	$M3$
K105	$O + O_2 + CO_2 \rightarrow O_3 + CO_2$	$k_0 = 1.4 \times 10^{-33}\ (T/300)^{-2.5}$	$M4$
		$k_\infty = 2.8 \times 10^{-12}$	$M3$
K106	$O + O_3 \rightarrow 2\ O_2$	$8.0 \times 10^{-12}\ e^{-2060/T}$	$A0$
K107	$O(^1D) + N_2 \rightarrow O + N_2$	$1.8 \times 10^{-11}\ e^{110/T}$	$A0$
K108	$O(^1D) + CO_2 \rightarrow O + CO_2$	$7.4 \times 10^{-11}\ e^{120/T}$	$A0$
K109	$O(^1D) + H_2O \rightarrow 2\ OH$	2.2×10^{-10}	$A0$
K110	$O(^1D) + H_2 \rightarrow H + OH$	1.1×10^{-10}	$A0$
K111	$O(^1D) + O_2 \rightarrow O + O_2(^1\Delta)$	$2.3 \times 10^{-11}\ e^{70/T}$	$A0M0$
K112	$O(^1D) + O_3 \rightarrow O_2 + O_2(^1\Delta)$	2.4×10^{-11}	$A0M9$
K113	$H + O_2 + N_2 \rightarrow HO_2 + N_2$	$k_0 = 5.7 \times 10^{-32}\ (T/300)^{-1.6}$	$A0$
		$k_\infty = 7.5 \times 10^{-11}$	$A0$
K114	$H + O_2 + CO_2 \rightarrow HO_2 + CO_2$	$k_0 = 2.0 \times 10^{-31}\ (T/300)^{-1.6}$	$A5$
		$k_\infty = 7.5 \times 10^{-11}$	$A0$
K115	$H + O_3 \rightarrow OH + O_2$	$1.4 \times 10^{-10}\ e^{-470/T}$	$A0$
K116	$O + HO_2 \rightarrow OH + O_2(^1\Delta)$	$6.0 \times 10^{-13}\ e^{200/T}$	$A0M9$
K117	$O + HO_2 \rightarrow OH + O_2$	$2.9 \times 10^{-11}\ e^{200/T}$	$A0$
K118	$O + OH \rightarrow O_2 + H$	$2.2 \times 10^{-11}\ e^{120/T}$	$A0$
K119	$OH + CO \rightarrow CO_2 + H$	$1.5 \times 10^{-13}\ (1.0 + 0.6\ P_{atm})$	$A0^*$
K120	$OH + H_2 \rightarrow H_2O + H$	$5.5 \times 10^{-12}\ e^{-2000/T}$	$A0$
K121	$OH + O_3 \rightarrow HO_2 + O_2$	$1.6 \times 10^{-12}\ e^{-940/T}$	$A0M9$

Table 5C.2: Kinetic Reactions in Nominal Photochemical Model (part 2)

	Reaction			Rate Coefficient	Reference
K122	$HO_2 + O_3$	$\rightarrow$	$OH + 2\ O_2$	$1.1 \times 10^{-14}\ e^{-500/T}$	$A0$
K123	$H + HO_2$	$\rightarrow$	$2\ OH$	7.3×10^{-11}	$A0h0$
K124	$H + HO_2$	$\rightarrow$	$H_2O + O$	1.6×10^{-12}	$A0h0$
K125	$H + HO_2$	$\rightarrow$	$H_2 + O_2(^1\Delta)$	1.3×10^{-13}	$A0h0$
K126	$H + HO_2$	$\rightarrow$	$H_2 + O_2$	6.4×10^{-12}	$A0h0$
K127	$OH + O_3$	$\rightarrow$	$HO_2 + O_2(^1\Delta)$	$3.2 \times 10^{-14}\ e^{-940/T}$	$A0M9$
K128	$OH + HO_2$	$\rightarrow$	$H_2O + O_2(^1\Delta)$	$9.6 \times 10^{-13}\ e^{250/T}$	$A0$
K129	$OH + HO_2$	$\rightarrow$	$H_2O + O_2$	$4.7 \times 10^{-11}\ e^{250/T}$	$A0M9$
K130	$2\ HO_2$	$\rightarrow$	$H_2O_2 + O_2(^1\Delta)$	$4.6 \times 10^{-15}\ e^{600/T}$	$A0M9$
K131	$2\ HO_2$	$\rightarrow$	$H_2O_2 + O_2$	$2.2 \times 10^{-13}\ e^{600/T}$	$A0M9$
K132	$OH + H_2O_2$	$\rightarrow$	$H_2O + HO_2$	$2.9 \times 10^{-12}\ e^{-160/T}$	$A0$
K133	$2\ H + N_2$	$\rightarrow$	$H_2 + N_2$	$1.5 \times 10^{-29}\ T^{-1.3}$	$D0$
K134	$2\ H + CO_2$	$\rightarrow$	$H_2 + CO_2$	$5.0 \times 10^{-29}\ T^{-1.3}$	$D5$
K135	$H + HCl$	$\rightarrow$	$H_2 + Cl$	$1.5 \times 10^{-11}\ e^{-1750/T}$	$M3$
K136	$OH + HCl$	$\rightarrow$	$Cl + H_2O$	$2.6 \times 10^{-12}\ e^{-350/T}$	$A0$
K137	$O + HCl$	$\rightarrow$	$OH + Cl$	$1.0 \times 10^{-11}\ e^{-3300/T}$	$A0$
K138	$Cl + H_2$	$\rightarrow$	$HCl + H$	$3.7 \times 10^{-11}\ e^{-2300/T}$	$A0$
K139	$Cl + OH$	$\rightarrow$	$HCl + O$	$1.2 \times 10^{0}\ e^{-510/T}$	$F1$
K140	$Cl + HO_2$	$\rightarrow$	$HCl + O_2(^1\Delta)$	$3.6 \times 10^{-13}\ e^{170/T}$	$A0M9$
K141	$Cl + HO_2$	$\rightarrow$	$HCl + O_2$	$1.8 \times 10^{-11}\ e^{170/T}$	$A0M9$
K142	$Cl + H_2O_2$	$\rightarrow$	$HCl + HO_2$	$1.1 \times 10^{-11}\ e^{-980/T}$	$A0$
K143	$Cl + O_3$	$\rightarrow$	$ClO + O_2(^1\Delta)$	$5.8 \times 10^{-13}\ e^{-260/T}$	$A0i8$
K144	$Cl + O_3$	$\rightarrow$	$ClO + O_2$	$2.8 \times 10^{-11}\ e^{-260/T}$	$A0i8$
K145	$ClO + O$	$\rightarrow$	$Cl + O_2(^1\Delta)$	$6.0 \times 10^{-13}\ e^{70/T}$	$A0M9$
K146	$ClO + O$	$\rightarrow$	$Cl + O_2$	$2.9 \times 10^{-11}\ e^{70/T}$	$A0M9$
K147	$ClO + OH$	$\rightarrow$	$HO_2 + Cl$	$1.1 \times 10^{-11}\ e^{120/T}$	$A0k0$
K148	$ClO + OH$	$\rightarrow$	$HCl + O_2(^1\Delta)$	$2.2 \times 10^{-13}\ e^{120/T}$	$A0k0$
K149	$ClO + HO_2$	$\rightarrow$	$HOCl + O_2(^1\Delta)$	$1.1 \times 10^{-14}\ e^{700/T}$	$M3M9$
K150	$ClO + CO$	$\rightarrow$	$CO_2 + Cl$	$1.0 \times 10^{-12}\ e^{-3700/T}$	$A9$
K151	$S + O_2$	$\rightarrow$	$SO + O$	2.3×10^{-12}	$A0$

Table 5C.2: Kinetic Reactions in Nominal Photochemical Model (part 3)

	Reaction	Rate Coefficient	Reference
K152	$S + O_3 \rightarrow SO + O_2$	1.2×10^{-11}	$A0$
K153	$SO + O + N_2 \rightarrow SO_2 + N_2$	$k_0 = 7.7 \times 10^{-31}$	$C0$
		$k_\infty = 5.3 \times 10^{-11}$	$C0$
K154	$SO + O + CO_2 \rightarrow SO_2 + CO_2$	$k_0 = 4.2 \times 10^{-30}$	$C0$
		$k_\infty = 5.3 \times 10^{-11}$	$C0$
K155	$SO + O_2 \rightarrow SO_2 + O$	$2.6 \times 10^{-13}\ e^{-2400/T}$	$A0$
K156	$SO + O_3 \rightarrow SO_2 + O_2(^1\Delta)$	$3.6 \times 10^{-13}\ e^{-1100/T}$	$A0M9$
K157	$SO + O_3 \rightarrow SO_2 + O_2$	$3.2 \times 10^{-12}\ e^{-1100/T}$	$A0M9$
K158	$SO + OH \rightarrow SO_2 + H$	8.6×10^{-11}	$A0$
K159	$O + SO_2 + N_2 \rightarrow SO_3 + N_2$	$4.0 \times 10^{-32}\ e^{-1000/T}$	$B0$
K160	$O + SO_2 + CO_2 \rightarrow SO_3 + CO_2$	$1.0 \times 10^{-31}\ e^{-1000/T}$	$B5$
K161	$OH + SO_2 + N_2 \rightarrow H + SO_3 + N_2$	$k_0 = 3.0 \times 10^{-31}\ (T/300)^{-3.3}$	$A0$
		$k_\infty = 1.5 \times 10^{-12}$	$A0$
K162	$OH + SO_2 + CO_2 \rightarrow H + SO_3 + CO_2$	$k_0 = 1.4 \times 10^{-30}\ (T/300)^{-3.3}$	$A4$
		$k_\infty = 1.5 \times 10^{-12}$	$A0$
K163	$HO_2 + SO_2 \rightarrow SO_3 + OH$	1.0×10^{-19}	$A7$
K164	$ClO + SO_2 + M \rightarrow Cl + SO_3 + M$	$1.0 \times 10^{-35}, 4.0 \times 10^{-19}$	$V7$
K165	$SO + ClO \rightarrow SO_2 + Cl$	2.8×10^{-11}	$A0$
K166	$SO + HO_2 \rightarrow SO_2 + OH$	2.8×10^{-11}	$G9$
K167	$2\ SO \rightarrow SO_2 + S$	$1.0 \times 10^{-12}\ e^{-1700/T}$	$N0$
K168	$Cl + SO_2 + M \rightarrow ClSO_2 + M$	$1.3 \times 10^{-34}\ e^{940/T}$	$M3$
K169	$Cl + O_2 + N_2 \rightarrow ClOO + N_2$	$2.7 \times 10^{-33}\ (T/300)^{-1.5}$	$A0$
K170	$Cl + O_2 + CO_2 \rightarrow ClOO + CO_2$	$9.0 \times 10^{-33}\ (T/300)^{-1.5}$	$A5$
K171	$ClOO + N_2 \rightarrow Cl + O_2 + N_2$	$5.7 \times 10^{-25}\ e^{2500/T}$	$A1$
K172	$ClOO + CO_2 \rightarrow Cl + O_2 + CO_2$	$5.7 \times 10^{-25}\ e^{2500/T}$	$A1$
K173	$Cl + H + M \rightarrow HCl + M$	1.0×10^{-32}	$G9$
K174	$CO + Cl + N_2 \rightarrow ClCO + N_2$	$1.3 \times 10^{-33}\ (T/300)^{-3.8}$	$A0$
K175	$CO + Cl + CO_2 \rightarrow ClCO + CO_2$	$4.2 \times 10^{-33}\ (T/300)^{-3.8}$	$A4$
K176	$ClCO + N_2 \rightarrow CO + Cl + N_2$	$1.6 \times 10^{-25}\ e^{4000/T}$	$A1$
K177	$ClCO + CO_2 \rightarrow CO + Cl + CO_2$	$1.6 \times 10^{-25}\ e^{4000/T}$	$A1$

Table 5C.2: Kinetic Reactions in Nominal Photochemical Model (part 4)

	Reaction	Rate Coefficient	Reference
K178	$ClCO + O_2 + M \rightarrow ClCO_3 + M$	$5.7 \times 10^{-15}\ e^{500/T}\ /\ (1 \times 10^{17} + 0.05\ n)$	*G*0
K179	$ClCO + O \rightarrow CO_2 + Cl$	3.0×10^{-11}	*G*9
K180	$ClCO + O \rightarrow CO + ClO$	3.0×10^{-12}	*G*9
K181	$ClCO + H \rightarrow HCl + CO$	1.0×10^{-11}	*G*9
K182	$ClCO + OH \rightarrow HOCl + CO$	1.5×10^{-10}	*P*9
K183	$ClCO + S \rightarrow CO + SCl$	3.0×10^{-11}	*M*9
K184	$ClCO + S \rightarrow OCS + Cl$	3.0×10^{-11}	*M*9
K185	$2\ Cl + N_2 \rightarrow Cl_2 + N_2$	$6.1 \times 10^{-34}\ e^{900/T}$	*F*4
K186	$2\ Cl + CO_2 \rightarrow Cl_2 + CO_2$	$2.6 \times 10^{-33}\ e^{900/T}$	*F*4
K187	$O + Cl_2 \rightarrow ClO + Cl$	$7.4 \times 10^{-12}\ e^{-1650/T}$	*Q*0
K188	$H + Cl_2 \rightarrow HCl + Cl$	$1.4 \times 10^{-10}\ e^{-590/T}$	*F*0
K189	$Cl + HO_2 \rightarrow OH + ClO$	$4.1 \times 10^{-11}\ e^{-450/T}$	*A*0
K190	$ClCO + Cl \rightarrow CO + Cl_2$	$2.2 \times 10^{-9}\ e^{-1670/T}$	*F*8
K191	$2\ ClCO \rightarrow COCl_2 + CO$	5.0×10^{-11}	*G*9
K192	$ClCO + Cl_2 \rightarrow COCl_2 + Cl$	6.4×10^{-2} K178 $(107\ \alpha + n)$	*R*0**
K193	$ClSO_2 + O \rightarrow SO_2 + ClO$	1.0×10^{-11}	*H*9
K194	$ClSO_2 + Cl \rightarrow SO_2 + Cl_2$	1.0×10^{-11}	*H*9
K195	$ClSO_2 + H \rightarrow SO_2 + HCl$	1.0×10^{-11}	*H*9
K196	$ClSO_2 + SCl \rightarrow SO_2 + SCl_2$	5.0×10^{-12}	*M*9
K197	$ClCO_3 + O \rightarrow CO_2 + Cl + O_2$	1.0×10^{-11}	*G*9
K198	$ClCO_3 + Cl \rightarrow CO_2 + Cl + ClO$	1.0×10^{-11}	*G*9
K199	$ClCO_3 + H \rightarrow CO_2 + Cl + OH$	1.0×10^{-11}	*G*9
K200	$Cl + O + M \rightarrow ClO + M$	5.0×10^{-32}	*G*9
K201	$ClO + HO_2 \rightarrow HOCl + O_2$	$5.5 \times 10^{-13}\ e^{700/T}$	*M*3*M*9
K202	$O_2(^1\Delta) + N_2 \rightarrow O_2 + N_2$	1.0×10^{-20}	*A*8
K203	$O_2(^1\Delta) + CO_2 \rightarrow O_2 + CO_2$	2.0×10^{-20}	*A*8
K204	$O_2(^1\Delta) + O \rightarrow O_2 + O$	2.0×10^{-16}	*A*8
K205	$O_2(^1\Delta) + O_2 \rightarrow 2\ O_2$	$3.6 \times 10^{-18}\ e^{-220/T}$	*A*0
K206	$O_2(^1\Delta) + CO \rightarrow O_2 + CO$	1.0×10^{-20}	*M*9
K207	$O_2(^1\Delta) \rightarrow O_2 + h\nu$	2.6×10^{-4}	*S*0

Table 5C.2: Kinetic Reactions in Nominal Photochemical Model (part 5)

	Reaction			Rate Coefficient	Reference
K208	$O_2(^1\Delta) + O_3$	$\rightarrow$	$2\ O_2 + O$	$5.2 \times 10^{-11}\ e^{-2840/T}$	$A0$
K209	$O + H_2$	$\rightarrow$	$OH + H$	$9.9 \times 10^{-32}\ T^{6.5}\ e^{-1460/T}$	$T0$
K210	$2\ OH$	$\rightarrow$	$H_2O + O$	$4.2 \times 10^{-12}\ e^{-240/T}$	$A0$
K211	$O + H_2O_2$	$\rightarrow$	$OH + HO_2$	$1.4 \times 10^{-12}\ e^{-2000/T}$	$A0$
K212	$S + OH$	$\rightarrow$	$SO + H$	6.6×10^{-11}	$A0$
K213	$S + HO_2$	$\rightarrow$	$SO + OH$	$3.0 \times 10^{-11}\ e^{200/T}$	$G9$
K214	$O(^1D) + HCl$	$\rightarrow$	$Cl + OH$	1.0×10^{-10}	$A0$
K217	$2\ S + M$	$\rightarrow$	$S_2 + M$	$k_0 = 1.2 \times 10^{-29}$	$n0$
				$k_\infty = 1.0 \times 10^{-10}$	$M9$
K218	$S + S_2 + M$	$\rightarrow$	$S_3 + M$	$k_0 = 1.0 \times 10^{-30}$	$M9$
				$k_\infty = 3.0 \times 10^{-11}$	$M9$
K219	$2\ S_2 + M$	$\rightarrow$	$S_4 + M$	$k_0 = 2.2 \times 10^{-29}$	$n0$
				$k_\infty = 1.0 \times 10^{-10}$	$r0$
K220	$S + S_3$	$\rightarrow$	$2\ S_2$	3.0×10^{-11}	$M9$
K221	$S + S_3 + M$	$\rightarrow$	$S_4 + M$	$k_0 = 1.0 \times 10^{-30}$	$M9$
				$k_\infty = 3.0 \times 10^{-11}$	$M9$
K222	$S_2 + S_3 + M$	$\rightarrow$	$S_5 + M$	$k_0 = 1.0 \times 10^{-30}$	$M9$
				$k_\infty = 3.0 \times 10^{-11}$	$M9$
K223	$2\ S_3 + M$	$\rightarrow$	$S_6 + M$	$k_0 = 1.0 \times 10^{-30}$	$M9$
				$k_\infty = 3.0 \times 10^{-11}$	$M9$
K224	$S + S_4$	$\rightarrow$	$S_2 + S_3$	3.0×10^{-11}	$M9$
K225	$S + S_4 + M$	$\rightarrow$	$S_5 + M$	$k_0 = 1.0 \times 10^{-30}$	$M9$
				$k_\infty = 3.0 \times 10^{-11}$	$M9$
K226	$S_2 + S_4 + M$	$\rightarrow$	$S_6 + M$	$k_0 = 1.0 \times 10^{-30}$	$M9$
				$k_\infty = 3.0 \times 10^{-11}$	$M9$
K227	$S_4 + M$	$\rightarrow$	$2\ S_2 + M$	$2.0 \times 10^{-27}\ e^{13000/T}$	$M31$
K228	$2\ S_4 + M$	$\rightarrow$	$S_8 + M$	1.0×10^{-30}	$M9$
				$k_\infty = 3.0 \times 10^{-11}$	$M9$
K229	$S + S_5$	$\rightarrow$	$S_2 + S_4$	3.0×10^{-11}	$M9$
K230	$S + S_5 + M$	$\rightarrow$	$S_6 + M$	$k_0 = 1.0 \times 10^{-30}$	$M9$
				$k_\infty = 3.0 \times 10^{-11}$	$M9$

Table 5C.2: Kinetic Reactions in Nominal Photochemical Model (part 6)

	Reaction			Rate Coefficient	Reference
K231	$S_2 + S_5 + M$	$\rightarrow$	$S_7 + M$	$k_0 = 1.0 \times 10^{-30}$	$M9$
				$k_\infty = 3.0 \times 10^{-11}$	$M9$
K232	$S + S_6$	$\rightarrow$	$S_2 + S_5$	3.0×10^{-11}	$M9$
K233	$S + S_6 + M$	$\rightarrow$	$S_7 + M$	$k_0 = 1.0 \times 10^{-30}$	$M9$
				$k_\infty = 3.0 \times 10^{-11}$	$M9$
K234	$S_2 + S_6 + M$	$\rightarrow$	$S_8 + M$	$k_0 = 1.0 \times 10^{-30}$	$M9$
				$k_\infty = 3.0 \times 10^{-11}$	$M9$
K235	$S_6 + M$	$\rightarrow$	$2\ S_3 + M$	$2.0 \times 10^{-29}\ e^{22000/T}$	$M31$
K236	$S + S_7$	$\rightarrow$	$S_2 + S_6$	3.0×10^{-11}	$M9$
K237	$S + S_7 + M$	$\rightarrow$	$S_8 + M$	$k_0 = 1.0 \times 10^{-30}$	$M9$
				$k_\infty = 3.0 \times 10^{-11}$	$M9$
K240	$O + S_2$	$\rightarrow$	$SO + S$	2.0×10^{-11}	$C9$
K241	$O + S_3$	$\rightarrow$	$SO + S_2$	2.0×10^{-11}	$M9$
K242	$O + S_4$	$\rightarrow$	$SO + S_3$	2.0×10^{-11}	$M9$
K243	$SO + O$	$\rightarrow$	$S + O_2$	$6.6 \times 10^{-13}\ e^{-2760/T}$	$I9$
K244	$2\ SO + M$	$\rightarrow$	$(SO)_2 + M$	$k_0 = 4.4 \times 10^{-31}$	$U0$
				$k_\infty = 1.0 \times 10^{-11}$	$M9$
K245	$(SO)_2 + O$	$\rightarrow$	$S_2O + O_2$	3.0×10^{-14}	$G9$
K246	$(SO)_2 + O$	$\rightarrow$	$SO + SO_2$	3.0×10^{-15}	$M9$
K247	$(SO)_2 + SO$	$\rightarrow$	$S_2O + SO_2$	3.0×10^{-14}	$U0$
K248	$(SO)_2 + M$	$\rightarrow$	$2\ SO + M$	$\dagger 1.0 \times 10^{-26}\ e^{10000/T}$	$M91$
K249	$(SO)_2 + S_2$	$\rightarrow$	$2\ S_2O$	3.0×10^{-14}	$M9$
K250	$S_2O + O$	$\rightarrow$	$2\ SO$	1.7×10^{-12}	$C0$
K251	$S_2O + S$	$\rightarrow$	$S_2 + SO$	2.0×10^{-13}	$M9$
K252	$2\ S_2O$	$\rightarrow$	$S_3 + SO_2$	1.0×10^{-14}	$M9$
K253	$S + O + M$	$\rightarrow$	$SO + M$	1.0×10^{-32}	$J9$
K254	$ClCO_3 + S$	$\rightarrow$	$Cl + SO + CO_2$	3.0×10^{-11}	$M9$
K255	$ClCO_3 + SO$	$\rightarrow$	$Cl + SO_2 + CO_2$	1.0×10^{-11}	$M9$
K256	$ClCO_3 + SO_2$	$\rightarrow$	$Cl + SO_3 + CO_2$	1.0×10^{-15}	$M9$
K257	$O + SO_2$	$\rightarrow$	$SO + O_2$	$8.0 \times 10^{-12}\ e^{-9800/T}$	$C0$

Table 5C.2: Kinetic Reactions in Nominal Photochemical Model (part 7)

	Reaction			Rate Coefficient	Reference
K258	$O + SO$	$\rightarrow$	SO_2	3.0×10^{-16}	$C0$
K259	$O_3 + SO_2$	$\rightarrow$	$SO_3 + O_2(^1\Delta)$	$6.0 \times 10^{-14}\ e^{-7000/T}$	$A8M9$
K260	$O_3 + SO_2$	$\rightarrow$	$SO_3 + O_2$	$2.9 \times 10^{-12}\ e^{-7000/T}$	$A8M9$
K261	$O + OCS$	$\rightarrow$	$SO + CO$	$2.1 \times 10^{-11}\ e^{-2200/T}$	$A0$
K262	$S + OCS$	$\rightarrow$	$S_2 + CO$	$4.0 \times 10^{-12}\ e^{-1830/T}$	$M3$
K263	$Cl + OCS$	$\rightarrow$	$SCl + CO$	1.0×10^{-17}	$A7$
K264	$ClO + OCS$	$\rightarrow$	$OSCl + CO$	1.0×10^{-17}	$V7$
K265	$SCl + OCS$	$\rightarrow$	$S_2Cl + CO$	3.0×10^{-16}	$M9$
K266	$S + Cl_2$	$\rightarrow$	$SCl + Cl$	$2.8 \times 10^{-11}\ e^{-290/T}$	$F0$
K267	$Cl + S_4$	$\rightarrow$	$S_2Cl + S_2$	2.0×10^{-12}	$M9$
K268	$O + SCl$	$\rightarrow$	$SO + Cl$	1.2×10^{-10}	$W0$
K269	$Cl + SCl$	$\rightarrow$	$S + Cl_2$	1.0×10^{-14}	$M9$
K270	$Cl + SCl + M$	$\rightarrow$	$SCl_2 + M$	$k_0 = 1.0 \times 10^{-30}$	$M9$
				$k_\infty = 5.0 \times 10^{-11}$	$M9$
K271	$SCl + O_2$	$\rightarrow$	$SO + ClO$	2.0×10^{-15}	$W7$
K272	$2\ SCl$	$\rightarrow$	$S_2 + Cl_2$	6.0×10^{-12}	$p0$
K273	$ClO + Cl + M$	$\rightarrow$	$Cl_2O + M$	5.0×10^{-32}	$L9$
K274	$ClCO + ClCO_3$	$\rightarrow$	$2\ CO_2 + 2\ Cl$	1.0×10^{-11}	$M9$
K275	$2\ ClO$	$\rightarrow$	$Cl + ClOO$	$3.0 \times 10^{-11}\ e^{-2450/T}$	$A0$
K276	$2\ ClO$	$\rightarrow$	$Cl_2 + O_2(^1\Delta)$	$2.0 \times 10^{-14}\ e^{-1590/T}$	$A0M9$
K277	$ClOO + O$	$\rightarrow$	$ClO + O_2(^1\Delta)$	5.0×10^{-13}	$X0M9$
K278	$ClOO + O$	$\rightarrow$	$ClO + O_2$	4.9×10^{-11}	$X0M9$
K279	$Cl + ClOO$	$\rightarrow$	$Cl_2 + O_2(^1\Delta)$	2.3×10^{-12}	$A0i0$
K280	$Cl + ClOO$	$\rightarrow$	$Cl_2 + O_2$	2.3×10^{-10}	$A0i0$
K281	$Cl + ClOO$	$\rightarrow$	$2\ ClO$	1.2×10^{-11}	$A0$
K282	$S + ClOO$	$\rightarrow$	$ClO + SO$	1.0×10^{-11}	$M9$
K283	$S + ClOO$	$\rightarrow$	$SCl + O_2$	4.0×10^{-11}	$M9$
K284	$SO + ClOO$	$\rightarrow$	$OSCl + O_2$	2.0×10^{-11}	$M9$
K285	$SO + Cl_2O_2$	$\rightarrow$	$OSCl + ClOO$	2.0×10^{-11}	$M9$
K286	$ClCO_3 + ClO$	$\rightarrow$	$ClOO + Cl + CO_2$	1.0×10^{-12}	$Y9$

Table 5C.2: Kinetic Reactions in Nominal Photochemical Model (part 8)

	Reaction	Rate Coefficient	Reference
K287	$ClCO_3 + HO_2 \rightarrow ClOO + OH + CO_2$	1.0×10^{-12}	$M9$
K288	$2\ ClCO_3 \rightarrow 2\ Cl + 2\ CO_2 + O_2$	5.0×10^{-12}	$Z9$
K289	$O(^1D) + COCl_2 \rightarrow ClCO + ClO$	3.6×10^{-10}	$A0$
K290	$SO + Cl + M \rightarrow OSCl + M$	$3.0 \times 10^{-33}\ (T/300)^{-5.0}$	$M9$
K291	$OSCl + M \rightarrow SO + Cl + M$	$1.0 \times 10^{-26}\ e^{5000/T}$	$M91$
K292	$OSCl + Cl \rightarrow Cl_2 + SO$	2.3×10^{-11}	$M9$
K293	$SO + OSCl \rightarrow SO_2 + SCl$	6.0×10^{-13}	$g0M9$
K294	$ClO + O_2 + M \rightarrow ClO_3 + M$	$k_0 = 1.0 \times 10^{-32}\ (T/300)^{-2.0}$	$a9$
		$k_\infty = 5.0 \times 10^{-12}\ (T/300)^{-2.0}$	$a9$
K295	$2\ ClO \rightarrow Cl + OClO$	$3.5 \times 10^{-13}\ e^{-1370/T}$	$A0$
K296	$2\ ClO + N_2 \rightarrow Cl_2O_2 + N_2$	$k_0 = 2.2 \times 10^{-32}\ (T/300)^{-3.1}$	$A0$
		$k_\infty = 3.5 \times 10^{-12}\ (T/300)^{-1.0}$	$A0$
K297	$2\ ClO + CO_2 \rightarrow Cl_2O_2 + CO_2$	$k_0 = 7.0 \times 10^{-32}\ (T/300)^{-3.1}$	$A5$
		$k_\infty = 3.5 \times 10^{-12}\ (T/300)^{-1.0}$	$A0$
K298	$ClOO + Cl_2 \rightarrow Cl_2O + ClO$	3.4×10^{-12}	$b0$
K299	$2\ ClOO \rightarrow Cl_2O_2 + O_2$	1.6×10^{-11}	$b0$
K300	$O + OClO \rightarrow ClO + O_2(^1\Delta)$	$4.8 \times 10^{-14}\ e^{-960/T}$	$A0M9$
K301	$O + OClO \rightarrow ClO + O_2$	$2.4 \times 10^{-12}\ e^{-960/T}$	$A0M9$
K302	$O + OClO + N_2 \rightarrow ClO_3 + N_2$	$k_0 = 1.9 \times 10^{-31}\ (T/300)^{-1.1}$	$A0$
		$k_\infty = 3.1 \times 10^{-11}$	$A0$
K303	$O + OClO + CO_2 \rightarrow ClO_3 + CO_2$	$k_0 = 6.0 \times 10^{-31}\ (T/300)^{-1.1}$	$A5$
		$k_\infty = 3.1 \times 10^{-11}$	$A0$
K304	$OClO + O_3 \rightarrow ClO_3 + O_2$	$2.1 \times 10^{-12}\ e^{-4700/T}$	$A0$
K305	$Cl + OClO \rightarrow 2\ ClO$	$3.4 \times 10^{-11}\ e^{160/T}$	$A0$
K306	$ClO + OClO + N_2 \rightarrow Cl_2O_3 + N_2$	$k_0 = 6.2 \times 10^{-32}\ (T/300)^{-4.7}$	$A0$
		$k_\infty = 2.4 \times 10^{-11}$	$A0$
K307	$ClO + OClO + CO_2 \rightarrow Cl_2O_3 + CO_2$	$k_0 = 2.0 \times 10^{-31}\ (T/300)^{-4.7}$	$A5$
		$k_\infty = 2.4 \times 10^{-11}$	$A0$
K308	$Cl + ClO_3 \rightarrow ClO + OClO$	1.0×10^{-10}	$b9$
K309	$Cl + ClO_3 \rightarrow Cl_2O + O_2$	1.0×10^{-10}	$L9$

Table 5C.2: Kinetic Reactions in Nominal Photochemical Model (part 9)

	Reaction	Rate Coefficient	Reference
K310	$ClO + ClO_3 \rightarrow Cl_2O_2 + O_2$	1.0×10^{-12}	$L9$
K311	$ClO + ClO_3 + M \rightarrow Cl_2O_4 + M$	$k_0 = 4.0 \times 10^{-31} (T/300)^{-4.7}$	$K9$
		$k_\infty = 5.0 \times 10^{-11}$	$K9$
K312	$ClO_3 + M \rightarrow ClO + O_2 + M$	$2.9 \times 10^{-26}\ e^{3700/T}$	$A81$
K313	$2\ ClO_3 \rightarrow Cl_2O_2 + 2\ O_2$	5.0×10^{-13}	$L9$
K314	$2\ ClO_3 + M \rightarrow Cl_2O_4 + O_2 + M$	$k_0 = 4.0 \times 10^{-31} (T/300)^{-4.7}$	$K9$
		$k_\infty = 5.0 \times 10^{-11}$	$K9$
K315	$O + Cl_2O \rightarrow 2\ ClO$	$2.7 \times 10^{-11}\ e^{-530/T}$	$A0$
K316	$Cl + Cl_2O \rightarrow Cl_2 + ClO$	$6.2 \times 10^{-11}\ e^{130/T}$	$A0$
K317	$O_3 + Cl_2O_2 \rightarrow ClOO + O_2 + ClO$	1.0×10^{-20}	$A7$
K318	$Cl + Cl_2O_2 \rightarrow Cl_2 + ClOO$	1.0×10^{-10}	$A0$
K319	$2\ Cl_2O_2 \rightarrow 2\ Cl_2 + 2\ O_2$	1.0×10^{-20}	$d8$
K320	$Cl_2O_2 + N_2 \rightarrow 2\ ClO + N_2$	$1.3 \times 10^{-27}\ e^{8744/T}$	$A1$
K321	$Cl_2O_2 + CO_2 \rightarrow 2\ ClO + CO_2$	$1.3 \times 10^{-27}\ e^{8744/T}$	$A1$
K322	$Cl_2O_3 + N_2 \rightarrow ClO + OClO + N_2$	$1.1 \times 10^{-24}\ e^{5455/T}$	$A1$
K323	$Cl_2O_3 + CO_2 \rightarrow ClO + OClO + CO_2$	$1.1 \times 10^{-24}\ e^{5455/T}$	$A1$
K324	$Cl_2O_4 + O \rightarrow OClO + ClO + O_2$	1.0×10^{-10}	$M9$
K325	$Cl_2O_4 + Cl \rightarrow OClO + 2\ ClO$	1.0×10^{-10}	$M9$
K326	$OH + OClO \rightarrow HOCl + O_2(^1\Delta)$	$9.0 \times 10^{-15}\ e^{800/T}$	$A0M9$
K327	$OH + OClO \rightarrow HOCl + O_2$	$4.4 \times 10^{-13}\ e^{800/T}$	$A0M9$
K328	$Cl_2O_4 + H \rightarrow HOCl + O_2 + ClO$	1.0×10^{-10}	$M9$
K329	$Cl_2O_4 + OH \rightarrow OClO + HOCl + O_2$	1.0×10^{-11}	$M9$
K330	$ClCO_3 + ClO \rightarrow OClO + Cl + CO_2$	1.0×10^{-12}	$Y0$
K331	$OH + COCl_2 \rightarrow CHClO + ClO$	5.0×10^{-16}	$B7$
K332	$OH + CHClO \rightarrow H_2O + ClCO$	1.4×10^{-13}	$e9$
K333	$Cl + CHClO \rightarrow HCl + ClCO$	$1.2 \times 10^{-11}\ e^{-815/T}$	$B0$
K334	$ClCO_3 + HO_2 \rightarrow OClO + OH + CO_2$	1.0×10^{-12}	$M9$
K335	$SO + OClO \rightarrow SO_2 + ClO$	1.9×10^{-12}	$A0$
K336	$SCl + S \rightarrow S_2 + Cl$	1.0×10^{-11}	$M9$
K337	$SCl + Cl_2 \rightarrow SCl_2 + Cl$	7.0×10^{-14}	$p0$

Table 5C.2: Kinetic Reactions in Nominal Photochemical Model (part 10)

	Reaction	Rate Coefficient	Reference
K338	$2\ SCl \rightarrow SCl_2 + S$	7.5×10^{-12}	$p8$
K339	$2\ SCl \rightarrow S_2Cl + Cl$	5.4×10^{-11}	$p0$
K340	$2\ SCl + M \rightarrow S_2Cl_2 + M$	4.0×10^{-31}	$M9$
		$k_\infty = 4.0 \times 10^{-12}$	$M9$
K341	$SCl_2 + H \rightarrow HCl + SCl$	2.0×10^{-11}	$M3$
K342	$2\ SCl_2 \rightarrow S_2Cl_2 + Cl_2$	1.0×10^{-20}	$M9$
K343	$Cl + SCl_2 \rightarrow Cl_2 + SCl$	1.0×10^{-19}	$p7$
K344	$S_2Cl + Cl \rightarrow Cl_2 + S_2$	1.0×10^{-11}	$M9$
K345	$S_2Cl + SCl \rightarrow SCl_2 + S_2$	1.0×10^{-12}	$M9$
K346	$Cl + S_2Cl_2 \rightarrow Cl_2 + S_2Cl$	4.3×10^{-12}	$f8$
K347	$SO + SOCl_2 \rightarrow SO_2 + SCl_2$	6.0×10^{-13}	$g0M9$
K366	$O(^1D) + O_2 \rightarrow O + O_2$	$9.0 \times 10^{-12}\ e^{70/T}$	$A0M0$
K367	$O(^1D) + O_3 \rightarrow 2\ O_2$	1.1×10^{-10}	$A0M9$
K368	$O(^1D) + O_3 \rightarrow O_2 + 2\ O$	1.1×10^{-10}	$A0M9$
K369	$2\ HO_2 + M \rightarrow H_2O_2 + O_2 + M$	$1.7 \times 10^{-33}\ e^{1000/T}$	$A0$
K370	$O(^1D) + HCl \rightarrow O + HCl$	1.4×10^{-11}	$A0q0$
K371	$O(^1D) + HCl \rightarrow H + ClO$	3.6×10^{-11}	$A0q0$
K372	$2\ ClO \rightarrow Cl_2 + O_2$	$9.8 \times 10^{-13}\ e^{-1590/T}$	$A0M9$
K376	$CO + O + O_2 \rightarrow CO_2 + O_2$	$3.4 \times 10^{-33}\ e^{-2180/T}$	$M5$
K377	$2\ CO + O \rightarrow CO_2 + CO$	$6.5 \times 10^{-33}\ e^{-2180/T}$	$E0$
K378	$CO + 2\ O \rightarrow CO_2 + O$	$3.4 \times 10^{-33}\ e^{-2180/T}$	$M5$
K379	$O + 2\ O_2 \rightarrow O_3 + O_2$	$k_0 = 5.9 \times 10^{-34}\ (T/300)^{-2.4}$	$M3$
		$k_\infty = 2.8 \times 10^{-12}$	$M3$
K380	$2\ O + O_2 \rightarrow O_3 + O$	$k_0 = 5.9 \times 10^{-34}\ (T/300)^{-2.4}$	$M5$
		$k_\infty = 2.8 \times 10^{-12}$	$M3$
K381	$O + O_2 + CO \rightarrow O_3 + CO$	$k_0 = 6.7 \times 10^{-34}\ (T/300)^{-2.5}$	$M4$
		$k_\infty = 2.8 \times 10^{-12}$	$M3$

Units are $cm^3\ s^{-1}$ for two-body reactions and $cm^6\ s^{-1}$ for three-body reactions. k_0 and k_∞ are the low and high pressure rate coefficients, respectively, for three-body reactions.

Table 5C.2: Kinetic Reactions in Nominal Photochemical Model (part 11)

† Our best estimate of this equilibrium constant is 1.0×10^{-28} exp$(6000/T)$.

* P_{atm} is the pressure in atmospheres.

** K178 is the rate for Reaction K178, α converts Torr to number density in cm^{-3}

Reference Codes: First letter is reference for reaction rate, second letter is reference for branching ratio, if applicable. The numbers after each letter describe type of information used to determine the rate.

References: (A) *DeMore et al.* [1997], (B) *Atkinson et al.* [1992], (C) *Singleton and Cvetanovic* [1988], (D) *Tsang and Hampson* [1986], (E) *Hampson* [1980], (F) *Baulch et al.* [1981], (G) *Yung and DeMore* [1982], (H) *Yung, Y.L.,* [personal communication, 1995] rates used for calculations in *DeMore et al.* [1985], (I) *Leen and Graff* [1988], (J) *Moses, J.,* [personal communication, 1995], (K) *Sander et al.* [1989], (L) *Prasad and Lee* [1994], (M) estimated for this study (see Appendix 5- D), (N) *Martinez and Herron* [1983], (P) *Chang et al.* [1987], (Q) *Wine et al.* [1985] from *Mallard et al.* [1994], (R) *Ohta* [1983], (S) *Badger et al.* [1965], (T) *Robie et al.* [1990] from *Mallard et al.* [1994], (U) *Herron and Huie* [1980], (V) *Eibling and Kaufman* [1983], (W) *Murrells* [1988b], (X) *Basco and Dogra* [1971] from *Mallard et al.* [1994], (Y) *DeMore, W.B.,* [personal communication, 1996], (Z) *Brahan, et al.* [1996], (a) *DeMore* [1990], (b) *Baer et al.* [1991], (d) *DeMore and Tschiukow-Roux* [1990], (e) *Libuda et al.* [1990], (f) *Krasnoperov et al.* [1984], (g) *Donovan et al.* [1969], (h) *Keyser* [1986] from *DeMore et al.* [1997], (i) *Choo and Leu* [1985], (j) *Leu et al.* [1987], (k) *Poulet et al.* [1986] from *DeMore et al.* [1997], (m) *Leu* [1982], (n) *Nicholas et al.* [1979], (p) *Murrells* [1988a], (q) *Wine et al.* [1986] from *DeMore et al.* [1997], (r) *Fowles et al.* [1967].

Data types: (0) Measured or critically evaluated rate, (1) Equilibrium constant, (3) Fit to or average of measured data, (4) Relative efficiency of third-body taken from measurements (usually at only one temperature), (5) Relative efficiency of third-body estimated, (7) 0.1 × reported upper limit, (8) Upper limit, (9) Estimate.

D Sources of Kinetic Reaction Data

The kinetic reaction rates used in the model calculations are summarized in Table 5C.2. Many rates, including some of the most important reactions in the model, were estimated either in previous studies or in the current investigation. The rates that were estimated in the current work are noted in Table 5C.2 with an "*M*." This appendix describes how these rates were estimated.

Enthalpies of Formation

Enthalpies of formation, primarily from *DeMore et al.* [1994], were used to determine if proposed reactions would be exothermic. Enthalpies of formation for the S_x species and for S_2Cl_2 were taken from the 1985 JANAF compilation [*Chase et al.* 1985]. *Billmers and Smith* [1991] found that the JANAF values for S_3 and S_4 did not agree with their spectroscopic measurements, so the JANAF values (which were based on calculations by *Rau et al.* [1973]) may have significant inaccuracies. However, we did not find any more recent work and the thermal decomposition reactions for the S_x species are slower than competing loss reactions at the temperatures found in the Venus middle atmosphere. The enthalpy of formation at 298 K for Cl_2O_4 was estimated to be 43 kcal/mol by *Greenwood and Earnshaw* [1984]. *Takacs* [1978] estimated the enthalpy of formation at 0 K for $ClSO_2$ is -66 kcal/mol and that for OSCl is -21 kcal/mol. Based on comparisons between our model profiles for SO and those retrieved by *Na et al.* [1990] and *Na et al.* [1994], we estimate the heat of formation of $(SO)_2$ is $\gtrsim -16$ kcal/mol.

Estimated Equilibrium Constants

The rate for the $(SO)_2$ decomposition reaction was estimated to be $\sim 1o^{-19}$ by *Yung and DeMore* [1982]. However, the decomposition reaction is likely to be a strong function of temperature so we decided, instead, to estimate the equilibrium constant for the association and thermal decomposition reactions. The equilibrium constant was adjusted so that our predicted SO profile would be similar to those retrieved by *Na et al.* [1990] and *Na et al.* [1994]. Our best estimate for the equilibrium constant is $1 \times 10^{-28} \exp(6000/T)$. For comparison, the equilibrium constant for ClO and Cl_2O_2

is 1.3×10^{-27} exp$(8744/T)$ [*DeMore et al.* 1997].

The enthalpies and entropies of formation for the polysulfur (S_x) species were taken from the 1985 JANAF compilation then equilibrium constants were computed as described in *DeMore et al.* [1997].

Estimated Quenching Reactions

The relative efficiency of CO for collisionally quenching $O_2(a^1\Delta)$ [*Slanger, T.*, Personal Communication, 1997] and $O(^1D)$ was considered to be the same as for N_2. The products of the collisional quenching of $O_2(a^1\Delta)$ that are listed in Table 5C.2 were estimated but the rates were taken from *DeMore et al.* [1997].

Estimated Association Reactions

2S $+M \rightarrow$**S**$_2 + M$ $(1.2 \times 10^{-29}, 1 \times 10^{-10})$

Nicholas et al. [1979] result agrees well with result from *Basco and Pearson* [1967] (even though *Basco and Pearson* [1967] rejected that rate as being too fast) but *Nicholas et al.* [1979] rate is factor of 10 faster than rate from *Fowles et al.* [1967] and a factor of 10^4 faster than rate from *Fair and Thrush* [1969] (see discussion in *Baulch et al.* [1976]). High-pressure limit was estimated to be the same as $2S_2 + M \rightarrow S_4 + M$.

S $+$ **S**$_2 + M \rightarrow$ **S**$_3 + M$ $(1 \times 10^{-30}, 3 \times 10^{-11}$)

Estimated upper limit is based on lack of evidence for autocatalytic cycle involving this reaction in the *Nicholas et al.* [1979] measurement of $2S + M \rightarrow S_2 + M$ and the analysis by *Basco and Pearson* [1967] of the rate required for their proposed autocatalytic cycle. Used 0.1× rate for $2S + M \rightarrow S_2 + M$. High-pressure limit was estimated to be 0.3× rate for $2S + M \rightarrow S_2 + M$.

S $+$ **S**$_3 + M \rightarrow$ **S**$_4 + M$ $(1 \times 10^{-30}, 3 \times 10^{-11})$

Used 0.1× rate for $2S + M \rightarrow S_2 + M$. High-pressure limit was estimated to be 0.3× rate for $2S + M \rightarrow S_2 + M$.

S$_2$+**S**$_3 + M \rightarrow$ **S**$_5 + M$ $(1 \times 10^{-30}, 3 \times 10^{-11})$

Used 0.1× rate for $2S + M \rightarrow S_2 + M$. High-pressure limit was estimated to be 0.3× rate for $2S + M \rightarrow S_2 + M$.

2S$_3 + M \rightarrow$ **S**$_6 + M$ $(1 \times 10^{-30}, 3 \times 10^{-11})$

Used 0.1× rate for 2S $+M \rightarrow S_2 + M$. High-pressure limit was estimated to be 0.3× rate for 2S $+M \rightarrow S_2 + M$.

$\mathbf{S} + \mathbf{S_4} + M \rightarrow \mathbf{S_5} + M$ $(1 \times 10^{-30}, 3 \times 10^{-11})$

Used 0.1× rate for 2S $+M \rightarrow S_2 + M$. High-pressure limit was estimated to be 0.3× rate for 2S $+M \rightarrow S_2 + M$.

$\mathbf{S_2}+\mathbf{S_4} + M \rightarrow \mathbf{S_6} + M$ $(1 \times 10^{-30}, 3 \times 10^{-11})$

Used 0.1× rate for 2S $+M \rightarrow S_2 + M$. High-pressure limit was estimated to be 0.3× rate for 2S $+M \rightarrow S_2 + M$.

$\mathbf{2S_4} + M \rightarrow \mathbf{S_8} + M$ $(1 \times 10^{-30}, 3 \times 10^{-11})$

Used 0.1× rate for 2S $+M \rightarrow S_2 + M$. High-pressure limit was estimated to be 0.3× rate for 2S $+M \rightarrow S_2 + M$.

$\mathbf{S} + \mathbf{S_5} + M \rightarrow \mathbf{S_6} + M$ $(1 \times 10^{-30}, 3 \times 10^{-11})$

Used 0.1× rate for 2S $+M \rightarrow S_2 + M$. High-pressure limit was estimated to be 0.3× rate for 2S $+M \rightarrow S_2 + M$.

$\mathbf{S_2}+\mathbf{S_5} + M \rightarrow \mathbf{S_7} + M$ $(1 \times 10^{-30}, 3 \times 10^{-11})$

Used 0.1× rate for 2S $+M \rightarrow S_2 + M$. High-pressure limit was estimated to be 0.3× rate for 2S $+M \rightarrow S_2 + M$.

$\mathbf{S} + \mathbf{S_6} + M \rightarrow \mathbf{S_7} + M$ $(1 \times 10^{-30}, 3 \times 10^{-11})$

Used 0.1× rate for 2S $+M \rightarrow S_2 + M$. High-pressure limit was estimated to be 0.3× rate for 2S $+M \rightarrow S_2 + M$.

$\mathbf{S_2}+\mathbf{S_6} + M \rightarrow \mathbf{S_8} + M$ $(1 \times 10^{-30}, 3 \times 10^{-11})$

Used 0.1× rate for 2S $+M \rightarrow S_2 + M$. High-pressure limit was estimated to be 0.3× rate for 2S $+M \rightarrow S_2 + M$.

$\mathbf{S} + \mathbf{S_7} + M \rightarrow \mathbf{S_8} + M$ $(1 \times 10^{-30}, 3 \times 10^{-11})$

Used 0.1× rate for 2S $+M \rightarrow S_2 + M$. High-pressure limit was estimated to be 0.3× rate for 2S $+M \rightarrow S_2 + M$.

$\mathbf{2SO} + M \rightarrow \mathbf{(SO)_2} + M$ $(4.4 \times 10^{-31}, 1 \times 10^{-11})$

Low pressure limit rate was taken from *Herron and Huie* [1980] even though newer result [*Cobos et al.* 1985] differs by two orders of magnitude. *Herron and Huie* [1980] had difficulty determining an absolute calibration for their results. However, *Cobos*

et al. [1985] seem to have used the spectrum for S_2O as the spectrum for $(SO)_2$ in analyzing their experiment. Confusion of the spectra for these species lasted for several decades so this was a common problem. No differentiation was made among third bodies. High pressure limit rate was estimated to be 0.1× rate for $2S+M \rightarrow S_2 + M$.

$ClO+ClO_3 + M \rightarrow Cl_2O_4 + M$ $(4 \times 10^{-31}(T/300)^{-4.7}, 5 \times 10^{-11})$

Relative estimate ($2\times$ ClO + OClO $+M \rightarrow Cl_2O_3 + M$) from *Sander et al.* [1989]. Rate for reference reaction from *DeMore et al.* [1994].

$2ClO_3 + M \rightarrow Cl_2O_6 + M$ $(4 \times 10^{-31}(T/300)^{-4.7}, 5 \times 10^{-11})$

Relative estimate ($2\times$ ClO + OClO $+M \rightarrow Cl_2O_3 + M$) from *Sander et al.* [1989]. Rate for reference reaction from *DeMore et al.* [1994].

$2SCl + M \rightarrow S_2Cl_2 + M$ $(4 \times 10^{-31}, 4 \times 10^{-12})$

Estimate low pressure limit rate for reaction is factor of 10 faster than $2ClO + M \rightarrow Cl_2O_2 + M$ at 250 K. Estimate high pressure limit rate is same as $2ClO + M \rightarrow Cl_2O_2 + M$ at 250 K.

$Cl+SCl + M \rightarrow SCl_2 + M$ $(1 \times 10^{-30}, 5 \times 10^{-11})$

Eibling and Kaufman [1983] suggest rate is much faster than Cl + OCS → SCl + CO. *Murrells* [1988a] finds production of SCl_2 but believes three-body rate is too slow so ascribes it to a heterogeneous reaction.

$SO+Cl+M \rightarrow OSCl+M$ $(3 \times 10^{-33}(T/300)^{-5.0})$

Temperature dependence extrapolated from those for $Cl+O_2 + M \rightarrow ClOO+M$ and $Cl+CO+M \rightarrow ClCO+M$ based on this reaction being much more exothermic than those forming ClOO and ClCO. Pre-exponential factor comparable to those for $Cl+O_2+M \rightarrow ClOO+M$ and $Cl+CO+M \rightarrow ClCO+M$.

$Cl+SO_2 + M \rightarrow ClSO_2 + M$ $(1.3 \times 10^{-34}\exp(940/T))$

Temperature dependence for M = Ar and $M = SO_2$ was measured by *Eibling and Kaufman* [1983]. Used temperature dependence that is the mean of that for M = Ar and $M = SO_2$. Relative efficiency for all third-bodies is that for $M = N_2$ as determined by taking the mean of the relative efficiencies measured by *Strattan et al.* [1979] for $M = N_2$ versus M = Ar and $M = SO_2$ at 295K.

$\mathbf{ClSO_2}+\ \mathbf{O_2} + M \rightarrow \mathbf{ClSO_4} + M\ (7 \times 10^{-31})$

Estimate by Yung [*Yung, Y.L.*, Personal Communication, 1996] that was used for October 24, 1984, (final) model calculations for *DeMore et al.* [1985].

Relative Efficiencies for Third-bodies

The mean relative efficiency for $M = CO_2$ compared to $M = N_2$ for all reactions for which both rates have been measured is 3.3. This mean ratio was used to determine the $M = CO_2$ rates for all reactions for which the rate has been measured but the relative efficiency has not. No differentiation was made among the third-bodies when the basic reaction rate is an estimate or there are significant uncertainties in the basic reaction rate (e.g., Reaction K244). The third-bodies for Reaction K178 were not differentiated because the rate for this reaction was measured with $M = CO_2$. [*DeMore et al.* 1997].

$\mathbf{CO} + \mathbf{O} + M \rightarrow \mathbf{CO_2} + M$

For $M = N_2$ used same temperature dependence as for $M = CO$ and relative rate from *Stuhl and Niki* [1971] and *Slanger et al.* [1972] in *Baulch et al.* [1976]. For $M = CO_2$ fit the data by *Slanger et al.* [1972], *Inn* [1973], and *Inn* [1974] in *Baulch et al.* [1976]. For $M = O_2$ used the same rate as for $M = N_2$. For $M = CO$ used *Hampson* [1980].

$\mathbf{2O} + M \rightarrow \mathbf{O}_2 + M$

For $M = N_2$ used *Hampson* [1980]. For $M = CO_2$ used *Morgan and Schiff* [1963] relative rate in *Baulch et al.* [1976]. For $M = O_2$ used *Marshall* [1962] and *Morgan and Schiff* [1963] relative rates in *Baulch et al.* [1976]. For $M = CO$ used same as $M = N_2$.

$\mathbf{O} + \mathbf{O_2} + M \rightarrow \mathbf{O_3} + M$

For $M = N_2$ did uncertainty-weighted fit to "preferred" data identified by *DeMore et al.* [1994] (*Klais et al.* [1980] and *Lin and Leu* [1982]), *Hampson* [1980] (*Arnold and Comes* [1979]), and *Baulch et al.* [1976] (*Kaufman and Kelso* [1967], *Stuhl and Niki* [1971], *Huie et al.* [1972], *Ball and Larkin* [1973]) plus a recent measurement [*Borrell et al.* 1985]. For $M = CO_2$ used the mean of the temperature exponents for $M = N_2$ and $M = O_2$ with relative efficiency derived from the mean value of

the measurements in *Baulch et al.* [1976] (*Kaufman and Kelso* [1967], *Bevan and Johnson* [1973]) at 300 K. For $M = O_2$ did uncertainty-weighted fit to "preferred" data identified by *DeMore et al.* [1994] (*Klais et al.* [1980] and *Lin and Leu* [1982]), *Hampson* [1980] (*Hogan and Burch* [1976], *Arnold and Comes* [1979]), and *Baulch et al.* [1976] (*Marshall et al.* [1960], *Kaufman and Kelso* [1964], *Mathias and Schiff* [1964], *Intezarova and Kondrat'ev* [1967], *Kaufman and Kelso* [1967], *Hochanadel et al.* [1968], *Stuhl and Niki* [1971], *Ball and Larkin* [1973], *Bevan and Johnson* [1973], *Snelling* [1974]) plus two other measurements (*Aref'eva et al.* [1978], *Flesca et al.* [1979]). For $M = CO$ used the mean of the temperature exponents for $M = N_2$ and $M = O_2$ with relative efficiency derived from the measurement in *Baulch et al.* [1976] (*Stuhl and Niki* [1971]) at 300 K. For $M = O$ used estimate by Allen [*Allen, M.A.*, Personal Communication, 1995] that the relative efficiency would be the same as for $M = O_2$. The high pressure limit is the mean of the measurements by *Croce de Cobos and Troe* [1984] and *Borrell et al.* [1985] as reported in *Mallard et al.* [1994].

The fits for $M = N_2$ and $M = O_2$ were done when it was noticed that the published fits had been done without considering the uncertainties associated with the measurements. The rates derived in these fits are $k_0 = 5.6 \times 10^{-34}(T/300)^{-2.5}$ for $M = N_2$ and $k_0 = 1.4 \times 10^{-33}(T/300)^{-2.5}$ for $M = O_2$. The assessed rate for M =air [*DeMore et al.* 1994] is $k_0 = (6.0 \pm 0.5) \times 10^{-34}(T/300)^{(-2.3\pm0.5)}$. The derived temperature dependence is within the assessed uncertainty, but the derived pre-exponential factor is almost three assessed standard deviations larger than that for the assessed rate. The Venus model is not sensitive to the differences between the derived rates and the assessed rates. However, models of the terrestrial mesosphere underpredict the ozone abundance [*Sandor et al.* 1997], so the rates proposed here should be evaluated in terrestrial photochemical models. *Siskind et al.* [1995] empirically found that an increase in the rates for production of ozone that is roughly comparable to that proposed here gave an improved fit to observations for the upper terrestrial stratosphere and mesosphere.

2H $+M \rightarrow$ **H** $_2 + M$

For $M = N_2$ used *Tsang and Hampson* [1986]. For $M = CO_2$ used mean relative rate.

For M=H_2 used *Baulch et al.* [1992].

$$\mathbf{O} + \mathbf{H} + M \rightarrow \mathbf{OH} + M$$

For $M = N_2$ used *Tsang and Hampson* [1986]. For $M = CO_2$ used mean relative rate. For $M = O_2$ used the same rate as for $M = N_2$. For $M = CO$ used the same rate as for $M = N_2$.

$$\mathbf{H} + \mathbf{O_2} + M \rightarrow \mathbf{HO_2} + M$$

For $M = N_2$ used *DeMore et al.* [1994]. For $M = CO_2$ used mean relative rate. For $M = O_2$ used the same rate as for $M = N_2$. For $M = CO$ used the same rate as for $M = N_2$.

$$\mathbf{H} + \mathbf{OH} + M \rightarrow \mathbf{H_2O} + M$$

For $M = N_2$ used *Baulch et al.* [1992]. For $M = CO_2$ used relative rate from *Black and Porter* [1962] in *Baulch et al.* [1972]. For $M = O_2$ used relative rate from *Black and Porter* [1962] in *Baulch et al.* [1972]. For $M = CO$ used the same rate as for $M = N_2$. For M=H_2O used *Baulch et al.* [1992].

$$\mathbf{2OH} + M \rightarrow \mathbf{H_2O_2} + M$$

For $M = N_2$ used *DeMore et al.* [1994]. For $M = CO_2$ used mean relative rate.

$$\mathbf{SO} + \mathbf{O} + M \rightarrow \mathbf{SO_2} + M$$

For $M = N_2$ used *Singleton and Cvetanovic* [1988]. For $M = CO_2$ used *Singleton and Cvetanovic* [1988].

$$\mathbf{O} + \mathbf{SO_2} + M \rightarrow \mathbf{SO_3} + M$$

For $M = N_2$ used *Atkinson et al.* [1992]. For $M = CO_2$ used mean relative rate.

$$\mathbf{OH} + \mathbf{SO_2} + M \rightarrow \mathbf{HOSO_2} + M$$

For $M = N_2$ used *DeMore et al.* [1994]. For $M = CO_2$ used relative rate from *Leu* [1982].

$$\mathbf{2Cl} + M \rightarrow \mathbf{Cl_2} + M$$

For $M = N_2$ used temperature dependence from *Baulch et al.* [1981] and the absolute rate from *Weng et al.* [1987] as reported in *Mallard et al.* [1994]. For $M = CO_2$ used temperature dependence from *Baulch et al.* [1981] and absolute rate from *Weng et al.* [1987] as reported in *Mallard et al.* [1994].

$$\mathbf{Cl} + \mathbf{O_2} + M \rightarrow \mathbf{ClOO} + M$$

For $M = N_2$ used *DeMore et al.* [1994]. For $M = CO_2$ used mean relative rate.

2ClO $+M \rightarrow$ **Cl_2O_2** $+ M$

For $M = N_2$ used *DeMore et al.* [1994]. For $M = CO_2$ used mean relative rate.

O + OClO $+M \rightarrow$ **ClO_3** $+ M$

For $M = N_2$ used *DeMore et al.* [1994]. For $M = CO_2$ used mean relative rate.

ClO + OClO $+M \rightarrow$ **Cl_2O_3** $+ M$

For $M = N_2$ used *DeMore et al.* [1994]. For $M = CO_2$ used mean relative rate.

Cl + CO $+M \rightarrow$ **ClCO** $+M$

For $M = N_2$ used *DeMore et al.* [1994]. For $M = CO_2$ used *Nicovich et al.* [1990]. See discussion in Section 2.2.8.

Estimated Two-body Reactions

Rates for the estimated two-body reactions listed in Table 5C.2 are repeated in Table 5D.1 along with the rationale for the estimated rate.

Effective Yields of $O_2(a^1\Delta)$

Crisp et al. [1996] evaluated the potential effective yield of $O_2(a^1\Delta)$ including both the direct yield and that resulting from collisional quenching of more highly excited states. Since that time, the laboratory measurements on which *Crisp et al.* [1996] based their assessment have been revised [*Slanger, T.*, Personal Communication, 1996]. A revised assessment of the effective yield of $O_2(a^1\Delta)$ from Reaction G3 follows.

(1) Calculated direct recombination yields from $2O + M \rightarrow O_2 + M$ [*Wayne* 1994] are $O_2(A^3\Sigma) = 0.12$, $O_2(A\prime^3\Delta) = 0.36$, $O_2(c^1\Sigma) = 0.08 - 0.09$, $O_2(b^1\Sigma) = 0.06$, $O_2(a^1\Delta) = 0.14 - 0.15$, and $O_2(X^3\Sigma) = 0.24$. These yields neglect possible formation of the $^5\Pi$ state. The $^5\Pi$ state has not been definitively identified, but laboratory studies of Reaction G3 have found a hitherto unidentified state of O_2 that is bound by 0.5 eV and could be the $^5\Pi$ state [*Slanger, T.*, Personal Communication, 1998].

(2) Quenching yields for $O_2^* + M \rightarrow O_2(b^1\Sigma) + M$ for $M = O_2$ are 0.13 [*Slanger, T.*, Personal Communication, 1996], for $M = N_2$ are 0.31 [*Slanger, T.*, Personal Communication, 1996], and for $M = CO_2$ are $\geq$ that for $M = N_2$ [*Slanger, T.*,

Table 5D.1: Estimated Rates for Two-body Reactions (Part 1)

Reaction	Rate	Comment
$S + S_3 \rightarrow 2S_2$	3×10^{-11}	[a]
$S + S_4 \rightarrow S_2 + S_3$	3×10^{-11}	[a]
$S + S_5 \rightarrow S_2 + S_4$	3×10^{-11}	same as $S + S_4 \rightarrow S_2 + S_3$
$S + S_6 \rightarrow S_2 + S_5$	3×10^{-11}	same as $S + S_4 \rightarrow S_2 + S_3$
$S + S_7 \rightarrow S_2 + S_6$	3×10^{-11}	same as $S + S_4 \rightarrow S_2 + S_3$
$O + S_3 \rightarrow SO + S_2$	2×10^{-11}	same as $O + S_2 \rightarrow SO + S$
$O + S_4 \rightarrow SO + S_3$	2×10^{-11}	same as $O + S_2 \rightarrow SO + S$
$(SO)_2 + O \rightarrow SO + SO_2$	3×10^{-14}	0.1×rate for $(SO)_2 + O \rightarrow S_2O + O_2$
$(SO)_2 + S_2 \rightarrow 2S_2O$	3×10^{-15}	same as $(SO)_2 + O \rightarrow S_2O + O_2$
$S_2O + S \rightarrow S_2 + SO$	2×10^{-13}	0.1×rate for $S_2O + O \rightarrow S_2 + SO$
$2S_2O \rightarrow S_3 + SO_2$	1×10^{-14}	Estimate
$S + OCS \rightarrow S_2 + CO$	4×10^{-12} $\exp(-1830/T)$	[b]
$Cl + S_4 \rightarrow S_2Cl + S_2$	2×10^{-12}	0.1×rate for $O + S_2 \rightarrow SO + S$
$OSCl + Cl \rightarrow Cl_2 + SO$	2.3×10^{-10}	same as $Cl + ClOO \rightarrow Cl_2 + O_2$
$OSCl + Cl \rightarrow ClO + SCl$	1.2×10^{-11}	same as $Cl + ClOO \rightarrow 2ClO$
$ClSO_2 + SCl \rightarrow SO_2 + SCl_2$	5×10^{-12}	0.5× rate for $ClSO_2 + Cl \rightarrow SO_2 + Cl$
$S_2Cl + Cl \rightarrow Cl_2 + S_2$	1×10^{-11}	[c]
$S_2Cl + SCl \rightarrow SCl_2 + S_2$	1×10^{-12}	[d]
$SCl + OCS \rightarrow S_2Cl + CO$	3×10^{-16}	Geometric mean of rates at 300K for S + OCS and Cl + OCS
$Cl + SCl \rightarrow S + Cl_2$	1×10^{-14}	[e]
$SCl + S \rightarrow S_2 + Cl$	1×10^{-11}	[f]
$SCl_2 + H \rightarrow HCl + SCl$	2×10^{-11}	mean of *Sung and Setser* [1978] and *Hildebrandt et al.* [1984]
$2SCl_2 \rightarrow S_2Cl_2 + Cl_2$	1×10^{-20}	[g]
$SO + OSCl \rightarrow SO_2 + SCl$	6×10^{-13}	[h]
$SO + SOCl_2 \rightarrow SO_2 + SCl_2$	6×10^{-13}	[h]
$ClCO + S \rightarrow OCS + Cl$	3×10^{-11}	same as $ClCO + O \rightarrow Cl + CO_2$
$ClCO + S \rightarrow SCl + CO$	3×10^{-11}	same as $ClCO + O \rightarrow Cl + CO_2$

[a] *Langford and Oldershaw* [1973] believed rate would be near the gas kinetic limit since it is strongly exothermic but *Nicholas et al.* [1979] found no evidence for reaction. [b] Temperature dependence from *Klemm and Davis* [1974] as reported in *Mallard et al.* [1994]. Rate at 300K, mean of *Jakubowski et al.* [1972], *Klemm and Davis* [1974], and *Breckenridge and Taube* [1970] as reported in *Mallard et al.* [1994]. [c] *Murrells* [1988a] found evidence of loss of S_2Cl at long reaction times and ascribed it to this reaction. [d] Alternate explanation proposed by *Murrells* [1988a] for loss of S_2Cl at long reaction times. [e] Based on *Murrells'* [1988a] conclusion that SCl does not react rapidly with Cl. [f] Based on *Murrells'* [1988a] opinion that this reaction is probably rapid. [g] *Murray et al.* [1976] reported that a sufficient amount of SCl_2 would self-react in 30 – 60 minutes that a sample cell containing SCl_2 would have to be replaced at that time interval. [h] Total rate for $SO + OSCl \rightarrow SO_2 + SCl$ and $SO + SOCl_2 \rightarrow SO_2 + SCl_2$ was inferred by *Donovan et al.* [1969]. Apportionment between rates is an estimate.

Table 5D.1: Estimated Rates for Two-body Reactions (Part 2)

Reaction	Rate	Comment
$Cl_2O_4+O \rightarrow OClO+ClO+O_2$	1×10^{-10}	same as $Cl+ClO_3 \rightarrow ClO+ClOO$
$Cl_2O_4+O_2 \rightarrow Cl_2O_6$	1×10^{-11}	same as $Cl+ClO_3 \rightarrow ClO+ClOO$
$Cl_2O_4+H \rightarrow HOCl+O_2+ClO$	1×10^{-10}	same as $Cl+ClO_3 \rightarrow ClO+ClOO$
$Cl_2O_4+OH \rightarrow OClO+HOCl+O_2$	1×10^{-11}	0.1× rate for $Cl_2O_4+O \rightarrow OClO+ClO+O_2$
$Cl_2O_4+Cl \rightarrow OClO+2ClO$	1×10^{-10}	same as $Cl+ClO_3 \rightarrow ClO+ClOO$
$ClO+HO_2 \rightarrow HOCl+O_2$	5.5×10^{-13} exp$(700/T)$	mean of *DeMore et al.* [1994] and *Laszlo and Sander* [1997]
$ClCO_3+ClCO \rightarrow 2Cl+2CO_2$	1×10^{-11}	same as $ClCO_3+O \rightarrow Cl+O_2+CO_2$
$ClCO_3+HO_2 \rightarrow OClO+OH+CO_2$	1×10^{-12}	same as $ClCO_3+ClO \rightarrow OClO+Cl+CO_2$
$ClCO_3+HO_2 \rightarrow ClOO+OH+CO_2$	1×10^{-12}	same as $ClCO_3+ClO \rightarrow OClO+Cl+CO_2$
$ClCO_3+S \rightarrow Cl+SO+CO_2$	3×10^{-11}	[i] 3× rate for $ClCO_3+O \rightarrow Cl+CO_2+O_2$
$ClCO_3+SO \rightarrow Cl+SO_2+CO_2$	1×10^{-11}	same as $ClCO_3+O \rightarrow Cl+CO_2+O_2$
$ClCO_3+SO_2 \rightarrow Cl+SO_3+CO_2$	1×10^{-15}	[i]
$O_2(^1\Delta)+CO \rightarrow O_2+CO$	1×10^{-20}	same as upper limit for $O_2(^1\Delta)+N_2$
$S+ClOO \rightarrow ClO+SO$	1×10^{-11}	0.2× rate for $O+ClOO \rightarrow ClO+O_2$
$S+ClOO \rightarrow SCl+O_2$	4×10^{-11}	0.8× rate for $O+ClOO \rightarrow ClO+O_2$
$SO+ClOO \rightarrow OSCl+O_2$	2×10^{-11}	0.4× rate for $O+ClOO \rightarrow ClO+O_2$
$SO+Cl_2O_2 \rightarrow OSCl+ClOO$	2×10^{-11}	0.4× rate for $O+ClOO \rightarrow ClO+O_2$
$ClO+CO \rightarrow CO_2+Cl$	1×10^{-12}	*DeMore et al.* [1994]
$H+HCl \rightarrow H_2+Cl$	1.5×10^{-11} exp$(-1750/T)$	Products estimated [j]
$H+Cl_2 \rightarrow HCl+Cl$	1.4×10^{-10} exp$(-590/T)$	mean of *Seeley et al.* [1993] and *Baulch et al.* [1981]

[i] products [*Yung, Y.L.*, Personal Communication, 1997]

[j] Temperature dependence is mean of *Baulch et al.* [1981], *Kita and Stedman* [1982], and *Miller and Gordon* [1981] as reported in *Mallard et al.* [1994] Rate at 298 K is mean of same studies

Personal Communication, 1995].

(3) Quenching yield for $O_2(b^1\Sigma) + M \rightarrow O_2(a^1\Delta) + M$ for $M = CO_2$ are > 0.9 [*Wildt et al.* 1988; *Fink et al.* 1991].

(4) Thus, the effective yield of $O_2(a^1\Delta)$ from $2O + M \rightarrow O_2 + M$ for $M = O_2$ is 0.30, for $M = N_2$ is 0.40 ± 0.19, and for $M = CO_2$ is $\sim 0.4 - 0.75$. The effective yield of $O_2(a^1\Delta)$ assumed in the nominal model for $M = O_2$ is 0.30, for $M = N_2$ and $M = CO$ is 0.40, and $M = CO_2$ is 0.60.

Yields of $O_2(a^1\Delta)$ that are based on measured direct yields but also include an estimate of the collisional quenching cascade from higher excited levels are given in Table 5D.2. Estimated effective yields of $O_2(a^1\Delta)$ from other reactions are given in Table 5D.3. If the direct yield of the $^5\Pi$ state in Reaction G3 is 50% as predicted in theoretical calculations [*Wayne* 1994] and if the quenching efficiency from the higher excited states to the $a^1\Delta$ state in a predominantly CO_2 atmosphere is $\sim 100\%$, then current laboratory and theoretical studies suggest the effective yield of $O_2(a^1\Delta)$ from Reactions K101 and K100 could be $\sim 90\%$.

Table 5D.2: Yields for $O_2(a^1\Delta)$ based on laboratory data

Reaction	Yield	Comment
$O(^1D)+ O_2 \rightarrow O + O_2(a^1\Delta)$	0.7	[a]
$H + HO_2 \rightarrow H_2+ O_2(a^1\Delta)$	0.02	see *Leu and Yung* [1987].
$2HO_2 \rightarrow H_2O_2+O_2(a^1\Delta)$	0.02	same as $H + HO_2 \rightarrow H_2+ O_2$ *Atkinson et al.* [1992]
$Cl + ClOO \rightarrow Cl_2+ O_2(a^1\Delta)$	0.01	*Choo and Leu* [1985] *DeMore et al.* [1994]
$Cl + O_3 \rightarrow ClO + O_2(a^1\Delta)$	0.02	*Choo and Leu* [1985] *DeMore et al.* [1994]
$ClO + O \rightarrow Cl + O_2(a^1\Delta)$	0.02	same as $H + HO_2 \rightarrow H_2+ O_2$ *Leu and Yung* [1987] *DeMore et al.* [1994]
$2ClO \rightarrow Cl_2+ O_2(a^1\Delta)$	0.02	same as $H + HO_2 \rightarrow H_2+ O_2$ *Choo and Leu* [1985]
$Cl +HO_2 \rightarrow HCl + O_2(a^1\Delta)$	0.02	same as $H + HO_2 \rightarrow H_2+ O_2$ *Leu and Yung* [1987]
$ClO + OH \rightarrow HCl + O_2(a^1\Delta)$	[b]0.02	*Poulet et al.* [1986] *Dubey and Smith* [1997]
$O + HO_2 \rightarrow OH + O_2(a^1\Delta)$	0.02	same as $H + HO_2 \rightarrow H_2+ O_2$ see *Leu and Yung* [1987]
$O+O_3 \rightarrow 2O_2$	0	*Ellis et al.* [1971] *Davis et al.* [1973]
$H + O_3 \rightarrow OH + O_2(a^1\Delta)$	0	same as $O(^3P)+ O_3 \rightarrow 2O_2$ *Washida et al.* [1980]

[a] *DeMore et al.* [1994] gives 0.8 for producing $O_2(b^1\Sigma)$. As discussed above, the yield of $O_2(a^1\Delta)$ from $O_2(b^1\Sigma)$ is > 0.9 for CO_2 as the quenching species.
[b] Laboratory data indicate yield of O_2 is < 0.14 [*DeMore et al.* 1994]. Salawitch has proposed yield of O_2 is 0.07 to obtain better fits to data from aircraft measurements. *Dubey and Smith* [1997] indicate the O_2 is formed in the $O_2(a^1\Delta)$ state. Branching ratio used (0.02) is from *Poulet et al.* [1986] as reported in *DeMore et al.* [1994].
Note: The indicated effective yields are based on measured direct yields from these reactions but the effective yields include an estimate of the contribution due to collisional quenching from higher excited levels. Consult the indicated references for further information.

Table 5D.3: Estimated Yields for $O_2(a^1\Delta)$

Reaction	Yield	Comment
$O(^1D) + O_3 \rightarrow O_2 + O_2(a^1\Delta)$	0.1	[a]
$SO + O_3 \rightarrow SO_2 + O_2(a^1\Delta)$	0.1	same as $O(^1D) + O_3 \rightarrow 2O_2$
$CS + O_3 \rightarrow OCS + O_2(a^1\Delta)$	0.1	same as $SO + O_3 \rightarrow SO_2 + O_2$
$OH + O_3 \rightarrow HO_2 + O_2(a^1\Delta)$	0.02	same as $H + HO_2 \rightarrow H_2 + O_2$
$OH + HO_2 \rightarrow H_2O + O_2(a^1\Delta)$	0.02	same as $H + HO_2 \rightarrow H_2 + O_2$
$SO_2 + O_3 \rightarrow SO_3 + O_2(a^1\Delta)$	0.02	same as $H + HO_2 \rightarrow H_2 + O_2$
$SH + O_3 \rightarrow HSO + O_2(a^1\Delta)$	0.02	same as $H + HO_2 \rightarrow H_2 + O_2$
$ClO + O_3 \rightarrow ClOO + O_2(a^1\Delta)$	0.02	same as $H + HO_2 \rightarrow H_2 + O_2$
$O + OClO \rightarrow Cl_2 + O_2(a^1\Delta)$	0.02	same as $H + HO_2 \rightarrow H_2 + O_2$
$ClO + HO_2 \rightarrow HOCl + O_2(a^1\Delta)$	0.02	same as $H + HO_2 \rightarrow H_2 + O_2$
$OH + OClO \rightarrow HOCl + O_2(a^1\Delta)$	0.02	same as $H + HO_2 \rightarrow H_2 + O_2$
$O + ClOO \rightarrow ClO + O_2(a^1\Delta)$	0.01	same as $Cl + ClOO \rightarrow Cl2 + O_2$
$O + OH \rightarrow H + O_2(a^1\Delta)$	0	insufficient energy
$HO_2 + O_3 \rightarrow OH + O_2(a^1\Delta)$	0	Estimate
$2HO_2 + M \rightarrow H_2O_2 + O_2(a^1\Delta) + M$	0	Three products
$2HO_2 + H_2O \rightarrow H_2O_2 + O_2(a^1\Delta) + H_2O$	0	based on *Mozurkewich and Benson* [1985]
$2HO_2 + HCl \rightarrow H_2O_2 + O_2(a^1\Delta) + HCl$	0	based on *Mozurkewich and Benson* [1985]
$S + O_3 \rightarrow SO + O_2(a^1\Delta)$	0	same as $O + O_3 \rightarrow 2O_2$
$O + SO_3 + M \rightarrow SO_2 + O_2(a^1\Delta) + M$	0	Three products
$(SO)_2 + O \rightarrow S_2O + O_2(a^1\Delta)$	0	Estimate
$2ClOO \rightarrow Cl_2O_2 + O_2(a^1\Delta)$	0	insufficient energy
$OClO + O_3 \rightarrow ClO + O_2 + O_2(a^1\Delta)$	0	Three products
$O_3 + Cl_2O_2 \rightarrow ClOO + O_2 + ClO$	0	insufficient energy
$2Cl_2O_2 \rightarrow 2Cl2 + O_2 + O_2(a^1\Delta)$	0	Three products
$ClCO + O_3 \rightarrow Cl + CO_2 + O_2(a^1\Delta)$	0	Three products
$ClCO_3 + O \rightarrow Cl_2 + CO_2 + O_2(a^1\Delta)$	0	Three products
$2ClCO_3 \rightarrow Cl2 + 2CO_2 + O_2(a^1\Delta)$	0	Three products

[a] *DeMore et al.* [1994] does not suggest a yield. Three references cited by *DeMore et al.* [1994] are *Davenport et al.* [1972], *Wayne* [1972], and *Amimoto et al.* [1978]. *Davenport et al.* [1972] combined with *Wayne* [1972] suggests $O_2(a^1\Delta)$ yield $\lesssim 0.3$ with yields of $2O_2$ and $O_2 + 2O$ as ~ 0.35 each. *Amimoto et al.* [1978] does not constrain $O_2(a^1\Delta)$ yield but find an average of one $O(^3P)$ produced for every $O(^1D)$ that reacts. Estimated yield for $O_2(a^1\Delta)$ is ~ 0.1.

E Catalytic Cycles

$$H + O_2 + M \rightarrow HO_2 + M$$

$$O + HO_2 \rightarrow OH + O_2$$

$$CO + OH \rightarrow CO_2 + H$$

$$net : CO + O \rightarrow CO_2 \qquad \text{(C1)}$$

$$2(H + O_2 + M \rightarrow HO_2 + M)$$

$$2HO_2 \rightarrow H_2O_2 + O_2$$

$$H_2O_2 + h\nu \rightarrow 2OH$$

$$2(CO + OH \rightarrow CO_2 + H)$$

$$net : \ 2CO + O_2 \rightarrow 2CO_2 \qquad \text{(C2)}$$

$$OCS + h\nu \rightarrow CO + S$$

$$S + OCS \rightarrow CO + S_2$$

$$S_2 + 2CO \rightarrow 2OCS$$

$$net : \ \text{nothing} \qquad \text{(C3)}$$

$$OCS + h\nu \rightarrow CO + S$$

$$3(CO_2 + h\nu \rightarrow CO + O)$$

$$2(2O + M \rightarrow O_2 + M)$$

$$S + O_2 \rightarrow SO + O$$

$$SO + OH \rightarrow SO_2 + H$$

$$H + O_2 + M \rightarrow HO_2 + M$$

$$SO_2 + HO_2 \rightarrow SO_3 + OH$$

$$SO_3 + H_2O + M \rightarrow H_2SO_4 + M$$

$$H_2SO_4 \rightarrow SO_3 + H_2O$$

$$SO_3 + 4CO \rightarrow 3CO_2 + OCS$$

$$net: \text{ nothing} \qquad \text{(C4)}$$

$$2(H_2S + h\nu \rightarrow SH + H)$$

$$2SH \rightarrow H_2S + S$$

$$S + OCS \rightarrow CO + S_2$$

$$net: \ H_2S + OCS \rightarrow 2H + CO + S_2 \qquad \text{(C5)}$$

$$H_2S + h\nu \rightarrow SH + H$$

$$SH + O_2 \rightarrow OH + SO$$

$$net: \ H_2S + O_2 \rightarrow H + OH + SO \qquad \text{(C6)}$$

$$2(H_2S + h\nu \rightarrow SH + H)$$

$$2SH \rightarrow H_2S + S$$

$$S + O_2 \rightarrow SO + O$$

$$net: \ H_2S + O_2 \rightarrow 2H + SO + O. \qquad \text{(C7)}$$

$$SO + h\nu \rightarrow S + O$$

$$S + O_2 \rightarrow SO + O$$

$$net: O_2 \rightarrow 2O \qquad \text{(C8)}$$

$$SO_2 + h\nu \rightarrow SO + O$$

$$2SO \rightarrow SO_2 + S$$

$$S + O_2 \rightarrow SO + O$$

$$net: \ O_2 \rightarrow 2O \qquad \text{(C9)}$$

$$2(SO_2 + O + M \rightarrow SO_3 + M)$$

$$2(SO_3 + H_2O + M \rightarrow H_2SO_4 + M)$$

$$net: \ 2SO_2 + 2O + 2H_2O \rightarrow 2H_2SO_4. \qquad \text{(C10)}$$

$$2(\mathrm{H} + \mathrm{O_2} + M \rightarrow \mathrm{HO_2} + M)$$

$$\mathrm{SO_2} + \mathrm{h}\nu \rightarrow \mathrm{SO} + \mathrm{O}$$

$$\mathrm{SO} + \mathrm{HO_2} \rightarrow \mathrm{SO_2} + \mathrm{OH}$$

$$\mathrm{O} + \mathrm{HO_2} \rightarrow \mathrm{OH} + \mathrm{O_2}$$

$$2(\mathrm{CO} + \mathrm{OH} \rightarrow \mathrm{CO_2} + \mathrm{H})$$

$$net: \ 2\mathrm{CO} + \mathrm{O_2} \rightarrow 2\mathrm{CO_2} \qquad \text{(C11)}$$

$$\mathrm{H} + \mathrm{O_2} + M \rightarrow \mathrm{HO_2} + M$$

$$\mathrm{SO_2} + \mathrm{h}\nu \rightarrow \mathrm{SO} + \mathrm{O}$$

$$\mathrm{SO} + \mathrm{HO_2} \rightarrow \mathrm{SO_2} + \mathrm{OH}$$

$$\mathrm{CO} + \mathrm{OH} \rightarrow \mathrm{CO_2} + \mathrm{H}$$

$$\mathrm{SO_2} + \mathrm{O} + M \rightarrow \mathrm{SO_3} + M$$

$$\mathrm{SO_3} + \mathrm{H_2O} + M \rightarrow \mathrm{H_2SO_4} + M$$

$$net: \ \mathrm{CO} + \mathrm{SO_2} + \mathrm{H_2O} + \mathrm{O_2} \rightarrow \mathrm{CO_2} + \mathrm{H_2SO_4}. \qquad \text{(C12)}$$

$$\mathrm{O} + \mathrm{O_2} + M \rightarrow \mathrm{O_3} + M$$

$$\mathrm{Cl} + \mathrm{O_3} \rightarrow \mathrm{ClOO_2}$$

$$\mathrm{ClO} + \mathrm{O} \rightarrow \mathrm{Cl} + \mathrm{O_2}$$

$$net: \ 2\mathrm{O} \rightarrow \mathrm{O_2}. \qquad \text{(C13)}$$

$$\mathrm{Cl} + \mathrm{CO} + M \rightarrow \mathrm{ClCO} + M$$

$$\mathrm{ClCO} + \mathrm{O_2} + M \rightarrow \mathrm{ClCO_3} + M$$

$$\mathrm{ClCO_3} + \mathrm{O} \rightarrow \mathrm{Cl} + \mathrm{CO_2} + \mathrm{O_2}$$

$$net: \ \mathrm{CO} + \mathrm{O} \rightarrow \mathrm{CO_2} \qquad \text{(C14)}$$

$$\mathrm{Cl} + \mathrm{CO} + M \rightarrow \mathrm{ClCO} + M$$

$$\mathrm{ClCO} + \mathrm{O_2} + M \rightarrow \mathrm{ClCO_3} + M$$

$$\mathrm{ClCO_3} + \mathrm{Cl} \rightarrow \mathrm{Cl} + \mathrm{CO_2} + \mathrm{ClO}$$

$$\mathrm{ClO} + \mathrm{O} \rightarrow \mathrm{Cl} + \mathrm{O_2}$$

$$net: \ \mathrm{CO} + \mathrm{O} \rightarrow \mathrm{CO_2}. \qquad \text{(C15)}$$

$$\mathrm{O} + \mathrm{O_2} + M \rightarrow \mathrm{O_3} + M$$

$$\mathrm{Cl} + \mathrm{O_3} \rightarrow \mathrm{ClO} + \mathrm{O_2}$$

$$\mathrm{ClO} + \mathrm{CO} \rightarrow \mathrm{CO_2} + \mathrm{Cl}$$

$$net: \ \mathrm{CO} + \mathrm{O} \rightarrow \mathrm{CO_2}. \qquad \text{(C16)}$$

$$\mathrm{Cl} + \mathrm{CO} + M \rightarrow \mathrm{ClCO} + M$$

$$\mathrm{ClCO} + \mathrm{O_2} + M \rightarrow \mathrm{ClCO_3} + M$$

$$\mathrm{ClCO_3} + \mathrm{Cl} \rightarrow \mathrm{Cl} + \mathrm{CO_2} + \mathrm{ClO}$$

$$\mathrm{SO_2} + \mathrm{h}\nu \rightarrow \mathrm{SO} + \mathrm{O}$$

$$\mathrm{ClO} + \mathrm{SO} \rightarrow \mathrm{Cl} + \mathrm{SO_2}$$

$$net: \ \mathrm{CO} + \mathrm{O_2} \rightarrow \mathrm{CO_2} + \mathrm{O} \qquad \text{(C17)}$$

$$\mathrm{Cl} + \mathrm{CO} + M \rightarrow \mathrm{ClCO} + M$$

$$\mathrm{ClCO} + \mathrm{O_2} + M \rightarrow \mathrm{ClCO_3} + M$$

$$\mathrm{ClCO_3} + \mathrm{S} \rightarrow \mathrm{Cl} + \mathrm{CO_2} + \mathrm{SO}$$

$$\mathrm{SO} + \mathrm{h}\nu \rightarrow \mathrm{S} + \mathrm{O}$$

$$net: \mathrm{CO} + \mathrm{O_2} \rightarrow \mathrm{CO_2} + \mathrm{O} \qquad \text{(C18)}$$

$$\mathrm{Cl} + \mathrm{CO} + M \rightarrow \mathrm{ClCO} + M$$

$$\mathrm{ClCO} + \mathrm{O_2} + M \rightarrow \mathrm{ClCO_3} + M$$

$$\mathrm{ClCO_3} + \mathrm{SO} \rightarrow \mathrm{Cl} + \mathrm{CO_2} + \mathrm{SO_2}$$

$$\mathrm{SO_2} + \mathrm{h}\nu \rightarrow \mathrm{SO} + \mathrm{O}$$

$$net: \ \mathrm{CO} + \mathrm{O_2} \rightarrow \mathrm{CO_2} + \mathrm{O} \qquad \text{(C19)}$$

$$\mathrm{Cl} + \mathrm{CO} + M \rightarrow \mathrm{ClCO} + M$$

$$\mathrm{ClCO} + \mathrm{O_2} + M \rightarrow \mathrm{ClCO_3} + M$$

$$\mathrm{ClCO_3} + \mathrm{SO_2} \rightarrow Cl + \mathrm{CO_2} + \mathrm{SO_3}$$

$$net: \ \mathrm{CO} + \mathrm{O_2} + \mathrm{SO_2} \rightarrow \mathrm{CO_2} + \mathrm{O} + \mathrm{SO_3} \qquad \text{(C20)}$$

$$\mathrm{OCS} + \mathrm{h}\nu \rightarrow \mathrm{CO} + \mathrm{S}$$

$$\mathrm{S} + \mathrm{Cl_2} \rightarrow \mathrm{SCl} + \mathrm{Cl}$$

$$\mathrm{O} + \mathrm{SCl} \rightarrow \mathrm{SO} + \mathrm{Cl}$$

$$2\mathrm{Cl} + M \rightarrow \mathrm{Cl_2} + M$$

$$\mathrm{SO} + \mathrm{O} + M \rightarrow \mathrm{SO_2} + M$$

$$\mathrm{SO_2} + \mathrm{O} + M \rightarrow \mathrm{SO_3} + M$$

$$net: \ \mathrm{OCS} + 3\mathrm{O} \rightarrow \mathrm{CO} + \mathrm{SO_3}. \qquad \text{(C21)}$$

$$2(\mathrm{OCS} + \mathrm{h}\nu \rightarrow \mathrm{CO} + \mathrm{S})$$

$$2(\mathrm{S} + \mathrm{Cl_2} \rightarrow \mathrm{SCl} + \mathrm{Cl})$$

$$2\mathrm{SCl} \rightarrow \mathrm{S_2} + \mathrm{Cl_2}$$

$$2(\mathrm{Cl} + \mathrm{SO_2} + M \rightarrow \mathrm{ClSO_2} + M)$$

$$\mathrm{Cl_2} + \mathrm{h}\nu \rightarrow 2\mathrm{Cl}$$

$$2(\mathrm{Cl} + \mathrm{ClSO_2} \rightarrow \mathrm{Cl_2} + \mathrm{SO_2})$$

$$net: \ 2\mathrm{OCS} \rightarrow \mathrm{S_2} + 2\mathrm{CO} \qquad \text{(C22)}$$

$$Cl_2 + h\nu \rightarrow 2Cl$$

$$2(Cl + SO_2 + M \rightarrow ClSO_2 + M)$$

$$Cl_2 + h\nu \rightarrow 2Cl$$

$$2(Cl + ClSO_2 \rightarrow Cl_2 + SO_2)$$

$$net: \text{ nothing} \qquad \text{(C23)}$$

F Condensation Versus Vertical Mixing Timescales

The vertical mixing time in our photochemical model is given by

$$\tau_{eddy} = \frac{H^2}{K_{eddy}}, \tag{5.F.1}$$

where H is the scale height and K_{eddy} is the eddy diffusion coefficient.

The timescale for condensation of water vapor onto pre-existing aerosols is given by

$$\frac{1}{\tau_{cnd}} = F_{cnd} = 4\pi r_{aer} D_{H_2O} n_{aer} \beta, \tag{5.F.2}$$

where F_{cnd} is the rate at which water molecules impact the surface of an aerosol particle, r_{aer} is the radius of the aerosol particle, D_{H_2O} is the molecular diffusion coefficient for H_2O through CO_2, n_{aer} is the local number density of aerosol particles, and β is a correction factor [*Seinfeld* 1986, pp. 327 - 338]. Equation 5.F.2 without β is valid only for the continuum regime, where the molecular mean free path is smaller than the particle size. β is a correction factor that enables the extension of equation 5.F.2 through the transition regime to the free molecular regime, where the molecular mean free path is larger than the particle size. One definition for β was developed by *Dahneke* [1983]:

$$\beta = \frac{1 + Kn}{1 + 2Kn(1 + Kn)}, \tag{5.F.3}$$

where

$$Kn = \frac{2D_{H_2O}}{r_{aer} v_{H_2O}}, \tag{5.F.4}$$

Kn is the Knudsen number for the flow, and v_{H_2O} is the mean molecular speed for an H_2O gas molecule. The behavior of the Dahneke transition formula asymptotically approaches the expected forms for both $Kn \rightarrow \{0, \infty\}$: (1) as $Kn \rightarrow 0$, $\beta \rightarrow 1$, and the condensation rate goes to that for continuum flow; (2) as $Kn \rightarrow \infty$, $\beta \rightarrow$

$(r_{aer} v_{H_2O})/(4D_{H_2O})$, and $F_{cnd} \rightarrow \pi r_{aer}^2 v_{H_2O}$.

The time scales for vertical mixing and condensation derived from Equations 5.F.1 and 5.F.2 are shown in Figure 5F.1. One can see from Figure 5F.1 that below $\sim$ 90 km altitude, the timescale for condensation is smaller than the vertical mixing time so the water vapor abundance below $\sim$ 90 km will be determined, primarily, by the equilibrium vapor pressure of water over H_2SO_4.

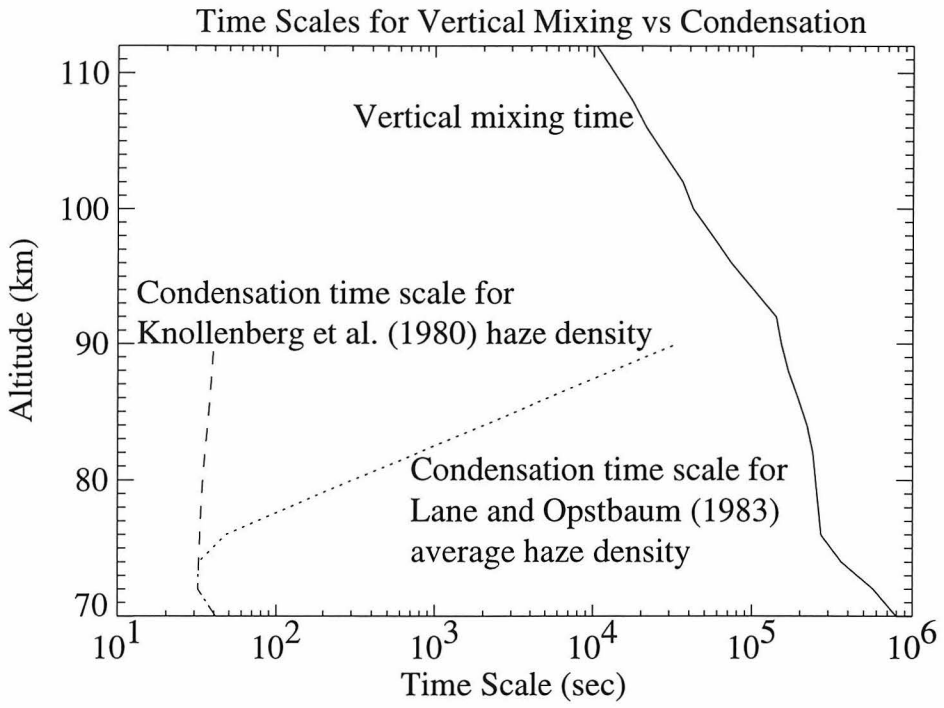

Figure 5F.1: Time Scales for Condensation vs. Vertical Mixing. Vertical mixing time scale was calculated for the nominal model eddy diffusion coefficient and density scale height. Condensation time scales were calculated for two aerosol profiles. Both aerosol profiles use the mode 1 and mode 2 number densities from Figure 16 of *Knollenberg and Hunten* [1980] for 58 - 64 km, the number densities from table 4 of *Knollenberg and Hunten* for 66 km, and the number densities given in the text on page 8072 of *Knollenberg et al.* [1980] for 68 - 70 km. For 72 - 90 km, the nominal profile uses the mode 1 number density in table 3 of *Knollenberg et al.* , while the alternate profile computes the mode 1 number density from the average number density and scale height at 84 km determined by *Lane and Opstbaum* [1983] from *Pioneer Venus* Orbiter Cloud Photopolarimeter observations.

G Vapor Pressure of H_2O Over H_2SO_4

The equilibrium vapor pressure of H_2O over 75 wt% H_2SO_4 for the nominal model was calculated, but primarily *extrapolated*, from the empirical relation given in *Donaldson et al.* [1997]):

$$wp = \frac{(-14.0508 + 0.708928Z)T + 3578.6}{45.5374 + 1.55981Z - 0.197298T}, \tag{5.G.1}$$

where wp is the concentration of the sulfuric acid solution in wt%, $Z = ln(P_{H_2O})$ for P_{H_2O} in mbar, and T is the local atmospheric temperature. *Donaldson et al.* [1997] indicate the range of validity for their relation is $10^{-4} < P_{H_2O} < 10^{-3}$ mbar, $40 < wp < 80$, and $190 < T < 230$ K. We have extrapolated their relation to lower temperatures (160 K) and lower water vapor partial pressures ($<< 10^{-6}$ mbar) so there are errors in our computed water vapor abundances. However, even errors of several orders of magnitude do not have an important impact on our calculations as shown in Section 2.3.2.

More recently, *Tabazadeh et al.* [1997] developed a series of relations for the equilibrium water vapor pressure over sulfuric acid that are valid for $10 \leq wp \leq 80$ and $185 < T < 260$ K.

$$P_{H_2O} = \exp[a + \frac{b}{T} + \frac{c}{T^2}] \tag{5.G.2}$$

where coefficients $a - c$, given in Table 5G.1, are derived from fits to the partial pressures calculated using the model of *Clegg and Brimblecombe* [1995]. (The *Clegg and Brimblecombe* [1995] model predicts water vapor pressures that are within 5% of the values measured by *Giauque et al.* [1960]) Given the larger temperature range over which the *Tabazadeh et al.* [1997] relations are valid, Relation 5.G.2 is probably a better source for the equilibrium vapor pressure of water over sulfuric acid than the Relation 5.G.1. Figure 5G.2 is the same as Figure 5G.1 but gives the equilibrium water vapor pressures obtained using the relations from *Tabazadeh et al.* [1997]. Over the range $10^{-4} \leq P_{H_2O} \leq 10^{-3}$ mbar, both relations (5.G.1 and 5.G.2) agree with

Table 5G.1: Coefficients for Equation 5.G.2

wt% H_2SO_4	a	b	c
10	19.726	-4364.8	-147620
15	19.747	-4390.9	-144690
20	19.761	-4414.7	-142940
25	19.794	-4451.1	-140870
30	19.883	-4519.2	-136500
35	20.078	-4644.0	-127240
40	20.379	-4828.5	-112550
45	20.637	-5011.5	-98811
50	20.682	-5121.3	-94033
55	20.555	-5177.6	-96984
60	20.405	-5252.1	-100840
65	20.383	-5422.4	-97966
70	20.585	-5743.8	-83701
75	21.169	-6310.6	-48396
80	21.808	-6985.9	-12170

each other, as expected. At the lower temperatures and higher sulfuric acid concentrations believed to exist in the Venus atmosphere (e.g., 160 K and 75 wt%), the two relations can differ by several orders of magnitude. The vertical profiles of water vapor predicted using Relations 5.G.1 and 5.G.2 are shown in Figure 5G.3 along with that assumed by *Yung and DeMore* [1982] and the retrieved values from *Encrenaz et al.* [1995].

Donaldson et al. [1997] and *Tabazadeh et al.* [1997] derived their relations based on the vapor pressure data measured by *Giauque et al.* [1960] rather than the calculations by *Gmitro and Vermeulen* [1964] that were used by *Steele and Hamill* [1981] to derive the vapor pressure relations that have been commonly used in the atmospheric science community. This was done because the data from *Giauque et al.* [1960] are believed to be more accurate at low temperatures [*Massucci et al.* 1996] than the calculations by *Gmitro and Vermeulen* [1964] because *Gmitro and Vermeulen* applied corrections to *Giauque et al.*'s [1960] data to achieve consistent partial pressures over

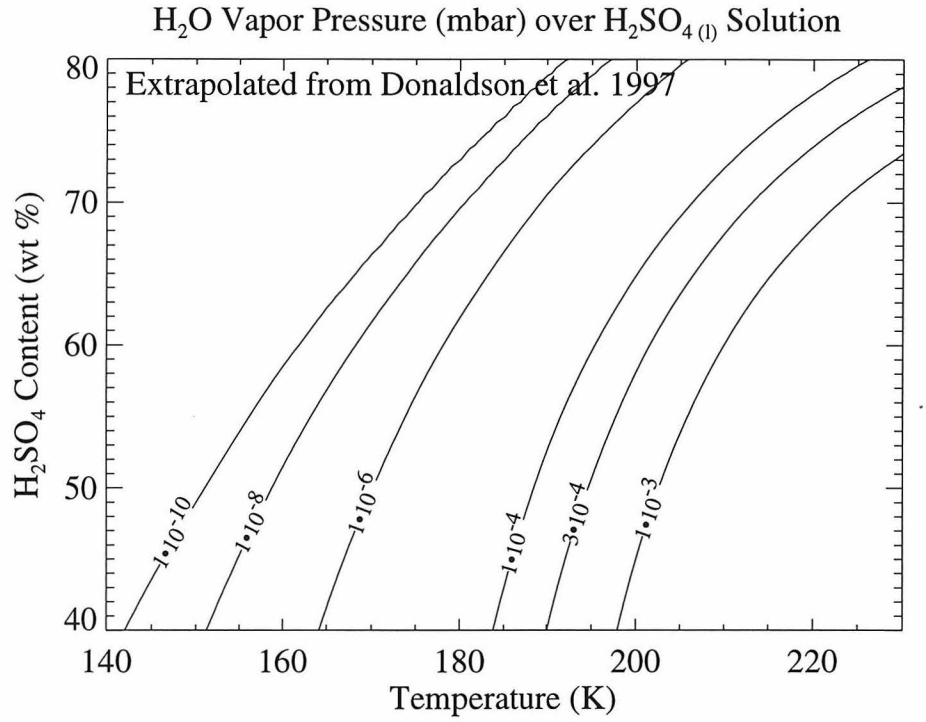

Figure 5G.1: H_2O Vapor Pressure (mbar) over $H_2SO_{4(l)}$ Solution. Equilibrium vapor pressure for water over a solution of liquid sulfuric acid based on Equation 5.G.1 from *Donaldson et al.* [1997]. *All values outside the range* $10^{-4} < P_{H_2O} < 10^{-3}$ *mbar are extrapolated outside the range of validity quoted by Donaldson et al.* [1997].

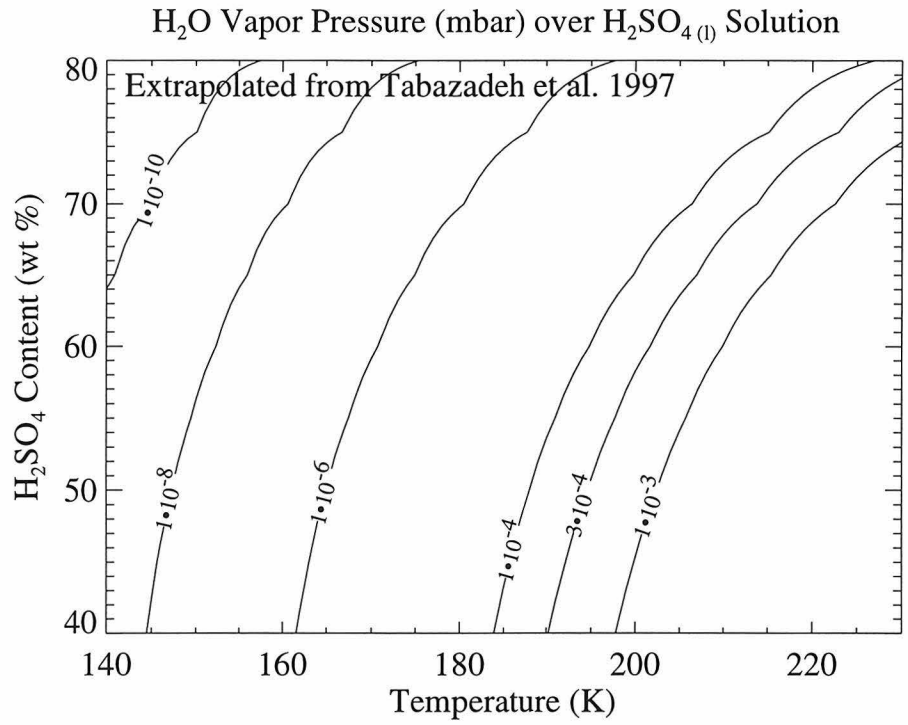

Figure 5G.2: H_2O Vapor Pressure (mbar) over $H_2SO_{4(l)}$ Solution. Equilibrium vapor pressure for water over a solution of liquid sulfuric acid based on Equation 5.G.2 from *Tabazadeh et al.* [1997]. *All values outside the range* $185 < T < 260$ *K are extrapolated outside the range of validity quoted by Tabazadeh et al.* [1997].

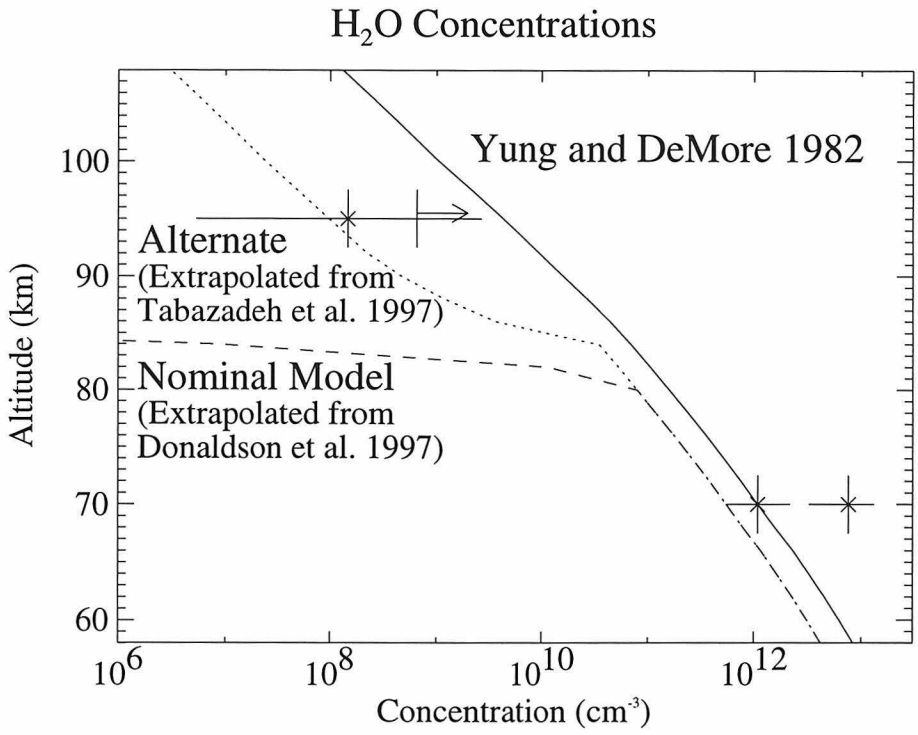

Figure 5G.3: Water vapor profiles calculated using Relations 5.G.1 (the nominal model) and 5.G.2 (an alternate parameterization). Also shown are the water vapor profile assumed in the *Yung and DeMore* [1982] models and the concentrations retrieved from microwave measurements by *Encrenaz et al.* [1995] ($\times$). One measurement gave only a lower limit on the water vapor abundance at $\sim$ 95 km altitude. The concentration uncertainties are those reported by *Encrenaz et al.* [1995]. The altitude uncertainties are estimated based on the discussion in their paper.

the temperature range 25 – 400° C. For this reason, the relations from *Steele and Hamill* [1981] may not be as accurate as desired for atmospheric studies at low temperatures.

H Radiative Transfer Calculation Parameters

The direct irradiance is calculated using the model atmospheres altitude grid at every wavelength bin specified in Table 2.4. The diffuse flux, however, was calculated only at the wavelengths marked with a † in Table 2.4 to reduce computation time. At the intermediate wavelengths, it was interpolated between the nearest calculated values.

The diffuse flux was calculated on a log-linear optical depth grid [*Michelangeli et al.* 1992]. This grid was designed to encompass the broad range of optical depths that are encountered in radiative transfer calculations for a planetary atmosphere while providing good resolution at the altitudes where photodissociation is most important with minimal computation time. The diffuse flux grid has 10 points per decade between the extinction optical depth above the model's upper boundary and optical depth = 0.1 (if the optical depth at the upper boundary is < 0.1). Between optical depths 0.1 and 2 (or the extinction optical depth at the lower boundary, whichever is smaller), the optical depth grid points are separated by a constant value ≤ 0.01. If the extinction optical depth at the lower boundary is > 2, the remaining range is divided so that there are at least 10 points per decade. The diffuse flux at each model altitude is determined by interpolation between the nearest points on the optical depth grid and then added to the direct solar irradiance for that altitude to determine the actinic flux.

The accuracy of the diffuse flux calculation depends primarily on the number of wavelengths included, the number of Gaussian angles, the number of terms in the azimuthal angle expansion, and the resolution of the optical depth grid. The values selected for the results presented in Section 2.3 are 46 wavelengths, 8 Gaussian angles, 16 azimuthal angle terms, and 400 points on a log-linear optical depth grid. The accuracy of the radiative transfer calculation for these computational parameters was assessed by comparison to a reference calculation in which diffuse flux was computed at 80 wavelengths using 30 Gaussian angles and 60 terms in the azimuthal angle expansion on a log-linear optical depth grid with 500 points. *Michelangeli et al.* [1992] found that test cases using 20 Gaussian angles, 40 azimuthal angle terms, and

320 optical depth grid points produced results that were typically within 1% of those calculated by *van de Hulst* [1980] so our reference calculation should be sufficiently accurate to serve as a benchmark.

The largest differences between our standard radiative transfer calculation and our reference calculation occur below 70 km altitude at $195 - 210$ nm and at $\lambda \geq 530$ nm. The differences at long wavelengths were $< 4\%$ and few molecules photodissociate at $\lambda \geq 530$ nm so the impact on our model results from these errors is negligible. The differences at shorter wavelengths are potentially important since they lie at the long wavelength edge of the CO_2 absorption band where HCl and SO_2 absorb strongly. The differences, however, are significant only where the slant optical depth is larger than 10. For example, if one considers actinic fluxes $> 10^3$ photon cm^{-2} s^{-1}, the standard actinic fluxes were within 11% of those in the reference calculation. If one considers only actinic fluxes $> 10^7$ photon cm^{-2} s^{-1}, the maximum difference is 8% and occurs at 195 nm for 68 km altitude. Our sensitivity studies (Section 2.3.2) found only small changes in the column oxygen abundance as a result of much larger changes in the actinic flux at these wavelengths, so the impact on our model results from these errors is not significant. Consequently, the accuracy of the photochemical results should not be limited by the accuracy of the radiative transfer calculations.

The nominal *wavelength-independent* Lambertian albedo for the lower boundary was chosen to be 0.6. This value is the geometric albedo for the upper cloud in *Moroz* [1983] at ~ 400 nm. Wavelengths $\lesssim 300$ nm are strongly absorbed within or above the upper cloud so the albedo of the middle cloud at these wavelengths should not be important for the photochemistry within the upper cloud. Wavelengths $\gtrsim 500$ nm are not absorbed strongly within the upper cloud but O_3 is the only important gas that photodissociates at these longer wavelengths so radiation at visual wavelengths should not be important for the photochemistry within the upper cloud. Hence, we assumed the scattering characteristics for the middle cloud were similar to those for the upper cloud and specified the albedo for the lower boundary as the geometric albedo for the upper cloud at ~ 400 nm.

I Rayleigh Scattering Calculations

Rayleigh scattering is not significant in the Venus middle atmosphere but has been included in our radiative transfer calculation for completeness. The Rayleigh scattering cross section for a mixture of CO_2 and N_2 was calculated from

$$\sigma = \frac{24\pi^3}{L^2\lambda^4}\left(\frac{n^2-1}{n^2+2}\right)^2\rho_0^t, \tag{5.I.1}$$

where L = Loschmidt's number, λ = wavelength of light, ρ_0^t is the depolarization factor for incident unpolarized light as defined in *Young* [1980], and n is the index of refraction. The index of refraction for CO_2 at wavelengths > 192.5 nm was from *Old et al.* [1971], the index of refraction for N_2 was from *Allen* [1976], and the depolarization factors for CO_2 and N_2 were from *Young* [1980]. Rayleigh scattering at $\lambda < 192.5$ nm was neglected since it is not clear how the index of refraction for CO_2 should be extrapolated to these wavelengths [*Edlen* 1966] and absorption by CO_2 is probably much stronger than scattering at these wavelengths. The Caltech/JPL photochemical model (KINETICS) defines the Rayleigh depolarization factor in a manner that differs from the notation in, for example, *Young* [1980] and *Goody and Yung* [1989],

$$KRDF = \frac{1-\Delta}{2+\Delta} \tag{5.I.2}$$

where

$$\Delta = \frac{I^{(l)}(\theta = \frac{\pi}{2})}{I^{(r)}(\theta = \frac{\pi}{2})}. \tag{5.I.3}$$

$KRDF$ is the KINETICS Rayleigh Depolarization Factor, Δ is the *Goody and Yung* [1989] depolarization factor, I is the intensity, and r and l are two orthogonal directions perpendicular to the direction of propagation [*Goody and Yung* [1989], page 298]. $\Delta = \rho_0^t = 0.078$ for CO_2 and $\Delta = 0.0210$ for N_2 *Young* [1980]. ρ_0^t is the Rayleigh Depolarization Factor for incident unpolarized (natural) light in the notation used by *Young* [1980].

J Aerosol Scattering Characteristics

The dominant source of diffuse flux is scattering by aerosol particles in the upper cloud and upper haze. The wavelength-dependent effective extinction cross sections for the mode 1 and mode 2 aerosol particles in the upper haze and upper cloud layer were taken from Tables IV and V in *Crisp* [1986]. The other parameters needed to characterize the aerosol scattering are the single-scattering albedo and the scattering phase function. The radiative transfer routines in our photochemical model consider these parameters to be independent of wavelength so it was necessary to approximate the wavelength-*dependent* values given in *Crisp* [1986]. We used a single-scattering albedo of 0.99 for $\leq$ 70 km altitude and 1.0 for higher altitudes. Our scattering phase function was a single Henyey-Greenstein function [*Henyey and Greenstein* 1941] with asymmetry parameter of 0.7. The extra ultraviolet absorption at $\gtrsim$ 300 nm that *Crisp* [1986] attributed to the mode 1 aerosols in the upper cloud was *not* included in our nominal model since this absorption could be produced by one of the gas-phase species examined in our model (e.g., Cl_2 [*Pollack et al.* 1980; *Yung and DeMore* 1982]).

K Sources of Solar Flux Data

The irradiances at Ly-α in Table 2.4 were estimated based on the relationship [*WMO* 1985],

$$F_0(Ly-\alpha) = 2.25 \times 10^{11} + (0.014 \times 10^{11}) \times (S_a(10.7\text{cm}) - 65), \qquad (5.K.1)$$

where F_0(Ly-α) is the irradiance at Ly-α at 1 AU in photons cm^{-2} s^{-1} line^{-1} and S_a(10.7 cm) is the 10.7-cm (2800 MHz) radio irradiance at 1 AU in units of 10^4 jansky (10^{-22} W m^{-2} Hz^{-1}). 10.7-cm index values (adjusted to the mean distance between the earth and Sun) were taken from those measured at the Penticton, British Columbia, Radio Astrophysical Observatory as published at */stp/SOLAR/FLUX/flux.html* and */STP/SOLAR_DATA/SOLAR_RADIO/FLUX* on the WWW site *http://www.ngdc.noaa.gov*. The 10.7-cm index for the day prior to the *Woods et al.* [1996] measurements was used because *London et al.* [1993] indicate the best (but not perfect [*Meier et al.* 1997; *WMO* 1985]) correlation between the two indices requires a one-day lag for the Ly-α index behind the 10.7-cm index. The adjusted 10.7-cm index values (185.4 for 28 Mar 1992 and 92.8 for 14 Mar 1993) published on the WWW site were multiplied by 0.9 (the recommended correction for antenna gain and ground reflections) then used in equation 5.K.1.

For the remainder of the 120.0 - 410.0 nm region, data from *Woods et al.* [1996] were used. (For the 120.0 - 122.5 nm region, the estimated Ly-α irradiance was subtracted from the integrated irradiance reported by *Woods et al.* [1996].) The data for high solar irradiance (29 March 1992) were from their Table 6 and the data for low solar irradiance (15 April 1993) were from their Table 7. These data are an uncertainty-weighted average of measurements by the SOLSTICE and SUSIM instruments on the UARS satellite. (UARS is the Upper Atmosphere Research Satellite; SOLSTICE is the SOLar STellar Irradiance Comparison Experiment; and SUSIM is the Solar Ultraviolet Spectral Irradiance Monitor.) The measurements were acquired

as part of a cross-comparison experiment between the two solar irradiance instruments on the UARS satellite (SOLSTICE and SUSIM) and two solar instruments on the shuttle ATLAS missions (ATLAS SUSIM and SSBUV). (ATLAS is the ATmospheric Backscatter UltraViolet experiment. SSBUV is the Shuttle Solar Backscatter UltraViolet experiment.) All measurements were collected on the same day, although at different times during the day. The spectral resolution for the average spectrum is 1.1-nm FWHM (full width at half maximum). The spectral resolution for the UARS SUSIM data was 1.1-nm and that for the UARS SOLSTICE data was 0.15-nm. Results from the four instruments agreed to within the 2 σ uncertainty of any one instrument, 5 - 10% for wavelengths $>$ 160 nm and for strong emission features at $<$ 160 nm. However, the results for the solar continuum at $130 - 160$ nm differ by $< 20\%$, and the results for the solar continuum at $<$ 130 nm differ by $\gtrsim 30\%$. The differing results from these instruments would not have a significant impact on our modeling since solar irradiance at $<$ 160 nm, with the exception of irradiance at Ly-α, is primarily absorbed above the upper boundary for our model so these differences would have a negligible impact on our results. At 310.0 - 400.0 nm, the *Woods et al.* [1996] data agreed well with the recommended solar irradiance in *WMO* [1985] (which had been taken from *Nicolet* [1981]). The differences between the irradiances measured on 29 March 1992 and 15 April 1993 were $< 10\%$ for $\gtrsim$ 200.0 nm and $< 1\%$ for $\gtrsim$ 300.0 nm.

For 410.0 - 805.0 nm, the solar irradiances reported by *Neckel and Labs* [1984] were used. These data are the recommended solar irradiances in *WMO* [1985], but the *Neckel and Labs* [1984] data were selected because the *WMO* [1985] compilation degraded the spectral resolution of the data.

L Comparison of S_2O Predictions

The S_2O abundances in the Nominal Model are several orders of magnitude smaller than in the calculations by *Na and Esposito* [1997] and the S_2O abundances in the One-Sigma and Highest ClCO Models are even smaller. The processes for production and destruction of S_2O are the same in the current models and in the *Na and Esposito* [1997] model, and the concentration of S_2O under the (valid) assumption of photochemical equilibrium is given by Equation 5.L.1 from *Na and Esposito* [1997].

$$[S_2O] = \frac{k_{K245}[(SO)_2][O] + k_{K247}[(SO)_2][SO]}{J_{P80} + k_{K250}[O] + k_{K251}[S] + k_{G13}[H_2O]} \tag{5.L.1}$$

Two of the estimated rate constants that affect the concentration of S_2O, however, differ by orders of magnitude in the current model and in the *Na and Esposito* [1997] model: the photolysis rate for S_2O (Reaction P80) and the thermal dissociation rate for $(SO)_2$ (Reaction K248). In the *Na and Esposito* [1997] model, S_2O was primarily lost via Reaction K250 which has a rate of $\sim 10^{-3}$ cm^{-3} sec^{-1} near 60 km altitude. In the current models, S_2O is primarily lost via Reaction P80 which has a the rate of $\sim 10^{-2}$ cm^{-3} sec^{-1} near 60 km altitude. In both the current models and the *Na and Esposito* [1997] model, S_2O was produced from $(SO)_2$, but the thermal dissociation reaction in the current models was estimated to be faster than in the *Na and Esposito* [1997] model. Consequently, the production rate for S_2O in the current models is smaller than in the *Na and Esposito* [1997] model and the loss rate for S_2O in the current model is larger. As a result of these differences, the predicted S_2O concentrations in the current model are much smaller than in the *Na and Esposito* [1997] model. Given the lack of laboratory data, the calculated results for minor sulfur species, such as S_2O, in both the current models and the *Na and Esposito* [1997] model should continue to be considered speculative.

The estimated cross sections used in the current models for photolysis of S_2O were based on semiquantitative information in the chemistry literature (Appendix B) and likely have a factor of 10 uncertainty. *Na and Esposito* [1997] do not detail the source for their estimated photolysis rate for S_2O (3×10^{-7}), but it is the same estimated

rate that was used by *Yung and DeMore* [1982] (who also do not provide a rationale for their estimate).

The rate for Reaction K248 in *Na and Esposito* [1997] was also, apparently, an estimated reaction rate from *Yung and DeMore* [1982]. The rates for this reaction in the current models were also estimates, but an explicit temperature dependence was included in the current estimates by formulating the thermal dissociation rate in terms of an equilibrium constant.

M Verification Tests for the Photochemical Model

Prior to undertaking the calculations reported in Chapter 2, the Caltech/JPL photochemical model (KINETGEN5) was tested for simple cases to verify its results were reasonable. These tests were also used to assess the differences that were found between the KINETGEN5 results and those from the *Yung and DeMore* [1982] and *DeMore et al.* [1985] models.

First, the results from a single short time step were compared to fixed input data such as the temperature to verify the data had been properly entered. Second, the pressures calculated by the model were compared to those calculated using the perfect gas law from the input temperature and number densities. Excellent agreement was found. Third, photolysis rates for a case in which CO_2 was the only photodissociating gas and one in which CO_2 and H_2O_2 were the only photodissociating gases were compared to calculations done outside KINETGEN5. Agreement between the calculations was better than 2% for the optical depth for every wavelength interval, the photolysis rate within every wavelength interval, and the total photolysis rate for each species. Fourth, tests were conducted to verify the species and reaction numbers within the model agreed with those in the standard input and output files.

A more extensive test was then conducted using the full set of chemistry for carbon and oxygen species (e.g., CO_2, CO, O_3, O_2, $O_2(^1\Delta)$, O, and $O(^1D)$). Excellent agreement was found between the KINETGEN5 radiative transfer calculations and order of magnitude estimates. The three-body kinetics rates computed by KINETGEN5 at the low and high pressure limits agreed with the input values, and the calculated kinetic rates at intermediate pressures were reasonable. The O_3 concentration calculated by the model at an intermediate altitude (86 km) agreed to within 25% with that estimated analytically based on a modified version of Chapman chemistry. The altitude at which the maximum airglow emission occurs was lower than then the altitude at which the maximum O concentration occurred. This agrees with models of the terrestrial dayglow, and differs from the assumption made in some calculations using the Venus Thermospheric General Circulation Model [*Bougher, S.*, Personal

Communication, 1995]. The calculated airglow emission for this simple model was within a factor of two of that estimated from scaling the Earth's dayglow, which is a reasonable level of agreement given the assumptions made in the scaling.

Finally, the parameters used for the photochemical modeling described in *DeMore et al.* [1985] were input to determine if the current version of the model would reproduce the results obtained in 1985. When the output photolysis rates from the 1985 model for all species were input to the current version of the model, then the results from the current version agreed to within a few percent with the 1985 results. This indicates the solution procedures in both models give the the same results when given the same input values. However, it was not possible to reproduce the 1985 photolysis rates using the current version of the model. The source for this disagreement (two orders of magnitude for the photolysis rate of H_2O and $\sim 10 - 20\%$ for other species) was not definitively identified. Circumstantial evidence indicates some of the input data used in the 1985 calculations may have been incorrect. Much of the input data (e.g., photodissociation cross sections) that were used in 1985 are no longer available, but significant differences were identified between some reaction rates used in the 1985 model and those published in *Yung and DeMore* [1982], and the photodissociation cross section for SO_3 that was used in the 1985 model differed from the values reported in the the original source by a factor of 10. Given these identified problems with the 1985 calculation and the fact that it used a calculation procedure that is no longer supported (and difficult to reintroduce), no further comparisons were attempted between the KINETGEN5 and the previous Venus model results.